Investigating the Chemical and Electronic Structure of $Fe_xNi_{1-x}(O,OH)_y$ Electrocatalysts in Relation to their OER Performance with Electron and Soft and Hard X-ray Spectroscopy

Zur Erlangung des akademischen Grades einer
DOKTORIN DER NATURWISSENSCHAFTEN
(Dr. rer. nat.)

von der KIT-Fakultät für Chemie und Biowissenschaften des
Karlsruher Instituts für Technologie (KIT) angenommene
DISSERTATION

von M.Sc. Ragini Sengupta

1. Referent: Prof. Dr. Clemens Heske
2. Referent: Prof. Dr. Tonya Vitova

Tag der mündlichen Prüfung: 29. Oktober 2025

Investigating the Chemical and Electronic Structure of $Fe_xNi_{1-x}(O,OH)_y$ Electrocatalysts in Relation to their OER Performance with Electron and Soft and Hard X-ray Spectroscopy

To obtain the academic degree of

Doctor of Natural Sciences

at the KIT- Faculty of Chemistry and Biosciences

Dissertation

By

M.Sc. Ragini Sengupta

1st Reviewer: Prof. Dr. Clemens Heske

2nd Reviewer: Prof. Dr. Tonya Vitova

Date of oral examination: 29th October 2025

Declaration of Authorship

I herewith affirm that I wrote the current thesis on my own and without the usage of any other sources or tools than the cited ones and that this thesis has not been handled neither in this nor in equal form at any other official commission.

Erklärung der Selbstständigkeit

Hiermit versichere ich, die vorliegende Arbeit selbstständig angefertigt zu haben und keine Hilfsmittel jenseits der kenntlich gemachten verwendet zu haben. Weiterhin habe ich weder diese noch eine äquivalente Version dieser Arbeit bei einer anderen Prüfungskommission vorgelegt.

Ort, Datum	Ragini Sengupta
Eggenstein-Leopoldshafen,	Unterschrift

Abstrakt

In dieser Arbeit werden die elektronischen und chemischen Strukturen von $Fe_xNi_{1-x}(O,OH)_y$-Dünnschicht-Elektrokatalysatoren in Abhängigkeit von ihrer Zusammensetzung und im Zusammenhang mit der Sauerstoffentwicklungsreaktion (OER) in alkalischen Medien untersucht. Ziel der Studie ist es, zu verstehen, wie die elektronischen Zustände und chemischen Umgebungen der Übergangsmetalle und des Sauerstoffs durch Veränderungen der Zusammensetzung und elektrochemische Behandlung beeinflusst werden, die für die Bestimmung der katalytischen Aktivität der Materialien verantwortlich sind. Zur Untersuchung der Katalysatoren sowohl an der Oberfläche als auch im Volumen wurde eine Vielzahl von spektroskopischen Techniken eingesetzt, darunter Photoelektronenspektroskopie und Röntgenspektroskopie, wie z. B. Weichröntgenabsorptions- und Emissionsspektroskopie sowie Hartröntgen-Photoelektronenspektroskopie.

Die Charakterisierung der hergestellten Filme zeigte, dass mit steigendem Fe-Gehalt sowohl für Fe als auch für Ni ein höherer Oxidationsgrad zu beobachten war, zusammen mit einer stärkeren Fe-O-Ni-Kovalenz. Das Zusammensetzungsfenster von 10-20 at. % Fe wurde als kritischer Punkt in der Probenreihe identifiziert, an dem die chemische Struktur signifikante Veränderungen durchläuft. Dieser Bereich fällt auch mit der maximalen elektrokatalytischen Effizienz zusammen, was auf einen direkten Zusammenhang zwischen der sich entwickelnden elektronischen und chemischen Struktur und der katalytischen Aktivität hindeutet.

Eine vergleichende Analyse von Proben mit derselben chemischen Zusammensetzung vor und nach der OER deutete auf eine Anreicherung von Fe an der Oberfläche nach der OER hin, was eine Neuordnung der Bindungsumgebungen von Fe, Ni und O an der Oberfläche impliziert. Auch die Sauerstoffumgebung scheint sich zu verändern, wobei die spektralen Merkmale eher oxidähnliche Eigenschaften aufweisen. Die Ergebnisse deuten auf ein Modell hin, bei dem Sauerstoff als Koordinator zwischen den Übergangsmetallen fungiert und deren Redoxaktivität reguliert sowie eine Rolle bei der Stabilisierung katalytisch aktiver Konfigurationen spielt.

Im späteren Teil der Arbeit wird über den Entwurf und die Entwicklung einer vakuumkompatiblen operando-Elektrochemiezelle berichtet, die in situ und operando-Weichröntgenspektroskopieuntersuchungen unter angelegter elektrochemischer Spannung ermöglicht. Vorläufige Offline-Tests haben die Funktionsfähigkeit der Zelle unter beamline-ähnlichen Bedingungen bestätigt.

Zusammen bilden die aus den spektroskopischen Untersuchungen gewonnenen Erkenntnisse und die Entwicklung der beamline-kompatiblen Operando-Zelle eine solide Grundlage für weitere In-situ-Untersuchungen, die eine Echtzeitbeobachtung der durch die OER induzierten mechanistischen Veränderungen ermöglichen.

Abstract

In this thesis, the electronic and chemical structures of $Fe_xNi_{1-x}(O,OH)_y$ thin film electrocatalysts are investigated as a function of their composition and in the context of the oxygen evolution reaction (OER) in alkaline media. The aim of the study is to understand how the electronic states and chemical environments of the transition metals and oxygen are influenced as a result of changing composition and electrochemical treatment, which are responsible for determining the catalytic activity of the materials. A broad variety of spectroscopic techniques, including photoelectron spectroscopy and x-ray spectroscopy, such as soft x-ray absorption and emission spectroscopy and hard x-ray photoelectron spectroscopy, have been employed to study the catalysts, both at the surface and the bulk.

Characterization of as-prepared films showed that with increasing Fe content, a greater degree of oxidation could be seen for both Fe and Ni, together with stronger Fe-O-Ni covalency. The compositional window of 10-20 at. % Fe was identified as a critical juncture in the sample series, where the chemical structure undergoes significant changes. This region also coincides with the maximum electrocatalytic efficiency, suggesting a direct correlation between the evolving electronic and chemical structure and catalytic activity.

A comparative analysis of samples with the same chemical composition before and after OER suggested Fe enrichment at the surface post OER, implying a reordering on the surface of the bonding environments of Fe, Ni, and O. The oxygen environment is seen to evolve as well, with spectral features leaning more towards oxide-like characteristics. The findings point towards a model where oxygen acts as a coordinator between the transition metals and regulates their redox activity, along with playing a role in stabilizing catalytically active configurations.

In the later section of the thesis, the design and development of a vacuum compatible *operando* electrochemical cell is reported, which enables in situ and *operando* soft x-ray spectroscopic studies under applied electrochemical potential. Preliminary offline tests have confirmed the cell's operability under beamline-like conditions.

Together, the insights obtained from the spectroscopic studies and the development of the beamline compatible *operando* cell lay a strong foundation for further in situ studies, enabling real-time observation of mechanistic changes induced by the OER.

Contents

List of Figures

List of Tables

1.1 Motivation

The world depends on fossil fuels as the primary source of energy and has done so for centuries. This has resulted in a depletion of the fossil fuel reserves, and the continued release of greenhouse gases such as methane, carbon monoxide and carbon dioxide have made it imperative to explore cleaner and more sustainable energy options. These gases cause global warming which raises the temperature of the earth's surface as a result of greenhouse effect, becoming one of the leading causes of climate change. Combustion of fossil fuels also causes air pollution, which directly impacts human health through respiratory diseases. A combination of these effects has made it essential to transition to alternative cleaner energy systems.

Hydrogen is one such promising alternative fuel and energy carrier. It can be used as fuel in combustion systems or fuel cells to generate electricity. It can also serve as an energy carrier, allowing for the storage and transport of electricity generated from renewable sources like wind and solar. Production of hydrogen can be sustainably achieved via electrochemical water splitting, commonly referred to as electrolysis, a process that uses electricity to split water into hydrogen and oxygen.

The electrolysis process is a redox reaction, involving two half reactions: hydrogen evolution reaction (HER) and oxygen evolution reaction (OER). The former is the cathodic half of the electrolysis reaction, where reduction results in the production of hydrogen and the latter is the anodic half reaction, which results in the production of oxygen. OER is a challenging reaction, as it involves a multi-electron transfer mechanism and is hence an energy intensive process. Theoretically, OER should occur at a potential of 1.229 V vs Standard Hydrogen Electrode (SHE)[1], however, in reality requires much higher applied potentials. The additional energy requirement is referred to as overpotential, which results mostly from sluggish kinetics of the multi-electron OER process and the several intermediates formed along the reaction pathway, that possess high activation energies. A more detailed discussion highlighting the reasons behind the requirement of this overpotential is presented in Chapter 2. The goal of developing an efficient electrocatalyst is to lower this overpotential.

Currently, the most effective OER catalysts are based on noble metals such as iridium and platinum, which are rare, expensive metals[2,3]. In laboratory scales, such catalysts are functional but challenges arise when transitioning into large-scale, real-world applications. As a result, recent research has focused on earth abundant transition metal oxides and hydroxides as probable OER catalysts[4,5,6,7,8]. Ni-based catalysts have shown promising activity as catalysts for HER in alkaline media[9,10,11,12]. However, HER is a relatively less energy-intensive process as compared to OER and these catalysts have unfortunatley not proven to be equally effective for OER. Eventually, it was discovered that doping the same Ni-based oxides and hydroxides with iron leads to drastic improvement of their activity as OER catalysts[13,14,15]. However, the precise mechanism by which iron enhances the catalytic activity of these oxides and hydroxides remains unknown.

Several hypotheses have been suggested regarding the role of iron: enabling the formation of new active sites, promoting a synergistic interaction between Fe and Ni centers, thereby stabilizing the

higher oxidation states of both metals as and when they undergo oxidation. At the same time, the stability of these catalysts remains a critical issue. Phenomena such as iron leaching, and structural and compositional transitions between the different phases of these metals under operating conditions can lead to degradation over time. A thorough understanding of the chemical and electronic structure of the catalysts is thus important as without a proper understanding, optimization of the catalysts will remain iterative rather than intentional. Throughout the rest of the thesis, in several places, the chemical and electronic structure of the catalyst will be referred to as simply "structure" to avoid redundancy.

To address this, in this thesis, soft and hard x-ray and electron spectroscopic techniques have been used to study the behavior of $Fe_xNi_{1-x}(O,OH)_y$ prepared by the Pennsylvania State University and shipped to KIT, right after their synthesis, as well as after their participation in electrochemical water splitting. The iron content (x) is systematically changed, to establish the correlation between composition and catalytic behavior. The aim is to determine how iron incorporation affects oxidation states, bonding environments, and overall catalyst structure. For the purpose of simplicity, the material system is referred to as FeNiOOH electrocatalysts.

A range of spectroscopic techniques have been used, each providing a different insight. X-ray photoelectron spectroscopy (XPS) and hard x-ray photoelectron spectroscopy (HAXPES) provide crucial information about the surface composition, oxidation states and chemical bonding environments and how it changes after OER, x-ray absorption spectroscopy (XAS) probes unoccupied electronic states and local coordination environments and x-ray emission spectroscopy (XES) provides information about the occupied states, along with additional insight into metal-ligand interactions.

Additionally, this work discusses the design and implementation of a novel *operando* electrochemical cell, developed to enable in situ measurements under electrochemical conditions at the synchrotron. The *operando* cell has been optimized to be implemented at the X-SPEC beamline at the KIT-Light Source. Maintaining the integrity of the vacuum environment while operating in a liquid environment is challenging, and the process of the development of the cell has been addressed and discussed in detail.

The thesis is structured as follows:

Chapter 2 provides the theoretical background, introducing the spectroscopic techniques and electrochemical principles relevant to the spectroscopic techniques relevant to the study of the $Fe_xNi_{1-x}(O,OH)_y$ electrocatalysts. It also provides a brief survey of the nature and properties of several electrocatalysts for water splitting9 and traces an evolution from the use of rare and precious metals to more readily available transition metal based catalysts.

Chapter 3 describes the experimental setup, including details of the laboratory infrastructure, beamline and associated instrumentation, synthesis and handling of samples as well as methods of data analysis, and describes the pathway to the development of the synthesis protocol for the samples studied in this dissertation.

Chapter 4 presents the spectroscopic characterization of the as-prepared $Fe_xNi_{1-x}(O,OH)_y$ electrocatalysts, establishing their initial chemical and electronic structure.

Chapter 5 explores the evolution of the catalysts' chemical and electronic structure and composition post oxygen evolution reaction (OER), both at a surface level and within the bulk of the material.

Chapter 6 integrates the key findings of this work, providing an overarching summary and interpretation.

Chapter 7 details the design, construction and preliminary testing of a novel *operando* electrochemical cell developed to be implemented at the X-SPEC beamline at the KIT Light Source, for in situ and operando studies.

Finally, Chapter 8 concludes with a summary of the research outcomes.

2 Theory and Background of Methodology and Material Systems

In this Chapter, the fundamental concepts of spectroscopic techniques and electrochemistry pertaining to the study of transition metal electrocatalysts studied through the course of this work will be discussed. To fully understand the involvement of these transition metals in electrolysis, it is essential to develop an understanding of the electrochemical aspects of the reactions as well as the materials themselves. Crucial insight can be gained with the help of these techniques such as XPS, HAXPES, XAS and XES, which shall be talked about in the following sections.

2.1 Spectroscopic Methods

2.1.1 Electron Spectroscopies

One of the most common and powerful techniques to study the electronic and chemical structures of materials is photoemission spectroscopy (PES). The underlying photoelectric effect was initially observed by Heinrich Hertz in 1887, the phenomenon was further investigated by William Hallwachs and others, leading to the realization that light induces the emission of negatively charged particles from metal surfaces[16]. Albert Einstein's groundbreaking work provided the theoretical foundation for the photoelectric effect, introducing the concept of photons and establishing the relationship between photon energy and emitted electron kinetic energy. This discovery led to him winning the Nobel Prize in Physics in 1921[17]. Subsequent experimental verification by Robert Millikan and others provided strong evidence supporting Einstein's explanation for the photoelectric effect. The photoelectric effect can be observed when an incident photon transfers its energy to an electron, allowing it to overcome the material's work function and escape into the vacuum[16]. PES is s direct implementation of this effect, which results in the emission of photoelectrons, when the investigated material is irradiated with x-rays. The kinetic energy of the emitted photoelectrons, with respect to the vacuum level can be given by the following expression:

$$E_{kin} = h\nu - E_{bin} - \phi \tag{2.1}$$

where $h\nu$ is the x-ray photon energy, E_{bin} is the binding energy of the electrons and ϕ is the work function of the sample. Figure 1 shows a schematic representation of the photoelectron effect. However, in practical photoelectron spectroscopy, since the sample and the spectrometer are in electrical contact, the measured kinetic energy is referenced to the analyzer's work function, as explained in Section 2.1.1.1

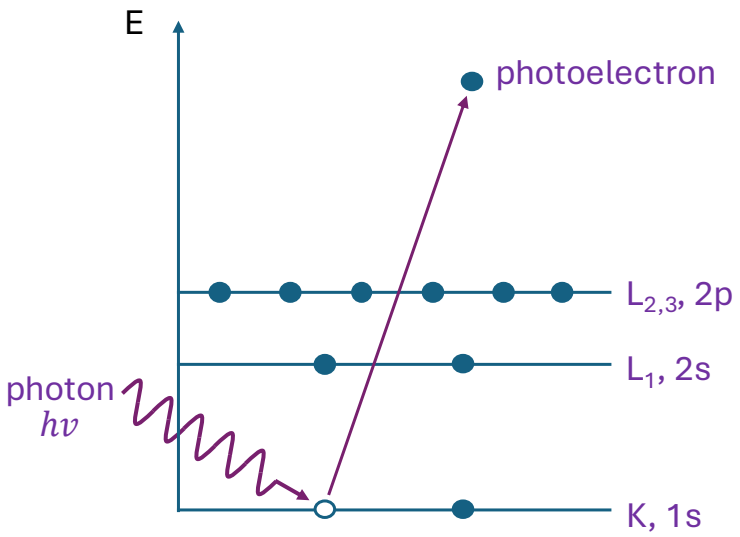

Figure 1: The photoelectric effect: an electron is ejected from the core level (1s in this example), and a photoelectron is emitted into the vacuum. For the purpose of simplicity, the spin-orbit splitting of the 2p level is not shown.

2.1.1.1 X-ray photoelectron spectroscopy

While photoemission spectroscopy (PES) provides valuable insights into the electronic structure of materials by analyzing emitted electrons, its probing depth and accessible electronic transitions depend on the energy of the incident photons. X-ray photoelectron spectroscopy or XPS is a direct application of the photoemission process, and thereby the photoelectric effect. X-ray photoelectron spectroscopy (XPS) was originally known as Electron Spectroscopy for Chemical Analysis (ESCA) and was first developed by Kai Siegbahn and his group in Uppsala, Sweden in 1950s-60s[18]. XPS typically uses lower photon energies (soft x-rays, 200-2000 eV) to eject photoelectrons with high surface sensitivity. In contrast, higher photon energies (hard x-rays, greater than 2 keV) can be used to probe deeper into materials, which then would be referred to as hard x-ray photoelectron spectroscopy (HAXPES).

The interaction between an electron's intrinsic spin and its orbital angular momentum (L≠0) results in a phenomenon known as spin-orbit splitting, which causes some energy levels to split into two distinct levels, forming a doublet[19]. This can be observed in orbitals with non-zero angular momentum, which are p, d, f and so on. The total angular momentum of these two distinct levels is denoted by j and can take two different values. For instance, for an electron that belongs to the 2p orbital, the possible values of j are 1/2 and 3/2. This results in two peaks in the spectra and their intensity ratio can then be determined following the 2j+1 rule. For the split states of the 2p orbital thus, the intensity ratio of the peaks is 1:2, for d levels it is 2:3 and for f, 3:4. For simplicity, the 2p level shown in Figure 1 is shown without the spin-orbit splitting.

For XPS as well, the kinetic energy of the emitted electrons can be determined by Equation (2.1). In the equation, the work function refers to that of the sample (ϕ_s), but the instrument itself has a fixed

work function, ϕ_i. Since the sample and instrument are in electrical contact, a contact potential difference, $\phi_s - \phi_i$ arises between the two, for equalization of the Fermi levels (E_F). The Fermi level is the highest energy level electrons are capable of occupying at 0 K in metals. In semiconductors, it serves as a statistical reference point to describe the distribution of electrons while in insulators, it does not physically correspond to an accessible energy level within the material itself. Owing to these differences, the Fermi level is a useful concept for distinguishing between metals, semiconductors and insulators. Although photoemission is referenced to the vacuum level of the sample in theory, in practical measurements, the analyzer's work function is used as a calibration factor, which corrects the measured kinetic energy such that the binding energies can be reported relative to the Fermi level of the sample.

The recorded kinetic energy, with respect to the vacuum level, is therefore given by the slightly modified version of equation (2.1):

$$E_{kin} = h\nu - E_{bin} - \phi_i \tag{2.1a}$$

This indicates that the data obtained from XPS measurements are independent of the sample's work function and rather are related to the instrument's work function. This is a constant value, which gets accounted for during calibration.

Spectral intensity, even though measured as a function of kinetic energy of the photoelectrons with respect to the vacuum level, $I(E_{kin})$ initially, is converted to binding energies relative to the Fermi level (E_F) using equation (2.1) which is defined as zero binding energy. The resulting spectrum, $I(E_{bin})$, provides material-specific binding energies, enabling the identification of elements in the material.

Generally, XPS is used for measuring solids in several forms such as single crystals, powders and thin films. These solids can be metals, semiconductors or insulators. However, since XPS requires sufficient sample conductivity, measuring insulators poses challenges due to the buildup of surface charge. Such charging effects can cause distortion of the measured spectra and complicate interpretation, which has resulted in XPS studies to be performed on conductive or semi-conductive materials. $Fe_xNi_{1-x}(O,OH)_y$ thin films (which will be introduced in Chapter 3) which can be characterized as a semiconductor, will be studied and the results discussed in this dissertation.

In semiconductors, the electron states are primarily categorized into distinct energy levels that are characteristic of their electrical and optical properties: core levels (CL), valence band (VB), and conduction band (CB). VB is the highest energy band that is completely filled at absolute zero (T = 0 K) with reference to the E_F. CB is the next available energy band above the VB which is free of electrons. CLs are deeply bound electronic states that are associated with the inner atomic orbitals. They are localized states that do not participate in chemical bonding. Therefore, they can be thought of as behaving like atomic orbitals, with no band dispersions. The key difference between the two however is the discernible chemical shift observed in the binding energy of CLs, that happens due to the varying chemical environments of the atom from which the electron is ejected. The VB is influenced by chemical shifts as well, but since the energy dispersion is much stronger, it cannot be evaluated. For example, higher oxidation states result in increased binding energy: because of loss of an electron from the atom, a stronger attraction between the nucleus and remaining core

electrons is established. In the $Fe_xNi_{1-x}(O,OH)_y$ thin films that will be discussed in this thesis, a shift to the higher binding energies of the Fe and Ni 2p core levels are generally indicative of the formation of higher oxidation states. Figure 2 shows a schematic representation of the XPS process.

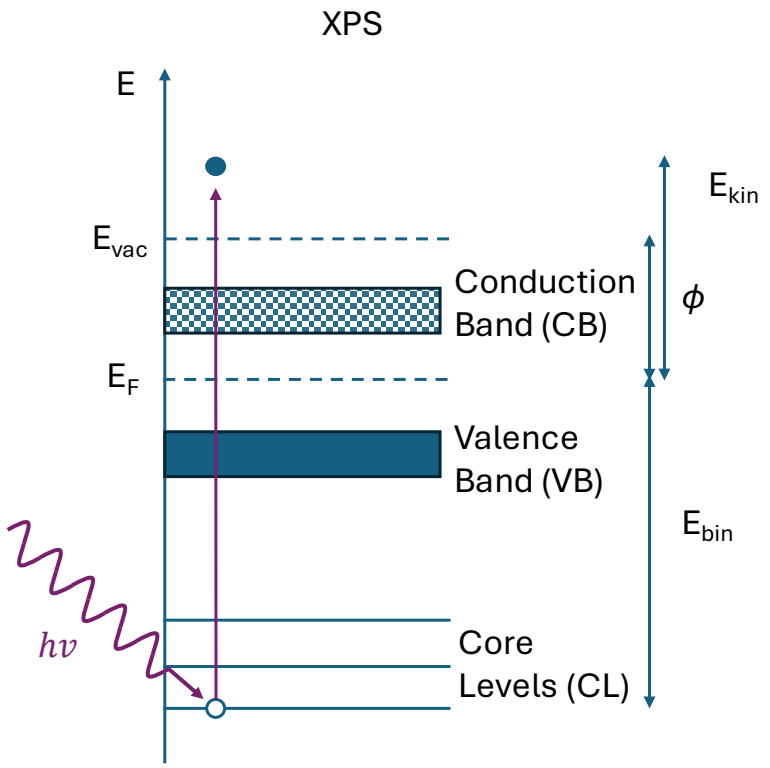

Figure 2: A schematic representation of XPS. E_{vac}, E_{kin}, E_{bin}, E_F and ϕ represent energy of the vacuum levels, kinetic energy of electron, Fermi energy and work function of electron, respectively.

In XPS, both CL and VB states can be probed. Probing the CLs helps obtain information on the chemical structure of the investigated material and probing the VB states provides information mainly about its electronic structure.

The experimental set up for XPS consists of the following three main components: the x-ray source, the analysis chamber under UHV (pressure in the order of 10^{-9} mbar) and the hemispherical electron analyzer. In the x-ray source, a filament acts as the cathode and the anode is made of the appropriate material of choice. The two most commonly used anode materials are Mg and Al, which are also the materials used in the laboratory based XPS measurements shown in this thesis. The filament or the cathode is heated by an electric current, generating electrons. A high potential difference (15 kV) is applied between the cathode and anode. The thermoelectrons, which are the electrons generated as a result of the heated-up filament, are accelerated towards the anode and on interaction with the anode material, x-rays are generated. The x-ray tube used by Röntgen in his 1895 discovery was fundamentally similar to modern designs, though with significant differences. Contemporary x-ray

tubes operate in a high-vacuum environment, whereas early versions functioned under partial vacuum, relying on ionization of residual air molecules to generate electrons.

The resultant x-ray spectra comprise of two components. The continuous spectrum due to the bremsstrahlung or braking radiation: the electrons emitted from the cathode are decelerated in the target material and emit radiation as a result. On top of the bremsstrahlung are the characteristic x-ray peaks. When an electron emitted from the cathode collides with the target material, it ejects an inner-shell electron, creating a core-hole. To restore stability, an electron from a higher energy level moves down to fill the vacancy, releasing an x-ray photon in the process. These electronic transitions must follow the angular momentum selection rule, $\Delta l = \pm 1$, meaning that s-s transitions are forbidden. The Siegbahn notation is used for characteristic x-ray transitions. It designates x-ray transitions based on electron movement between atomic energy levels. Transitions from the $L_{2,3}$ (2p) to the K (1s) level are the K_α emission lines, $M_{2,3}$ (3p) to K (1s) are the K_β lines, and so on. The Mg K_α x-ray source has an energy of 1253.6 eV and line width of 0.7 eV and the Al K_α source has an energy of 1486.7 eV and a line width of 0.85 eV. In our laboratory for Al Kα radiation, a monochromator (a quartz crystal) is used to eliminate the Kβ line, bremsstrahlung and make the line width narrower. Even though this reduces the intensity of the photoelectron beam, the resolution is improved manifold. The photoelectron beam refers to the electron stream that is emitted from the sample as a result of irradiation by the beam.

The photoelectrons are slowed down by electrostatic lenses before entering the hemispherical electron analyzer, which consists of two concentric hemispheres with a potential difference applied between them. This potential difference determines the pass energy which is the specific kinetic energy required for photoelectrons to traverse the analyzer. To maintain a constant energy resolution, the applied voltages are typically kept constant.

The inelastic background makes a significant contribution to the x-ray spectra obtained. It arises due to the loss of energy of the electrons undergoing inelastic scattering as they travel through the material before reaching the detector. As the electrons interact with the atoms within the sample, they lose energy to generate a continuous background signal in the spectra. The shape of the background signal varies with photon energy, nature of sample and sample thickness. Careful and detailed analysis of the background is therefore necessary. A more detailed description of the different ways in which this background can be analyzed is given in Section 2.1.1.3.

A theoretical understanding of the photoemission process can be developed using the time-dependent first order perturbation theory. The transition probability per unit time, W_{fi}, from the initial state, which is the ground state of the system, to the final state (1 electron ejected from the material, changing the system to an *(N-1)* electron system) is given by Fermi's golden rule[20]:

$$W_{fi} \propto \frac{2\pi}{h} \left| \langle \varphi_f | \widehat{H'} | \varphi_i \rangle \right|^2 \delta(E_i - E_f - h\nu) = \frac{2\pi}{h} \left| M_{fi} \right|^2 \delta(E_i - E_f - h\nu) \qquad (2.2)$$

Here φ_i and φ_f are the initial and final eigenstates and E_i and E_f are the initial and final eigenvalues of the unperturbed Hamiltonian $\widehat{H_o}$. $\widehat{H'}$ is the interaction Hamiltonian describing the perturbation, M_{fi} are the transition matrix elements and the delta function ensures energy conservation.

The interaction Hamiltonian is given by:

$$\widehat{H'} = -\frac{e}{mc}\vec{A} * \vec{p} \tag{2.3}$$

Where $\vec{A}$ is the vector potential of the electromagnetic field, $\vec{p}$ is the momentum of the electron, m and e are the mass and charge of the electron respectively, and c is the speed of the light.

A few approximations are made when writing down Equation 2.3: The scalar potential is set to zero and a linear optical regime is assumed, allowing the omission of the quadratic term in $\vec{\mathrm{A}}$. Additionally, the dipole approximation is used, which implies that spatial variations of $\vec{\mathrm{A}}$ over atomic distances are neglected, resulting in $\nabla\vec{\mathrm{A}} = 0$. Furthermore, the commutation relation $\left[\vec{\mathrm{p}},\ \vec{\mathrm{A}}\right] = \mathrm{i}\hbar\nabla\vec{\mathrm{A}}$ is applied to obtain Equation[20] 2.3.

Considering that the investigated surface is homogeneous and of infinite thickness, the photoelectrons are detected perpendicular to the sample and the angle between the x-ray source and analyzer is the magic angle (54.7°) in the laboratory XPS set up. The intensity of an XPS spectrum is approximated by the following relation:

$$I \sim \sigma N \lambda(E) T(E) \tag{2.4}$$

The magic angle ensures that the angular asymmetry factors can be presumed to be unity[21]. In the above equation, σ is the photoionization cross-section which is a measure of the probability of photoemission to occur and is proportional to the square of the matrix element: $\sigma \propto \Sigma_{\mathrm{f}}|\mathrm{M}_{\mathrm{fi}}|^2$.

N is the concentration of the element in the investigated sample and λ is the inelastic mean free path or IMFP. The IMFP describes the distance an electron travels through a material before the intensity of the electron beam decreases to 1/e of its initial volume. It is a function of the kinetic energy and can be approximately described by the universal curve[22] shown in Figure 3. T is the transmission function of the analyzer, which depends both on the kinetic energy and the pass energy of the analyzer.

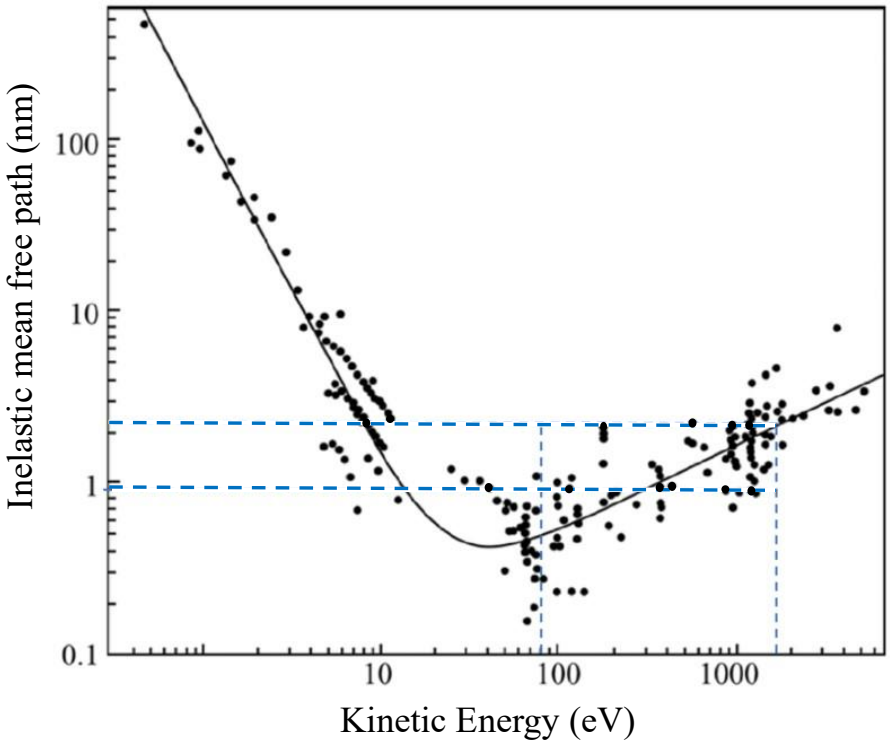

Figure 3: The inelastic mean free path (IMFP) is shown as a function of kinetic energy. Experimental data from various materials are averaged to derive the universal curve. The typical kinetic energy range explored in XPS along with the corresponding IMFP values is highlighted by the blue dashed lines. Figure reproduced from ref[22].

Figure 3 highlights that for XPS generated by Mg K_α and Al K_α sources, the kinetic energy of the photoelectrons typically ranges between 100 to 1500 eV, while the IMFP varies between 1 and 3 nm. This indicates that XPS is a surface sensitive technique. On the contrary, hard x-ray photoelectron spectroscopy or HAXPES ($h\nu$ > 2100 eV) enable slightly more bulk sensitive measurements.

In case of transition metals, XPS spectra can show multiplet splitting, which is a result of the strong electron-electron interactions between the core-hole and the partially filled 3d valence shell. When an electron is removed from the core level during photoemission, the resulting core-hole interacts with the valence electrons to give rise to multiple final states. This results in various multiple final states, each characterized by different combinations of spin and orbital angular momentum. The various final states give rise to a characteristic multiplet structure in the XPS spectrum, where instead of a single feature associated with a specific binding energy, a multiplet structure is observed.

The underlying fundamental principle behind this phenomenon is the fact that the Coulombic exchange between the core-hole and the d-electrons causes the energy levels to split into different configurations. The final states manifest themselves as a series of peaks or shoulders in the measured XPS spectra, producing a complex profile that cannot be explained by a simple single-electron picture. In transition metals with unfilled d orbitals, such as Mn^{2+}, Fe^{3+} or $Ni^{2+,}$ the multiplet split features reflect the various possible ways the core-hole can couple to the spin and orbital

momenta of the remaining electrons in the d-orbital. The pattern and position of peaks is highly sensitive to the oxidation states of the transition metals, their local coordination environment and the symmetry effects of the surrounding ligands. Multiplet splitting thus provides a fingerprint that helps to identify the chemical environment of the metal center.

Furthermore, ligand fields around the metal centers, such as oxides and hydroxides, can modify the multiplet states by introducing additional splitting through metal-ligand interactions. These ligand field effects therefore impact the energy separation of the final states, reflecting the extent to which the d electrons are stabilized or distorted as a result of their surrounding chemical and electronic environment. This significantly affects the catalytic activity of the metal centers.

In addition to the atomic multiplet effects, the XPS spectra of transition metal compounds can also be affected by charge transfer interactions between the metal centers and coordinated ligands. In systems with significant hybridization between metal d orbitals and ligand p orbitals, electron density can be redistributed during the photoemission process. The different features arising from these interactions reflect the degree of metal-ligand covalency and can provide valuable insight into the nature of the bonding environment of the metals. For the electrocatalysts studied in this work, namely Fe and Ni based oxyhydroxides, interpreting this covalency is critical as it impacts the redox abilities of the catalytic centers during operation.

It should be acknowledged that beyond its chemical aspects, the phenomenon of multiplet splitting can also be explained quantitatively, which is commonly done in physics literature. One of the more well-known explanations include the model put forth by Fadley and Shirley[23], using exchange interactions between the core-hole and the d shell. They showed that the energy difference between the final states can be approximated by a term known as the exchange term, which is determined by the spin alignment between the created core-hole and the valence electrons. In the simplest form, the energy separation can be estimated as proportional to (2S+1), where S is the total spin of the d electrons, reflecting the difference between parallel and antiparallel configurations. Although the detailed and complete calculations of these exchange terms is beyond the scope of this thesis, this mathematical framework provides a more quantitative understanding of the origin of multiplet features and their dependence on the electronic configuration of the transition metal centers.

2.1.1.2 X-ray Auger electron spectroscopy

When a core-hole is created by an x-ray and is subsequently filled by an electron from a higher level, which could either be from another core level itself or the valence band and the residual energy is invested in the emission of a second electron, x-ray Auger electron spectroscopy (XAES) occurs. The emitted electron is known as the Auger electron. The process is schematically represented in Figure 4.

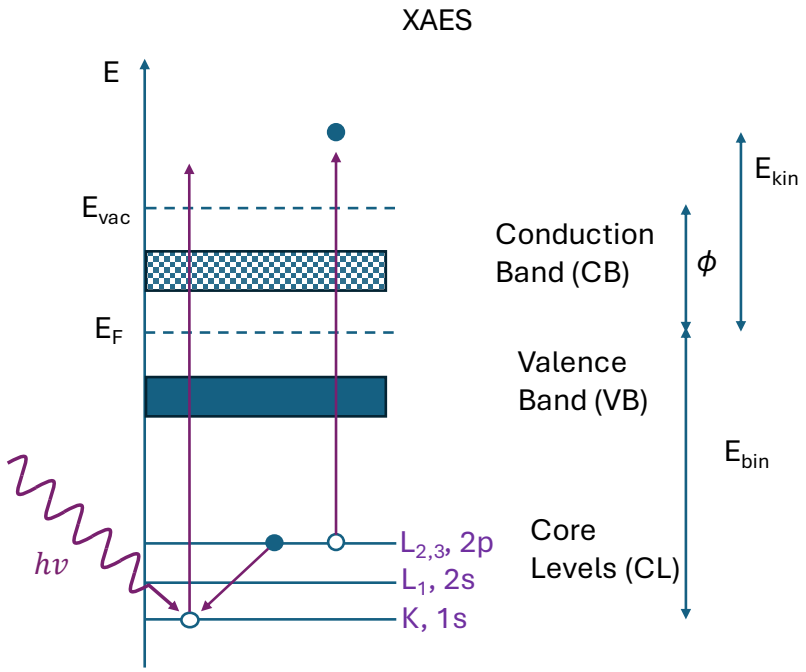

Figure 4: Schematic representation of the XAES process, after the creation of the core-hole in XPS. The spin orbit splitting of the 2p level is omitted for the time being. The figure does not include the hole-hole interaction energy visualization.

In Figure 4 the kinetic energy of the Auger electron is given by:

$$E_{Auger} = E_K - E_{L1} - E_{L2,3} - \phi - U \tag{2.5}$$

where E_K, $E_{L1,}$ and $E_{L2,3}$ are the binding energies of the 1s, 2s and 2p orbitals respectively and ϕ is the work function. U is the hole-hole interaction term, which represents the electrostatic interaction between the two vacancies created initially. This additional interaction, which by nature is Coulomb repulsion, raises the energy of the final state, so the emitted Auger electron has less kinetic energy than can be predicted by a simplistic sum of the binding energies.

Thus, the Auger kinetic energy is independent of the initial photon energy. Contrary to spectroscopic notation used in XPS, the Auger process uses x-ray notation.

A competing process of the Auger emission is x-ray fluorescence, which is a more probable route for relaxation for the heavier elements. For lighter elements through, (Z<30) and the K shell, Auger emission is more likely to occur[24], as is evident from Figure 5.

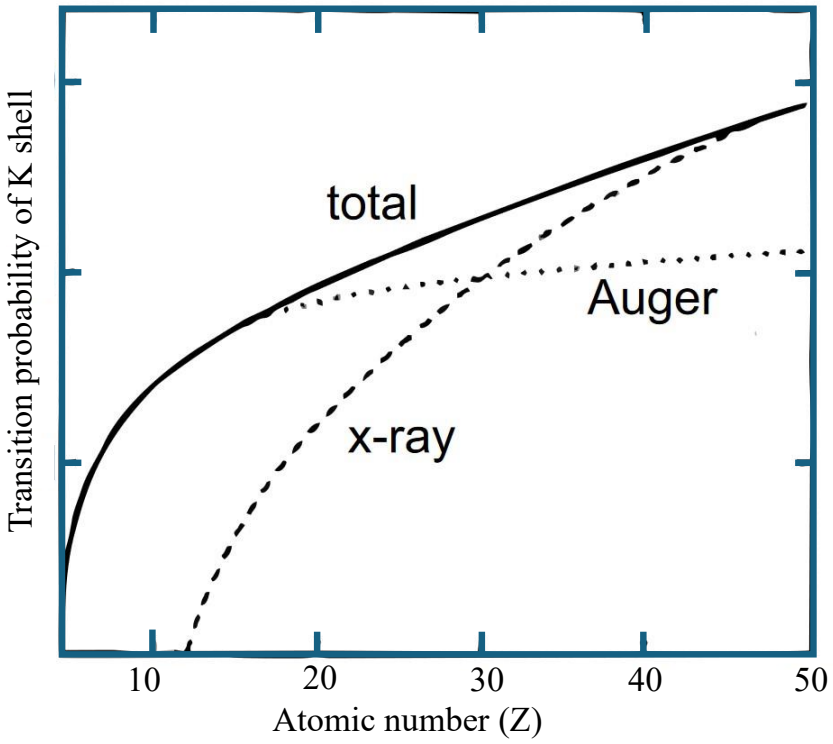

Figure 5: Calculated probability for K shell for competing Auger and x-ray emission, as a function of the atomic number Z. Plot adapted from ref[24].

2.1.1.3 Synchrotron based (hard) x-ray photoelectron spectroscopy

A synchrotron is a circular particle accelerator where an electric field is used to accelerate the particles and a magnetic field to bend their trajectory (bending magnets). The principle was first proposed by Vladimir Veksler in 1944[25], while Edwin McMillan independently developed and built the first electron synchrotron in 1945[26].

By virtue of travelling with a constant speed in a circular trajectory, the particles develop centripetal acceleration. According to the classical theory of electromagnetism, they emit radiation because of this acceleration. This radiation can be used as the light source for various experiments. One of the essential components of a synchrotron is the storage ring, where electrons circulate at nearly constant energy, providing a stable photon flux over a long period of time. At the KIT Light Source, the storage ring is known as KARA, where electrons travel around the storage ring at 2.5 GeV[27]. Synchrotron radiation is generated at bending magnets and specialized insertion devices, known as wigglers and undulators, which are placed in the straight sections of the ring to enhance brilliance. The components of a synchrotron will be discussed in further details in Chapter 3. Beamlines are positioned tangentially to these sources, capturing the emitted radiation as it exits the storage ring. When high energy electrons are injected into the undulator from the storage ring, they are forced to oscillate and consequently lose energy to produce synchrotron radiation. The layout of the KIT Light Source[28] is shown in Figure 6.

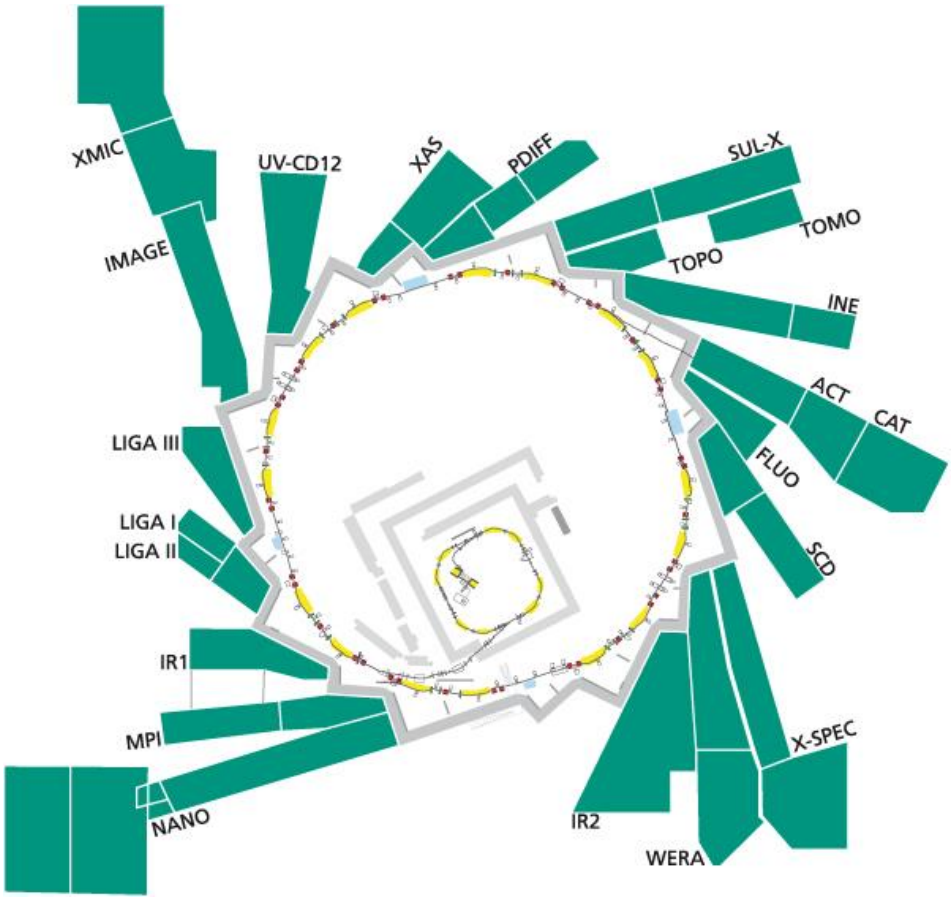

Figure 6: Schematic layout of the KIT Light Source: microtron, storage ring, and beamlines (X-PEC beamline is on the lower right side). Figure reproduced from ref[28].

In Section 2.1.1.1 it has been noted that bremsstrahlung contributes to the background in the spectra obtained from laboratory-based x-ray sources, thereby obscuring weak signals. Synchrotron sources, in contrast, enable the use of monochromators to precisely select a monochromatic and tunable photon beam from the broad spectrum, consisting of a broad bremsstrahlung, that arises from the bending magnets. The tunability of the synchrotron beam is one of its most significant advantages, allowing researchers to optimize excitation conditions for specific chemical environments to achieve enhanced surface sensitivity. Additionally, synchrotron-based x-ray sources provide higher energy resolution, reduce instrumental broadening and improve signal to noise ratios, resulting in sharper peaks in the spectra obtained. This makes synchrotron sources ideal for high-precision studies of chemical shifts, oxidation states, and electronic structures in materials.

In this dissertation, hard x-ray photoelectron spectroscopy or HAXPES measurements were performed at the double undulator X-SPEC beamline at the KIT Light Source[29]. The x-ray beam has a high photon flux and is more intense and collimated than the laboratory-based x-ray sources. Additionally, for the materials studied in this thesis, it is imperative to separate the Auger lines from the core level peaks for the latter to be investigated properly. As it has been observed that there were significant overlaps of the Auger peaks (Fe LMM and Ni LMM) with the core level peaks (Fe 2p and Ni 2p). By changing the excitation energy, the Auger lines can be shifted relative to core levels because

the Auger electron energies depend solely on the atomic energy levels involved in the transition, rather than the excitation source. Contrarily, core-level binding energies are measured relative to the photon energy used to excite the electrons, as explained in Section 2.1.1.1. When the excitation energy increases, the measured binding energy of the core-level electrons shifts accordingly, but Auger electron energies remain constant since they are determined by the difference between internal energy levels of the atom.

The experiments performed at the X-SPEC beamline for this work were conducted with a photon energy of 2.1 keV, which characterizes them as HAXPES measurements.

As pointed out in Equation 2.4 in Section 2.1.1.1, there exists a relation between the concentration of the element investigated, photoionization cross section, the transmission function, the intensity and the inelastic mean free path or IMFP. For this dissertation, the ratio of concentrations of two elements are determined from the HAXPES peaks with similar kinetic energies. In this case, λ and T can be considered to be nearly identical. Also, it is assumed that the sample is uniformly distributed within the analysis depth, ignoring surface segregation, contamination and inhomogeneities, which may skew stoichiometric calculations. Then the ratio of the concentration of two elements A and B in the sample can be written as:

$$\frac{N_A}{N_B} = \frac{I_A/\sigma_A}{I_B/\sigma_B} \tag{2.6}$$

Specifically, the Fe 2p/Ni 2p ratio can be determined from this relation, which is a crucial value that will aid in the analysis of the electrocatalysts and the effect of oxygen evolution reaction (explained in the next section of this chapter) on them. It is however worth mentioning that the measurements at the X-SPEC beamline were conducted with the analyzer positioned at 90^0 relative to the incident x-ray beam, therefore parallel to the direction of polarization of photon, instead of the magic angle, described in Section 2.1.1.1.

The inelastic background in the XPS spectra could both be a hindrance, or a treasure-trove of information about the nature of the materials and the different peaks. Analyzing the shape of the inelastic background provides information about the depth distribution of elements in a material in some cases, while in some other cases, it is important to strip the background efficiently to reveal the true intensities of the peaks of the elements. Several models can be used to describe the background in an XPS spectrum: the **Shirley** background, which assumes the background intensity to be proportional to the number of electrons at higher binding energies that have undergone energy loss. This is most appropriate for metals, especially alkali metals. **Linear** background, which is a simple straight-line approximation, that although is not the best depiction of the inelastic background, is the simplest approximation to use as the expected error is small enough to not disturb the evaluation. The **Tougaard** background, which incorporates an energy-dependent loss function to account for the electron-electron scattering processes, making it more accurate for quantitative analysis. It uses material-specific parameters to describe energy loss probabilities. In materials with significant inelastic scattering, the Tougaard background is most suited. Figure 7 shows the different types of background approximation for a Au 4f spectrum[30].

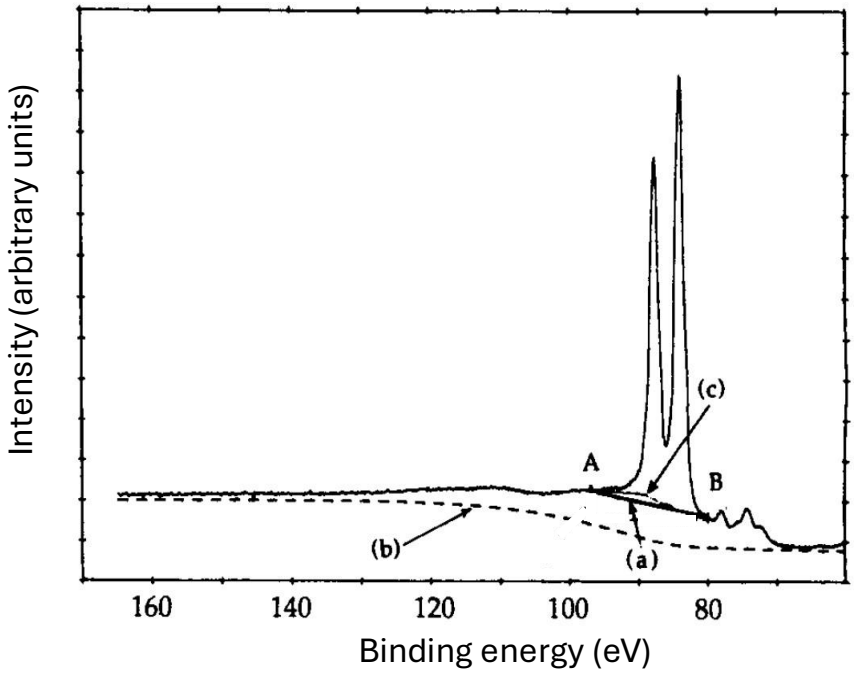

Figure 7: Inelastic background approximation for Au 4f line: (a) linear background, (b) Tougaard background, (c) Shirley background. Figure reproduced from ref[30].

The core-hole formed as a result of ejection of photoelectron has a finite lifetime τ, in the order of 10^{-15} s which by Heisenberg's uncertainty principle corresponds to a lifetime broadening of $\Gamma = \frac{\hbar}{\tau}$, which is in the order of 0.1 eV. This intrinsic lifetime broadening contributes to the broadening of the photoemission peaks and is described by a Lorentzian function. The lifetime broadening also depends on the measured orbitals. Furthermore, there are various factors contributing to the experimental broadening, such as the resolution of the electron analyzer and the line widths of the x-ray source, along with thermal, pressure and vibrational broadening. Collectively, experimental broadening can be accounted for by a Gaussian function. For certain spectra such as the O1s spectra, along with an appropriate background subtraction, fitting the spectra with a Voigt[31] profile also becomes essential for spectral deconvolution.

2.1.2 X-ray Spectroscopies

2.1.2.1 X-ray absorption spectroscopy

The origins of x-ray absorption spectroscopy (XAS) can be traced back to the early 20th century, following the development of tunable x-ray sources. The first recorded instance of XAS was presented by Walther Kossel in his 1919 paper, *Zum Bau der Röntgenspektren*, where he documented the 3d to 4f transitions in uranium and thorium[32]. However, it was not until the 1960s, with the advent of synchrotron light sources capable of generating intense and tunable x-rays, that XAS became widely utilized for material characterization across various scientific fields. Since then, the fine structure observed in absorption spectra has proven to be an essential tool for investigating the electronic, magnetic, and chemical properties of materials. XAS measures how likely an x-ray photon is to be absorbed by a sample as a function of photon energy. The incident photon energy is varied in stepwise increments, while measuring a signal proportional to the absorption coefficient μ of a solid, liquid or gaseous sample. μ is directly related to the absorption cross section σ of the material, which defines the probability of x-ray absorption. The absorption cross section and the absorption coefficient can be related via the following relation:

$$\mu = N\sigma \tag{2.7}$$

N is the density of atoms in the material, thus the μ describes the amount of x-ray intensity absorbed per unit thickness of material. The spectrum that is obtained as a result has the following key features: with the increase in energy, the overall photon absorption decreases, reflecting the quantum-mechanical nature of x-ray absorption by atoms. The absorption edges give rise to sharp increases in the absorption coefficient, which is unique for each element and hence gives rise to the absorption edges. Beyond the absorption edge, small oscillations in the absorption coefficient reveal several structural details such as interatomic distances and coordination numbers, specifically for molecules and solids.

Figure 8 shows the schematic representation of the x-ray absorption process at an atomic level, which is illustrative of an incident x-ray photon exciting an electron form a core-level to an unoccupied state in the conduction band, as in this representation, or even the vacuum level.

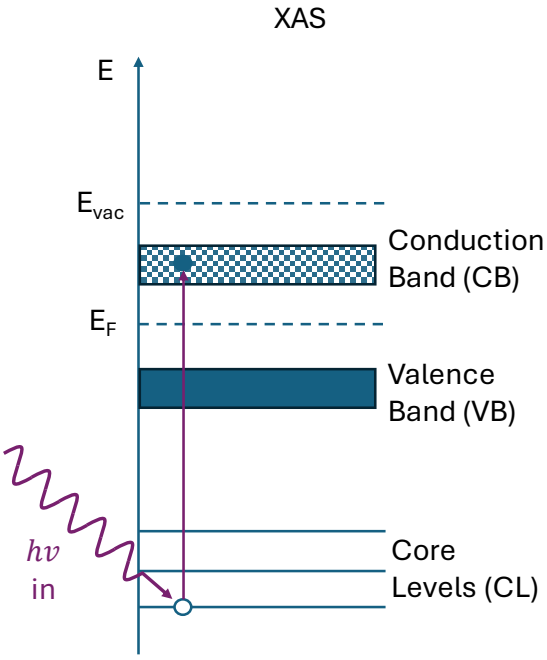

Figure 8: Schematic representation of XAS.

The nomenclature for x-ray absorption features represents the core orbital from which the electron is ejected. Figure 9 shows how the absorption edges react to the variation of incident photon energies[33].

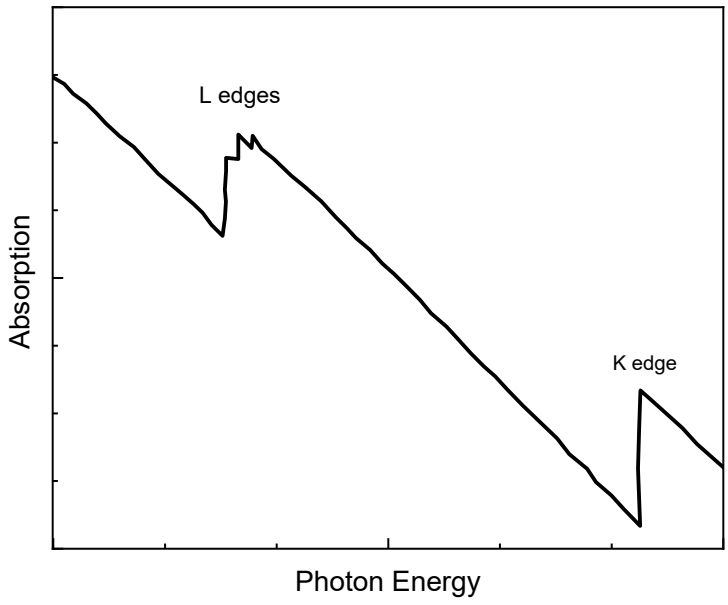

Figure 9: Schematic representation of variation of the atomic x-ray absorption coefficient as a function of the photon energy. The characteristic saw-tooth like features with a sudden increase of the absorption at certain energies mark the absorption edges. Picture derived from ref[33].

The discontinuities in the spectra are labeled according to the atomic shell from where the excited electron originates[34]. "K" describes a transition from 1s orbital, "L" from 2s or 2p and so on. The angular momentum and spin-orbit coupling affect the energy of the ionization threshold, generating a singlet for the K-transition and the L-transition appears as a triplet, with L_1 (2s) and L_2, L_3 (2p). Similarly, an M-transition will be a quintet.

Looking closely into one of the absorption edges in Figure 9, a fine structure of the spectrum can be seen, which is a representation of the energy dependence of μ. This gives rise to three distinct regions to the spectra at each of the absorption edges: pre-edge, near-edge and post-edge. In the **pre-edge** region, the energy of the incident photon is slightly lower than the ionization threshold of the core level, allowing weak transitions to localized unoccupied states. As a result, only valence and outer core electrons can be excited into the vacuum in the pre-edge region, yielding a relatively small and gradually decreasing μ. The **near-edge** region, also known as x-ray absorption near edge structure (XANES) for hard x-rays and near-edge x-ray absorption fine structure (NEXAFS) for soft x-rays, occurs when the energy of the incident photon approaches the binding energy of the core electron. At this threshold, called the **main absorption edge**, transitions become possible from the ground state to an excited state consisting of a core-hole, resulting in the photoionization of the core electron and its ejection into the vacuum level. Beyond this energy, in the post-edge region, the absorption coefficient μ continues to decrease gradually but also exhibits oscillations due to interference between the emitted photoelectron and atoms in its surrounding environment. These oscillations, known as extended x-ray absorption fine structure (EXAFS), provide valuable information about the structure of the material, such as the distance between neighboring atoms and, under high-quality data conditions, the atomic number of the scattering atoms. Figure 10 shows a depiction of these regions. XANES exhibits a more detailed fine structure compared to EXAFS due to reduced lifetime broadening during measurement[35]. This is due to the fact the photoelectron in EXAFS undergoes more inelastic scattering than those in XANES and hence have a shorter lifetime. The core-hole lifetime and transition energy are related by an uncertainty principle, which causes Lorentzian broadening of the discrete transitions of the absorption spectrum. This property is particularly helpful in "fingerprint analysis" of samples by comparing them to the spectra of reference materials.

EXAFS is beyond the scope of discussion in relevance to this work. NEXAFS or soft x-ray absorption spectroscopic measurements are best suited to study the transition metal L-edges, as the 3d core levels can be directly probed and K edges of lighter elements such as oxygen and carbon, whose 1s core binding energy lies in the soft x-ray regime.

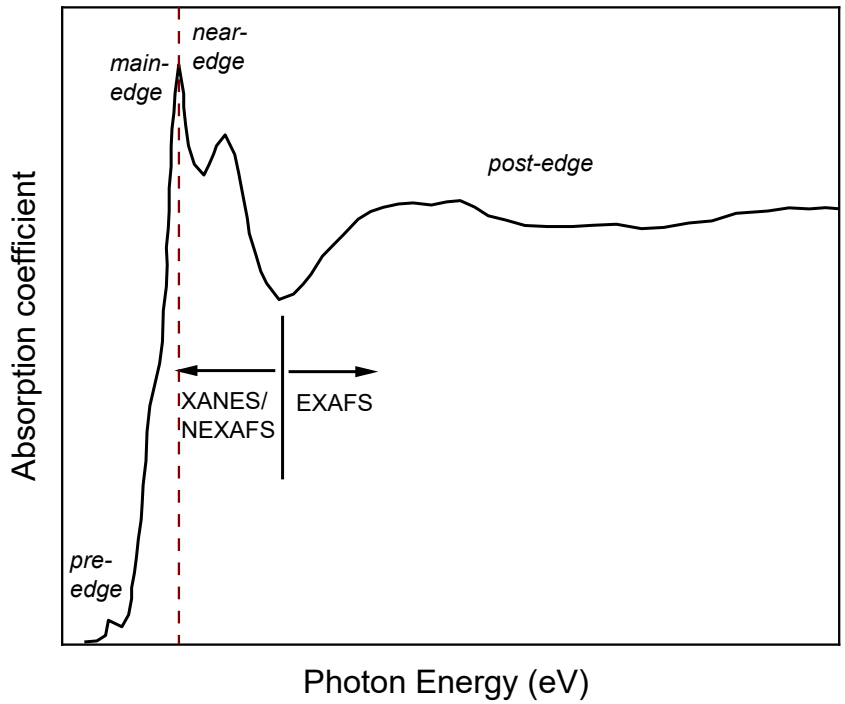

Figure 10: K-edge x-ray absorption of a solvated transition metal complex. The division into the two characteristic spectral regions, namely XANES and EXAFS are marked with a vertical line.

2.1.2.1.1 Detection modes in XAS

X-ray absorption spectra can be recorded using different yield modes, each suited to specific experimental conditions and nature of sample.

1. X-ray transmission mode

One of the most widely used methods to record the absorption spectrum is the x-ray transmission mode. The observable intensity detected in the experiment is the transmitted intensity of the x-ray beam I_t. To relate the x-ray absorption coefficient with it, Beer-Lambert law can be used:

$$I_t = I_0 e^{-\mu d} \tag{2.8}$$

Where I_0 is the incident x-ray intensity and d is the sample thickness. The absorption coefficient μ is a measure of the total absorbed x-ray intensity by the sample, which includes not only the atom whose absorption one wants to measure, but all other atoms as well, which makes this a rather unspecific mode of detection. Experimentally, a transmission measurement is most commonly performed using an x-ray monochromator. A particular wavelength of the x-ray beam is selected and both incident and transmitted intensities are measured for a varied range of wavelengths. Transmission is performed mostly for the hard x-ray regime, where photons have sufficient penetration depth to pass through moderately thick samples. In the soft x-ray regime, however,

transmission measurements generally require ultra-thin samples, which could not be made possible for the samples studied in this work.

2. Electron yield measurements

Electron yield measures the current generated by the backflow of electrons that fill the holes left behind after emission of electrons from the sample following x-ray absorption. The energy distribution of the emitted electrons is not considered in the case of total electron yield (TEY). Techniques like partial electron yield (PEY) and Auger electron yield (AEY) use an electron analyzer to examine specific energy windows. TEY is widely used due to its simplicity and effectiveness, particularly for studying thin films, surfaces and interfaces of conductive samples where bulk-sensitivity is not necessary. However, a primary limitation of this technique is sample charging effects, making the method unsuitable for analyzing certain material systems, especially insulating systems. If a sample is not conductive, charge transfer through the sample may not happen fast enough to neutralize the charge removed from the sample through polarization. This may result in significant shifts in the peaks observed.

Soft x-ray photons have penetration depths in the order of a few hundred nanometers, whereas the photoelectrons and Auger electrons generated by them have a mean free path of only a few nanometers. The photoelectrons generated within the bulk of the sample scatter inelastically, subsequently triggering a chain reaction of electron emission and typically are unable to reach the surface. This characterizes the electron yield measurements as highly surface sensitive[36].

The electron yield measurements discussed in this thesis were measured using TEY that was recorded using sample drain current method[37]. For the reference materials, a thin layer of each of the powdered samples were smeared on the surface of conductive silver tape to ensure charge transport and avoid charging effects.

3. Fluorescence yield measurements

Fluorescence yield measurements use a photon sensitive detector to track changes in the number of photons emitted from the sample, as a result of the core-hole decay, as the incident x-ray energy scans through an absorption edge. This is a bulk sensitive technique.

When an x-ray photon is absorbed, a core-hole is created, leaving the atom in an unstable state. This is followed by a rapid decay, as the core-hole is filled, typically by an electron from a lower lying energy state. The excess energy can be released as either a fluorescence photon or through an Auger electron emission. The probability of a core-hole to decay via fluorescence is however low for K shell transitions of light elements, as the Auger process dominates at lower x-ray energies.

To ensure accurate measurements, a biased mesh or a grounded thin filter is placed between the sample and the detector, to minimize interference from emitted electrons. If the sensitivity of the detector is equal across all fluorescence energies, the output of the measurement is referred to as total fluorescence yield (TFY). If the detector can sieve out emissions of only a specific energy range, partial fluorescence yield (PFY) measurements are possible.

This filtering of energy is usually achieved with the help of a dispersive element, such as a grating based spectrometer. At the X-SPEC beamline, a plane grating monochromator (PGM) is used for this purpose. The PGM uses a plane diffraction grating in grazing incidence mode to separate the fluorescence photons by energy[38]. A practical advantage of the PGM is that it can maintain fixed entrance and exit slits while scanning different photon energies, over an expansive energy range, by adjusting a parameter known as the fixed-focus constant. This constant describes the incidence and diffraction angles on the grating, preserving the focus with changing wavelengths. Therefore, by carefully setting this constant, energy resolution and photon flux can be balanced, depending on the nature and needs of the experiment.

Most modern PGMs, like the one at X-SPEC use a variable line spacing (VLS), which helps correct optical aberration and maintain a high energy resolution across a broad range of energy. By working at grazing incidence, the PGM is able to suppress the higher diffraction orders that could overlap with the desired signal. These features hence make the PGM ideally suited for fluorescence yields in the soft x-ray regime, where crystal monochromators would be less efficient.

Fluorescence yield is considered bulk-sensitive since emitted photons can escape from depths up to hundreds of nanometers, depending on the incident x-ray energy[39]. This is because fluorescence photons typically have similar or lower energy than the incident beam, allowing them to penetrate the sample and reach the detector with minimal reabsorption.

Saturation effects and self-absorption

Saturation effect is a phenomenon that might hamper the signal obtained from both electron yield measurements[40]. It is a result of limited escape depth of secondary electrons. During the process of XAS, electrons generated only within a few nanometers below the surface are capable of escaping to the detector. Absorption of x-rays deeper in the material does not add to the detected signal any further. As a result, the measured signal stops increasing and appears to be saturated as it plateaus with further increase in intensity of irradiating x-rays.

In fluorescence yield measurements, **self-absorption** happens when the fluorescence photons are reabsorbed before they can reach the detector[41]. This is possible when the emitted fluorescence photons have energies overlapping with the absorption edges of the material. This reduces the intensity of the detected photons, particularly for the photons emitted from deeper within the material. In electron yield measurements, secondary electrons are reabsorbed before they can escape to the surface and be detected. In materials with a high absorption or scattering cross section, this is more likely to occur, as some of these electrons will either be reabsorbed or scattered before they reach the surface, resulting in a lower measured electron yield. Self-absorption is enhanced in cases of thick samples, hence, to minimize this, the samples studied were not thicker than 100 nanometers. However, self-absorption effects are more likely to be observed in fluorescence yield measurement due to the relatively longer escape depth of the fluorescence photons as compared to that of the secondary electrons is electron yield measurements.

2.1.2.1.2 Multiplet splitting

Incident x-ray excites a core electron and leaves behind a core-hole, which then interacts with valence electrons, leading to relaxation effects that modify the final state of the system[42]. In transition metal oxides, this core-hole induced relaxation can lead to multiplet splitting of the XAS spectra: the resultant absorption spectrum shows multiple peaks corresponding to different final-state configurations of the system. Additionally, spin-orbit coupling and different external ligand fields also play a significant role in determining these final states and therefore the nature of the multiplets. These effects are particularly pronounced in systems with localized states at the Fermi level, where the core-hole can induce shifts in the energy levels of the final states. This splitting is a result of the core-hole-induced relaxation and the strong electron-electron interactions, which are not adequately described by either the one-electron band model or the strongly correlated limit. To understand the shifts and splitting of the spectra in the final state, multiplet theory can be applied[43]. The multiplet theory accounts for Coulomb interactions between electrons and the influence of the ligand field. In the case of transition metals such as Fe, the final state of the system depends on the spin orbital configuration of the 3d electrons.

Multiplet splitting observed in XAS of transition metal is governed by the core-hole creation. Strong Coulomb interactions are experienced between the core-hole and the partially filled 3d valence shell, when an electron from the 2p core level is promoted to an unoccupied 3d orbital resulting in a $2p^5\ 3d^{(n+1)}$ configuration. These interactions lift the degeneracy of the possible final states, thereby producing the multiplet structure of the final states, reflecting the allowed spin and orbital couplings of the system.

The surrounding ligand field further distorts the symmetry of the d orbitals, splitting their energy levels and modifying the distribution of intensity among the multiplet features. Additionally, hybridization between the metal d states and the ligand p orbitals result in mixed electronic configurations, also contributing to the multiplet structure. Collectively, these effects such as the formation of the core-hole, the local Coulomb interactions, crystal field splitting and metal-ligand hybridization, produce the multiplet structure of the transition metals in XAS.

The observed multiplet structure of the transition metal XAS can be described mathematically using configuration-interaction models, where parameters such as Coulomb repulsion, charge-transfer energies and hybridization integrals define the relative energies and intensities of the final states. It is essential to recognize that these symmetry allowed final states are responsible for the multiplets observed in XAS, providing valuable insights into oxidation states, coordination environments, and catalytic function of the transition metals.

2.1.2.2 X-ray emission spectroscopy

X-ray emission is a photon in-photon out process, in which a core-hole is filled by an electron from the valence band. To create the initial state, a core electron has been removed and hence a core-hole is created by a photon. The energy of the photon emitted in x-ray emission spectroscopy (XES) is the energy difference between the levels involved in the transition. Figure 11 shows a schematic representation of the XES process. The initial state of XES already consists of the core-hole, created earlier and is not a part of XES, but for ease of understanding is shown in the figure in grey. The emission process is shown in red. The XES process is governed by the dipole selection rule, $\Delta l = \pm 1$, l being the angular momentum quantum number.

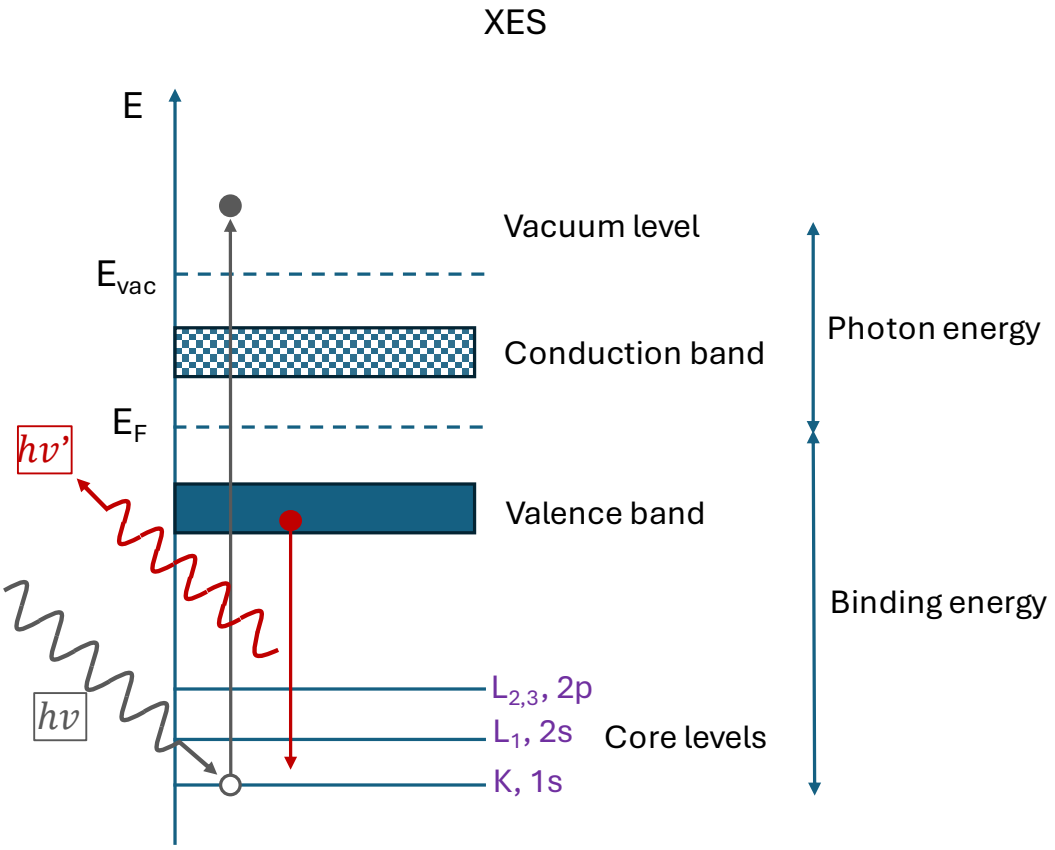

Figure 11: Schematic of the x-ray emission process. The first step is shown in grey and the emission process is shown in red.

The intensity of the emitted photons in XES also depends on Fermi's golden rule. Additionally, the intensity of the XES signal is also governed by the exponentially attenuated intensity of the incoming and outgoing photon. The attenuation lengths of x-ray through many types of materials are tabulated in the literature[44]. The x-ray emission process is in competition with the Auger emission process. The Auger emission dominates for low atomic numbers, specifically for the K-shell. XES is a complementary technique to XAS, as it probes the occupied states. It is a helpful tool to determine the oxidation states of elements and changes in the oxidation states can be tracked with the shift in

the emission spectra. Similarly to XAS, “fingerprint analysis” is possible in XES as well, by comparing the spectra of the samples to similar reference materials.

2.2 Electrochemical Background

2.2.1 Introduction

Electrolysis of water is a redox reaction that uses electricity to convert water (H_2O) into hydrogen (H_2) and oxygen (O_2)[45]. The reaction is induced by an external energy input, such as an electric potential, applied to the electrochemical cell, in which the reaction occurs.

The overall redox reaction for electrochemical water splitting is given by:

$$H_2\,O_{(l)} \rightarrow\ H_{2(g)} + \frac{1}{2}O_{2(g)} \tag{1.1}$$

The oxidation process is the oxygen evolution reaction (OER) which occurs at the anode and the reduction process is the hydrogen evolution reaction (HER), which occurs at the cathode.

In acidic medium, the HER reaction is the following:

$$2H^+ + 2e^- \rightarrow\ H_2 \tag{1.2}$$

And the OER reaction is the following:

$$H_2O \rightarrow \frac{1}{2}O_2 + 2H_2 + 2e^- \tag{1.3}$$

And in alkaline medium, the HER reaction is the following:

$$H_2O + e^- \rightarrow \frac{1}{2}H_2 + OH^- \tag{1.4}$$

And the OER reaction is the following:

$$2OH^- \rightarrow H_2O + \frac{1}{2}O_2 + 2e^- \tag{1.5}$$

Electrochemical water splitting in alkaline medium is schematically represented in Figure 12.

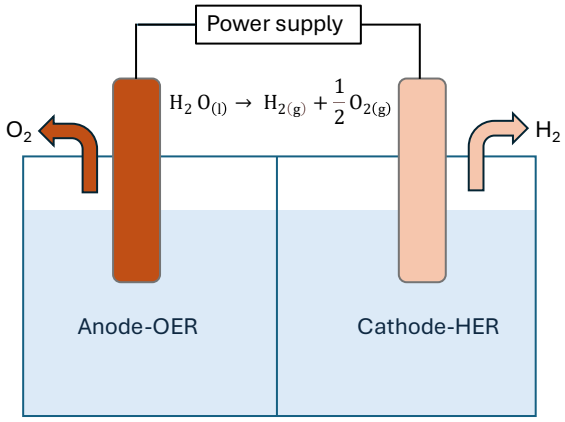

Figure 12: Schematic representation of water splitting in alkaline medium. OER results in O_2 generation (left) and HER in H_2 generation (right).

The standard potential for water splitting is 1.229 V at normal temperature (298.15 K) and pressure (101.325 kPa)[1]. However, this potential is affected by changes that occur to these nominal conditions and other factors such as thermal effects, catalytic activity, nature of electrodes and electrolyte and kinetics of the reaction. Because of reaction barriers, the actual electrode potential required to break the bonds in water is significantly higher. In acidic media, the cell voltage for successful splitting of water is around 1.7-2.2 V, while in alkaline media, water splitting usually occurs between 1.7-2.4 V[46]. Processes such as nucleation, growth, detachment and transport of oxygen and hydrogen gas bubbles results in an increase of the required potentials[47]. The excess potential is referred to as overpotential, η.

To lower the overpotential, the reaction is catalyzed by appropriate materials. Several such catalysts have been explored and studied and the landscape of current research involving these catalysts will be discussed in the next Section. In this thesis, the catalyst that will be studied is $Fe_xNi_{1-x}(O,OH)_y$. Its proven exceptional ability to catalyze electrolysis of water makes it an appropriate choice for further analysis.

2.2.2 Electrochemical cell setup and electrodes

Apart from electrolysis, several analytical techniques that help characterize and compare the efficiencies of several electrocatalysts can be performed in the electrochemical cell. The construction of electrochemical cells involves understanding the fundamental processes that require to be performed within the cell. Studying the voltametric behavior of electrode and cell materials to optimize the design of the cell is hence essential.

In the present discussion, a customized three-electrode cell setup is used, manufactured by Redox.me. The cell is made of PEEK (polyether ether ketone), which is a high-performance polymer[48]. Its merits include exceptional chemical resistance, mechanical strength and thermal stability, making it a good candidate for use with corrosive electrolytes and under high temperatures, if demanded by the reaction. The cell operates with a three-electrode setup, featuring separate working, counter, and reference electrodes. A schematic representation of the front and the top view of the cell is shown in Figure 13.

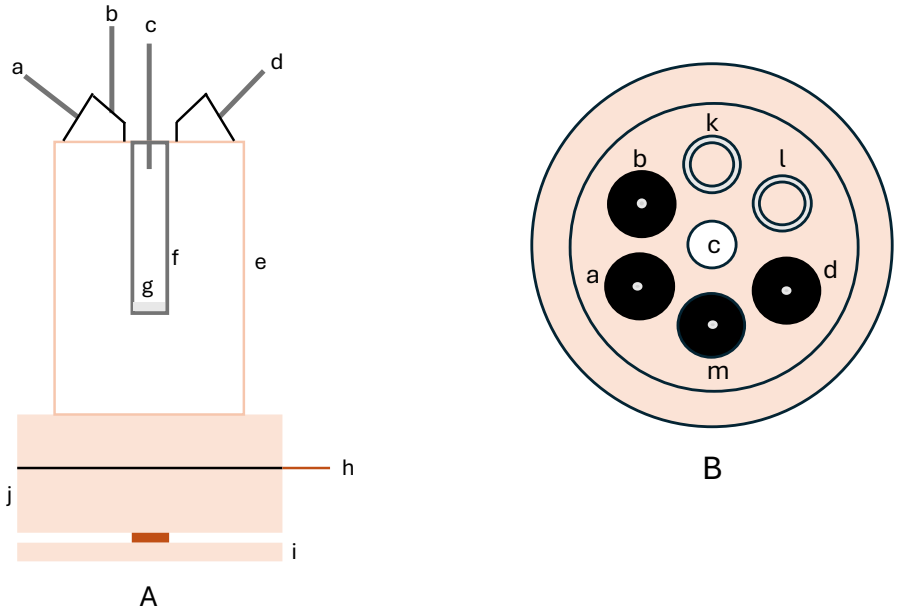

Figure 13: Front (A) and top (B) views of the three-electrode cell set up. (a) is the CE outlet, (b) WE inlet, (c) CE, (d) CE inlet, (e) PEEK body, (f) glass chamber for counter electrode, (g) ceramic frit, (h) Cu contact for WE, (i) clamp screw (j) sample or WE mount, (k) reference electrode, (l) lid for chamber for introducing gas, (m) WE outlet.

The schematic representation allows a view of the counter electrode (CE) outlet (a), working electrode (WE) inlet (b), CE (c) and CE inlet (d). The body of the cell (e) is made of PEEK and the chamber that holds the CE is made of glass (f) with a ceramic frit at the bottom (g). The electrolyte of choice is introduced into this chamber and subsequently the counter and reference electrodes are immersed in the electrolyte through their respective chambers. The working electrode is mounted on a platform (j), which is screwed in with a clamp screw (i) and the copper plate (h) establishes contact between the working electrode and the source of external potential. The reference electrode (RE) (k) is next to the lid (l) which can be used to introduce gas into the cell, such as Ar or other inert gases, with the intention of degassing the electrolyte, to get rid of dissolved oxygen or other impurities. The CE and the WE outlets respectively (a, m) are passages for escape of gas bubbles that may form at the CE and WE while an electrochemical reaction takes place. The CE inlet (d) acts as an entry port for the electrolyte flow into the CE compartment, when an electrochemical flow reaction is underway, but that is beyond the scope of this thesis. The working electrode is mounted on a platform (j), which is screwed in with a clamp screw (i) and the copper plate (h) establishes contact between the working electrode and the source of external potential.

The **working electrode (WE)** is the component where the reaction of interest occurs. In this work, the working electrode is the $Fe_xNi_{1-x}(O,OH)_y$ film electrodeposited onto a gold coated wafer, providing a well-defined active surface. The gold coated wafer provides a highly conductive and chemically inert substrate that ensures uniform current distribution across the working electrode. This helps in reproducible film growth during electrodeposition and minimizes variations in electrochemical behavior, making it a reliable choice for preparing and characterizing the electrocatalyst films.

An ideal **reference electrode (RE)** must hold its integrity of composition for the duration of an experiment, to provide a stable potential for controlled regulation of the working electrode (WE) potential[49]. It should be nonpolarizable, i.e. its potential should remain constant irrespective of the current that flows through the RE. The reaction taking place at the electrode should be reversible, allowing for the potential to be calculated from the Nernst equation and revert to its original potential after the passage of current. The Standard Hydrogen Electrode (SHE) or Reference Hydrogen Electrode (RHE) is the standard reference point for standard electrochemical reduction potentials, with its potential E^0 defined as 0.0000 volts (V) at all temperatures by convention. Platinum is the chosen metal for the production of most reference electrodes, because of its chemical inertness and its catalytic activity for the hydrogen redox reaction, which ensures fast and reversible photon exchange at the electrode. The redox process for this electrode is as follows:

$$2H^+ + 2e^- \rightleftharpoons H_2, E^0{}_{Pt/H_2,H^+} \equiv 0 \tag{1.6}$$

The SHE is however not practical for use in the laboratory owing to challenges such as the need for hydrogen gas at 1 atm, a platinum electrode coated with platinum black[50] and precise pH control at 0, which makes it fragile and complex to set up. Instead, alternative options have been resorted to. The most regularly used electrode is the Ag/AgCl electrode, owing to its simplicity, affordability and non-toxicity. The electrode solvent for such an electrode is generally 3 M KCl, which can be refilled. The controlling redox reaction is the following:

$$AgCl + e^- \rightleftharpoons Ag + Cl^-, E^0_{Ag/AgCl} = 0.222\ V\ vs\ RHE \tag{1.7}$$

The potential of such a reference electrode however, requires pH correction[51] when comparing or converting potentials measured with an Ag/AgCl reference electrode to the standard reference potential scale, i.e. the SHE. The relationship that converts the measured potential to the SHE scale originates from the Nernst equation, which relates the electrode potential to the activity of the reacting species[52]. The conversion can be expressed as:

$$E_{SHE} = E_{measured} + E^0_{reference} \tag{1.8}$$

Where:

E_{SHE} = Potential vs SHE

$E_{measured}$ = Potential vs chosen reference electrode (Ag/AgCl)

$E^0_{reference}$ = Standard potential of the reference electrode relative to SHE

For an Ag/AgCl electrode, equation 1.8 becomes:

$$E_{SHE} = E_{measured} + E^0_{Ag/AgCl} + 0.059 * pH \tag{1.9}$$

The 0.059*pH term arises from the logarithmic dependence of hydrogen activity on the potential, as described by the Nernst equation, at 25^0 C.

In cases where a conventional electrode is not practical or available, a pseudo or quasi reference electrode is used[49]. It is usually an inert metal wire, like gold or platinum or even silver, provided that

it does not interfere with the system. The potential of a pseudo reference electrode is prone to drifting which is changing with time while in use. To make sure that it provides a reliable reference measurement, it is often compared to a conventional reference electrode to establish a standard. It is a low-independence electrode, i.e. it has a low resistance to the flow of electric current, which helps to compensate for its lack of fixed potential.

The **counter electrode (CE)** is essential for closing the electrical circuit[53]. The processes occurring at the CE are complementary to those at the WE; if an anodic (oxidation) process occurs at the WE, a cathodic (reduction) process occurs at the CE and vice versa. The potential of the counter electrode is established according to the electrochemical reactions taking place in the cell. The material chosen for the CE must be electrically conductive, should be chemically stable over a wide range of potential in various electrolytes and should be mechanically stable. A convenient choice therefore is Pt, which exhibits these properties.

2.2.3 Electrochemical techniques

Understanding the reactions requires monitoring of parameters such as overpotential, charge transfer, resistance and current density, which are key indicators of catalytic activity and stability. **Cyclic voltammetry (CV)** is one such key technique. In CV, the potential of the WE immersed in an electrolyte is cycled and the resulting current is measured[54]. The changing potential of the WE is monitored with the help of the RE. The voltage sweep is performed at a fixed rate. To conduct a CV, the appropriate potential window, comprising of an initial, switching and final potential that would be scanned during the experiment is set. A tentative range for performing such a potential sweep, on an $Fe_xNi_{1-x}(O,OH)_y$ thin film with an Ag/AgCl electrode is 0-0.85 V[55]. The scan usually begins at the open circuit potential (OCP), where the solution is at equilibrium and no net current flows through the system. A gradual increase to the switching potential occurs, where oxidation takes place, followed by a reversal to the initial potential, allowing for reduction to occur. The current response, as a function of the changing potential is recorded, which is referred to as a cyclic voltammogram[54]. A cyclic voltammogram of $Fe_{10}Ni_{90}$ is represented in Figure 14.

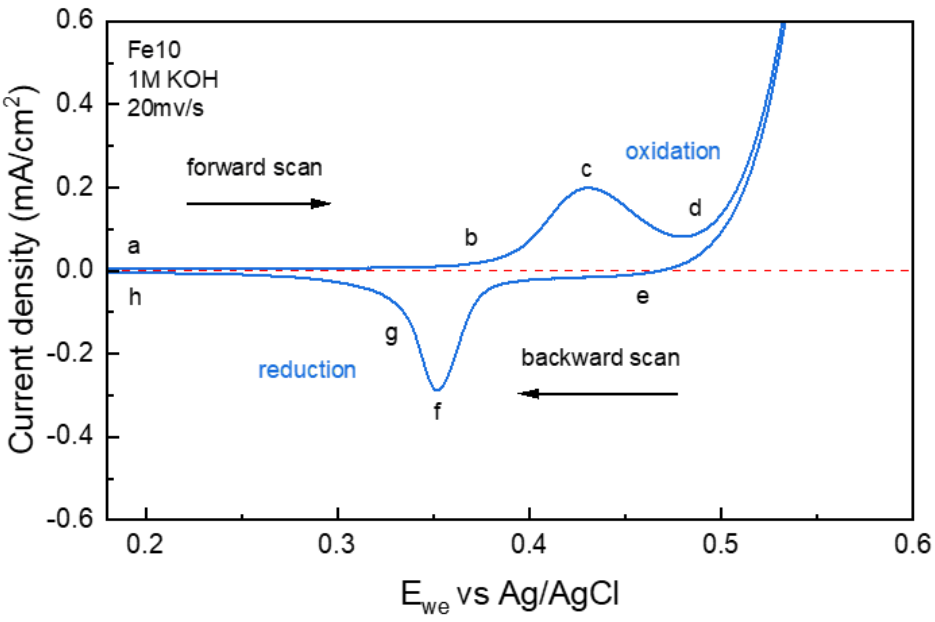

Figure 14: Cyclic voltammogram of $Fe_{10}Ni_{90}(O,OH)$. a denotes the start of the reaction, a-d is the forward scan. b marks the onset potential, c is the anodic peak and d represents the onset of the OER reaction. e marks the reversal in the direction of current, f marks the cathodic peak. g is where the transition back to a state closer to equilibrium starts and the reaction terminates at h.

The electrolyte used is 1 molar potassium hydroxide (KOH). The counter electrode used is a Pt wire and the scan is performed at a rate of 20 mV/s. As the experiment begins, the current is minimal due to the capacitive[56] behavior of the WE. This behavior is denoted by "a". Here the current is proportional to the scan rate, indicating that the response arises from surface redox reactions, rather than reactions involving bulk electron transfer. "b" marks the onset potential, where a significant increase in current occurs. The anodic peak[54] is denoted by "c", which coincides with the highest current response during oxidation process. During the forwards scan "a-d," oxidation occurs at the WE where an electron lost by the reacting species from the WE is transferred to the counter electrode. As a result, the current rises and the electrode potential reaches a maximum. The peak "c" marks the point where the oxidation rate is maximized, before the rate decreases again as the reacting species deplete near the electrode surface. "d" marks the onset of the OER reaction, where the current increases rapidly due to the highly demanding nature of the OER reaction in terms of energy. This point is significant in determining the overpotential for OER. "e" denotes the reduction process, where the current reverses its direction. "e-h" represents the backward scan and "f" is the cathodic peak, which is the reductive counterpart of "c" and represents the minimum current generated by the system during reduction. The transition after the reduction process is marked by "g", where the current starts to decrease, indicating that the system is transitioning back to a state closer to equilibrium. The reaction is made to drive back to the starting potential, which in the case of the reaction shown in Figure 14 is the OCP.

2.3 Landscape of Current Research in Electrocatalysts for OER

The phenomenon of water electrolysis was first observed by Trootswijk and Diemann[57] in 1789 and has since been broadly investigated by researchers. As explained in Chapter 2.2, the electrolysis of water has two fundamental half reactions: hydrogen evolution reaction or HER at the cathode and oxygen evolution reaction or OER at the anode. To drive the electrochemical water splitting thermodynamically, the energy barrier of 237.2 kJ mol^{-1} needs to be overcome, which corresponds to an applied voltage of 1.229 V in the electrochemical cell[1]. The actual potential for OER though is much higher, between 1.7-2.2 V[58], due to several factors such as nature of electrodes and reaction kinetics, as discussed in Chapter 2.2. This warrants for the development of more active catalysts that lower the over potential η for OER, in order to improve the overall efficiency of water electrolysis.

While numerous classes of oxide-based catalysts have been studied, increasing attention has shifted toward specific layered transition metal systems that offer exceptional performance, a theme explored in detail later in this chapter.

2.3.1 From noble metals to earth abundant alternatives: established trends in OER catalysts

Several novel materials have emerged as OER catalysts, such as metal chalcogenides[59,60,61], oxides[62,63], nitrides[64,65] and polymer systems[66,67]. Ru- and Ir-based oxides are among the most widely studied and industrially employed OER catalysts, owing to their high activity in acidic media[2,3]. However, in acidic media, both RuO_2 and IrO_2 undergo further oxidation and subsequent dissolution under high applied voltages, making them unstable during electrolysis[68,69]. Ru and Ir are also expensive metals, which limits their large-scale applicability. In contrast, alkaline media allow for the replacement of noble metal catalysts with more abundant and stable transition metal-based alternatives[70,71]. Understanding the limitations of these conventional catalysts is essential for contextualizing ongoing efforts to develop cost-effective and durable materials, a central focus of current electrocatalyst research.

Transition metal oxides represent a key class of materials for oxygen evolution reaction (OER) catalysis, owing to their structural diversity and tunable electronic properties. Gaining insight into the different types of oxide catalysts is crucial for rational catalyst design, as it enables a deeper understanding of how specific transition metals and their coordination environments influence OER activity. Currently, a wide range of compositions of transition metal oxides are under investigation to find the most efficient catalyst for OER, in terms of cost-effectiveness, accessibility, activity, and long-term stability. These catalysts can be broadly grouped into three categories: complex perovskite oxides[4,5], spinel oxides[6,7] and layered oxy-hydroxides[8,13].

Perovskite transition metal oxides are considered viable electrocatalysts due to their tunable electronic structure and high intrinsic activity[72]. They typically adopt an ABO_3 structure, where the A-site cations are rare-earth or alkaline earth metals, 12-fold coordinated with oxygen, while transition metals occupy the B-site, positioned at the center of corner-sharing oxygen octahedra. Substituting

the A-site cation can influence the electronic environment of the B-site metal and thus modulate catalytic performance. For example, replacing Sr^{3+} with La^{3+} in compounds such as $Sr_xLa_{1-x}FeO_3$ ($0 \leq x \leq 1$) has been shown to significantly enhance OER activity[73,74].

Spinel oxides have also demonstrated promising performance as efficient OER catalysts[75]. These oxides adopt the general formula AB_2O_4, where transition metal cations occupy the A-site in tetrahedral coordination, while B-site cations are in octahedral coordination. This structural arrangement allows for the incorporation of multiple transition metals in varying valence states, facilitating the synthesis of a wide variety of compositions. The chemical environment of the transition metal in the octahedral site can be tuned through both composition and synthesis conditions, thereby enabling control over the material's catalytic activity[76,77]. For instance, in $Ni_xCo_{3-x}O_4$ ($0 \leq x \leq 1$), varying the Ni content significantly influences OER performance.

Transition metal oxyhydroxides are among the most investigated and promising catalyst systems for the oxygen evolution reaction (OER) in alkaline media,[78,79] owing to their high activity and easy availability.

In an experimental study by Sadiek et al. in 2011[9], NiO nanoparticles were deposited onto glassy carbon electrodes and tested for OER activity in 1.0 M KOH solution using cyclic and linear sweep voltammetry. The NiO-modified glassy carbon electrodes demonstrated enhanced catalytic performance, with reduced overpotentials and improved stability over multiple cycles, highlighting the benefits of increased surface area and conductive pathways provided by the NiO nanostructure. However, the study did not include detailed structural or surface characterization (e.g., particle size or morphology), leaving uncertainties about the precise active sites responsible for the observed activity. Li et al. in 2020[10] conducted a theoretical investigation on γ-NiOOH, revealing that the formation of Ni vacancies on the surface leads to fourfold-coordinated nickel sites, which exhibit substantially lower overpotentials compared to pristine surfaces. These findings suggest that defect engineering can dramatically enhance catalytic efficiency. Nonetheless, the study was limited to computational modeling and lacked experimental validation of the predicted active sites.

While pure Ni based catalysts were studied and explored, several approaches also coupled Ni with other materials to gauge their involvement in the OER process. In a study by Liao et al. in 2019[11], the focus was on improving the OER performance of NiO by combining it with a conductive support material such as polymeric carbon nitride (CN). This study explored a composite approach to enhance practical catalytic performance. The NiO/CN composite materials were synthesized through an in situ method and tested for OER activity in both 1 M KOH and phosphate buffer (pH 6.9). The best performing sample achieved an overpotential of 261 mV at 10 mA cm^{-2} in alkaline media, showing clear improvement over pure NiO and even outperforming commercial RuO_2 at higher current densities, for instance 356 mV/cm^2 vs 379 mV for RuO_2. The enhancement was attributed to better electrical conductivity and stronger interaction between NiO and the support material. However, the study did not examine how the catalyst structure changes during OER, nor did it directly confirm whether active NiOOH phases form during operation, a key factor in understanding long-term performance. The work therefore highlights the value of composite design strategies for improving Ni-based OER catalysts but also underscores the need for further investigation into their active phases and long-term behavior.

In a 2023 study by Gallenberger et al.[12], the stability of the NiOOH phase, considered the active species during OER in alkaline media, was investigated in detail using sputtered NiO thin films. The authors focused not on catalytic performance metrics but on understanding how stable NiOOH remains when external potential is no longer applied. The electrocatalytic testing was conducted in 1 M KOH using chronoamperometry and cyclic voltammetry. The key finding was that NiOOH, although formed under OER conditions, is highly unstable once the applied potential is removed. It quickly decomposes back to $Ni(OH)_2$ both in the electrolyte and in air, with the rate of degradation varying depending on the environment and how the sample was handled post-electrolysis. The study also proposed that even trace moisture (e.g., water vapor in air) can induce this phase reduction, and that applying protective surface layers like dried KOH might slow the process but not prevent it entirely. While this work provides valuable insights into the transient nature of NiOOH under practical conditions, it also underscores a major limitation of Ni-based catalysts for OER: the active phase may not persist beyond operation, complicating both catalyst evaluation and long-term viability.

Therefore, it is evident that while nickel-based oxides have shown considerable promise as OER catalysts, they have limitations such as poor conductivity, limited activity in neutral media, and instability of the active NiOOH phase outside operational conditions. Although composite systems like NiO/CN have demonstrated improved performance, they often present challenges in pinpointing the actual active phase under operating conditions. This raised the need to design catalyst systems that not only enhance activity and stability but also allow the active site to be clearly identified and studied over time.

2.3.2 Introduction and role of Fe in Ni-based oxide and hydroxide catalysts

Doping is a proven method to modify the properties of transition metal oxides and enhance their catalytic activity. Introducing iron (Fe) into Ni- and Co-based oxyhydroxides has led to significant improvements in OER performance. Thereby, NiFe-based oxides and oxyhydroxides have emerged as one of the most promising catalyst systems for electrolysis in alkaline media. However, the specific chemical and electronic effects by which Fe enhances activity are not yet fully understood. This section explores studies which have attempted to describe how Fe incorporation influences catalyst behavior and contributes to improved OER performance.

This growing interest in NiFe-based systems is also reflected in comparative activity studies across a range of OER catalysts. One widely used approach is the volcano plot, which relates catalytic performance to the binding energies of reaction intermediates. It illustrates that both overly strong and overly weak adsorption can limit activity, with the highest performance observed at an optimal intermediate strength. As shown in Figure 15, NiFe oxyhydroxides appear near the apex of the curve, highlighting their favorable balance in adsorption energies and confirming their position among the most active OER catalysts in alkaline media. The plot has been reproduced from ref[80].

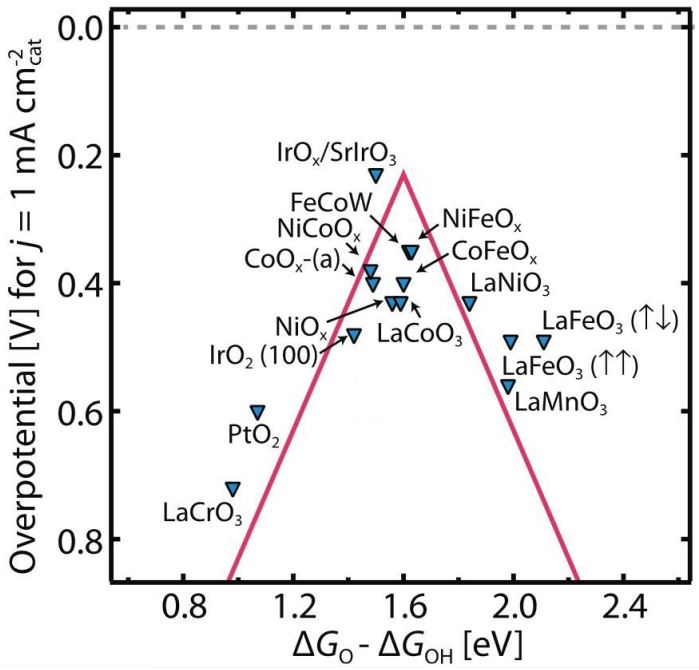

Figure 15: Volcano plot showing the relationship between OER overpotential and intermediate binding energies for various catalysts. NiFe-based systems appear near the apex, indicating high catalytic activity. Plot reproduced from ref[80].

In one of the earliest studies on NiFe systems, Corrigan in 1987[81] observed that small amounts of iron, initially introduced unintentionally from the electrolyte, significantly improved the OER activity of nickel oxide films. This effect was later confirmed through controlled addition of Fe, which consistently enhanced catalytic performance. The results suggested that iron alters the electronic environment of the nickel-based catalyst, making it more active. This study laid the groundwork for research into intentionally incorporating Fe in Ni based oxide and hydroxide catalysts.

Trotochaud et al. in 2014[15] advanced earlier observations on Fe-enhanced Ni-based catalysts by systematically distinguishing the inherent activity of pure $Ni(OH)_2$ from the enhanced performance observed in Fe-containing systems. By using purified electrolytes and controlled film synthesis, they showed that previously reported high activity in $Ni(OH)_2$ systems was largely due to undetected Fe incorporation. Their results demonstrated that Fe alters the electronic properties of the Ni oxyhydroxide matrix in a way that enhances catalytic behavior, independent of conductivity or crystallinity. This work shifted the understanding of Ni-based catalysts and firmly established Fe as an essential component in achieving high OER activity.

Louie and Bell in 2013[14] investigated electrodeposited Ni-Fe oxide films with varying Fe content to understand the role of Fe in enhancing OER activity. By systematically controlling the Fe:Ni ratio, they observed that introducing Fe significantly improved catalytic performance, with peak activity at ~40% Fe. Fe incorporation stabilized the amorphous Ni-Fe structure of the films during electrochemical cycling. While the number of accessible redox-active Ni sites decreased at high Fe incorporation, the authors did not determine whether Ni remained the sole active site. The study concluded that Fe

plays a critical electronic role in improving OER kinetics but left the identity of the active site unresolved.

Friebel et al. in 2015[13] investigated the structural origin of the high OER activity in mixed NiFe oxyhydroxides using *operando* high-energy resolution fluorescence detection X-ray absorption spectroscopy (HERFD-XAS) and complementary DFT+U calculations. They systematically varied Fe content in Ni-based thin films and found that the exceptional activity correlates with the substitution of Fe^{3+} into the γ-NiOOH lattice. A crucial aspect of the study was the identification of Fe as the active site, as the Fe atoms in octahedral coordination exhibited shortened Fe–O bonds, providing favorable binding strength for key oxygen-containing intermediates involved in the OER process, which is essential for maintaining high catalytic activity. Beyond ~25% Fe content, inactive γ-FeOOH domains begin to form, reducing overall performance. Thus, this work firmly established Fe as the key catalytic center in NiFe oxyhydroxides and shaped future efforts to tailor electronic environments for optimized OER performance.

Ahn and Bard in 2016[82] used surface interrogation scanning electrochemical microscopy (SI-SECM) to directly probe the surface kinetics of Ni, Fe, and Ni-Fe oxyhydroxide catalysts for OER in 2 M KOH. By applying time-resolved redox titration, they quantified how surface-active species evolved and reacted, revealing two distinct types of sites: "fast" and "slow." Importantly, in $Ni_{1-x}Fe_xOOH$ films ($x < 27\%$), the proportion of "fast" sites correlated closely with Fe content, providing the first direct experimental evidence that Fe atoms in a NiOOH matrix are responsible for high OER activity. However, at higher Fe concentrations (>25%), phase segregation was observed, leading to less predictable behavior and reduced activity. While the study confirmed Fe as the likely active site in well-dispersed NiFe systems, limitations included the uncertainty in site assignment and challenges in reproducibly synthesizing films without phase separation persisted, because of poor control over the amount of Fe in the samples. Care has been taken to rectify this for the samples discussed in this work.

Chen et al. in 2015[83] investigated the oxidation states of Fe in NiFe and Fe-only oxyhydroxide electrocatalysts under OER conditions using *operando* Mössbauer spectroscopy. Catalysts were synthesized directly on carbon paper to ensure mechanical stability and eliminate binder effects. Their key finding was the first direct observation of Fe^{4+} in NiFe catalysts during active oxidation of water. Although Fe^{4+} was detected at up to 21% of total Fe, it has been suggested that these sites were not responsible for catalysis, as they could be found even when no external potential was applied. While the study provided strong evidence for flexibility of oxidation state of Fe and its role in enabling high-valent states, it did not definitively identify the active site and was limited by the inability of Mössbauer spectroscopy to detect low-concentration, transient species. Nonetheless, this work highlighted the unique capacity of the NiOOH lattice to stabilize Fe^{4+} and the likely involvement of Fe-centered mechanisms in OER activity.

Görlin et al. In 2016[84] investigated mixed Ni-Fe oxyhydroxide catalysts across a wide range of compositions to resolve the ongoing debate around their OER mechanism and the roles of Ni and Fe during catalysis. Using a combination of *operando* differential electrochemical mass spectrometry (DEMS) and quasi-in situ X-ray absorption spectroscopy (XAS), they tracked how faradaic charge was distributed between oxygen evolution and metal redox changes. The study found that in Ni-rich

systems, Ni was oxidized to +4 during OER, while in Fe-rich or mixed catalysts, Fe remained mostly at +3 and the increase of the oxidation state of Ni was hindered. This suggested that Fe helps stabilize the Ni in lower oxidation states and enhances the OER activity indirectly. While the exact active site was not pinpointed, the data indicated a synergistic interaction where Fe promotes higher OER selectivity and possibly catalytic turnover. A limitation of this study was the inability to detect the short-lived Fe states with higher valency.

Li et al. in 2017[85] examined the effects of Fe incorporation in the electronic structure and OER activity of Ni oxide catalysts, focusing on the changes in Ni valency. Using ultrathin films and a combination of XAS and electron energy loss spectroscopy (EELS), they demonstrated that doping with Fe promotes the formation of Ni^{4+} species up to a plateau at ~10% Fe. This finding correlated with enhanced activity and it was determined that Fe acts as a Lewis acid, stabilizing the Ni species in higher oxidation states. Spectroscopic data supported this by showing greater Ni-O covalency with increased Fe content. It was inferred that Fe enhances OER performance indirectly by promoting Ni-based reactivity, without definitively identifying an active site.

While Chen et al. in 2015[83] observed the formation of Fe^{4+} during OER and suggested high-valent Fe species could be catalytically relevant, Li et al. 2017[85] argued that Fe does not act as the active site but instead promotes the formation of high-valent Ni^{4+}, which drives the reaction. This fundamental disagreement over whether Fe directly participates in the catalytic cycle or merely enhances Ni reactivity reflects the ongoing discourse regarding the NiFe system and reinforces the need for further studies regarding this system of electrocatalysts.

Zhang et al. in 2021[86] addressed the ongoing debate over the active site in NiFe electrocatalysts by combining electrochemical measurements with mechanistic analysis on planar electrodes prepared via pulsed laser ablation (PLA). They argued that Ni is unlikely to serve as the catalytic center, based on its inability to reach high oxidation states in aqueous media and electronic structure considerations. Instead, they proposed high-valent Fe species, including Fe^{4+} and Fe^{6+}, as the most plausible active intermediates for OER. This assertion was supported by earlier *operando* spectroscopic data and further reinforced by studies in non-aqueous media that allowed direct observation of Fe^{6+} reactivity. While the study strongly favored an Fe-centered mechanism, it relied largely on indirect observations and theoretical arguments, and the precise nature and stability of Fe^{6+} under real aqueous operating conditions remain unresolved.

2.3.3 Active site of Fe-Ni oxyhydroxide catalysts and their chemical and electronic structures: explored via electron and x-ray spectroscopic techniques

Despite extensive research on Fe-Ni oxyhydroxides, the identity of the active site and the specific role of Fe remain actively debated. As discussed previously, studies have proposed that Fe either promotes[14,86] or inhibits[87,88] Ni oxidation or alters the catalyst's electronic structure in more complex ways. To resolve these ambiguities, researchers have increasingly turned to advanced electron and

x-ray spectroscopic techniques which offer element-specific insight into oxidation states, coordination environments, and electronic interactions ex-situ as well as under *operando* conditions.

Direct comparison between Ni-Fe based catalysts is complicated by differences in synthesis methods, substrates, and testing conditions. However, many studies report a distinct redox peak corresponding to the Ni^{2+}/Ni^{3+} redox couple, for the solid-state transition between $Ni(OH)_2$ and NiOOH prior to the onset of OER. This peak often shifts anodically in the presence of Fe, whether intentionally added or present as a trace impurity. While this shift is commonly observed in electrochemical analyses, its structural and electronic origin remains unclear. X-ray spectroscopic techniques can help elucidate whether this shift reflects changes in Ni oxidation states, Fe–Ni electronic interactions, or structural rearrangements. This section highlights key spectroscopic investigations that have helped shape current understanding of the chemical and electronic structure of NiFe based catalysts and their relationship to catalytic performance.

Wartner et al. in 2023[89] applied *operando* resonant photoelectron spectroscopy (RPES) to directly probe valence band features at the O 1s absorption edge, revealing the presence of metal-oxygen hybridized states. These features, which align well with the Fermi level under applied potential, were interpreted as possible indicators of active electronic states that facilitate charge transfer during catalysis. Complementary measurements using partial electron yield x-ray absorption spectroscopy (PEY-XAS) at the Ni L_3-edge indicated the oxidation of Ni species, though the resolution was insufficient to distinguish between resultant Ni^{3+} and Ni^{4+}. A significant limitation of RPES, as noted by the authors, is its limited probe depth, which restricts analysis to near-surface regions and requires correlation with bulk-sensitive techniques for a complete understanding. Nonetheless, the study demonstrated how carefully chosen spectroscopic windows can offer valuable insight into the active electronic environment of working Fe-Ni catalysts.

Drevon et al. in 2019[90] investigated the electronic structure of Fe-Ni (oxy)hydroxide catalysts during the oxygen evolution reaction using in situ soft X-ray absorption spectroscopy (sXAS) at both the O K-edge and metal K-edges. The thin film samples were electrodeposited and contained varying amounts of Fe (typically around 25%). sXAS was performed under electrochemical OER conditions, providing real-time insight into changes in bonding and oxidation states of the metal centers. At the O K-edge, a pre-edge feature near 529 eV was observed and attributed to electron-deficient oxygen species, potentially linked to the oxidation of nearby Ni or Fe centers. Notably, the Ni K-edge showed a distinct edge shift from +2 to +3 under applied potential, confirming redox activity of Ni during OER. In contrast, the Fe K-edge exhibited only minor changes, suggesting Fe remains largely in the +3 state, although the authors could not rule out the existence of Fe^{4+} completely. The study emphasized the synergistic role of Ni and Fe, with enhanced catalytic activity attributed to their electronic interaction rather than the formation of higher-valent Fe alone. Active oxygen species were also proposed as probable participants in the redox reaction, though their exact role remains yet to be resolved. Overall, the work highlighted the value of in situ sXAS for analyzing redox contributions and identifying oxidation state dynamics during OER catalysis.

In the study by Friebel et al. in 2015[13], previously discussed in section 2.3.2, bulk-sensitive *operando* x-ray absorption spectroscopy (XAS) and extended x-ray absorption fine structure (EXAFS) analysis

were employed to investigate the Fe-Ni oxyhydroxide system under OER conditions. The spectroscopic data, supported by DFT calculations, indicated that Fe^{3+} ions embedded within the NiOOH lattice are likely the primary active sites for catalysis, while Ni plays a more passive role, as structural support. However, the authors also acknowledged that K-edge XAS provides a bulk-sensitive signal and may not fully reflect changes occurring at catalytically active surface sites. This highlights the need for complementary surface sensitive techniques to fully capture the reaction dynamics driving the OER activity.

Song et al. in 2018[62] performed *operando* hard x-ray absorption spectroscopy at the Fe and Ni K-edges to study oxidation state and structural changes in Fe-Ni oxyhydroxide catalysts during OER. They observed that Fe remained in the +3 state, while Ni was oxidized from +2 to +3, with changes in Fe-Ni distances suggesting reorganization of the structure under applied potential. EXAFS was used to analyze local coordination environments, but its dependence on model-based fitting can introduce challenges in interpreting subtleties in complex systems. The study reinforces the value of combining multiple spectroscopic techniques to gain a more complete picture of redox behavior and structural evolution during catalysis.

Despite extensive investigation, the identity of the active site in Fe-Ni oxyhydroxide catalysts remains unresolved, with studies supporting either Fe or Ni as probable active sites, or even a synergistic interaction between them. This ongoing discourse is further complicated by the limitations of commonly used techniques like hard XAS, EXAFS, and lab-based XPS, which often lack the surface sensitivity or electronic resolution needed to fully capture catalytic behavior, if employed individually. For instance, Fe K-edge spectra are relatively insensitive to oxidation state changes due to core-level screening, while EXAFS relies more on model-dependent fitting that can obscure complex local environments. In contrast, soft XAS and synchrotron-based HAXPES directly probe valence-level 3d states, critical to catalytic activity, offering greater sensitivity to oxidation and bonding changes at the catalyst surface.

The work in this thesis attempts to address these gaps by employing a combination of these advanced techniques, available at the X-SPEC beamline, to gain clearer insight into the local electronic structure and help resolve the question of the active site in Fe-Ni oxyhydroxide electrocatalysts.

3 Experimental setup

3.1 The Materials for Energy Laboratory

The initial XPS measurements were performed at the Materials for Energy (MFE) Laboratory, which is located next to the KIT Light Source at Institute for Photon Science and Synchrotron Radiation (IPS)/Institute for Technical Chemistry and Polymer Chemistry (ITCP). The laboratory also houses the Ar-filled gloveboxes that are used for sample storage and handling, which will be explored in detail in the next section.

Two types of x-ray sources can be used: the DAR-450 twin-anode x-ray tube that provides non-monochromatized Al Ka and Mg Ka radiation with a characteristic energy of 1486.6 eV and 1253.6 eV respectively and the SIGMA Surface Science MECS monochromatized Al Kα source with also a characteristic energy of 1486.6 eV. For the purpose of this thesis, initially, measurements were performed using both the monochromatized Al K_α and non-monochromatized Mg K_α sources. A major difference between the two is the absence of the bremsstrahlung and radiation from secondary transitions of the materials such as K_β transitions in materials as a result of the monochromatized x-ray source. Photoelectrons and Auger electrons are detected by the Scienta Omicron Argus CU analyzer. However, the spectra obtained in both cases revealed that there were significant overlaps of the Auger peaks (Fe LMM and Ni LMM) with the core level peaks (Fe 2p and Ni 2p). Figure 16 shows a picture of the MFE lab with the key components marked.

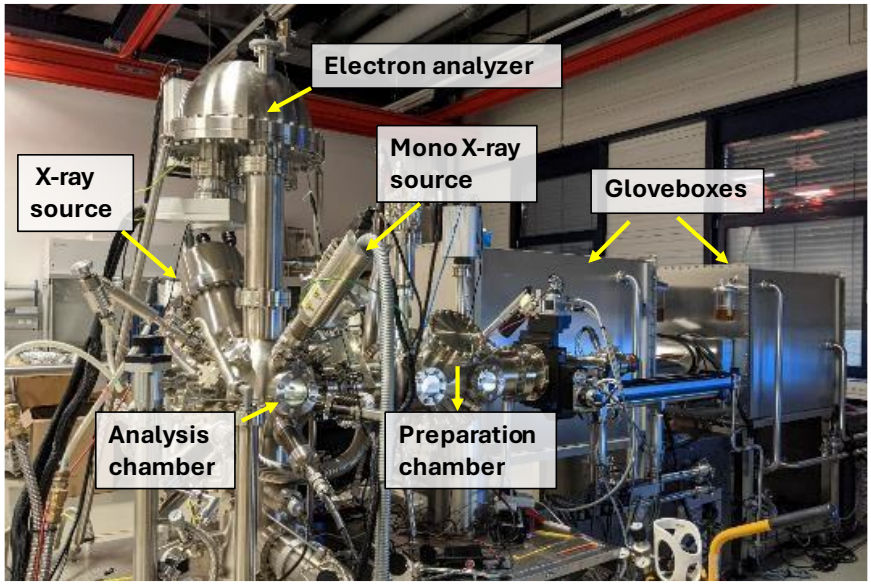

Figure 16: MFE lab, with the key components highlighted.

3.2 Sample handling and storage

The samples, $Fe_xNi_{1-x}(O,OH)_y$ thin films (that will be discussed in Chapter 3), were prepared by and shipped to KIT by the collaboration partners at the Pennsylvania State University[91]. They were stored and handled in the Ar-filled gloveboxes (marked in Figure 16) to limit air exposure, as well as to ensure that surface oxidation is avoided, as the concentrations of O_2 and H_2 are maintained below 1 ppm inside the gloveboxes. They were directly introduced into the ultra-high vacuum (UHV) system through the load lock, transferred to the preparation chamber and finally to the analysis chamber, where XPS measurements are performed. The base pressure of the analysis chamber is lower than 10^{-9} mbar for the measurements. For measurements at the X-SPEC beamline, the samples were transported via customized transport chambers, which can be loaded within the glovebox and unloaded via the load lock directly at the end station where the samples are to be measured. Figure 17 shows the closed (a) and disassembled (b) design of the transport chamber.

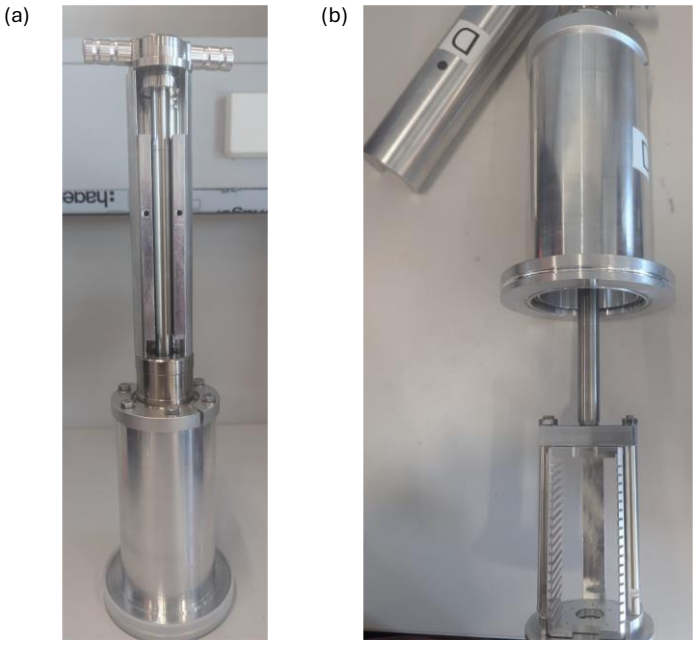

Figure 17: Custom transport chamber used to transfer samples from the glovebox in the MFE lab to the beamline, without exposing them to air.

3.3 X-SPEC beamline at the KIT Light Source

The HAXPES, XAS and XES measurements were performed at the X-SPEC beamline[29] at the KIT Light Source. The X-SPEC beamline facilitates measurements in the photon energy range of 70 eV-15 keV. The most unique and convenient aspect of the X-SPEC beamline is the ability to perform experiments with both soft and hard x-rays at the same sample spot position. This is achieved by the careful placement of the different components of the beamline and switching them from one setup to another as and when required. For photoemission spectroscopy, the photoionization cross section rapidly decreases with increasing photon energy[92], hence when performing HAXPES, ($h\upsilon$ = 2 keV or

higher), a beam source with high photon flux, that is a high intensity of photons delivered per second, is required-a criterion which the X-SPEC beamline fulfils by minimizing the number of optical elements. The beamline layout is shown in Figure 18.

X-rays are generated by the double undulator, as shown on the left of Figure 18. Each undulator consists of a series of alternating magnetic poles that create a periodic magnetic field. The undulators have a periodic length of 28 mm and 50 mm (U28 and U50 as shown in the figure) used respectively for creating hard and soft x-rays. For the utilization of hard x-rays, all the soft x-ray components are moved out of the beam path and vice versa. The undulator's magnetic field can be adjusted by adjusting the undulator gap mechanically to shift the energy of the emitted x-rays, enabling precise tuning for different experiments. A bending magnet or a wiggler also serves similar purposes as an undulator: the former keeps electrons on a closed orbit within the storage ring, and when deflected by the magnetic field, emits radiation tangential to its path; the latter is similar to an undulator in design, but operates with a stronger magnetic field and higher deflection parameter, which causes the electrons to follow broader, fewer oscillations and results in a broader spectrum. However, for the X-SPEC beamline, the undulators' ability to produce sharp, tunable peaks and narrow bandwidth radiation are more well suited.

Hard x-rays are monochromatized by a double-crystal monochromator (DCM) with pairs of Si (111) or Si (311) crystals and the monochromatic beam is then focused by mirrors M1 and M2 onto the samples at the different end-stations, which are the UHV and the in situ end-stations, marked as A and B in Figure 18. Using both these crystals, an energy resolution of better than 0.6 keV can be achieved up to an energy of 8 keV. This is an acceptable value for general HAXPES measurements.

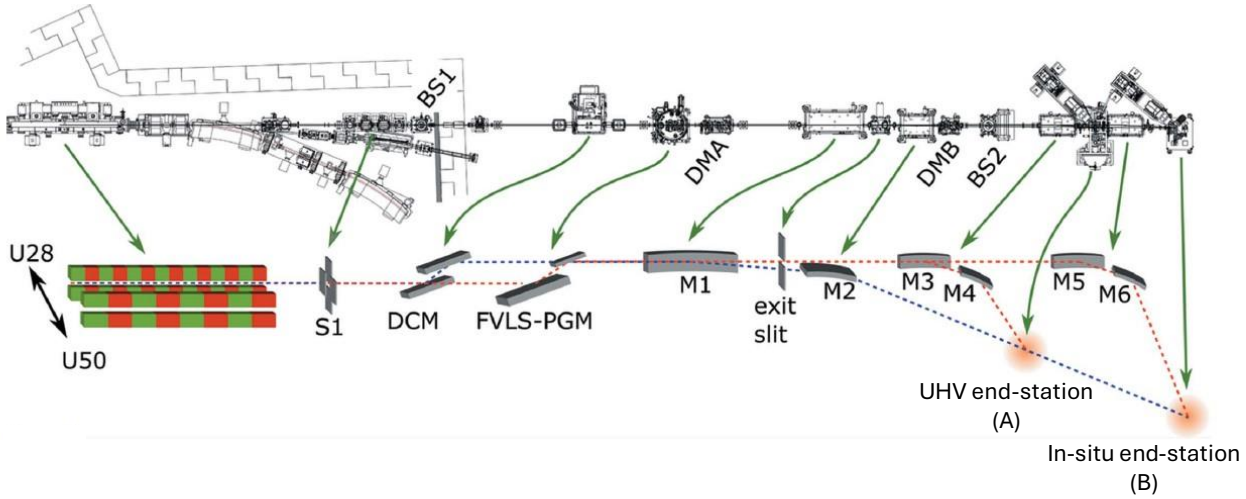

Figure 18: Schematic of the X-SPEC beamline. The top shows a bird's eye view of the design drawing. The bottom highlights the most important components. Some of the key components are, from left to right: The undulator source with the two magnetic structures(U28 and U50), the hard x-ray monochromator (DCM), the soft x-ray monochromator (FVLS-PGM), the two hard x-ray mirrors (M1 and M2), and the two pairs of soft x-ray mirrors, used to focus the beam into A, the UHV end-station (M3 and M4), and B, the in situ end-station (M5 and M6), respectively. The path of hard x-rays is shown in blue, and the path of soft x-rays is shown in red. Figure reproduced from ref[29].

At higher energies, high flux experiments with larger experimental widths are valuable for several applications as well.

Similarly, the soft x-rays are monochromatized by a focusing variable-line-space (FVLS) plane grating monochromator. The PGM allows the choice between three gratings, and one can be chosen to cover the entire soft energy range (below 2 keV). The three gratings possible to choose from are 400, 800 and 1200 lines mm^{-1}. The different gratings offer a trade-off between energy resolution and photon flux. The XES measurements discussed in this work were performed with the 400 lines mm^{-1}. Based on the energy range and the requirements of the particular experiment, the 800 and 1200 lines mm^{-1} gratings are a likely choice for XAS and PES experiments. The resolutions that can be achieved with these gratings stay well below 0.1 eV, up to a photon energy of 1 keV and are only slightly above 0.2 eV at 2 keV. The XAS measurements reported in this thesis were performed using either the 800 lines mm^{-1} or the 400 lines mm^{-1}. For HAXPES measurements, the energy resolution was determined from gold Fermi edge and 4f measurements, taking the experimental broadening of the electron analyzer, which comes out to be 15 eV.

Two pairs of mirrors focus the soft x-ray beam onto the end-stations: M3 and M4 for the UHV and M5 and M6 for the in situ end-station. The resultant spot size for soft x-rays is <5 µm (vertical) × 90 µm (horizontal). For hard x-ray operation, the beam goes directly to the DCM, and the monochromatic beam is then focused onto either of the end-stations with the help of mirrors M1 and M2. For HAXPES as well, a small spot size is desirable, to enable the operation of the electron spectrometer with high transmission lens modes. It also allows measurements in the grazing incidence mode to maximize the photon absorption in the probing volume. The hard x-ray beam spot size is <50 µm (vertical) × 700 µm (horizontal) for the first end-station, while the values are approximately 30% larger for the second end-station.

The two end-stations of the X-SPEC beamline are the UHV and the in situ end-stations, marked as A and B respectively in Figure 18. The former is tailored for ultra-high vacuum conditions, with a base pressure in the order of 10^{-9} – 10^{-11} mbar. It is equipped for sample preparation techniques such as sputtering, annealing and cleaving, and is kept contamination free. It is ideally suited for studying surfaces and interfaces of samples. The latter, the in situ end-station is optimized for studying materials under *operando* or near realistic conditions. The sample and the beamline environment can be separated at this end-station and that enables the real-time monitoring of processes such as catalysis and corrosion. In Figure 18, the path of the hard x-rays is shown in blue and the path of the soft x-rays is shown in red. For HAXPES measurements, a Phoibos 225 electron analyzer (SPECS) is used for detection of photoelectrons. It allows measurements of electrons up to a kinetic energy of 15 keV. The photoelectrons are collected at 90^0 with respect to the incoming x-ray beam. For XES experiments, each of the end-stations is equipped with a high transmission soft x-ray spectrometer with a resolving power of 2000 to 4000 and an energy range from 50 to 2000 eV is used which was developed in-house[93]. For XAS measurements, different measurement detection schemes are possible (discussed at length in Chapter 2), including TEY via sample current measurement, PFY detection using different detectors at the two different end-stations. Both detectors have windows, the one at the UHV end-station has a Kapton window and the in situ end-station has an aluminum window.

3.4 Sample Preparation and Synthesis

3.4.1 Sample Overview

The samples studied in this dissertation are $Fe_xNi_{1-x}(O,OH)_y$ electrocatalyst thin films, prepared and shipped to KIT by the collaboration partners at the Pennsylvania State University[91].

The films are metallic FeNi alloys with compositions controlled by the electrodeposition conditions. For preparation of these catalysts, several research groups have explored various techniques such as spray coating[94], chemical co-precipitation[95] and electrodeposition[13,14,96]. Extensive studies have shown that electrodeposition is the most efficient way of obtaining these thin films, as the electrolyte composition can be engineered to provide the desired composition and nature of the electrocatalysts. It is a low-cost, scalable technique and does not require very extreme reaction conditions. In comparison, chemical co-precipitation may lead to poor uniformity and require additional steps to transfer the material onto the substrates while spray coating limits the control over catalyst morphology, making them less favorable techniques.

By varying the amount of Fe and Ni ions in the solvent used as electrolyte for electrodeposition, the nominal Fe and Ni content in the sample can be varied, to fit the needs of the experiment. The catalytic efficiency or the OER activity of the FeNi alloys is seen to increase for compositions with up to 20 atomic % Fe[14,97, ,98,99] and studies for this dissertation have been concentrated for up to 50 atomic % Fe. A compact morphology with uniform coverage over the substrate is expected. The electrodeposition is performed on a gold coated silicon wafer, with a titanium adhesion layer in between. The gold coating serves as a conductive base, ensuring efficient charge transfer during electrochemical studies and spectroscopic measurements such as photoemission and surface sensitive x-ray absorption. FeNi alloys are poorly conductive, especially in their oxidized or hydroxide forms, limiting their activity without the presence of a conductive band, which is compensated for by the Au coating.

Figure 19(a) shows a schematic representation of the different layers forming the sample. The catalyst layer is representative of the FeNi alloy electrodeposited on the film. Figure 19(b) shows the sample after electrodeposition, marked in the red circle.

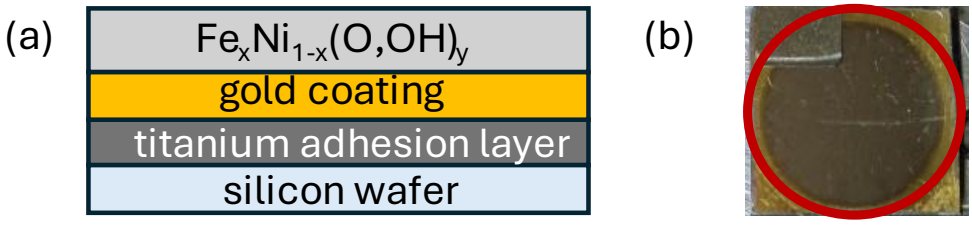

Figure 19: (a) Schematic representation of the different layers comprising the sample. (b) Sample after electrodeposition, marked by the red circle.

To confirm the composition of the resulting films, two elemental analysis techniques were used, namely inductively coupled plasma mass spectrometry (ICP-MS)[91,100] using an Agilent 7850 and energy dispersive spectroscopy (EDS)[91,101] using a Thermo Scientific Apero instrument. ICP-MS allows for quantitative determination of the elements present in the film and EDS helps to obtain qualitative information about the elements by detecting characteristic x-rays emitted from the sample when bombarded with electrons. The Fe and Ni quantities were determined based on the examination of their K-lines.

The physical characterization of the films was performed by measuring film thickness and surface structure. The thickness of the films is calculated by measuring the charge passed through the working electrode, in this case the substrate used for electrodeposition of sample, during the electrodeposition process[102]. The deposition time is varied from 30 seconds to 3 minutes, producing catalysts with thicknesses ranging from 20 to 200 nm. However, it was discovered through several electrochemical experiments that changes in thickness did not affect the OER activity of the samples which show similar performance characteristics. The thickness of the samples studied in this dissertation vary from 50-200 nm.

Cross-sectional SEM imaging (Figure 20 (a)) measured the underlying layers of the sample for precise identification and measurement of film thickness. Surface SEM imaging (Figure 20 (b)) provided an idea of the surface morphology of the films: the surface looked relatively homogeneous and free from severe visible defects.

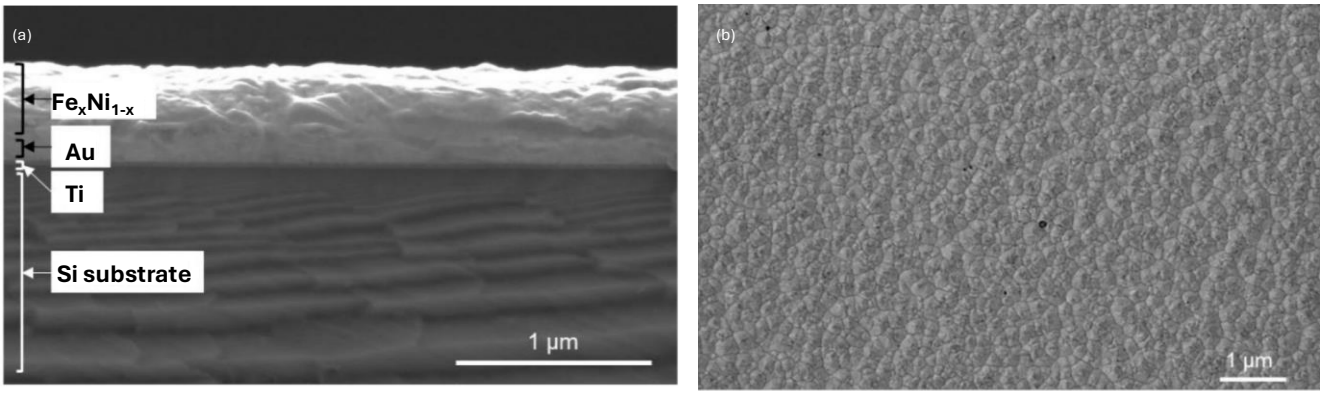

Figure 20: (a) Cross-sectional SEM image of the film (b) SEM image showing the film morphology. Images from ref[90].

The chemical and electronic properties of the catalyst (top-most layer in Figure 20(a) and the region marked by the red circle in Figure 20(b)) are studied via several electron and x-ray spectroscopic techniques.

For simplicity, in certain sections of the text, the $Fe_xNi_{1-x}(O,OH)_y$ thin films will also be referred to as FeNiOOH thin films.

3.4.2 Synthesis protocol of samples

Gold-coated aluminosilicate glass slides (Platypus Technologies) were used as substrates for the electrodeposition experiments. They were cleaned with UV-generated ozone for 15 minutes (SC-UV-I, Setcas LLC) to remove organic contaminants. Containers made of PEEK, Teflon, or polypropylene were used exclusively to prevent contamination from Fe leaching, which can occur when glass is etched by alkaline solutions. All containers were cleaned with 10% nitric acid to remove residual Fe and Ni traces, and ultrapure water (18.2 MΩ-cm, EMD Millipore) was used for rinsing.

The electroplating solution contained 10 mM of metal salts. Fe and Ni stock solutions were prepared using iron (II) sulfate heptahydrate (Sigma Aldrich, 215422, >99% pure), and nickel (II) sulfate heptahydrate (99.999% trace metals basis, Sigma Aldrich, 203890) dissolved in 0.1 mM sulfuric acid (99.999%, Sigma Aldrich, 339741). The solution also included 0.1 mM sulfuric acid, 0.1 mM acetic acid (99.99% purity, Sigma Aldrich, 64-19-7), and 0.1 M sodium sulfate (99%, Sigma Aldrich, 7757-82-6). The sulfuric acid acts as the primary electrolyte, sodium sulfate as the supporting electrolyte and acetic acid as the buffer, which is responsible for maintaining the optimum pH of the solution

Electrochemical experiments were conducted in a custom PEEK reactor based on a modified 2-compartment cell with a 50 ml electrolyte volume (Redox.me, see chapter 2). A mini-Hg/HgO electrode with 1 M KOH (85% ACS reagent, Sigma Aldrich, 131-58-3) served as the reference electrode, while a coiled Pt wire was used as the counter electrode. FeNi films were electrodeposited as metallic layers at a constant cathodic potential of -0.176 V vs RHE (-1.1 V vs MMO in 1 M KOH). Deposition durations ranged from 30 to 180 seconds to achieve the desired thickness.

All electrochemical measurements were performed using purified KOH electrolyte, 1 M in concentration. Before it can be used as electrolyte, the KOH undergoes a rigorous purification process to remove trace Fe contaminants. This is done to improve control over the exact concentration of Fe in the electrolyte, so the intended concentration of Fe in the electrocatalyst is not compromised with. The purification process involves the precipitation of Fe impurities via $Ni(OH)_2$ formation by the addition of nickel nitrate hexahydrate (99.999% trace metal basis, Sigma Aldrich, 203874), which has been thoroughly discussed in the literature elsewhere[15]. ICP-MS and the absence of a Ni redox peak shift ensures that the electrolyte is free of Fe contamination. This ensures the prevention of unwanted incorporation of Fe into the electrolyte and/or the surface of the electrodes and electrocatalyst. Before conducting OER measurements, the purified KOH was saturated with oxygen for a minimum of 30 minutes. All electrochemical OER measurements were carried out in the same reactor used for electrodeposition, with 20 ml of purified KOH. The scan rates used for cycling were either 10 mV/s or 100 mV/s, until a steady state was reached. The voltage window for conducting the cyclic voltammetry experiments was determined based on the Fe content, ranging from 0.98 V vs SHE to between 1.6 and 1.9 V vs SHE, with the potential decreasing with increasing Fe content.

Before experiments, the electrolyte was deoxygenated by purging with argon for at least 30 minutes. Sulfuric acid for stock solution preparation was also degassed to eliminate dissolved oxygen before adding metal salts.

3.4.3 Modification to electrolyte recipe for sample optimization

In the electrochemical synthesis protocol developed by the Penn State University, changes were introduced to improve the control over catalyst composition and tackle the challenges faced due to pH instability. These optimizations include the replacement of boric acid with sodium sulfate-supported acetic acid as buffer and the implementation of a purification process for the commercially available KOH.

Buffering is an essential step during the electrodeposition of transition metal oxides and hydroxides to maintain a stable local pH at the electrode surface[103,104,105]. In the absence of an appropriate buffer, the pH of the solution can increase due to hydrogen evolution and local hydroxide generation. Deposits formed under alkaline conditions lacking a buffer, exhibited inconsistent Fe content and poor film morphology. These limitations were found to be related to local pH fluctuations at the electrode surface, due to hydroxide generation during hydrogen evolution[103]. To investigate the pH dependence of the Fe and Ni metal species in solution, Pourbaix diagrams[106] for Fe and Ni were examined, along with the relevant solubility products[107] for their hydroxides. It was found that Fe ions are prone to precipitate at significantly lower pH than Ni[108], resulting in the need to develop an electrolyte recipe with a buffer capable of maintaining the local pH within a controlled window, to ensure the deposition of Fe and Ni deposition is as intended.

Boric acid is commonly used in alkaline deposition media for electrodeposition of Fe and Ni oxides and hydroxides[109,110]. However, it was found unsuitable here due to its limiting buffering capacity. Instead, acetic acid was selected, offering stronger buffering in the desired pH range of 4.5-6. To support the low conductivity of acetic acid, sodium sulfate was added as a chemically inert supporting electrolyte. Additionally, the initial samples were prepared in an open electrolyte bath, which did not consider the possibility of contamination from the ambient air. The reaction vessel thus was also updated with the electrolyte components, as a chamber made of PEEK that allows for it to be sealed while the reaction takes place was used. The design and further utility of this chamber has been explained at length in Chapter 2.

Parallelly, the possibility of Fe incorporation from trace Fe contamination from the KOH used to conduct electrochemical experiment was addressed. This can affect the Fe to Ni ratio in the sample and obscure the impact of intentional doping. This becomes a significant concern when working with samples in the low Fe regime.

3.4.4 Overview of sample sets and treatment history

Table 1 shows the tabulated sample matrix explaining the chemical history, buffer system used in the electrolyte system and the reaction vessel used for preparation of each sample.

Series 1 samples (S1) were prepared using boric acid buffer in an open electrolyte bath and Series 2 samples (S2) were prepared using acetic acid and sodium sulfate as a buffer system in a sealed PEEK cell. x denotes the atomic percentage of Fe content in the samples.

Sample description (x, as prep/wt/wo OER)	Buffer system	Reaction vessel
x=1 as prep, S1	Boric acid	Open electrolyte bath
x=15 as prep, S1	Boric acid	Open electrolyte bath
x=30 as prep, S1	Boric acid	Open electrolyte bath
x=50 as prep, S1	Boric acid	Open electrolyte bath
x=1 as prep, S2	sodium sulphate + acetic acid	Sealed PEEK Electrochemical cell
x=3 as prep, S2	sodium sulphate + acetic acid	Sealed PEEK Electrochemical cell
x=10 as prep, S2	sodium sulphate + acetic acid	Sealed PEEK Electrochemical cell
x=13 as prep, S2	sodium sulphate + acetic acid	Sealed PEEK Electrochemical cell
x=16 as prep, S2	sodium sulphate + acetic acid	Sealed PEEK Electrochemical cell
x=20 as prep, S2	sodium sulphate + acetic acid	Sealed PEEK Electrochemical cell
x=40 as prep, S2	sodium sulphate + acetic acid	Sealed PEEK Electrochemical cell
x=50 as prep, S2	sodium sulphate + acetic acid	Sealed PEEK Electrochemical cell
x=1 wt/wo OER, S2	sodium sulphate + acetic acid	Sealed PEEK Electrochemical cell
x=5 wt/wo OER, S2	sodium sulphate + acetic acid	Sealed PEEK Electrochemical cell
x=20 wt/wo OER, S2	sodium sulphate + acetic acid	Sealed PEEK Electrochemical cell
x=50 wt/wo OER, S2	sodium sulphate + acetic acid	Sealed PEEK Electrochemical cell

Table 1: Overview of the sample sets and treatment history. x represents the Fe content in the sample and S1 and S2 determine which synthesis method was followed for each sample.

3.4 Data analysis

The Tougaard background analysis for the Fe and Ni 2p spectra was performed using the Quantitative Analysis of Surfaces by Electron Spectroscopy or the QUASES Tougaard software developed by Sven Tougaard[111] for accurate removal of inelastic background which is characteristic of transition metals. The software uses theoretical cross-sections and energy loss functions tailored to specific material systems.

For certain spectra such as the O1s HAXPES spectra, along with an appropriate background subtraction, fitting the spectra with a Voigt profile also becomes essential for spectral deconvolution. The Voigt profiles are a combination of Gaussian and Lorentzian profiles, enabling adjustments in instrumental and lifetime broadening. The fits were performed in the Fityk[112] software, where the ratio between the Gaussian and Lorentzian functions can be varied to obtain an optimal fit.

3.5 Constraints of conventional laboratory-based x-ray sources and the need for HAXPES measurements

To establish a preliminary understanding of the surface composition, XPS was measured using conventional laboratory-based x-ray sources at the MFE laboratory.

The samples studied here are $Fe_xNi_{1-x}(O,OH)_y$ thin film electrocatalysts, with the following nominal x values: x = 1, 15, 30, and 50. This composition range was selected based on earlier studies indicating that significant improvements in OER activity occur at relatively low Fe doping levels, often peaking below or around 20 at.% Fe, with limited further enhancement beyond 50 at.% Fe[97,98,99,113,]. The compositions are referred to as nominal, reflecting the precursor solution compositions used during synthesis rather than the exact stoichiometry in the films deposited. This convention accounts for factors such as preferential incorporation, local pH fluctuations, and differential solubility, which may cause deviations between the input and final film compositions[114]. Although the improved synthesis protocol allows better control over Fe incorporation, these uncontrollable factors can still influence the distribution of Fe and Ni in the final product.

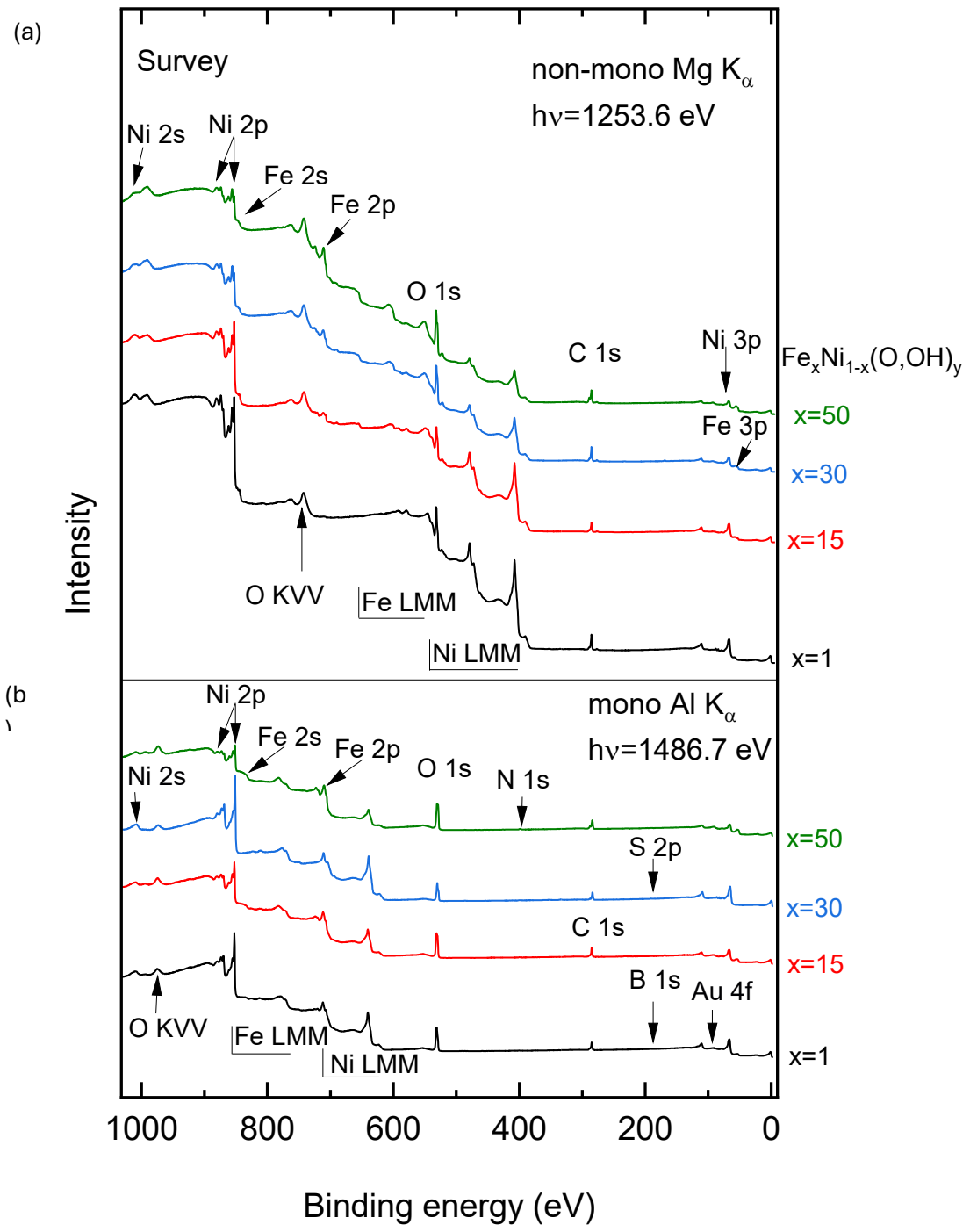

Figure 21: XPS survey spectra of $Fe_xNi_{1-x}(O,OH)_y$ thin films (a) measured with non-monochromatic Mg K_α x-ray source and (b) measured with monochromatic Al K_α x-ray source in the MFE laboratory.

Figure 21 shows the XPS survey spectra of the samples. Figure 21(a) shows the survey spectra measured with a non-monochromatic Mg K_α x-ray source, with an excitation energy of 1253.6 eV, and Figure 21(b) shows the survey spectra obtained with a monochromatic Al K_α x-ray source, with an excitation energy of 1489.7 eV. Energy calibration was performed using sputter-cleaned Cu, Ag, and

Au foils. All survey spectra reveal the presence of Ni and O in all samples. Fe is present in most samples, although the signal is weak in the x=1 sample. The Ni 2p and Fe 2p peaks appear at ~852 eV and ~710 eV, respectively. The O 1s peak is observed at ~532 eV. A prominent C 1s peak is observed at ~284 eV. This feature is generally attributed to adventitious carbon; a thin layer of hydrocarbons that accumulate on most surfaces exposed to the ambient atmosphere. The binding energy matches the position for C–C and C–H bonds, and the absence of any intentional C source in the synthesis supports this assignment and the reasoning behind C's presence. Similar peaks are reported across a wide range of materials, including oxides and metals, due to surface adsorption of airborne organic molecules or residual contamination from handling samples. Furthermore, the absence of higher energy components of the peak which would signify the presence of other C-containing compounds such as C–O or O–C=O, supports this inference[19,115,116]. The C 1s peak is a feature in most XPS analyses and is commonly reported in transition metal electrocatalysts exposed to air during transfer or storage.

The presence of several other elements can be noted that are not intentional additions to the sample, such as N 1s at ~398 eV, S 2p at ~168 eV, B 1s at ~190 eV, and Au 4f at ~84 eV. Assumptions can be made regarding their source, some with greater certainty than others. The likely source of the Au 4f signal is the gold coating over the aluminosilicate glass substrate, implying that the sample might not have been homogeneously distributed across the sample, or a scratch might have been present at the measurement spot. B could have been introduced onto the surface of the sample from the boric acid used as buffer in the first synthesis protocol. Additionally, trace amounts of S can be present as impurities or introduced during manufacturing of the aluminosilicate glass, especially if sulfate-based raw materials are used[117]. The N 1s signal is not expected based on the sample composition and may result from trace environmental contamination introduced during handling or exposure to laboratory conditions, such as adsorption of organic nitrogen compounds from the atmosphere, contact with gloves or tools, or residue from earlier sample analysis within the analysis chamber.

Figure 22 shows the HAXPES survey spectra of the same samples, measured with 2.1 keV excitation energy, at the X-SPEC beamline. To improve the visibility of lower-intensity features, the intensity of the Ni 2p region (845-900 eV) was attenuated by multiplying it by a factor of 0.7. The Auger region (1229-1619 eV), which includes transitions such as Fe LMM, Ni LMM and O KVV were magnified by a factor of 5 and overlaid above the full spectra for better visualization. Different from the laboratory data presented above, the Auger peaks do not overlap with the Ni and Fe 2p peaks. This makes HAXPES an essential technique to study the FeNiOOH thin films. Similar to XPS, Au 4f peak is visible in the HAXPES spectra as well. The Si 1s peak likely originates from the aluminosilicate glass substrate itself. The Si 1s electrons have a kinetic energy of approximately 260 eV, they can only escape from the top 1-2 nm (IMFP of Si) of the material without losing energy. As a result, the measurement remains highly surface-sensitive, and signals from deeper layers, such as the substrate, would normally not be detected unless the overlayer is very thin, uneven, or has local discontinuities. Therefore, in samples with local discontinuities or scratches or thin coverage, substrate signals may become visible in the spectra, as it happens in the case of these samples studied.

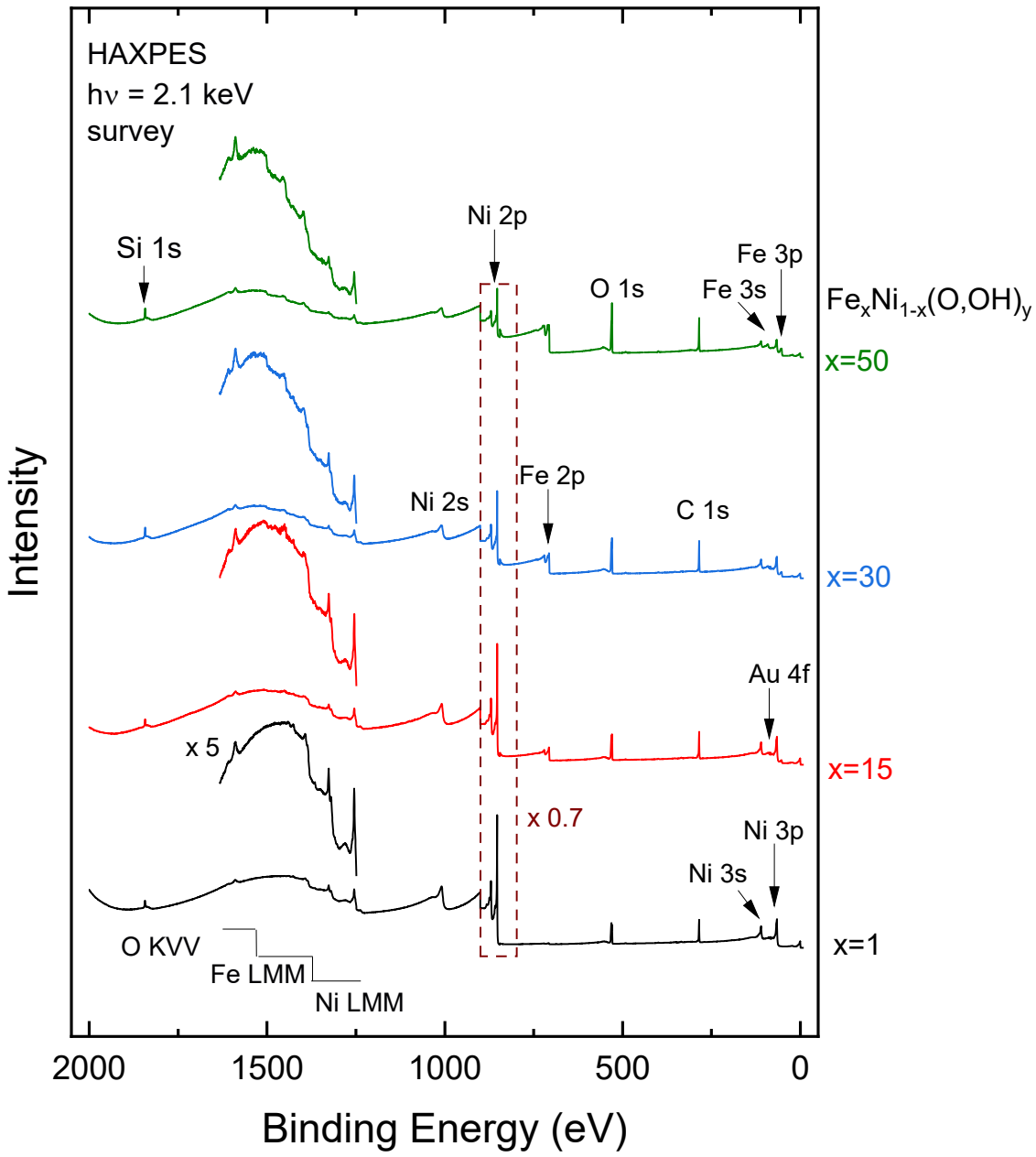

Figure 22: HAXPES survey spectra of the FeNi thin film electrocatalysts, obtained at the synchrotron with an excitation energy of 2.1 keV. To improve visibility of lower-intensity spectral features, the Ni 2p region (845-900 eV) has been multiplied by a factor of 0.7. The Auger region (1229-1619 eV) is magnified by a factor of 5 and overlaid above the full spectra. All other portions of the spectra were left as they were.

3.6 Compositional complexity indicated by trends in Fe 2p spectra of initial series

The following section examines the initial sample set used in this study, focusing on highlighting the limitations that motivated the modifications of the synthesis approach, from both a chemical and spectroscopic point of view.

Preliminary attempts to analyze the Fe 2p HAXPES spectra using a two-component fitting model revealed limitations in how well the initial sample set could be interpreted. The approach was based on the assumption that the compositions at x=1 and x=50 represented distinct and relatively well-defined chemical states of Fe, and that spectra from intermediate compositions could be described as linear combinations of these two extremes. While this strategy provided a simple framework, the resulting fits showed significant deviations from the measured spectra for several compositions. This indicated that the electronic environment of Fe does not evolve in a linear or spectroscopically additive manner across the composition range, and that the assumptions underlying the model were too simplistic for the system under investigation. These limitations made it difficult to draw reliable conclusions about the chemical trends in the series and pointed to the need for a more systematic sample set to investigate the evolution of Fe states more effectively.

Figure 23(a) shows the Fe 2p spectra of all the samples and Figure 23(b) and Figure 23(c) show the fit sum plots for samples x=5 and x=30. The former shows clear deviation from the experimentally obtained spectrum.

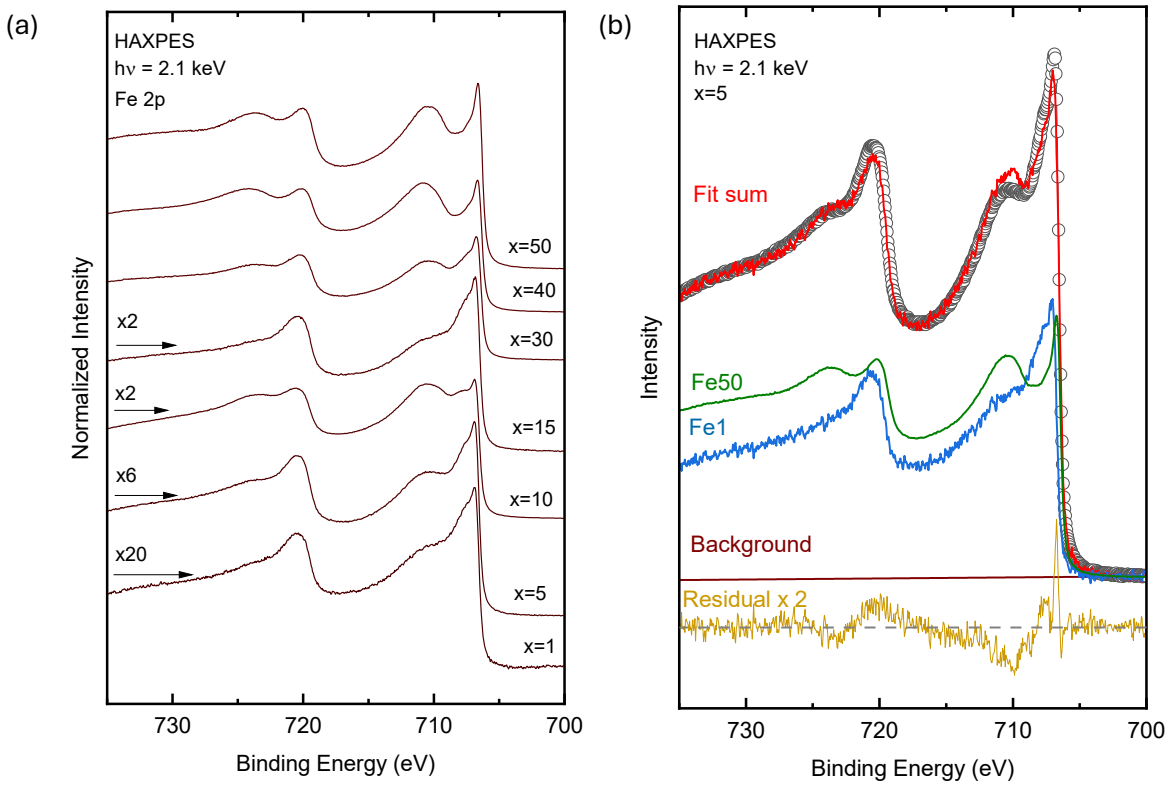

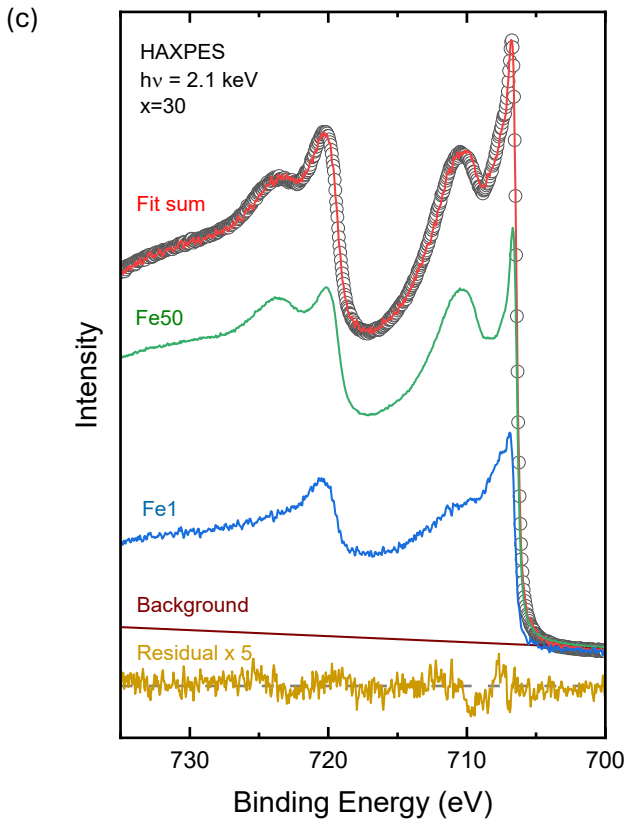

Figure 23: (a) HAXPES spectra of Fe 2p core level. Gradual changes can be observed in the Fe 2p spectra of the different samples, as the composition changes. Attempted 2 component fitting of (b) x=5 and (c) x=30. The fit for x=5 is poor, as is evident from the residual and the fit sum deviating from the spectra of the sample. The spectrum for x=30 is reasonably well described by a linear composition of the two references, implying that it is a coherent intermediate state.

3.7 Transition to modified sample preparation: methodology and justification

Limitations observed in electrochemical studies by the collaborators motivated a transition to a modified electrodeposition protocol[91]. Essentially, uncontrolled and unpredictable Fe enrichment, particularly in the low Fe regime hindered efforts to systematically corelate composition with the observed catalytic activity. Even small deviations in Fe content caused significant changes in oxygen evolution reaction (OER) performance, making it difficult to resolve the sharp enhancement in activity.

To overcome this, a modified synthesis approach was employed, incorporating buffering agents such as sodium sulphate and acetic acid, as a replacement to boric acid, to maintain a local pH of 4.5-6, which stabilized the Ni and Fe ions in solution, minimizing unwanted precipitation.

This refinement enabled a near-linear correspondence between Fe concentration in the precursor solution and in the final films, especially in the low Fe regime, where compositional precision is critical as literature reports show them to be the most efficient in promoting OER. This is depicted in Figure 24 as can be seen[91].

The film composition was determined using a combination of inductively coupled plasma mass spectrometry (ICP-MS) and energy-dispersive X-ray spectroscopy (EDS), as reported in a related study by the collaborating group[91]. This correlation held across the entire compositional range, including both low and high Fe content samples, and provided a more reliable foundation for subsequent spectroscopic analysis.

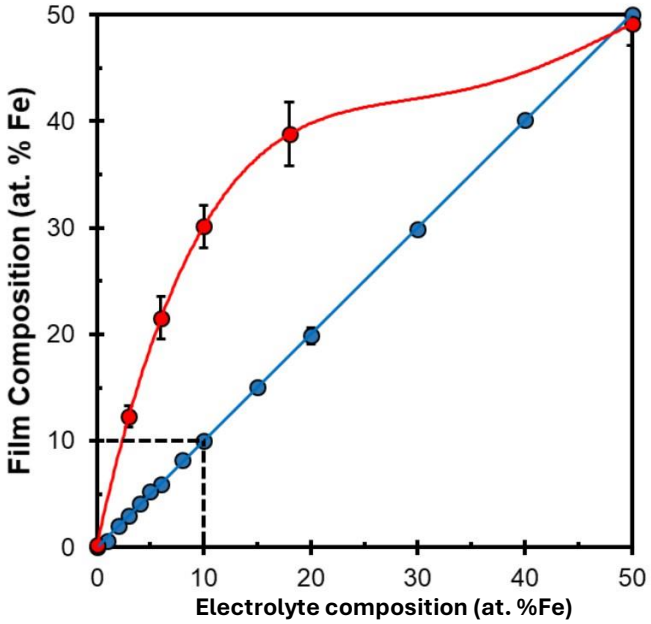

Figure 24: Film composition vs precursor solution composition for FeNi films deposited using the improved protocol (blue). The red line corresponds to data from the literature. The improvement brought on can be clearly seen. Adapted from ref[113] and ref[91].

Although spectroscopic complexity in the initial series did not directly drive the protocol change, they later underscored the importance of having a better-defined and reproducible sample set. The improved synthesis laid a stronger foundation for subsequent spectroscopic interpretation and correlation between structure and activity, reinforcing the value of the refined electrochemical control.

4. Chemical and Electronic Structure of the As-Prepared $Fe_xNi_{1-x}(O,OH)_y$ Electrocatalysts

This chapter presents the results of spectroscopic investigations of the $Fe_xNi_{1-x}(O,OH)_y$ thin film electrocatalysts, investigating how the incorporation of iron affects the local chemical and electronic stricture of the material. A combination of XPS, XAS and XES is used to probe changes in surface composition, oxidation states, coordination environment and electronic states of Ni, Fe and O across different sample compositions and treatments.

The work in this dissertation aims to address the open questions regarding the role of Fe in enhancing catalytic activity, the condition of the active sites after OER, and the respective contributions of Fe and Ni to the overall catalytic function. The spectroscopic results are corelated when possible, with trends reported in the literature, in order to establish a relationship between observed structural and electronic changes and catalytic behavior of the electrocatalysts.

4.1 Establishing the chemical and electronic state of the as-prepared samples

To determine the active chemical states of Fe and Ni during the oxygen evolution reaction (OER), it is important to first characterize and analyze the nature of the as-prepared FeNi thin film catalysts. The initial findings provide a basis to which electrochemical changes can later be compared to. The analysis in this section focusses on the samples prepared by the modified synthesis protocol, which has proven to have better control over the intended Fe to Ni ratio.

The subsequent spectroscopic analysis will focus on the Fe 2p, Ni 2p and O 1s core levels. To aid the interpretation of the different spectral features, they will be studied in relation to spectra of reference materials, representative of relevant chemical environments. The reference materials provide a structural framework for studying the samples against, to distinguish between different chemical states of both transition metals. Analysis of the O 1s spectra allows to determine the relative contribution of oxide and hydroxide chemical states in the samples. FeNi thin film samples with x=1, 3, 10, 13, 16, 20, 40 and 50 are studied.

HAXPES measurements were conducted for the samples at the X-SPEC beamline, with an excitation energy of 2.1 keV, to obtain information about the film composition and to verify their nominal chemical composition. Figure 25 shows the survey spectra of all samples.

The presence of Fe 2p, Ni 2p and O 1s peaks is consistent with the targeted composition of the electrocatalysts. A clear trend is visible in the survey spectra: the intensity of the Fe 2p peak increases with increasing x, while the corresponding Ni 2p peak decreases, consistent with the nominal Fe-Ni distribution across the samples. The O 1s peak shows only minimal changes across the different samples in the survey spectra, indicating that a closer look is necessary to be able to identify the changes in the features of the spectra. The Auger peaks are shifted with respect to the core level peaks, allowing for a clear view of the latter. To aid visibility, two changes have been made

to the plotted data: the Ni 2p region has been scaled down by a factor of 0.7 to prevent it from dominating the spectral features of other elements and the Auger peaks have been amplified by a factor of 5 and overlaid on top of each spectra to highlight them.

As detailed in Section 3.5, a C 1s signal is detected across all samples at ~285 eV, attributed to surface adventitious carbon. Si 1s and Au 4f signals are also consistently present across all samples. The presence of these substrate-related peaks may be attributed to local inhomogeneities in the film, such as thin regions or scratches on the surface.

A significant difference compared to previous films is the presence of the Na 1s signal, whose source is likely the sodium sulfate used as buffer in the improved synthesis protocol. Additionally, traces of Cu 2p is visible in several spectra. This could be an artefact arising from the Cu-contact used to establish electrical conductivity between the sample substrate and the source of electric potential in the new reaction chamber, the design of which has been discussed at length in Chapter 2.

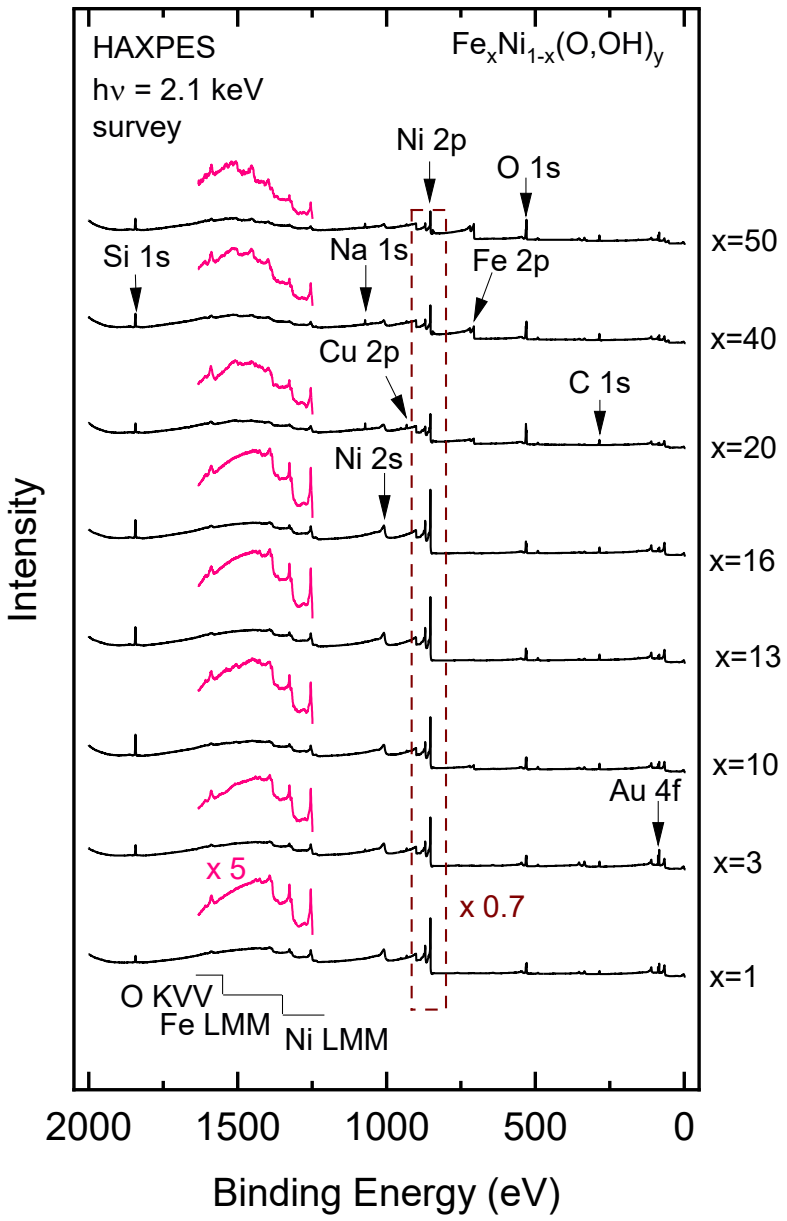

Figure 25: survey of as-prepared $Fe_xNi_{1-x}(O,OH)_y$ thin films measured at 2.1 keV excitation energy. The Fe 2p, Ni 2p, O 1s core levels are clearly observed, alongside signals from C1s, Na 1s, Si 1s and Cu 2p. The Ni 2p region is scaled down (x0.7) and the Auger region is magnified (x5) and overlaid above the spectra to improve visibility.

4.1.1 Probing iron's electronic environment: insights from Fe 2p HAXPES

The Fe 2p HAXPES spectra of the FeNiOOH thin film samples are shown in black and the spectra of reference materials such as Fe metal, FeOOH, Fe_2O_3 and Fe_3O_4 are shown in blue in Figure 26(a). Figure 26(b) shows the spectra overlaid on top of each other, which helps with identifying the changes across the composition and the steady development of oxide nature. Across all compositions, a clear spin-orbit splitting can be seen that results from the coupling between the spin and angular momentum of the 2p electron, as explained in Chapter 2. This gives rise to the two principal

components of the spectra: the Fe $2p_{3/2}$ at ~706.6 eV and the Fe $2p_{1/2}$ peak at ~719.9 eV, with a spin-orbit splitting value of approximately 13eV[22].

Additionally, the spectra also show multiplet splitting, evident as broader features and shoulders to the main $2p_{3/2}$ and $2p_{1/2}$ regions[118]. The multiplet splitting occurs due to electron-electron interactions in the final state after photoemission, as explained in Chapter 2. The unpaired 2p core-hole couples with the valence electrons, resulting in a complex spectral structure. The magnitude and complexity of the multiplet structure depends strongly on the oxidation state of Fe and its interaction with the surrounding Ni and O atoms. For instance, high-spin Fe^{3+} ions typically exhibit more pronounced multiplet splitting compared to Fe^{2+} due to the larger number of unpaired electrons interacting with the core-hole.

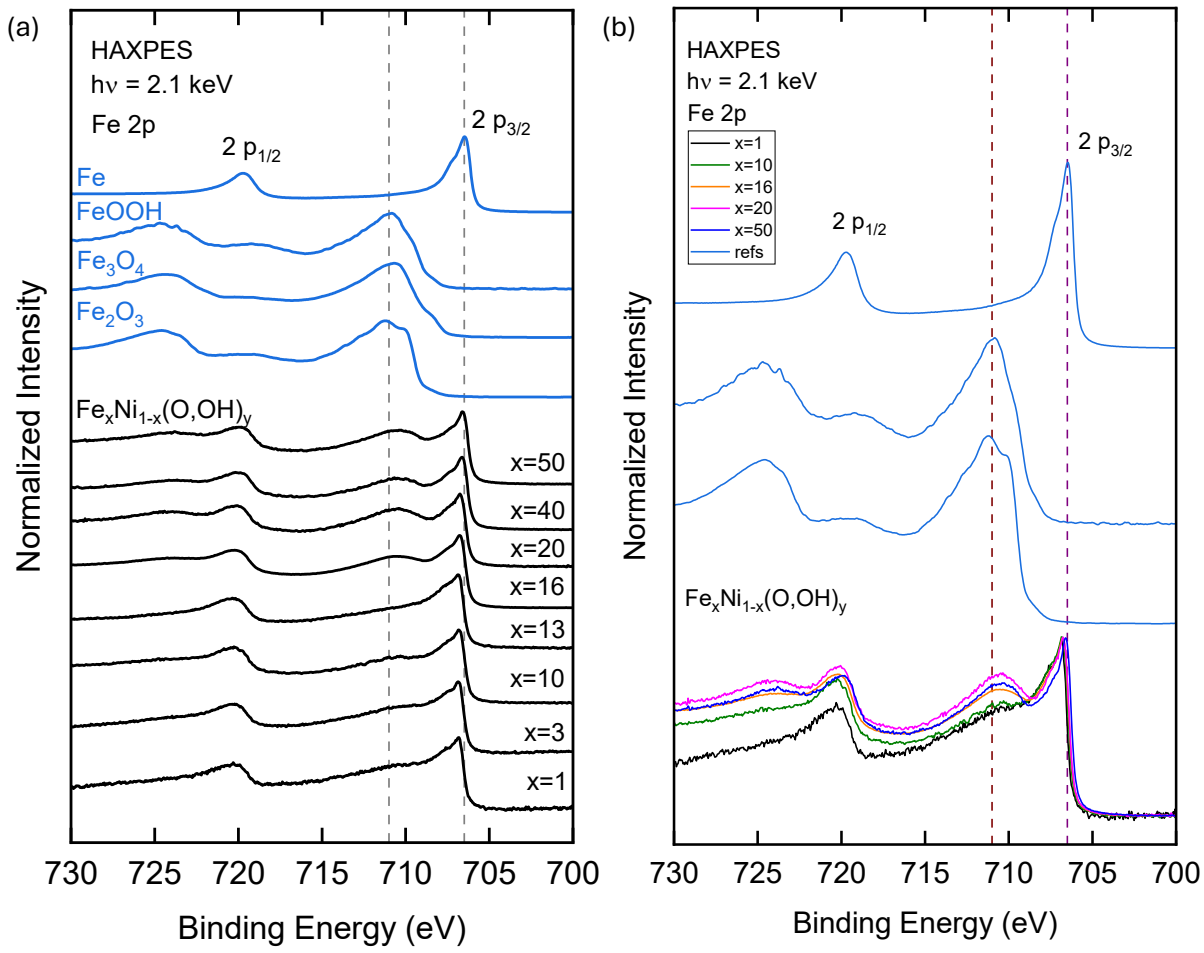

Figure 26: (a) Fe 2p HAXPES spectra of as-prepared $Fe_xNi_{1-x}(O,OH)_y$ thin films obtained at an excitation energy of 2.1 keV, shown in black. Spectra of Fe metal, FeOOH , Fe_3O_4, Fe_2O_3 are shown in blue. The characteristic spin-orbit splitting between the Fe $2p_{3/2}$ and Fe $2p_{1/2}$ components is observed in all samples. Pronounced multiplet features are visible, consistent with the spectra of the oxide references. (b) A closer look into the Fe 2p spectra of the samples, stacked on top of each other. The spectra for $Fe_xNi_{1-x}(O,OH)_y$ with x=1 is shown in black, x=10 is green, x=16 is orange, x=20 is pink, x=50 is indigo and the spectra of the reference materials are shown in blue.

To understand the chemical environment of the transition metals in the $Fe_xNi_{1-x}(O,OH)_y$ electrocatalysts, it is beneficial to compare the different spectra of these samples with some known reference materials with well-defined chemical compositions. This approach is referred to as "fingerprinting" and is helpful in forming a fair idea about the neighboring environment of the Fe and Ni in the samples. Figure 26 shows the comparison of the Fe 2p spectra of the samples with some selected reference materials. The peak at ~706.6 eV corresponds to Fe metal, with a zero-oxidation state. The Fe 2p spectra also exhibit a broad peak centered at 710.6 eV, which becomes more prominent with increasing Fe content, indicative of iron in an oxidized state. As is evident from the spectra of the reference materials, the binding energy of the broader peak aligns with reported values for both Fe^{2+}, as for Fe_2O_3 and FeOOH and Fe^{3+} species, as for Fe_3O_4 suggesting the presence of a mixed valence phase. The broadening of this peak at 710.6 eV could also be due to ligand effects, such as the nature of coordinated oxygen (oxide or hydroxide environments). The shoulder may also represent an Fe-O-Ni bonding in the FeNiOOH thin films[13,119]. The distinct peak at ~706.6 eV suggests that the surface is only partially oxidized, as it resembles the Fe metal reference.

To analyze the Fe 2p core levels in the modified sample set, the two-component fitting approach previously applied to the initial samples was repeated. While the model was found to be inadequate for the initial series, as discussed in Section 3.6, it is applied here again to assess whether the improved synthesis results in more consistent and chemically sound fits. This allows a direct comparison of how the synthesis protocol and thereby the quality of samples influences the applicability of the model. The two extreme compositions: x=1 and x=50 were used as reference spectra, representing FeNiOOH thin films with the least and most Fe content, respectively. This approach was based on the assumption that these two compositions correspond to distinct and relatively well-defined chemical states of Fe, and that intermediate compositions could be described as a linear combination of the two. This model effectively tests whether the evolution in spectral shape across the series can be explained by a varying ratio of two fixed components, rather than implying the presence of continuous or overlapping chemical states. From Figure 26, it is evident that the peak at ~706.6 eV is predominant in the x=1 sample, while the feature at ~710.6 eV dominates in the x=50 sample. This trend indicates that metallic Fe is more prominent in the low-Fe sample, and that increasing Fe content corresponds with a progressive oxidation of the Fe species, culminating in the most oxidized state at x=50, as an initial hypothesis.

For each sample, the fitting was performed individually, but with a consistent approach. A linear background was applied to all, and the amplitudes and binding energies (minor energy shifts, creating offsets) of the two fitting components were allowed to vary during the fitting process. As a first approximation, a linear background was applied to all spectra to keep the fitting approach consistent and sufficiently simple for this stage of analysis. However, it should be acknowledged that a linear background is not the best background estimation for systems with transition metals such as Fe and Ni, as explained in Chapter 2. A much better background estimation is the Tougaard background[30], which will be applied to the spectra discussed in subsequent sections, where a comparative study between as-prepared samples and post-OER treated samples will be performed. Subtle changes in the post-OER samples are more critical and their interpretation requires more rigorous approximations than a simplified linear background. For the purpose of the two-component fitting, however, the linear background approximation provides satisfactory results.

No additional broadening was applied to either of the components. This approach was adopted to preserve the intrinsic line shapes of the spectra, without introducing any artificial modifications to the spectral profiles. The fit was performed over an energy window of approximately 705 eV to 737 eV, taking into account both the Fe $2p_{3/2}$ and Fe $2p_{1/2}$ regions. The residual is a measure of how well the fit works and was used as a guide for optimizing the fit results.

The results of the two-component fitting procedure for all samples are summarized in

Table 2.

Sample (x)	Amplitude x=1	Amplitude x=50	Offset (eV) x=1	Offset (eV) x=50
1	1.00	0.00	0.00	-
3	0.8089	0.2301	0.0293	0.1333
10	0.8127	0.2065	-0.1205	0.3100
13	0.6138	0.3260	0.0531	0.1741
16	0.3700	0.6425	0.0124	0.0100
20	0.0627	0.9900	0.03773	0.1330
40	0.2853	0.7275	0.3663	0.0688
50	0.00	1.00	-	0.00

Table 2: Summary of fitting parameters obtained from the two-component analysis of the Fe 2p HAXPES spectra of all the samples. The amplitudes and energy offsets of the x=1 and x=50 components of the $Fe_xNi_{1-x}(O,OH)_y$ thin films are reported. The fit was performed in an energy window of 705-737 eV, with a linear background which was allowed to optimize itself for the best fit. No additional broadening was applied.

Across the series, a trend is observed between the relative components of the two end points, reflecting the variation in the chemical environment of Fe with composition. The energy offset remained typically below 0.15 eV, confirming the stability of the reference components. The residuals observed were low, validating the fit models.

The fits are shown for samples x=3, 10, 16 and 20 in Figure 27. The x=1 fitting component is shown in blue and the x=50 is shown in green while the fit sum is shown in red.

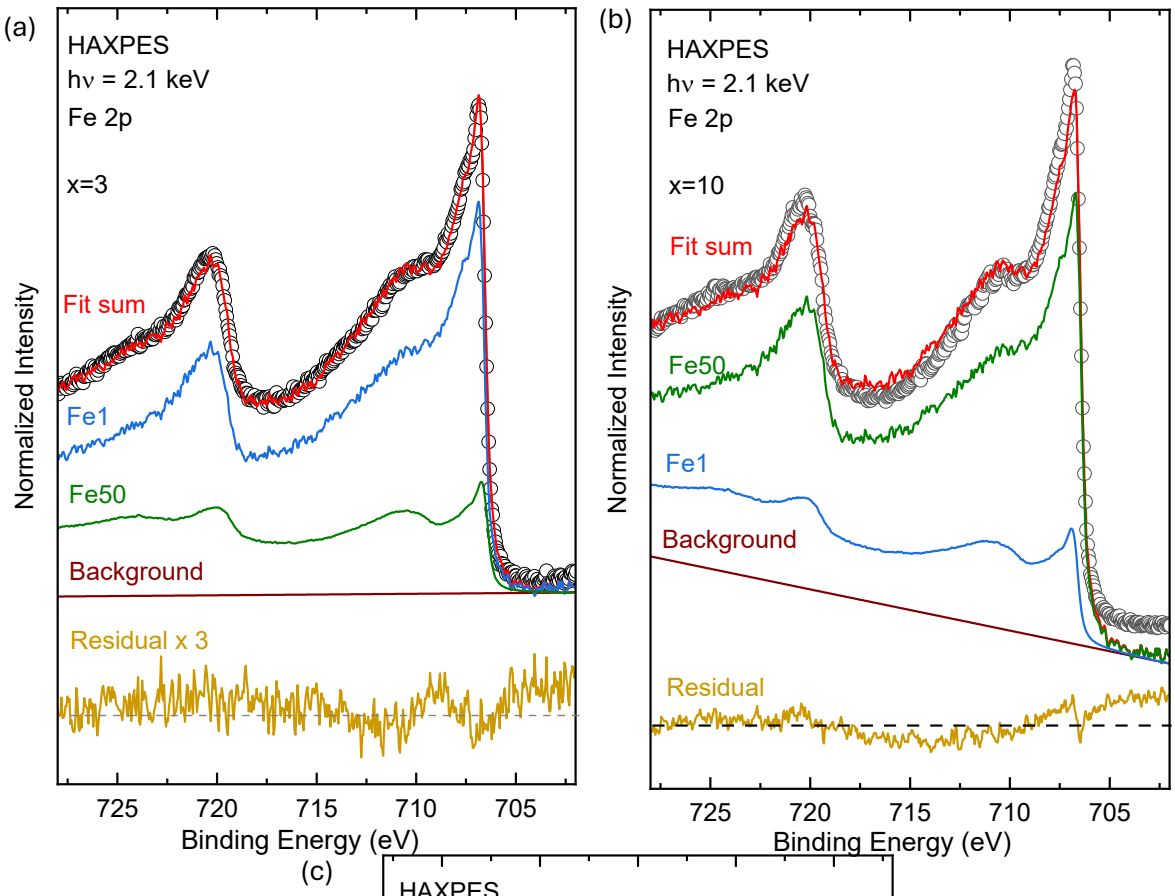
(a)
HAXPES
hν = 2.1 keV
Fe 2p
x=3
Fit sum
Fe1
Fe50
Background
Residual x 3
Normalized Intensity
725
720
715
710
705
Binding Energy (eV)
(b)
HAXPES
hν = 2.1 keV
Fe 2p
x=10
Fit sum
Fe50
Fe1
Background
Residual
Normalized Intensity
725
720
715
710
705
Binding Energy (eV)

(c)

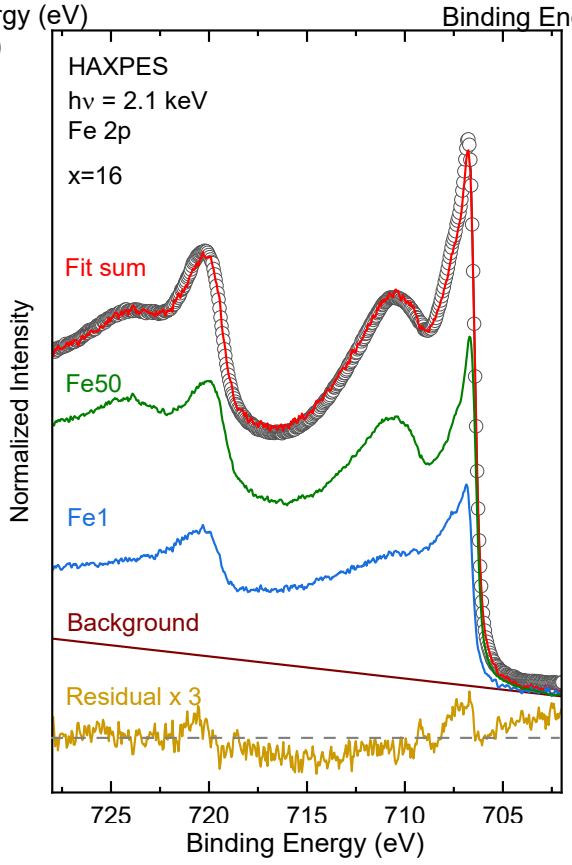
HAXPES
hν = 2.1 keV
Fe 2p
x=16
Fit sum
Fe50
Fe1
Background
Residual x 3
Normalized Intensity
725
720
715
710
705
Binding Energy (eV)

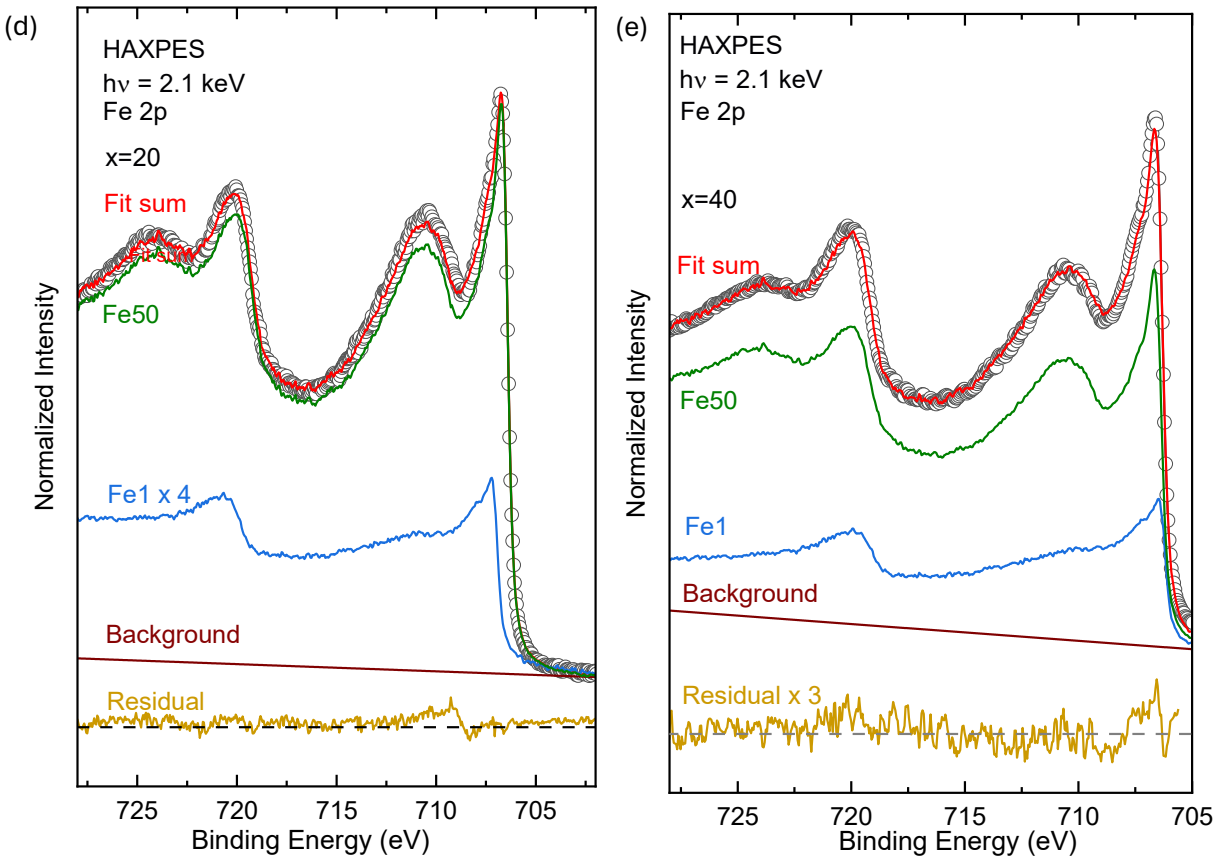

Figure 27: Two-component fits of the Fe 2p spectra for samples with x=3 (a), x=10 (b), x=16 (c), x=20 (d) and x=40 (e). The experimental data (black symbols) are fitted using a linear combination of the x=1 (blue) and x=50 (green) components. A linear background was applied, shown in brown. The agreement between the fit sum (red) and data represents the soundness of the fit, also reflected in the residual, shown in yellow.

The good agreement between the experimental data and fit sum represents the soundness of the fit model, also establishing that the spectra of the intermediate samples can be represented as a linear combination of the two extremes. The residual is shown in yellow.

To further analyze the evolution of the chemical environment of the Fe across the series, the relative contributions of the two components were extracted from the fits and plotted as a function of the sample composition, in Figure 28. The error bars shown for each data point reflect the variation in contributions from the components by slightly varying the fitting region, providing an estimate of the uncertainty of the fit, depending on the energy window.

While the Fe 2p spectra of the intermediate samples can be effectively reproduced using a linear combination of the x=1 and x=50 reference spectra, the variation in the relative contributions of these components does not follow a linear trend with increasing Fe content. As can be seen in Figure 28, the relative contributions of the x=1 and x=50 components remain relatively stable with increasing Fe content, until ~10 at.% and above ~20 at.% Fe, with the most significant changes occurring

between the two. This suggests that the chemical state of Fe may shift more abruptly within this narrow composition window, rather than evolving gradually across the entire series. Therefore, while the spectral shapes are well approximated by a two-component model, the material system likely exhibits more complex chemical behavior than a simple interpolation between just the two discrete states.

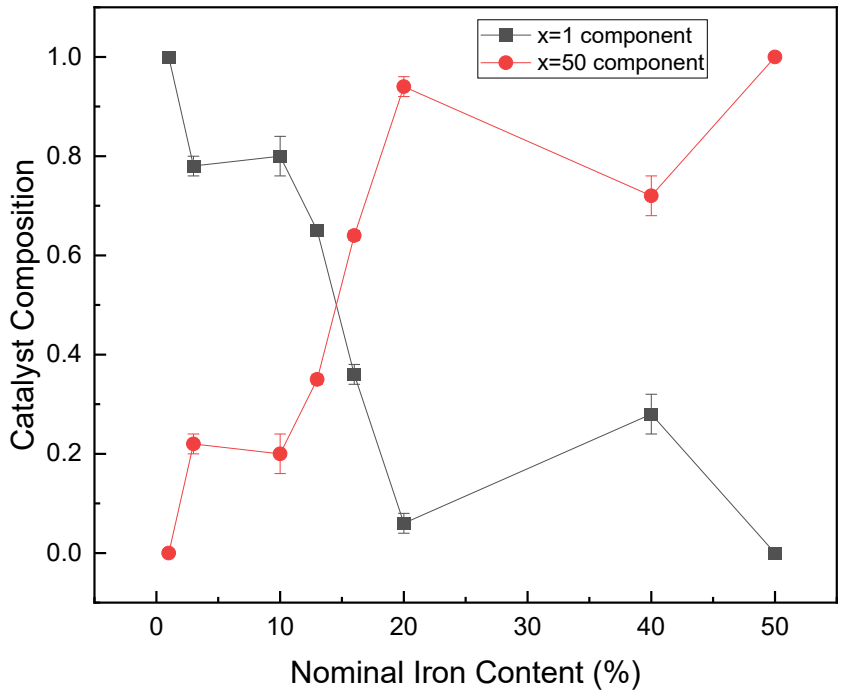

Figure 28: Relative contribution of the x=1 and x=50 components in the two-component fit for the Fe 2p spectra across the different FeNiOOH sample series. The x=1 component corresponds to the most reduced Fe environment, while the x=50 component reflects the most oxidized state. The data show a non-linear trend in component contributions, with minimal variation at low and high Fe contents and a sharper transition observed between x=10 and x=20.

4.1.2 Insights from the evolution of Ni across the different compositions

To gain a more complete view of the chemical environment of all the samples across the different compositions, the Ni 2p region was analyzed.

Changes in the chemical environment of Ni are expected across the different FeNiOOH samples. As shown in the Fe 2p analysis, Fe exhibits a composition-dependent shift towards more oxidized chemical states, particularly between the 10 and 20 at. % Fe. Such changes in one transition metal species often have implications for the local electronic structure of its neighboring elements in mixed metal systems such as the FeNiOOH electrocatalysts studied in this dissertation.

The Ni 2p region is characterized by a strong spin orbit splitting between the Ni $2p_{3/2}$ and Ni $2p_{1/2}$ peaks, at ~869.7 eV and ~852.6 eV, respectively, hence separated by 17.1 eV[19]. As was noted for Fe 2p, multiplet splitting is seen in the case of Ni 2p as well. It appears as broad shoulders at higher binding energies as compared to the main $2p_{1/2}$ and $2p_{3/2}$ peaks[120,121]. The main Ni $2p_{3/2}$ peak appears

at an energy close to that of metallic Ni, with only weak features resembling other reference materials, suggesting a predominantly metallic or reduced state for Ni prior to electrochemical treatment, especially in the low Fe, high Ni regime.

Comparison with reference spectra for NiO and $Ni(OH)_2$ (digitized from ref[121] and ref[122] respectively) helps assign identities to the different spectral features observed in the Ni 2p spectra of the sample series. The dominant peak in all samples at ~869.7 eV closely resembles metallic Ni, a second, well-defined peak at approximately 855.3 eV becomes increasingly prominent with decreasing Ni content (i.e., increasing Fe content), as shown by the dashed maroon line in Figure 29.

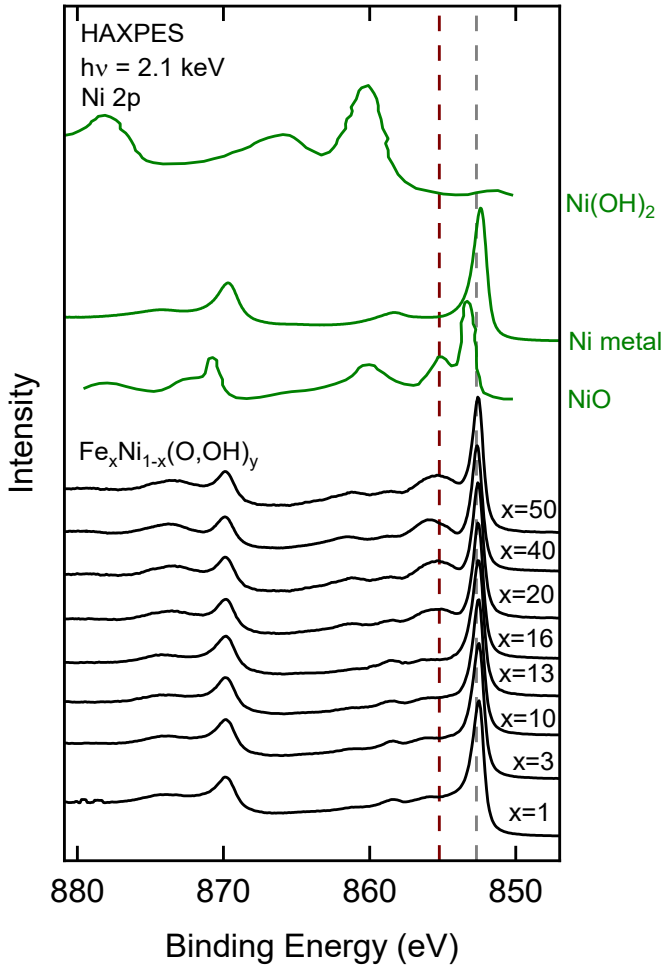

Figure 29: Ni 2p spectra of the as-prepared FeNiOOH thin film samples, shown in black, compared with the spectra of Ni metal, NiO and $Ni(OH)_2$ shown in green. The NiO and the $N(OH)_2$ spectra have been digitized from ref[122] and ref[123].

This binding energy is characteristic of Ni^{2+} in NiO environments[121,123] , indicating that an increase in oxide character occurs with increasing Fe incorporation. However, the absence of strong satellite features as seen in the cases of NiO and $Ni(OH)_2$[122] is strong indication that in the as-prepared samples, Ni remains largely in a low oxidation state.

To complement the analysis of the Fe 2p spectra, a similar two-component fitting approach was applied to the Ni 2p region. As was done for the Fe 2p spectra, each intermediate spectrum is modelled as a linear combination of the two end states, the x=1 and x=50 components. The application of this approach to Ni aims to determine whether Ni undergoes changes comparable to Fe 2p or maintains a stable chemical state across the series. A linear background was applied to each fit and no additional Lorentzian or Gaussian broadening was applied.

The results of the two-component fitting procedure for all samples are summarized in Table 3.

Sample (x)	Amplitude x=1	Amplitude x=50	Offset (eV) x=1	Offset (eV) x=50
1	1	0.00	0.00	-
3	0.89331	0.1136	-0.0102	0.0462
10	0.9447	0.0539	0.0041	0.0006
13	0.9919	0.0353	-0.0044	0.1428
16	0.3543	0.63409	0.0117	-0.0016
20	0	1	0	1e-05
40	0.8946	0.0879	0.0643	0.0028
50	0.00	1	0.00	-

Table 3: Summary of fitting parameters obtained from the two-component analysis of the Ni 2p HAXPES spectra of all the samples. The amplitudes and energy offsets of the x=1 and x=50 components of the $Fe_xNi_{1-x}(O,OH)_y$ thin films are reported. The fit was performed in an energy window of 850-875 eV, with a linear background which was allowed to optimize itself for the best fit. No additional broadening was applied.

Table 3 summarizes the parameters extracted from the two-component fitting. For each sample, the table lists the optimized amplitude (relative contribution) and energy offset for both components. A trend is observed in the relative contributions of the two end-member components, reflecting changes in the chemical environment of Ni with increasing Fe content. The amplitude shift is particularly pronounced between x=13 and x=20, marking a distinct transition in the dominant Ni species. Energy offsets remained within ±0.15 eV, indicating the spectral features of the reference

components remained stable throughout the fitting process. The low residuals across all samples further validate the reliability of the two-component fitting model used for Ni.

The relative contribution of the two components is shown in Figure 30. The two-component analysis of the Ni 2p spectra shows a pronounced shift in dominant spectral features between x=13 and x=20, consistent with the transition region identified in the Fe 2p component trend. From x=1 to x=13, the x=1 component dominates, indicating minimal change in the Ni chemical environment at lower Fe contents. A sharp transition occurs at ~x=13 beyond which the x=50 component becomes the primary contributor. This abrupt change suggests that while the Ni oxidation state remains stable at low Fe concentrations, it is significantly altered at higher Fe content, likely due to Fe-induced structural or electronic modifications. The parity between the Fe and Ni inflection points highlights a coupled effect in the FeNiOOH sample matrix, although the nature of change in Ni appears more abrupt than gradual.

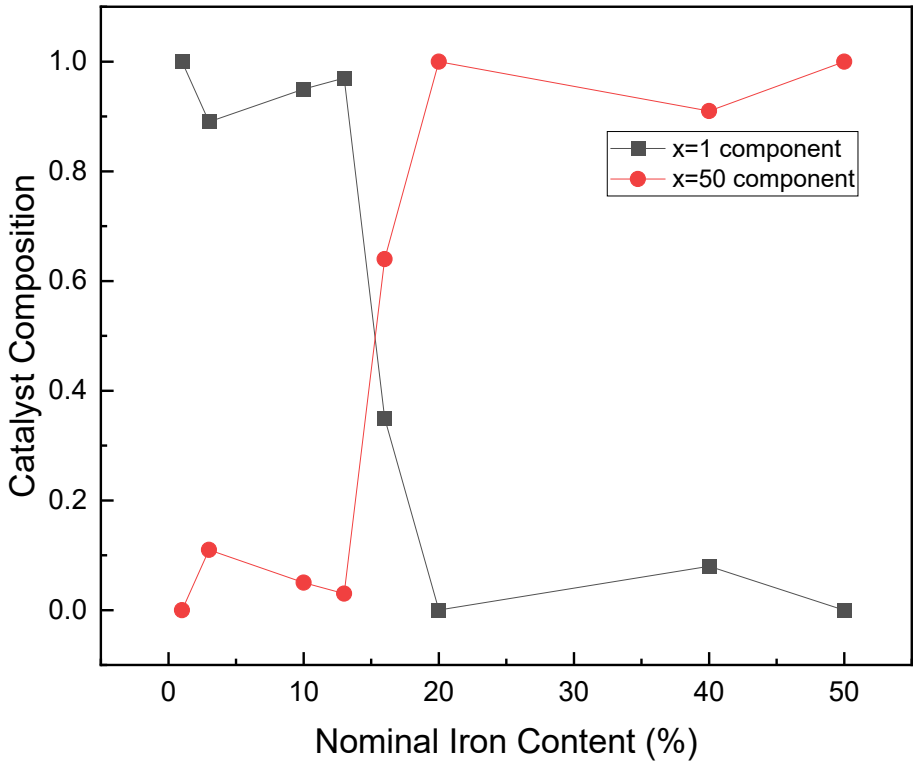

Figure 30: Relative contributions of the x=1 and x=50 reference spectra in the two-component fitting of Ni $2p_{3/2}$ spectra across the FeNi sample series. The x=1 spectrum represents a more reduced Ni environment, while the x=50 spectrum corresponds to a more oxidized state. A sharp transition in dominant Ni species is observed between x=10 and x=20 suggesting a composition-driven shift in Ni's chemical state, consistent with the evolution identified in the Fe 2p analysis.

Quantitative analysis of the Ni 2p spectra reveals a clear transition in composition that closely resembles the trend observed in the Fe 2p region. While the Ni chemical state remains mostly unchanged at low Fe content, a pronounced shift in spectral character is observed between x=10

and x=20, with a growing contribution from Ni^{2+}-like features. This is the same compositional regime where the Fe 2p spectra exhibit their most significant changes, indicating a synchronized chemical evolution of both metal centers. These results suggest that rather than remaining chemically inert, Ni participates in the structural and electronic response to increasing Fe incorporation.

4.1.3 Qualitative analysis of O 1s spectra prior to electrochemical treatment

The oxygen environment plays a crucial role in determining the structure, stability, and electrochemical properties of FeNiOOH electrocatalysts[124,125]. Oxygen can possibly exist in multiple chemical states, including but not limited to oxide and hydroxide-like environments, each potentially influencing catalytic performance by altering the coordination environment, electronic structure, or oxidation state of the active metal centers.

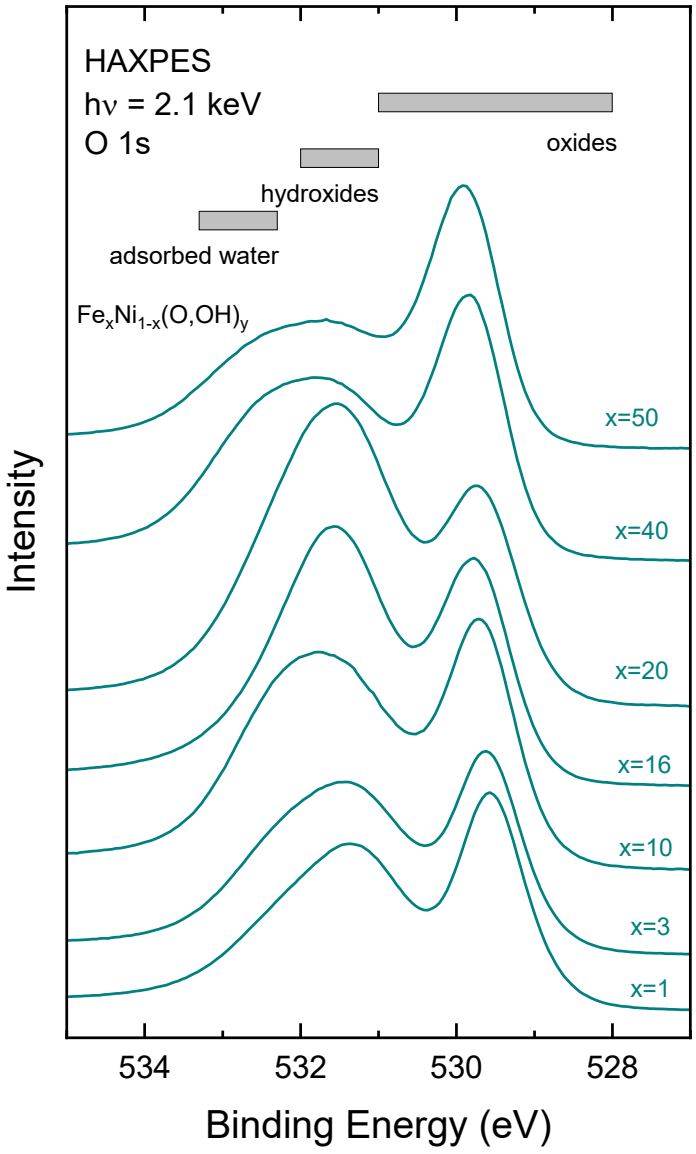

Figure 31: O 1s HAXPES spectra of as-prepared FeNiOOH thin films. Two main features are observed, corresponding to oxides (lower binding energies) and hydroxides (higher binding energies). The broadness of the hydroxide peak is suggestive of possible contributions from other oxygen species as well, such as adsorbed water.

Figure 31 shows the O 1s spectra of all samples. Two main contributions can be seen, the first centered around ~529.5–531 eV, which is typically assigned to O^{2-} in transition metal oxides, consistent with literature reports on transition metal oxides and mixed metal oxides[126,127,128]. The second broader feature appearing between ~531–532 eV is generally attributed to hydroxide species (OH^-), commonly observed in transition metal oxides[126,127,128]. The regions are marked by grey bars, to clearly demarcate between the oxygen environments. The higher energy region of ~532.3–533.3 eV is consistent with surface adsorbed water[129]. The clear substructure within the broad O 1s feature in each sample suggests that multiple oxygen species coexist. The shaded energy bands serve as visual guides for interpreting the overlapping contributions from oxide, hydroxide, and adsorbed water on

the surface of the samples. Subsequently, quantitative fitting of the spectra was performed, to assess the changing relative contributions of the oxide and hydroxide chemical environments to the spectra overall.

Figure 32 shows the representative fit for the sample x=10. The fits were performed using Voigt profiles to determine individual chemical compositions of oxide-like and hydroxide-like environments as a preliminary approximation, along with a linear background. The overall fit reproduces the spectrum well. The same model was applied to all samples and they were fit simultaneously. The soundness of the fit can be gauged by the residual.

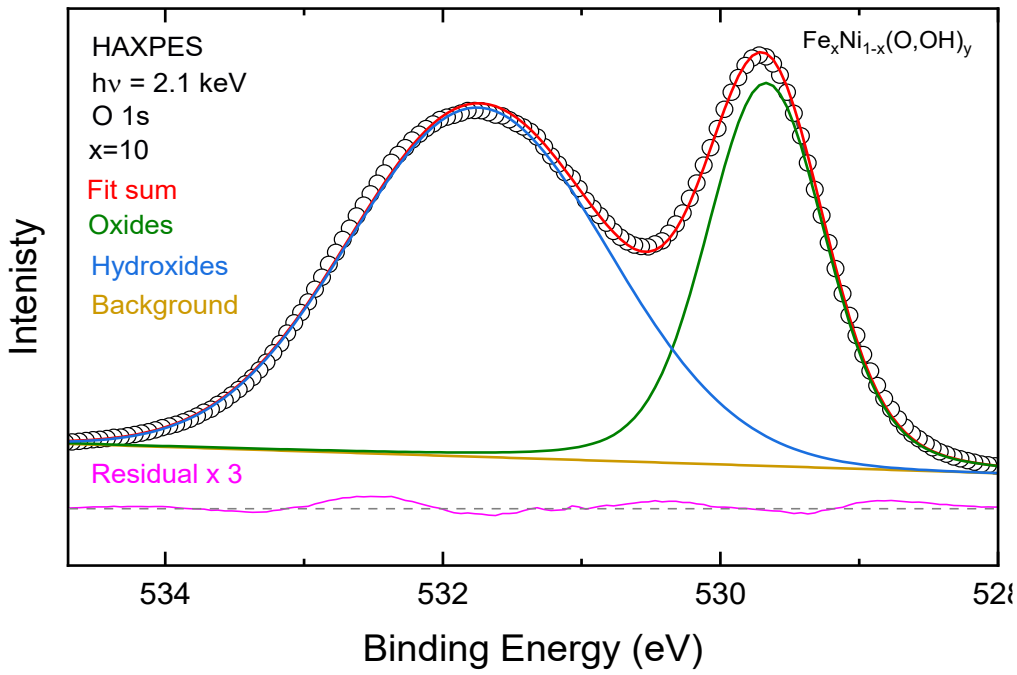

Figure 32: Representative O 1s HAXPES spectrum (x=10), showing fitted components corresponding to an oxide environment in the material (O^{2-}, ~529.5–530.0 eV), and a combination of the hydroxide and adsorbed surface water (OH^-, ~531–532 eV and ~532.3–533.3 eV respectively). The quality of fit supports the spectral interpretation used in the quantitative comparison across compositions.

Figure 33 shows the relative contributions of the deconvoluted components to the overall O 1s spectra. As discussed above, the higher energy peak also has contributions from surface adsorbed water. A non-monotonic evolution of the relative intensities of these features were observed with increasing Fe content. The hydroxide contribution significantly increases from x=10 to x=20, where it reaches a maximum, before steadily declining again at higher Fe concentrations. At the same time, the oxide content displays a corresponding decrease within the same compositional window, before increasing again for x=40 and x=50. This closely mirrors the behavior observed in the Fe and Ni 2p HAXPES fits, where the window between x=10 and x=20 stands out, as the range where Fe and Ni are

seen to undergo significant electronic changes. A relatively high hydroxide contribution has been reported in similar studies of Fe and Ni oxides, where surface associated OH^- and H_2O species play a direct role in mediating redox transitions through proton-coupled electron transfer mechanisms[130,131,132]. The subsequent decrease in hydroxide content at higher Fe levels may reflect a reorganization of the surface or the emergence of more ordered, less hydrated oxide phases[133].

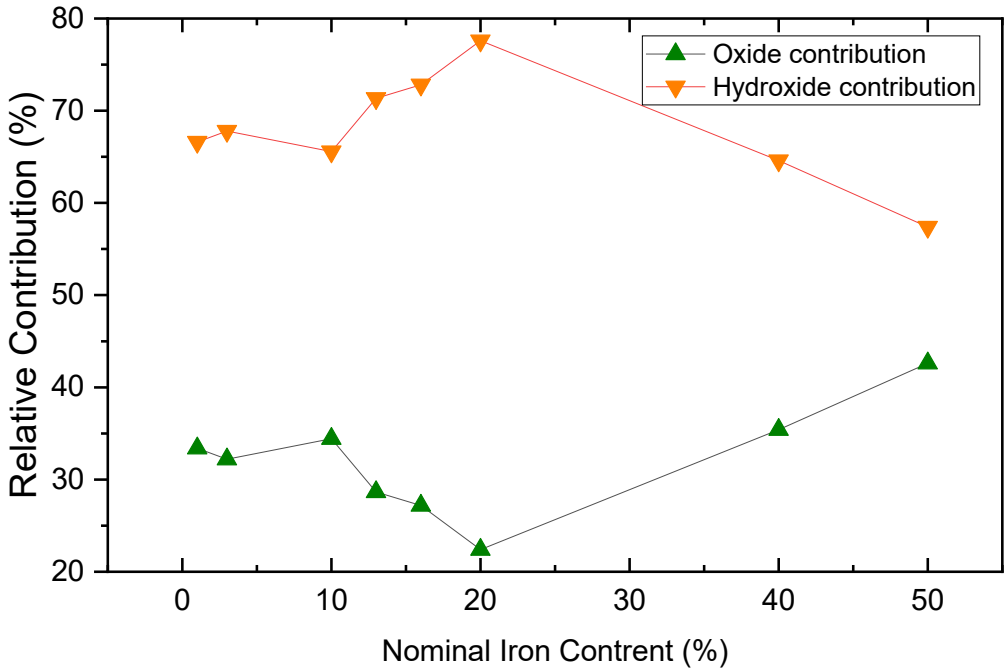

Figure 33: Relative oxide and hydroxide plus water contributions from O 1s HAXPES fits across the $Fe_xNi_{1-x}(O,OH)_y$ series. An increase in the contribution of hydroxide can be noted within the compositional window of x=10 and x=20, consistent with increases in surface hydration and metal oxidation.

4.1.4 Complementary insights into the Fe and Ni electronic structure from L-edge XAS

PES provided important insights into the chemical states and environments of the metal and oxygen species in the catalyst materials by probing the occupied electronic states. To obtain a more complete picture of the electronic structure of the FeNiOOH electrocatalysts, particularly the unoccupied states and the local coordination environments of the Fe and Ni, XAS is employed at the Fe and Ni L edges. XAS probes unoccupied electronic states and is highly sensitive to oxidation state, local symmetry, and metal-ligand interactions. In the following section, Fe and Ni L edge spectra will be looked at, in correspondence to the spectra of some known references.

XAS measurements were recorded in both TEY and PFY modes. While a key difference between the two lies in their depth sensitivity, there are also differences in detection mechanisms and sensitivity to sample conditions, discussed in detail in Chapter 2. TEY, which detects electrons via the drain current, is more surface sensitive and can be influenced by charging and roughness. PFY, which measures emitted photons as a result of fluorescence, has a greater information depth and is more

bulk sensitive, making it more suitable for probing features beyond the surface. In this context, PFY is complementary to HAXPES.

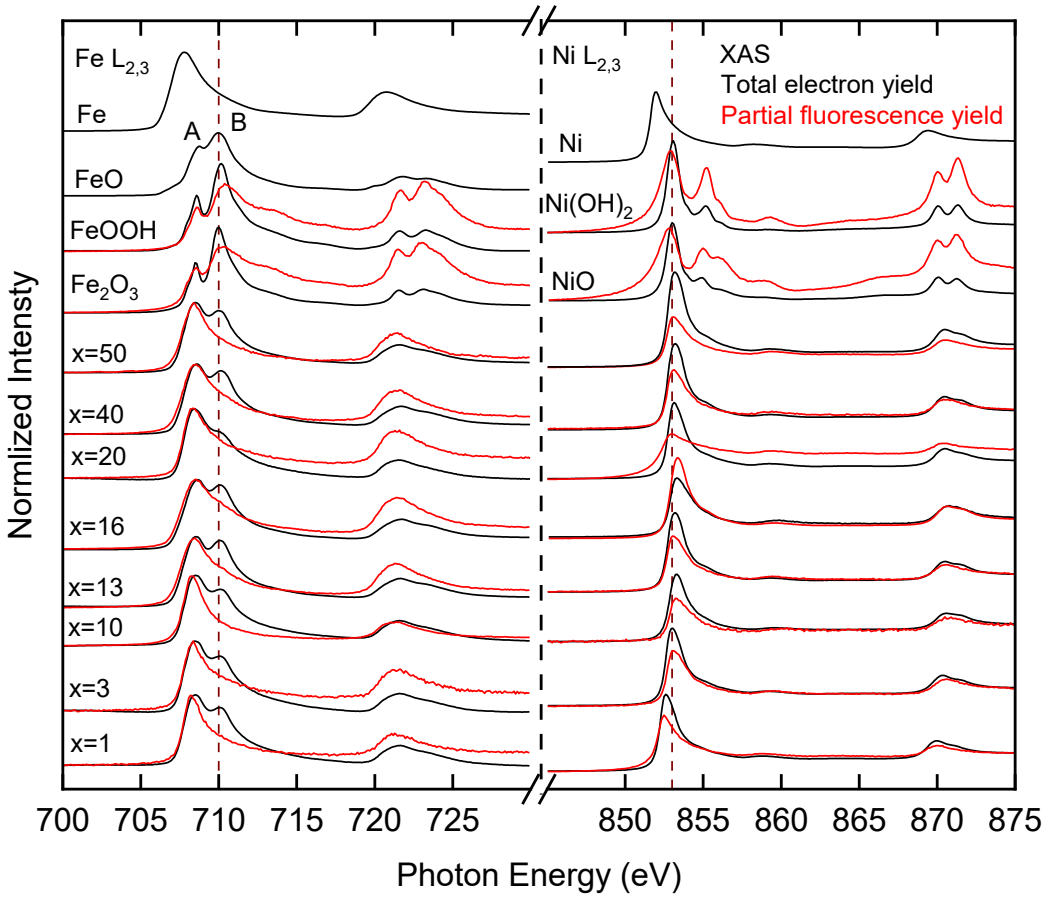

Figure 34: XAS spectra of Fe and Ni L edges of the FeNiOOH thin films and some reference compounds. The dashed lines mark prominent features in the spectra.

The Fe and Ni L -edge XAS spectra of the samples, recorded in both TEY and PFY modes are shown in Figure 34. Both the Fe and Ni L-edge XAS spectra exhibit pronounced multiplet structures, arising from $2p^6 3d^n \rightarrow 2p^5 3d^{n+1}$ dipole transitions, controlled by Coulomb interactions, spin-orbit coupling and ligand field effects.[134,135,136] The spectral features observed are explained in the context of charge transfer multiplet splitting theory (CTMS)[136], surface and bulk differences and by comparing them to the spectra of known references.

The Fe L_3-edge XAS spectra in Figure 34 evolve with increasing Fe content. Two primary features are observed: a low-energy peak near 706–707 eV (labelled A) and a higher-energy multiplet centered around 710 eV (labelled B). In low-Fe samples, peak A is more prominent, while in higher Fe content samples, peak B intensifies.

The Fe L_3 edge appears at 705-715 eV photon energy and displays a splitting pattern with multiple peaks resolved across samples. The fundamental interactions responsible for the multiplet features are such as:

Several electronic interactions in the final state of the Fe orbitals occur. These are primarily Coulomb interactions between the 2p core-hole and the 3d valence electrons following the 2p → 3d excitation and are further shaped by the ligand field imposed by the surrounding oxygen environment[137,138]. In an octahedral coordination geometry, this results in the splitting of the otherwise degenerate 3d orbitals and gives rise to multiple transitions with distinct energy and intensities[137,138]. These features are consistent with high-spin Fe^{3+} species in oxide-like coordination, as observed in Fe_2O_3 and FeOOH references. Additional broadening of the peaks can be attributed to charge transfer hybridization between Fe 3d and O 2p orbitals, which is typical in transition metal oxides with significant covalency, contributing to the complexity of the multiplet structure[74,139,140,].

A lower-energy feature appearing around 705–706 eV is especially pronounced in samples with lower Fe content. This feature is not prominent in the FeOOH and Fe_2O_3 references but closely resembles the L_3 edge of metallic Fe. Although its energy position is slightly shifted compared to pure Fe metal (~706 eV), such deviations may result from local structural distortions, partial tetrahedral coordination[141], or alloying effects with Ni[136]. The possible presence of Fe^{2+}-like species such as FeO or Fe_3O_4 cannot be ruled out entirely, particularly in compositions exhibiting mixed valency.

The presence of both metallic Fe and oxidized Fe species confirms that the as-prepared samples contain chemically heterogeneous Fe environments. Such mixed-valence configurations have been reported to be beneficial for catalytic activity[142,143], as metallic Fe can enhance electronic conductivity, while oxidized Fe sites (Fe^{2+}/Fe^{3+}) can participate directly in redox reactions during the oxygen evolution process. This combination of conductive and redox-active components may contribute to the overall enhancement of electrocatalytic performance of the material[144,145,146].

Comparison with reference spectra provides a clearer basis for interpreting these features. Metallic Fe exhibits a strong, sharp signal at ~706 eV, while FeO, which has Fe in a +2 oxidation state, also contributes significant intensity in this region. In contrast, FeOOH and Fe_2O_3, representative of Fe^{3+} in octahedral environments, display a pronounced peak B, typical of high-spin Fe^{3+}. The spectral evolution across the catalyst series suggests a transition from chemical environments containing metallic or Fe^{2+}-like species toward predominantly Fe^{3+}-based coordination at higher Fe contents.

Although the lower energy peak A resembles metallic Fe L_3 feature, its presence in FeO and other oxidized references indicates that it cannot be assigned exclusively to Fe^0. Rather, the cumulative evidence points to a mixed-valence Fe environment in the as-prepared samples, involving coexisting Fe^0, Fe^{2+}, and Fe^{3+} species. This interpretation is consistent with the Fe 2p HAXPES analysis presented earlier, discussed in Section 4.1.1.

In transition metal complexes such as this, the surrounding ligands break the degeneracy of the 3d orbitals through crystal field splitting. In an octahedral environment, this results in the splitting of the d orbitals into lower energy t_{2g} orbitals and higher energy e_g orbitals, as described by the ligand field theory. X-ray absorption at the Fe L_3 edge results in transitions from the occupied core level to these unoccupied 3d -derived states, resulting in the signature multiplet splitting of the spectra. The two

dominant peaks, referred to as A and B in the Figure 34 therefore are qualitatively associated with transitions into the t_{2g} and e_g orbitals, respectively.

Additionally, the Fe-L_3 edge XAS spectra have been evaluated by measuring the energy separation between the two dominant multiplet features at ~710 eV and ~708.47 eV. This approach is rooted in the ligand field multiplet theory, which considers the effects of 2p-3d Coulomb interactions and crystal field splitting on the final-state electronic configuration following the 2p → 3d transition[140,147]. The ligand field theory forms the foundation of the CTMS, discussed earlier. CTMS builds on this by also considering the interaction between the metal and its surrounding ligands. The spectral shape is thus sensitive to the oxidation state and local coordination environment of the Fe center, with the energy separation between peaks serving as a fingerprint for specific chemical states[138,148].

The energy separation is calculated as following: difference in energy positions of the higher energy peak B and the slightly lower energy peak A, as shown in Figure 34. This value evolves non-monotonically across the sample series, as can be seen from Figure 35 and transitions observed in trends are intrinsic features of the spectra. The data exhibit a distinct inflection at x=20, where the separation reaches a maximum value of ~2.01 eV. Below and above this composition, the values range in between ~1.5 and 1.7 eV. This is in agreement with the trend observed in the analysis of the Fe 2p HAXPES spectra, where the two-component fit approach revealed abrupt changes in the relative contributions of the reference components between samples x=10 and x=20. This observation supports the hypothesis that discrete changes occur in the electronic configuration within this range[136, 137,138,]. The energy separation values of FeNiOOH thin films with Fe concentrations up to 10 at. % are comparable to those of FeOOH and Fe_2O_3, implying the presence of Fe^{3+}. It is suggestive that the x=20 sample goes through significant structural rearrangement, which gives rise to its relatively higher energy separation of the multiplets. A decrease in the values can be noted again, from x=20 to x=50, but as they do not conform to any of the reference materials specifically, Fe can be presumed to exist in a mixed-valence state in these sample compositions, as hypothesized earlier.

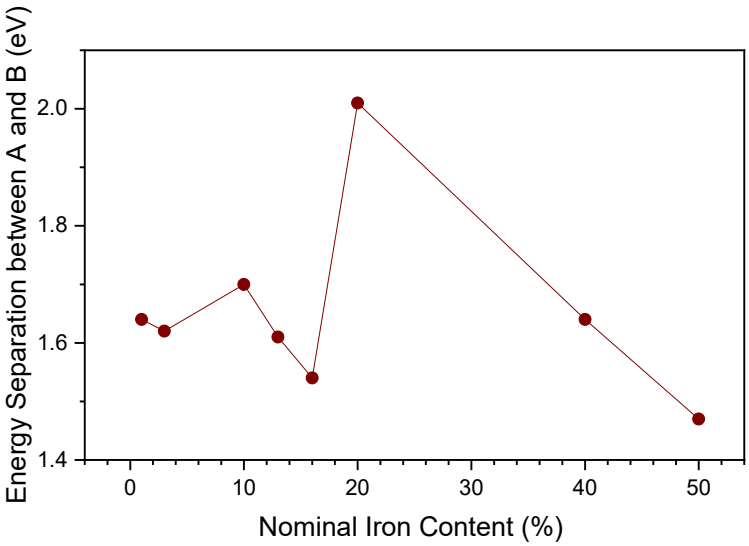

Figure 35: Multiplet splitting energy at the Fe L_3-edge as a function of Fe content in the $Fe_xNi_{1-x}(O,OH)_y$ thin films. A distinct jump in the trend is observed between x=10 and x=20, corresponding to a compositional transition also identified in analysis of Fe 2p HAXPES spectra, indicating changes in the electronic environment of Fe.

Even though the evolution of the spectra suggests a predominantly octahedral ligand environment for Fe, the possibility of tetrahedral environments cannot be completely eliminated owing to the now established mixed-valence nature of Fe. In such cases, the orbitals resulting from the splitting are reversed in terms of energy, and the e orbitals lie at a lower energy as compared to the t_2 orbitals. However this configuration has not been resolved in the current spectra.

Clear differences can be observed between the spectra measured in TEY mode, and that measured in PFY mode in Figure 34. TEY, which probes the top few nanometers[36] of the sample, exhibits a distinct higher energy multiplet feature at ~710 eV at the L_3 edge, arising from Fe^{3+} sites in octahedral coordination, as deduced above. In contrast, the PFY spectra, that probes deeper into the bulk of the sample[149], displays a single, broad maximum centered around ~707 eV, with no corresponding peak arising from multiplet splitting. This disparity indicates that the oxidation state and local chemical environments of Fe differ significantly between the surface and the bulk. The uniform spectral shape in PFY suggests that the bulk is chemically more homogeneous, with a predominance of Fe environments that are either less oxidized or structurally disordered. Similar differences between the surface and the bulk have been reported in Fe (oxy)hydroxides and mixed-valence oxides, particularly in systems prone to ambient surface oxidation[150,151,152].

To interpret the PFY data, it is important to consider detection specific artefacts. Fluorescence spectra is susceptible to self-absorption and saturation effects, which results in the attenuation of edge intensities, as discussed at length in Chapter 2. This effect is more prominently visible in the L_2 edge. Compared to the L_3 edge, fewer fluorescence photons are produced after the excitation of the L_2 edge, resulting in a weaker signal. The L_2 and L_3 edges also differ in terms of their origin, as the former corresponds to $2p_{1/2} \rightarrow 3d$ transitions and the latter corresponds to $2p_{3/2} \rightarrow 3d$ transitions[153].

Similarly, the Ni L edge XAS spectra were also recorded in TEY and PFY modes, as shown in Figure 34.

The Ni L-edge XAS spectra of the FeNiOOH samples reveal a pronounced L_3 absorption feature centered at ~852.6–853.0 eV, but notably lack the pronounced satellite feature at ~855 eV that is typically observed in classical Ni^{2+} compounds such as NiO and $Ni(OH)_2$ as can be seen from the spectra in Figure 34.

In the spectra of the reference compounds, the satellite at ~855 eV arises from multiplet splitting associated with a localized high spin $3d^8$ Ni^{2+} configuration in an octahedral ligand field[154,155,156]. Its absence in the as-prepared FeNiOOH electrocatalysts implies that Ni does not exist in +2 oxidation state[157]. Instead, a Ni-O covalency is implied, consistent with more delocalized 3d states[90,158,159]. In the context of the sample system studied in this work, this behavior reflects a combination of the following: partial oxidation of Ni, a mixed valence state and modification of the ligand environment due to the incorporation of Fe.

From the analysis of the two-component fitting results of the Ni 2p HAXPES spectra, a change in the Ni structure is observed in the intermediate compositions between x=13 and x=20, but this is not accompanied by the development of a distinct satellite feature at ~855 eV in the L-edge TEY spectra to signify the presence of Ni^{2+} as is seen in NiO. This indicates that while Fe promotes Ni oxidation, the resulting Ni environment is electronically and structurally distinct from that in stoichiometric NiO. The agreement between the HAXPES quantification and the subtle spectral shifts in XAS supports a model where Fe induces oxidation of Ni, but within a chemically modified coordination structure that does not give rise to known multiplet fingerprints that align with those of the references studied.

In contrast to the Fe L-edge spectra, the Ni L-edge XAS spectra show no significant difference between TEY and PFY modes across the different compositions. As it was established that the absence of the satellite feature at ~855 eV in the TEY spectra eliminates the possibility of the existence of a conventional Ni^{2+} octahedral environment on the surface, likewise, the PFY spectra confirms that the bulk mirrors this behavior. Incorporation of Fe into the samples therefore, has no effect on the Ni species present within the bulk of the sample.

4.2 Initial electronic structure and its implications

The combined core-level and X-ray absorption spectroscopies reveal a composition-dependent evolution of the local chemical environment in the as-prepared FeNiOOH electrocatalysts. Fe 2p HAXPES and L-edge XAS analyses show that Fe is present in mixed-valent states across all compositions, with features resembling a more reduced state of Fe persisting at the lower concentration of Fe in the sample series. Multiplet splitting in the Fe L_3 edge varies non-linearly with composition, indicating changes in oxidation state and ligand field strength, with x=20 emerging as a key inflection point. Ni 2p HAXPES fitting confirms that Fe incorporation promotes Ni oxidation, with a sharp increase in oxidized-like character between x=13 and x=20. However, Ni L-edge XAS spectra lack the characteristic satellite features of classical Ni^{2+} oxides, suggesting that oxidation occurs within a disordered or covalent coordination environment rather than as distinct NiO phases. This interpretation is further supported by the O 1s HAXPES results, which reveal a correlated rise in hydroxide and surface adsorbed water content in the same compositional range, peaking at x=20.

The consistent trends across all measurements point to a chemically significant transition near x=20, where Fe and Ni undergo coupled oxidation. Beyond this point, the oxide and hydroxide signatures diminish, suggesting a restructuring of environments that are active for the redox reactions. Together, these findings establish a comprehensive picture of the electronic and chemical structure in the as-prepared films and define the compositional threshold at which the Fe-O-Ni interaction most strongly alters the surface and bulk properties of the material.

5 Electronic and Chemical Structure Evolution of $Fe_xNi_{1-x}(O,OH)_y$ Electrocatalysts upon OER Treatment

Understanding how electrocatalysts evolve following electrochemical operation is critical to gaining insights into the origins of their catalytic activity and long-term stability. In heterogeneous electrocatalysis, such as the catalysis promoted by the $Fe_xNi_{1-x}(O,OH)_y$ thin films studied in this dissertation, the surface of the material plays a significant role in determining the catalyst's performance. The oxygen evolution reaction (OER) is initiated by the adsorption of reactive intermediates on the catalyst surface, as is typical in such systems. As a result, the surface of the FeNiOOH thin films after OER can undergo reorganization due to the redox reactions such as leaching or enrichment of Fe or Ni and changes in the coordination environment of the active metal centers.

In this chapter, the transformations in a series of electrodeposited $Fe_xNi_{1-x}(O,OH)_y$ thin film samples, prepared and shipped to KIT by the collaboration partners at the PSU[91] are examined, by comparing the as-prepared films with their post-OER counterparts

To track both surface and bulk related changes of electronic and chemical environments of Fe, Ni and O as well as the changing oxidation states of Fe and Ni, complementary HAXPES, XAS, and XES spectroscopies are used, which have been discussed in Chapter 2 and applied in Chapter 4.

By integrating the findings of the different measurements, a depth resolved picture of the transformations brought in by OER, in relation to the constituent species of the $Fe_xNi_{1-x}(O,OH)_y$ catalysts will be developed.

5.1 Probing catalyst surface chemistry before and after OER via HAXPES

The samples studied in this section consist of FeNiOOH thin films with nominal Fe at. % of 0,1,5,20 and 50. For each composition, two samples were prepared: one as-prepared (without any electrochemical treatment) and one subjected to the oxygen evolution reaction (OER). The scan rates used for cycling were either 10 mV/s or 100 mV/s, until a steady state was reached. The voltage window for conducting the cyclic voltammetry experiments was determined based on the Fe content, ranging from 0.98 V vs SHE to between 1.6 and 1.9 V vs SHE, with the potential decreasing with increasing Fe content.

For simplicity, the samples are denoted as "wt OER" (with OER) and "wo OER" (without OER).

Investigation of the x=0 sample, which is essentially a pure Ni film, helps examining modifications on the surface of the Ni induced by OER thereby establishing a baseline for interpreting Fe-induced changes in the mixed systems.

The HAXPES survey spectra was recorded for samples with and without OER treatment and are shown in Figure 36 in red and black respectively. Fe, Ni, O core level peaks are visible across the

series. The Fe 2p peak increases in intensity with increasing Fe content, becoming most pronounced in the x=50 sample. Post OER, a subtle increase in the Fe signal is observed, even in the low Fe samples. Contrastingly, the Ni 2p signal is most prominent in the low Fe samples, decreasing in intensity as expected, with increasing Fe content. The Ni 2p spectra have been scaled by a factor of 0.7, for clear visualization of the other weaker peaks. A trend can be observed in the Ni 2p peak signals where the peak intensity decreases slightly post OER. Enhancement of the O 1s peak can be noticed after OER. Further analysis of detailed spectra will enable interpretation of the changing peak intensities.

Weaker peaks attributed to Na, Si and Au are also detected. As discussed at length in Chapter 4, Na is likely from residual buffer salts used during synthesis. The presence of Au and Si signals, despite the nominal film thickness exceeding the IMFP of the corresponding photoelectrons, indicates that the FeNiOOH film may be locally thin, uneven, or discontinuous.

Additionally, signals corresponding to Cu, Zn and Sn are detected in certain samples. The Cu signal likely originates from the copper strip used to electrically connect the sample to the external power supply. Trace Zn and Sn signals may arise from residual contamination in the sample preparation chamber, as they were not observed consistently across all samples. Given their inconsistency, these elements are not considered intrinsic to the FeNiOOH catalyst's composition or central to its observed activity. A more detailed discussion of compositional and spectral changes with Fe content and OER treatment follows in subsequent sections, but broadly, a decrease in Ni 2p intensity and changes in O 1s signal are consistently observed post-OER.

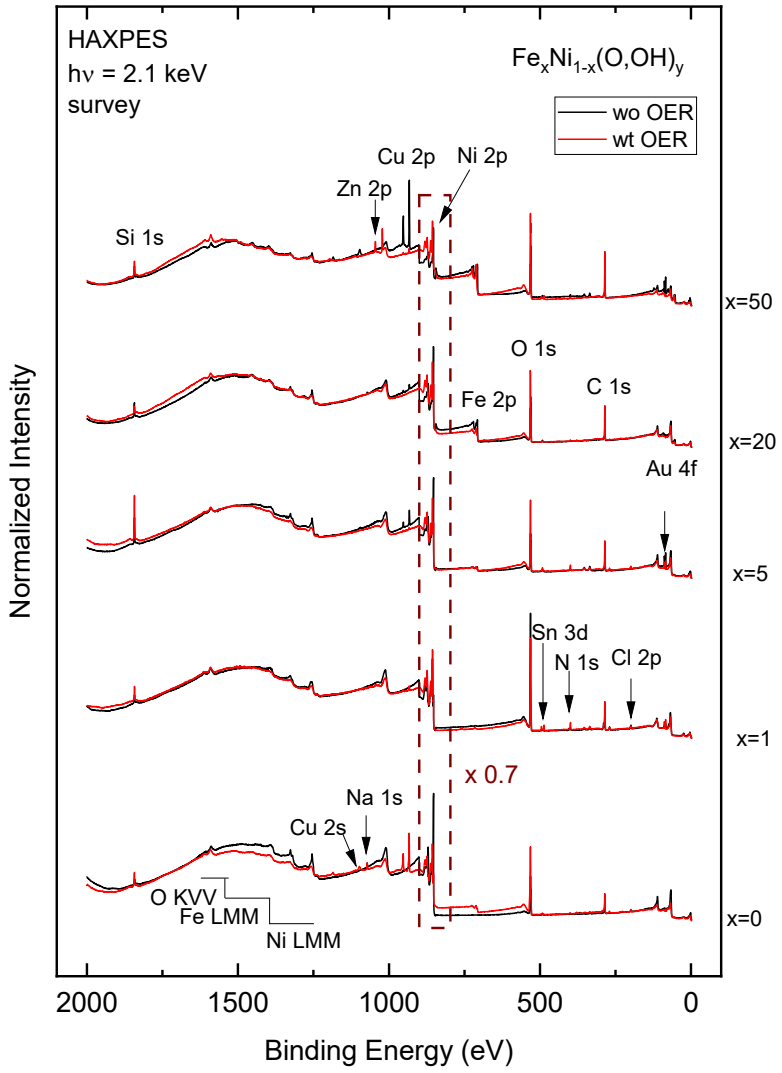

Figure 36: HAXPES survey spectra (hv = 2.1 keV) of $Fe_xNi_{1-x}(O,OH)_y$ thin films (x = 0, 1, 5, 20, 50), before (wo OER, black) and after (wt OER, red) OER treatment. Ni 2p signals in the pre-OER spectra have been scaled by 0.7 to help make other, weaker peaks more visible. Peaks corresponding to Na, Si, Au, Cu, Zn, Sn, Cl, and N are marked.

Figure 37 shows the Fe 2p HAXPES spectra, measured at an excitation energy of 2.1 keV. Reference spectra of Fe metal, FeOOH, Fe_2O_3, and Fe_3O_4 are shown in green for comparison. All spectra display two primary features in the Fe $2p_{3/2}$ region: a distinct peak at ~706.6 eV, and a broader peak centered around ~710.6 eV, the distinct low energy peak resembles the position of Fe^0 in metallic reference spectra, and the high energy feature is associated with oxidized Fe species. As seen in the references and highlighted by dashed lines, this higher binding energy peak overlaps with features from both Fe^{2+} (as in Fe_3O_4) and Fe^{3+} (as in FeOOH and Fe_2O_3) and therefore cannot be unambiguously assigned to a single oxidation state[160,161] as was also seen for the as-prepared samples in Chapter 4. Instead, it reflects a distribution of oxidized Fe environments, likely involving mixed-valence states and delocalized electronic structures. In the post-OER samples, a clear increase in the intensity of the oxidized Fe component is observed, accompanied by a relative decrease in the Fe^0-like feature, indicating a shift toward a more oxidized Fe environment at the surface.

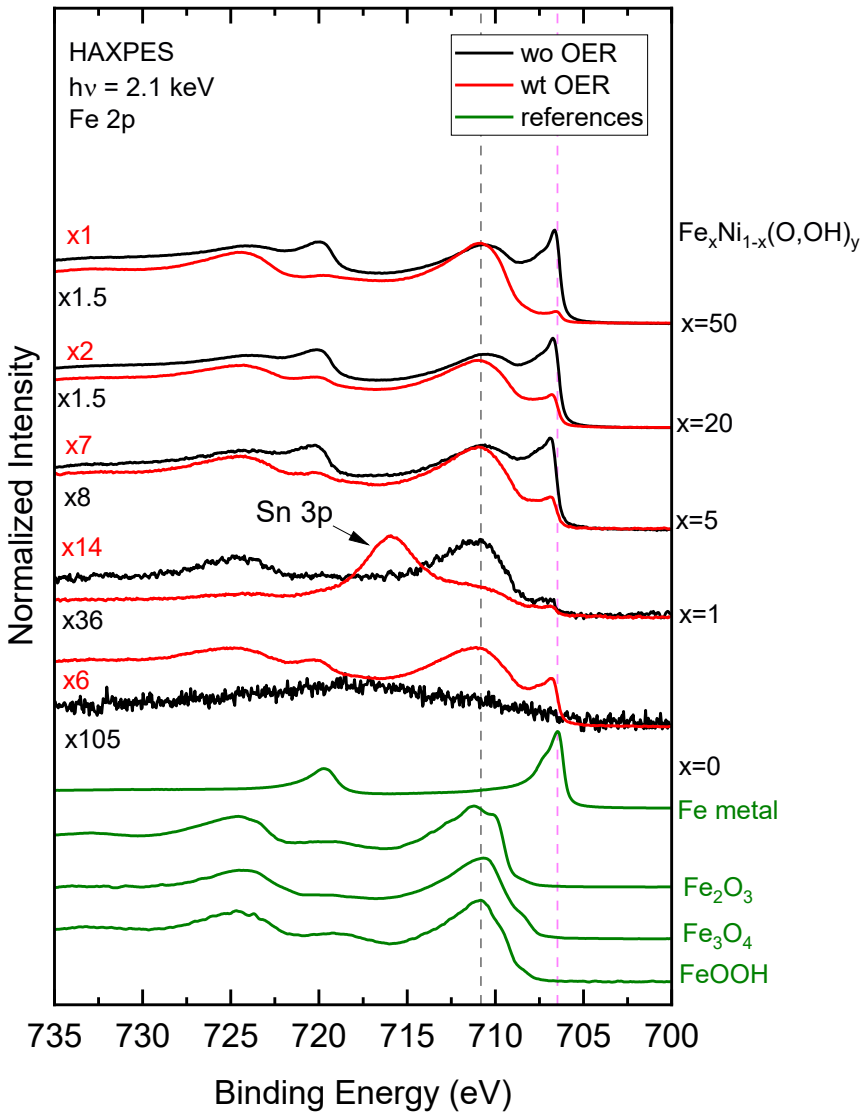

Figure 37: Fe 2p HAXPES spectra measured at 2.1 keV. Samples before (black) and after (red) overlaid and compared with the spectra of some known references (green). Spectra have been normalized and scaled to the intensity of the Fe 2p$_{3/2}$ peak of x=50, wt OER sample, for uniform comparison of signal intensity across all samples. Sn 3p signal is visible in the x=1, wt OER sample.

At low Fe contents such as x=1 and x=5, the intensity of the Fe 2p spectra becomes more pronounced after OER, primarily due to the growth of the broad peak centered at ~710.6 eV, associated with more oxidized species. This is indication that the Fe on the surface becomes more oxidized upon electrochemical cycling. At the same time, for both low and intermediate Fe contents such as x=20, with the increase in intensity of the oxide-like peak, the metallic peak is attenuated, but not completely eliminated, suggesting that while the surface transitions into more oxide-related species, some of the iron remains reduced.

However, this observation varies for different compositions: for x = 5, 20, and 50, the metallic peak diminishes post-OER, while for x=0 and to some extent for x=1, an increase in the signal representing

metallic Fe is observed, suggesting differential behavior of electrons on the surface depending on the nominal amount of Fe present in the samples. Additionally, the x=1, wt OER sample shows a significant Sn 3p peak which is likely an artefact of sample preparation and can contribute to the evolution of the spectra post OER. The coexistence of Fe, Fe^{2+} and Fe^{3+}-like signals suggests a chemically heterogeneous surface, potentially involving Fe-O-Ni bridging environments that arise from local coordination with Ni centers in the mixed-metal hydroxide, which has been observed in other such materials[13,119].

For a qualitative assessment of the changes in surface Fe content, the spectra in Figure 37 were normalized with reference to the peak height of the Fe $2p_{3/2}$ signal of the x=50, wt OER sample. As a general trend, the as-prepared samples required larger scaling factors compared to their post-OER counterparts. Although not strictly followed across all compositions, this trend suggests an increase in the overall surface Fe signal after OER treatment, consistent with Fe enrichment at the surface.

A significant observation from the Fe 2p spectra in Figure 37 is the appearance of a clear Fe signal in the x=0 sample after OER, despite being a nominally pure Ni film. The signal is absent in the pre-OER sample, indicating that Fe might have been introduced during the electrochemical treatment. The most likely explanation is contamination from the reaction chamber, which might have retained Fe residues from the preparation of other Fe rich samples. A similar increase in Fe is also observed in the x=1 wt OER sample, suggesting that a similar phenomenon might have occurred in this case as well.

Similarly, the Ni 2p HAXPES spectra were also measured with an excitation energy of 2.1 keV and are shown in Figure 38. The Ni $2p_{3/2}$ region in the pre OER samples is dominated by a sharp peak at ~852.4 eV, characteristic of metallic Ni, as can be seen from spectrum of the Ni metal reference (denoted by the gray dashed line). After OER treatment, a distinct shoulder at ~855.5 eV emerges and grows in intensity with increasing Fe content. This feature aligns with the peak observed in the NiO reference spectrum, digitized from ref[121] (marked with purple dashed line), indicating progressive oxidation of the Ni species on the surface, post OER.

An exception to this trend is the x=1, wo OER sample, where this feature is already present in the pre-OER spectrum. When viewed together with the Fe 2p spectra of the same sample showing a significant shoulder representing oxide-like characters even pre OER, it can be deduced that this particular sample and composition may follow an evolutionary pathway that might be distinctly different from the others. Even though the reason for such behavior remains unclear, the correlated observations point towards an unusual distribution of electrons on the surface.

At higher Fe contents, the peak at ~855.5 eV, such as in x=20 and x=50 is present in low intensity in the samples wo OER and increases significantly for those wt OER, indicating that with or without OER treatment, increasing the Fe content in the samples increases oxidation of Ni, and OER enhances and supports this oxidation further. Furthermore, the coexistence of the two features implies that the Ni species exist in a mixed valence state on the surface of the catalysts.

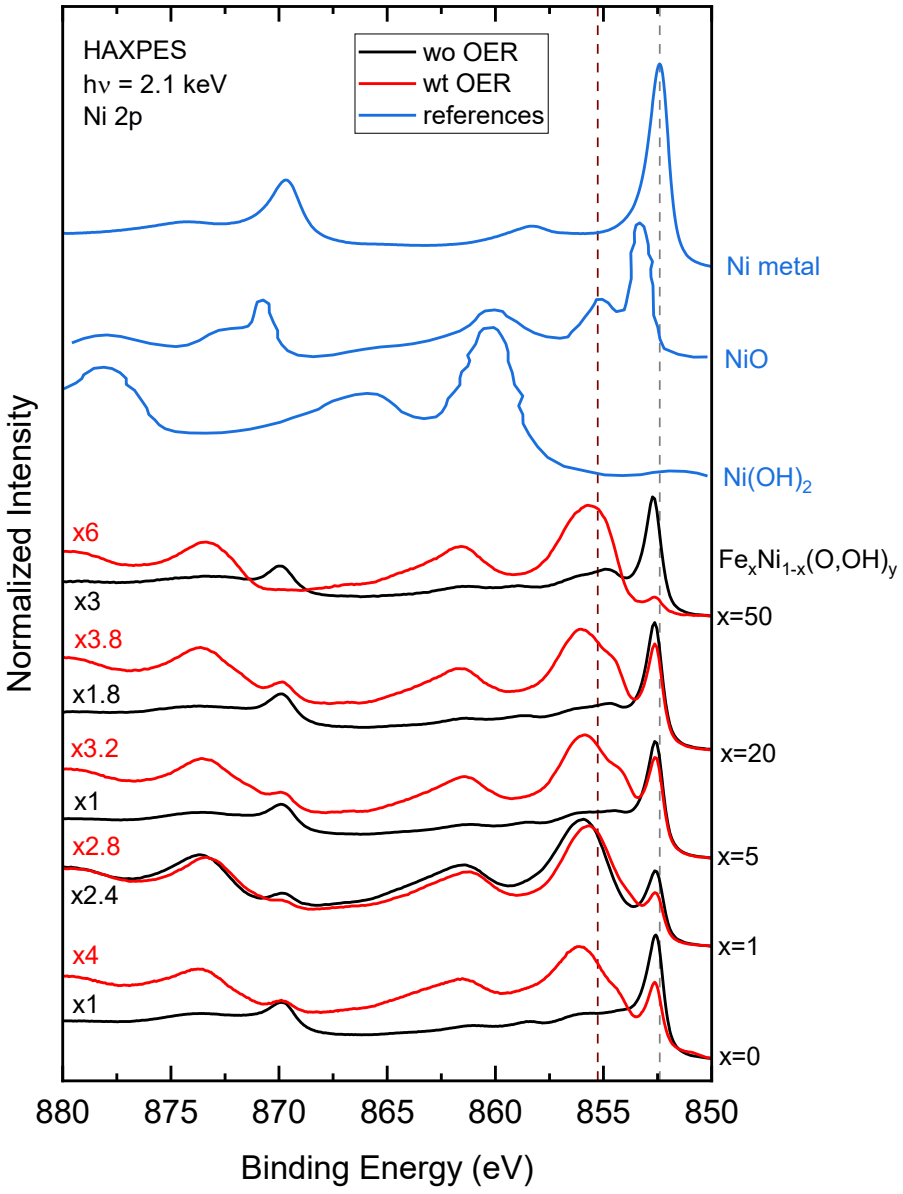

Figure 38: Ni 2p HAXPES spectra of the FeNiOOH thin films, before (black) and after (red) OER treatment, compared with spectra of known references such as NiO, $Ni(OH)_2$ and Ni metal, shown in blue. Spectra have been normalized and scaled to the intensity of the Ni $2p_{3/2}$ peak of x=50, wt OER sample, for uniform comparison of signal intensity across all samples. The NiO and the $Ni(OH)_2$ spectra have been digitized from ref[123] and ref[122] respectively.

To assess the relative changes occurring on the surface of Ni with respect to OER treatment, as was done for Fe, the Ni 2p spectra in Figure 38 were normalized to the intensity of x=0, wo OER. Compared to the as-prepared samples, post-OER spectra consistently required higher scaling factors, indicating a relative attenuation of the overall Ni signal at the surface.

This trend is generally attributed to Ni leaching, surface Fe enrichment, or a combination of both mechanisms that have been reported in Fe-Ni OER systems using techniques such as XPS, HAXPES, and in situ spectroscopies[13,162,163]. For instance, studies have demonstrated Fe segregation to the

surface during OER, accompanied by a decrease in Ni signal intensity, suggesting surface reorganization and compositional changes[13,162,163].

Figure 39 presents a comparative analysis of the relative scaling factors used to normalize the Fe 2p (a) and Ni 2p (b) spectra across the sample set. As mentioned earlier, the scaling factors were determined through manual normalization, aligning the dominant spectral features across compositions to enable a qualitative comparison. This is a commonly employed approach in analysis of XPS spectra, to facilitate the variation of relative intensities across different samples with similar compositions[164,165].

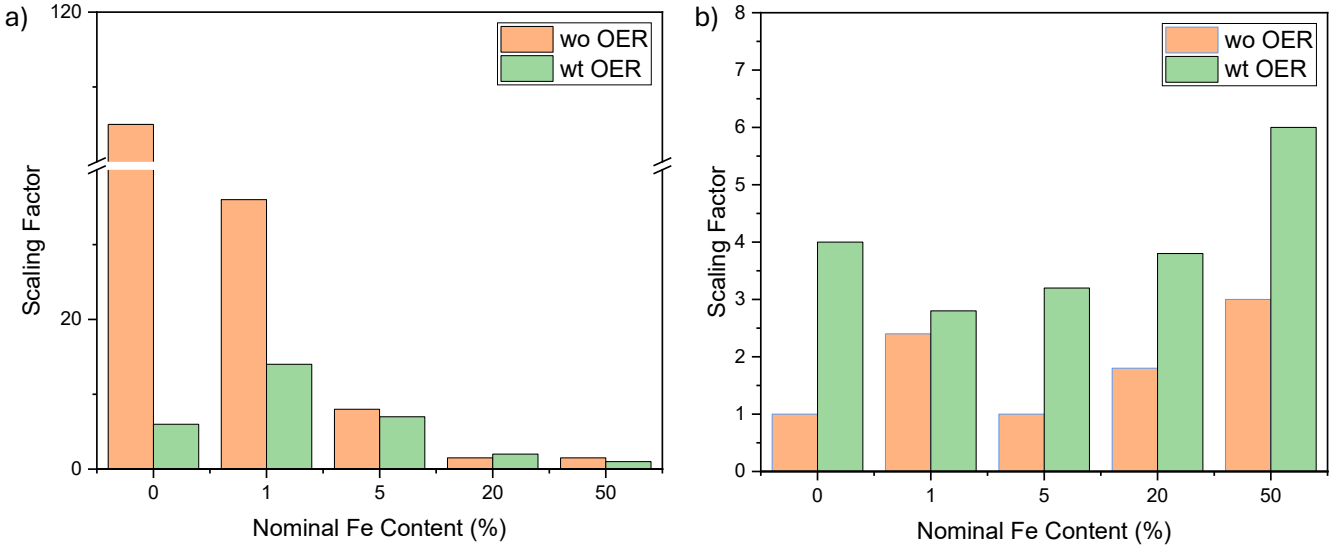

Figure 39: The relative scaling factors plotted as a function of composition for (a) Fe 2p core level and (b) Ni 2p core level. The orange bars denote the scaling factors for the samples wo OER and the green bars denote the scaling factors for the samples wt oer. For Fe 2p, the scaling factor is larger before OER as a general trend. While for Ni 2p, the scaling factors are larger after OER.

For Fe 2p, the samples wo OER generally required larger scaling factors than their post OER counterparts, consistent with an overall trend of surface Fe enrichment following electrochemical treatment. In the case of Ni 2p, the trend is reversed: post OER samples consistently higher scaling factors, indicating a relative attenuation of the Ni signal after OER. This implies that changes on the surface occur post OER, induced by the OER itself, wherein the surface becomes more Fe rich.

5.2 Quantitative surface composition from background-corrected HAXPES

The scaling factor approach explored in Section 5.1 provides a useful qualitative estimation for the comparison of Fe and Ni signals on the surface and helped form a preliminary hypothesis regarding the effect of OER on the samples. However, the interpretation of the analysis is inherently limited by the significant and complex background present in all Fe and Ni spectra alike. Without accounting for the inelastic scattering, the peak intensities cannot be accurately estimated, making it difficult to draw conclusive quantitative inferences. To address this, a more rigorous analysis was carried out using background corrected spectra.

Tougaard background subtraction was applied to the Fe 2p and Ni 2p spectra, to isolate the photoemission signal from the surrounding inelastic loss structure.

The background was calculated using the QUASES-Tougaard software[111], employing material-specific reflection electron energy loss spectra (REELS) to model inelastic scattering more accurately. REELS data for NiO and Fe_2O_3, measured at a kinetic energy of 2000 eV and obtained from literature sources[166,167], were used to develop tailored backgrounds for each spectrum. These materials were chosen as representative oxides for Fe and Ni, as their inelastic scattering characteristics are supposed to bear close resemblance to those expected in the mixed metal oxide environment of the samples. In contrast, using metallic Fe or Ni, or only mixed-valence compounds like Fe_3O_4, would reflect the energy loss behavior insufficiently. This method offers a physically realistic representation of energy loss, arising from the spectral complexity caused by overlapping features and consistent multiplet splitting.

The four plots in Figure 40 show the Fe 2p and Ni 2p HAXPES spectra of $Fe_xNi_{1-x}(O,OH)_y$ samples, with x=20, before (a and b) and after (c and d) OER.

In each case, the raw spectrum (red) is shown with the inelastic background (blue), calculated using the QUASES Tougaard software. The region shaded in grey between the spectrum and the background is the area considered for quantitative analysis.

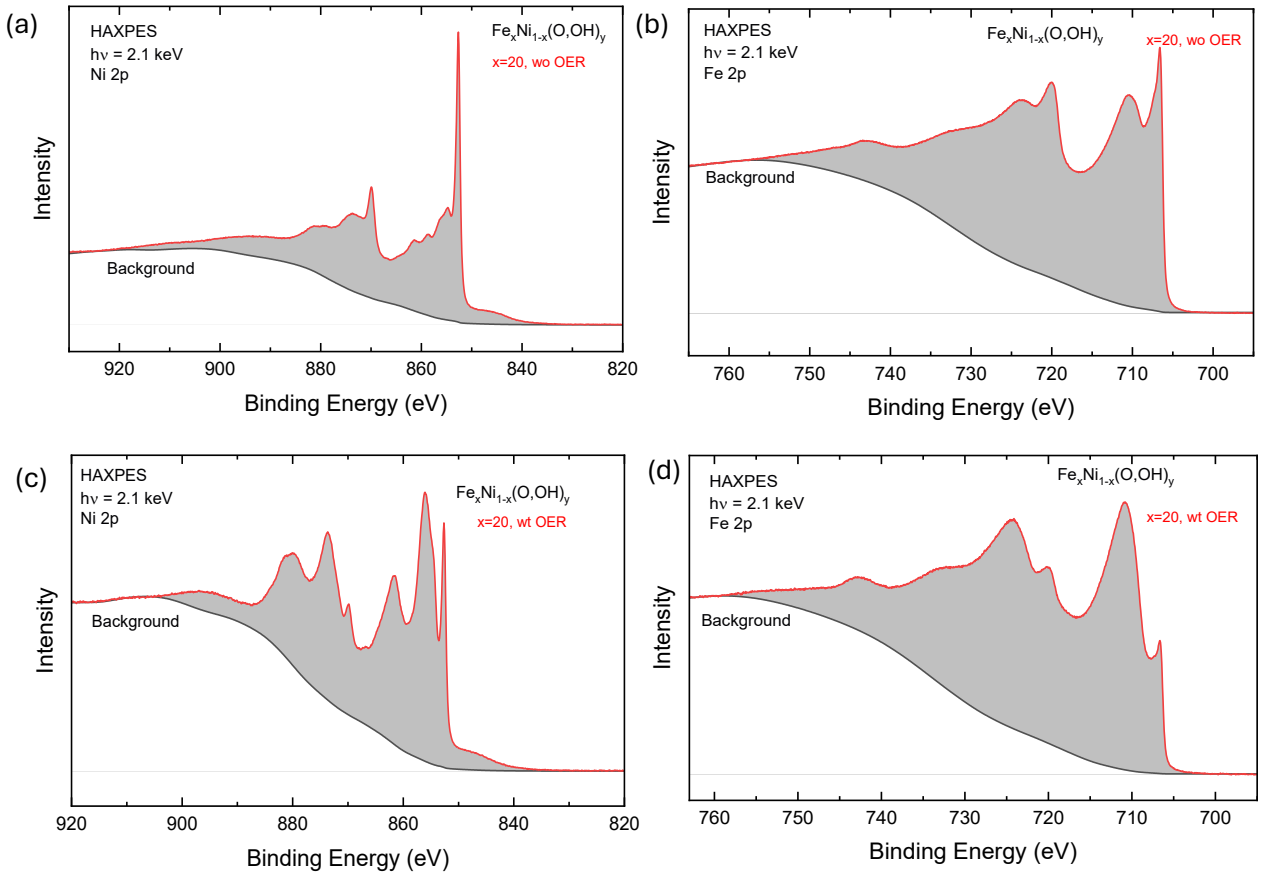

Figure 40: Background subtracted HAXPES spectra of Ni 2p (a) and (c) and Fe 2p (b) and (d) regions for $Fe_xNi_{1-x}(O,OH)_y$, x=20 before and after OER. The background was modeled using REELS-derived Tougaard functions for Fe_2O_3 and NiO, and the regions shaded in grey indicate the area used for analysis of the intensity.

The shaded region of all four spectra were numerically integrated to obtain the total Fe and Ni photoemission intensities. These background-subtracted intensities were then used to calculate the Fe:Ni ratio at the surface for each composition in the series, before and after OER. These ratios are then plotted as a function of nominal Fe content, which then is interpreted to gauge the degree of surface compositional changes induced by OER. The results from this analysis provide strong support to the conclusions obtained from the qualitative analysis with the help of scaling factors.

Figure 41 shows the ratios plotted for the with (red) and without (black) OER samples. To obtain these values, the integrated intensities of the Fe and Ni $2p_{3/2}$ peaks were converted to stoichiometric values, using a relation derived from Fermi's golden rule[168], described in Chapter 2. It is as follows:

$$I \sim \sigma N \lambda(E) T(E) \qquad (2.4)$$

Where I is the measured photoemission intensity, N is the atomic number density, σ is the photoionization cross-section, λ(E) is the inelastic mean free path, and T(E) is the instrumental transmission function. While λ(E) and T(E) are held constant under nominally identical experimental conditions, synchrotron-based setups such as X-SPEC require additional consideration of the

angular distribution of emitted photoelectrons. As such, observed surface intensities are influenced not only by the elemental cross-sections but also by angular-dependent terms in the photoemission process, including asymmetry parameters and measurement geometry.

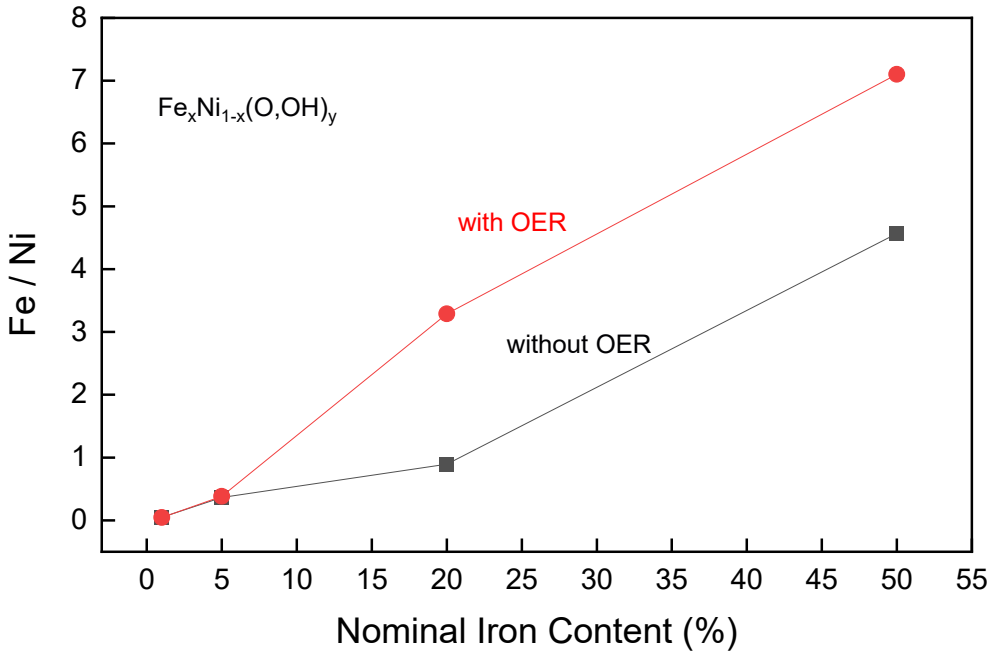

Figure 41: Estimated Fe:Ni surface ratios derived from background-corrected Fe and Ni $2p_{3/2}$ spectra using the respective photoionization cross-sections. The ratios are plotted in red for the samples with OER and in black for the samples without OER.

As explained in Chapter 2, the relative surface concentrations of two elements, A and B, can be estimated using the simplified relation:

$$\frac{N_A}{N_B} = \frac{I_A/\sigma_A}{I_B/\sigma_B} \tag{2.6}$$

where *I* is the measured photoemission intensity, and σ is the literature-based photoionization cross-section. This model assumes uniform distribution within the analysis depth and neglects effects that might potentially arise from surface segregation, contamination, and matrix-induced attenuation. Under these assumptions, particularly valid for comparisons made at similar kinetic energies and under identical measurement conditions T is rendered effectively constant for both Fe and Ni. While minor variations in inelastic mean free paths cannot be completely ruled out, they are not expected to significantly alter the relative intensities. The Fe:Ni ratio provides a quantitative measure of surface composition.

Figure 41 shows the Fe:Ni surface atomic ratio across the samples series as a function of Fe content and electrochemical treatment, namely OER, calculated from the background-corrected Fe and Ni 2p spectra taking into account the photoionization cross sections obtained from literature[44].

The results from both the scaling factor approach and the more quantitative stoichiometric analysis of the Fe and Ni 2p core level spectra confirm that Fe becomes more prominent at the surface after OER treatment. This observation is consistent with a reorganization of the surface species during electrochemical activation[13,14,169,170]. However, it should be emphasized that increase in the Fe content at the surface does not linearly corelate with increased catalytic performance, as seen from Figure 42 below[91]. The highest catalytic activity occurs within the compositional window of 10-20 at. % Fe, peaking at x=20.

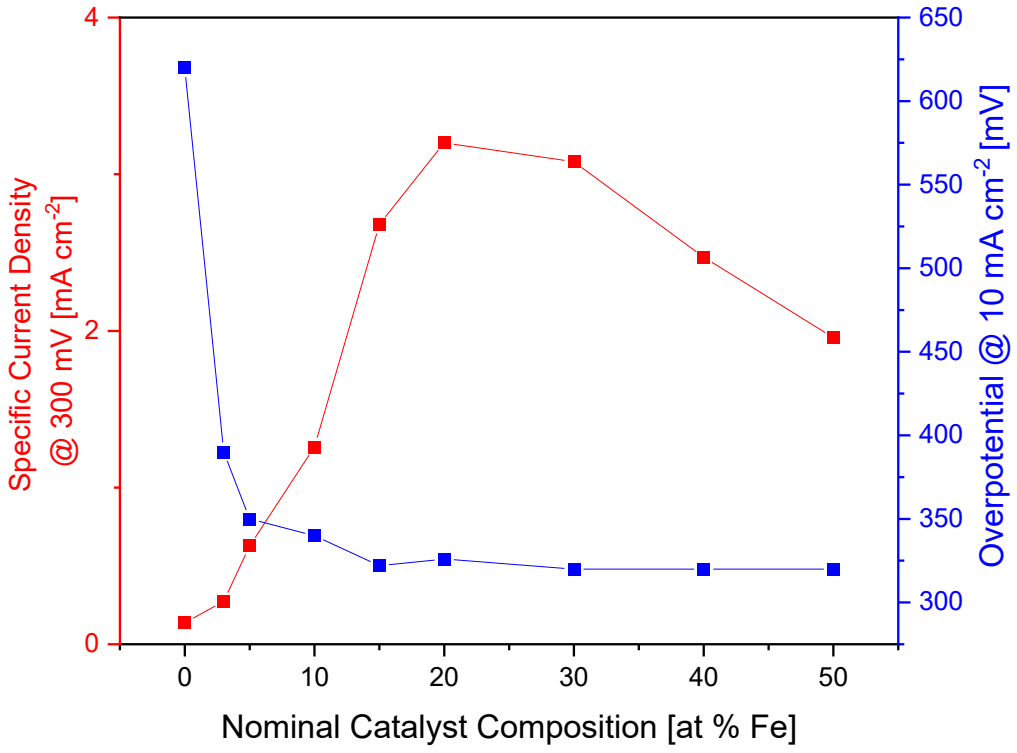

Figure 42: Specific activity and overpotential of $Fe_xNi_{1-x}(O,OH)_y$ electrocatalysts as a function of nominal Fe content. The red curve shows the specific current density measured at 300 mV overpotential, while the blue curve represents the overpotential required to reach 10 mA cm $^{-2}$. The plot was obtained from ref.[91]

Beyond this window, further addition of Fe causes a decline in catalytic activity. The electrochemical measurements shown in Figure 42 were conducted in collaboration with Daneshpour et.al[91] at the Penn State University and have been included here to correlate spectroscopic trends with catalytic performance.

Importantly, even in the as-prepared samples studied as a function of Fe content in Chapter 4, this very compositional window was seen to stand out due to consistent indications of chemical and electronic reorganization seen from the two component fits performed for Fe and Ni 2p core level spectra. Following OER, the same window continues to show distinct changes in the chemical environments, not only in terms of surface modifications but also in its correlation with increased catalytic activity.

5.3 Fe and Ni coordination: complementary information from L-edge XAS

To build on the insights obtained from the HAXPES measurements, the FeNiOOH electrocatalysts are further explored using soft X-ray absorption spectroscopy (XAS) at the Fe and Ni $L_{2,3}$-edges. While HAXPES provided surface-sensitive information about changes in Fe and Ni content following OER, L-edge XAS offers complementary information which is element specific in its sensitivity to oxidation states, crystal field effects and the extent of 2p-3d hybridization, which as stated in Chapter 4, are crucial to understanding the catalytic activity of the samples.

In this section, both pre- and post-OER states of the catalysts are analyzed.

Figure 43 shows the Fe $L_{2,3}$-edge XAS spectra measured in total electron yield (TEY) mode for the FeNiOOH samples before and after OER shown in black and red respectively. Two key features are observed at the L_3 edge, labeled A (~708.5 eV) and B (~710.5 eV), which are associated with Fe $2p_{3/2} \rightarrow 3d$ transitions. Peak A is generally assigned to Fe^{2+} or mixed-valence states in relatively weak or symmetric ligand fields, while peak B is more indicative of Fe^{3+} species in stronger crystal fields, particularly those with distorted octahedral coordination[145]. These assignments are supported by comparisons to reference compounds (top panel), where Fe^{2+}-rich environments (e.g., FeO, Fe_3O_4) show dominant peak A, while Fe^{3+} references (Fe_2O_3, FeOOH) exhibit more pronounced peak B.

Upon close observation of the TEY spectra of the samples, several trends were observed across the sample series. For x=1, both peaks A and B decrease in intensity after OER, implying dampening of the spectral signature. This reflects an altered coordination environment for Fe post-OER. For x=5, peak A increases while B decreases upon OER, suggesting a partial reduction of the Fe center. Contrarily, for x=20 and 50, A is suppressed and B intensifies post OER, indicating a greater degree of surface oxidation. These trends are highlighted with the help of red arrows, their direction indicating the direction of change of intensity of features A and B.

These observations are consistent with the trends described in Chapter 4, where the energy separation between A and B was interpreted as a measure of crystal field splitting. The increase in B relative to A at higher Fe content and after OER suggests oxidation, as well as a shift in ligand symmetry and coordination strength at the surface. Peak B, corresponding to transitions into e_g orbitals in an octahedral field[23,136,171] , becomes more prominent with increased Fe^{3+} character and strength of ligand field.

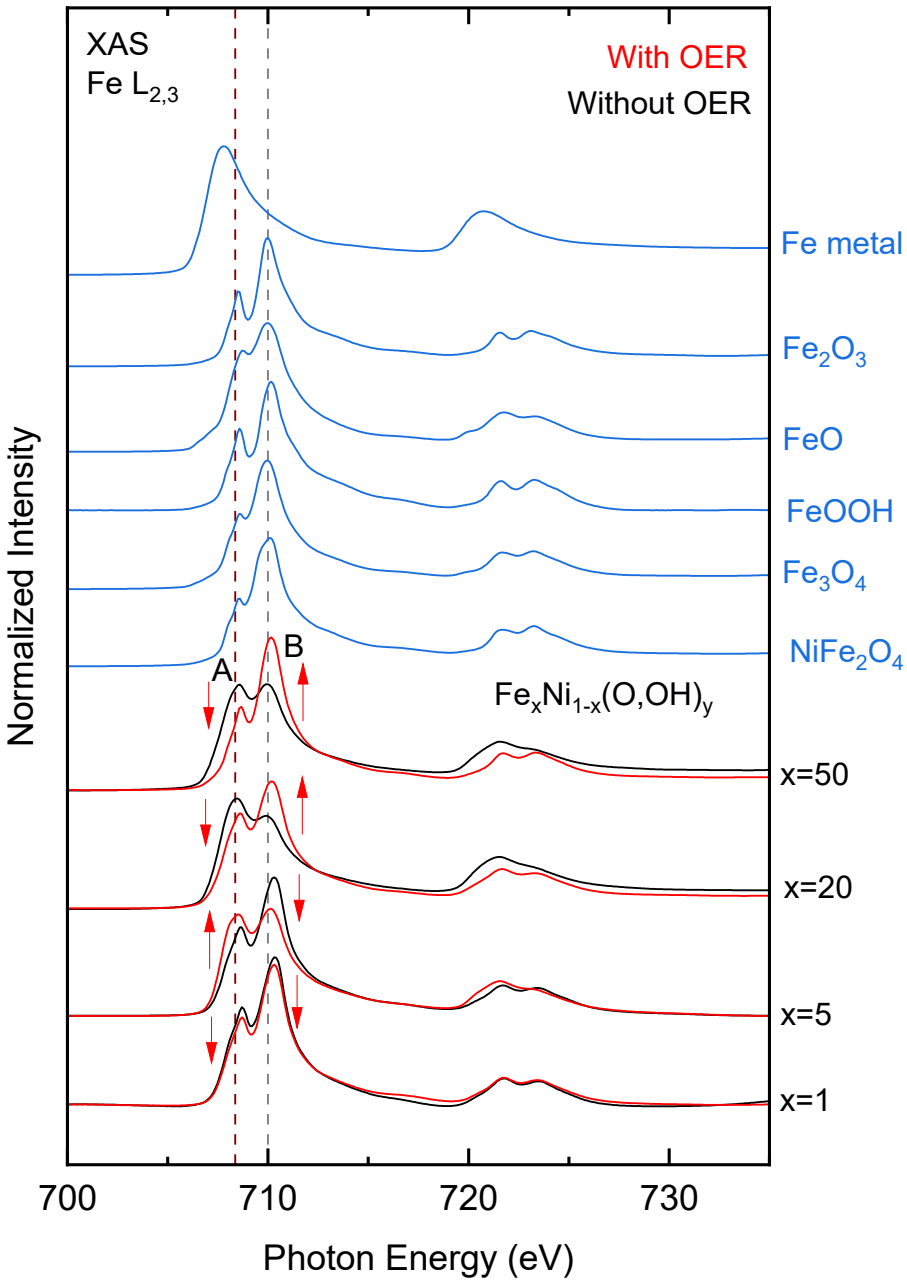

Figure 43: Fe $L_{2,3}$ XAS spectra collected in TEY mode for samples wo and wt OER, shown in black and red respectively. The spectra of certain reference compounds are shown in blue alongside that of the samples for comparison. Red arrows indicate the direction of increase or decrease of features A and B of the spectra wt OER.

Although the trend is not monotonic with respect to the Fe content of the samples, a pattern can be identified: surface Fe undergoes non-uniform but composition-dependent reorganization after OER, with x=20 standing out as the composition where peak B is most enhanced post-OER relative to its intensity before OER. This indicated surface oxidation and when correlated with the activity of catalyst compositions shown in Figure 42, x=20 shows catalytically relevant configuration.

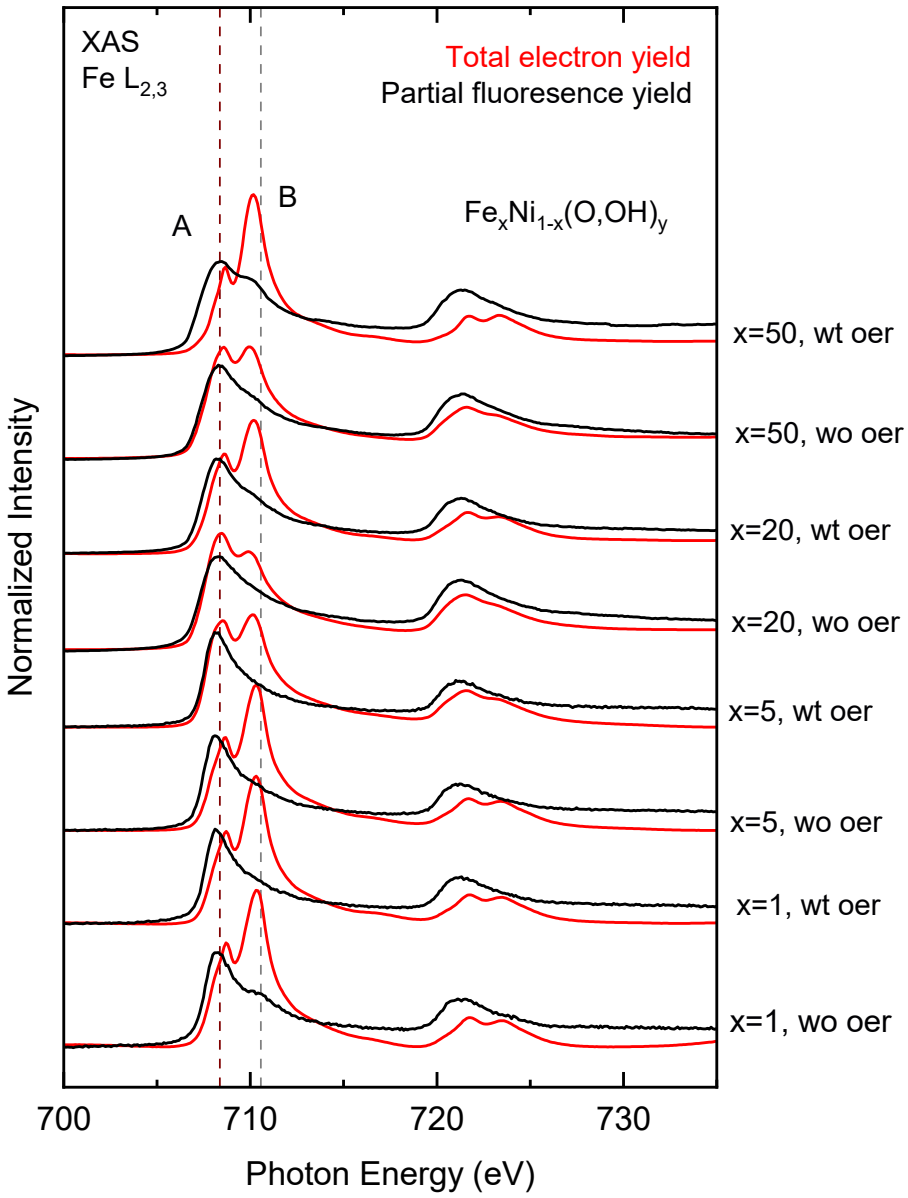

Figure 44: Fe $L_{2,3}$ XAS spectra of the FeNiOOH samples, collected in TEY (red) and PFY (black) modes. The spectra are compared for the pre and post OER samples. The TEY and PFY spectra of each sample have been overlaid to track the differences.

Figure 44 compares Fe $L_{2,3}$-edge XAS spectra acquired in total electron yield (TEY) and partial fluorescence yield (PFY) modes for the samples with and without OER, enabling a depth-resolved view of the electronic structure across the $Fe_xNi_{1-x}(O,OH)_y$ sample series. The nature of Fe on the surface has already been discussed as revealed by the TEY spectra and previously by the HAXPES spectra in Section 5.1 and Section 5.2. The following section investigates the bulk of the samples.

It is observed that the TEY spectra exhibit pronounced changes after OER, particularly in the relative intensity of peaks A (~708.5 eV) and B (~710.5 eV), reflecting surface oxidation and ligand field modifications. In contrast, the PFY spectra remain mostly unchanged across OER treatment and

composition, indicating that the bulk Fe environment is comparatively stable and largely unaffected by the reorganization caused at the surface by the electrochemical reactions.

However, subtle exceptions emerge. In the x=1, wo OER sample, PFY shows a faint shoulder at higher energies, indicating some level of oxidation. This is significant as x=1, wo OER has shown unexpected behavior earlier as well. Similarly, the PFY spectra of x=50, wt OER also shows a slight shoulder in the higher energy region. This could indicate that as Fe content is increased beyond a certain point, oxidation could affect more than just the surface of the electrocatalyst.

These isolated alterations in the PFY spectra highlight that while electrochemical activation primarily affects the surface, it can influence deeper into the bulk depending on composition, especially at the extremes.

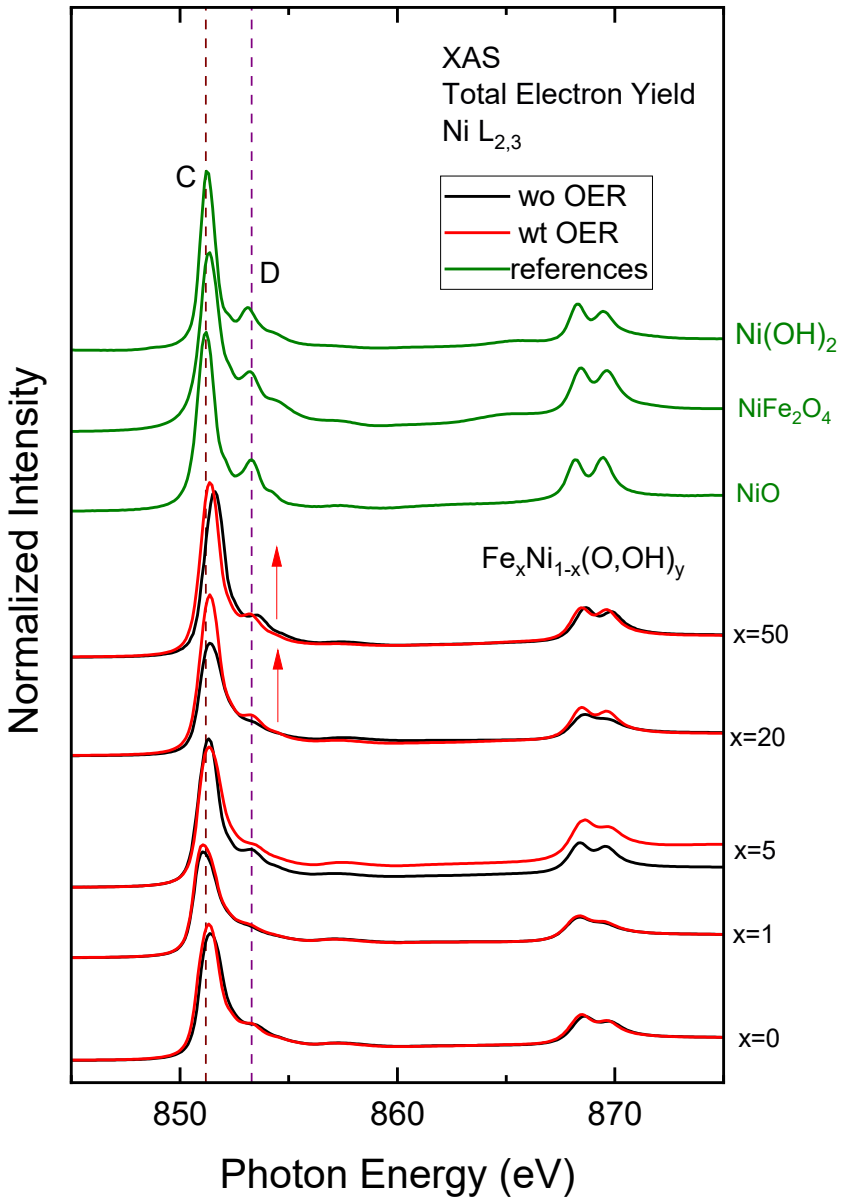

Figure 45: Ni $L_{2,3}$ spectra of the FeNiOOH samples in TEY mode, for samples before (black) and after (red) OER. The spectra of some known references are shown in green for comparison. Red arrows indicate the relative increase of peak D with respect to peak C in the spectra wt OER for samples x=20 and x=50.

Figure 45 shows the Ni $L_{2,3}$ XAS spectra in the TEY mode for the FeNiOOH electrocatalysts for the samples wo and wt OER, shown in black and red respectively. The spectra of some known references are shown in green for comparison. The spectra display two key features, C (~852.6 eV) and D (~855.0 eV) marked by dashed lines, corresponding to multiplet structures arising from Ni $2p_{3/2}$ → 3d transitions. In the x=0 and x=1 samples, the L_3 edge is dominated by peak C, with minimal intensity at D, indicating a greater unoxidized or metallic nature[157] both before and after OER, with only slight increase in spectral intensity at peak C post OER.

Upon Fe incorporation and subsequent OER treatment, distinct changes are observed. In particular, x=20 and x=50 post-OER samples show an increase in the intensity of peak D relative to C, as indicated by red arrows in Figure 45. This suggests partial oxidation of Ni and the formation of Ni^{2+} states. The evolution of the L_3 edge from a C-dominant to a more balanced C/D intensity profile supports the hypothesis that Fe incorporation facilitates electronic and structural modifications of the Ni site during OER. This reordering does not create pure Ni^{2+} oxidation states, but a more mixed state, influenced by Fe–O–Ni interactions and dynamic oxidation processes[15,87,172,173].

Figure 46 shows the TEY and PFY spectra of each sample overlaid with each other for comparison of changes at the surface and in the bulk, as a function of OER. In all compositions, TEY spectra exhibit more pronounced changes than PFY, confirming that electrochemical reorganization is confined to the surface. In the x=0 sample, both TEY and PFY spectra remain nearly identical before and after OER, indicating that without Fe, Ni remains mostly unaltered both at the surface and within the bulk, as seen in Figure 45. For x=1 and x=5, subtle changes appear in TEY, particularly around peak D (~855 eV), while PFY remains relatively constant, reflecting surface related modifications.

At higher Fe contents, in contrast to the TEY spectra, whose changes have already been discussed, the PFY spectra show little change. Across the series, the depth-resolved XAS data confirm that while Ni undergoes structural adaptation in response to Fe incorporation and OER treatment, these changes are mostly localized to the surface of the catalyst and diminish toward the bulk. These observations are quite contrasting to those from the as-prepared samples in Chapter 4, where very little difference could be noted between the TEY and PFY spectra of the Ni $L_{2,3}$ spectra.

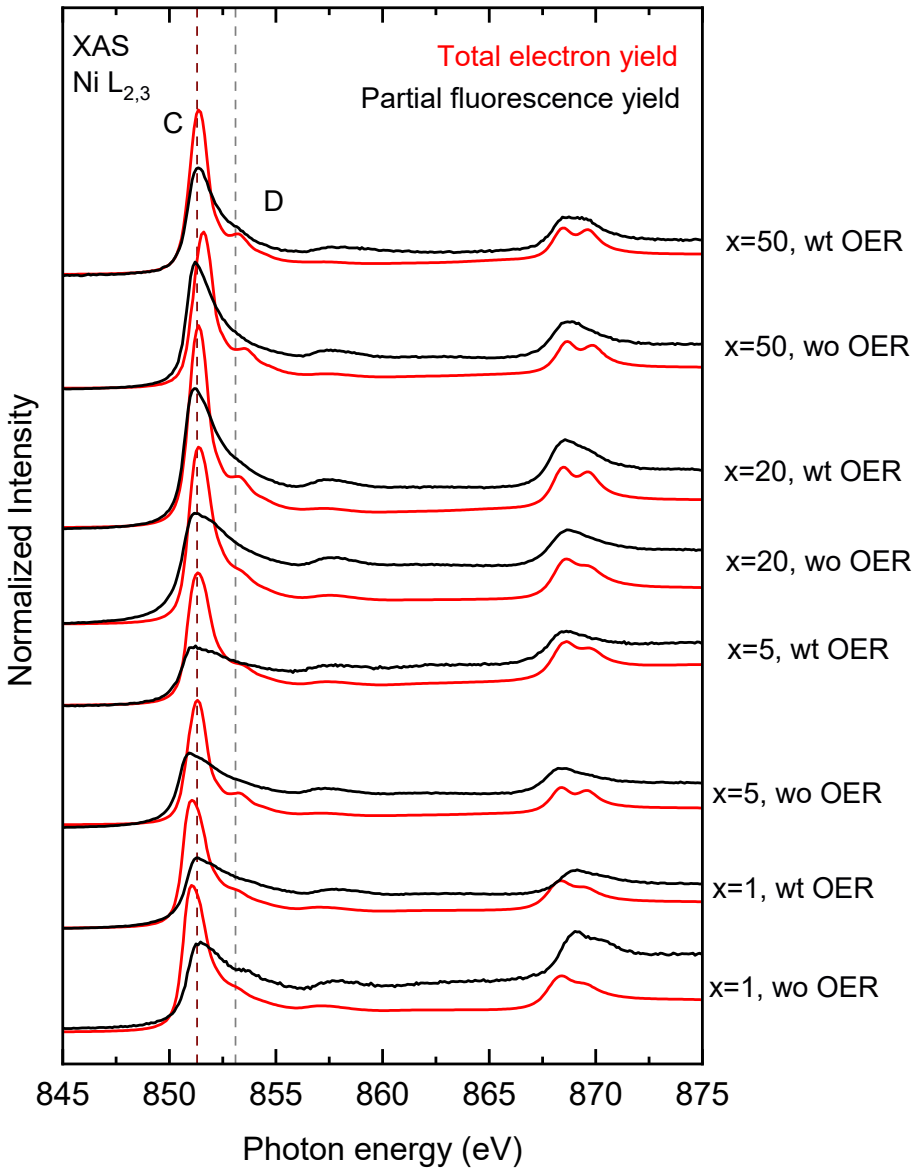

Figure 46: Ni $L_{2,3}$-edge XAS spectra of $Fe_xNi_{1-x}(O,OH)_y$ samples collected in total electron yield (TEY, red) and partial fluorescence yield (PFY, black) modes before and after OER.

5.4 Evolution of the oxygen electronic structure across catalyst states

After examining the behavior of the transition metals across the surface and bulk of the $Fe_xNi_{1-x}(O,OH)_y$ system, the next step is to understand the role of oxygen in shaping the electronic structure of the catalyst. Oxygen is not merely a passive ligand but plays an active role in tuning and stabilizing the electronic configuration of the metal centers[124,125]. This section therefore continues the evaluation of the O 1s core level spectra, whose presence has already been noted from the HAXPES survey spectra shown in Figure 36.

Figure 47 shows the O 1s HAXPES spectra for the samples with (red) and without (black) OER. The spectra reveal two distinct features across all samples indicating the presence of at least two distinctly different chemical environments. The peak centered around 529.5–530 eV is attributed to oxides[126,127,174], while the broader peak at 531–532.5 eV aligns with the presence of hydroxide species[126,127,174]. The as-prepared samples discussed in Chapter 4 exhibited a pronounced feature near ~533 eV across all compositions, consistent with adsorbed surface water. While the intensity of this high binding energy component decreases after OER, it remains significant in both wo and wt samples shown in Figure 47.

Across the sample series, a general increase in the overall intensity of the O 1s spectra is observed from x=5 to x=50 post OER, both in the higher and lower binding energy regions. This trend is consistent with increased oxygen incorporation and the established fact that increasing Fe content leads to greater surface oxidation. Sample x=0 also shows a similar increase after OER. However, sample x=1 behaves conversely, the intensity of both oxide and hydroxide components diminish after OER, deviating from the pattern seen in the rest of the samples. As previously noted in the analysis of Fe and Ni centers, x=1 shows consistent outlying behavior, suggesting the occurrence of additional or different phenomena in this specific sample.

The varied nature of the O 1s spectra thus warrants for a more rigorous, quantitative investigation, explored in the following sections.

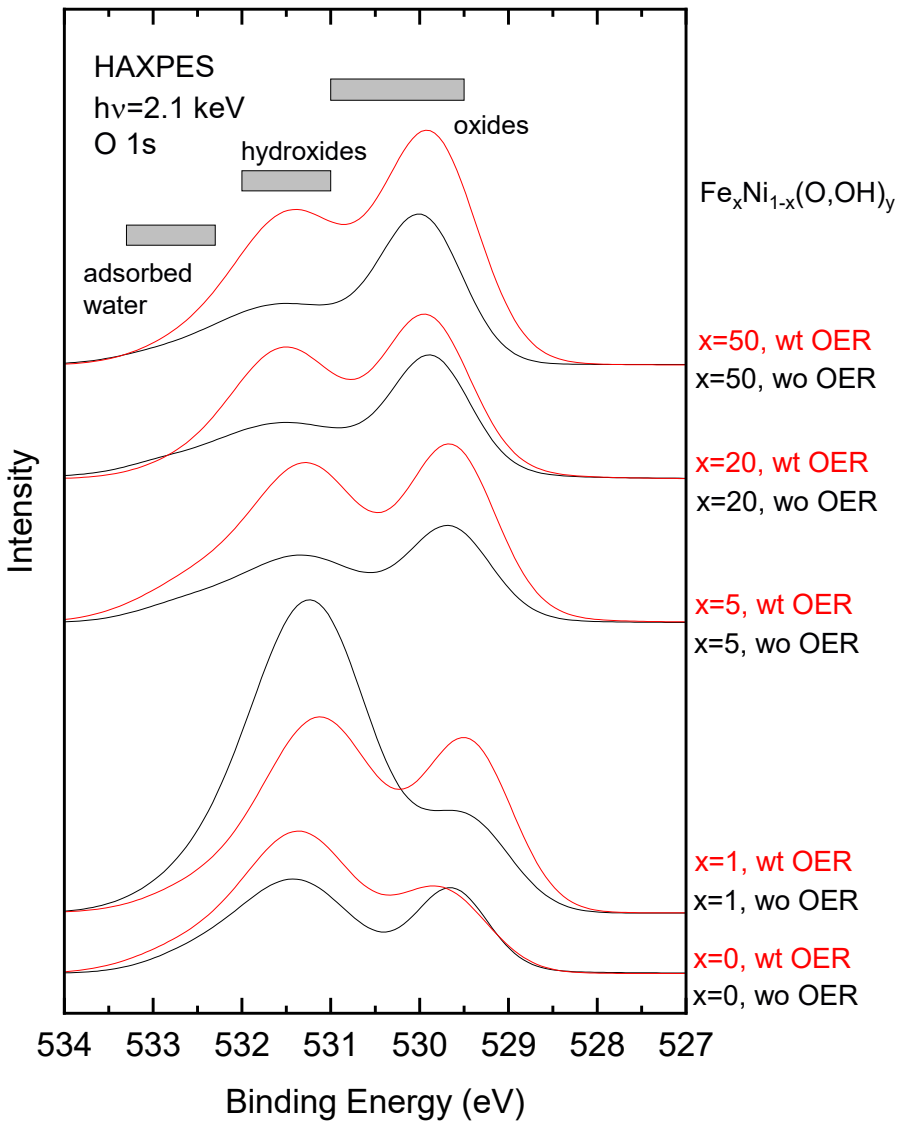

Figure 47: O 1s HAXPES spectra for all compositions before (black) and after (red) OER, showing the evolution of surface oxygen species. Two main peaks corresponding to oxide and hydroxide environments are clearly visible across all samples.

To assess the evolution of oxygen chemical environments quantitatively across the sample series, the O 1s HAXPES spectra were analyzed using a refined fitting approach, accounting for the differences in observed surface chemistry before and after OER. Each spectrum was modelled using Voigt profiles corresponding to distinct oxygen species, namely, oxide, which was centered around ~529.4 eV as a starting parameter, hydroxide, centered around ~531.2 eV for the samples without OER. These peak positions were based on literature values and served as starting parameters for the fits, but were not fixed, small adjustments were allowed within chemically reasonable ranges to account for the variations in sample composition and environment. Following OER, an additional intensity at higher binding energy (~532.5 eV) was observed, which has been attributed to surface

adsorbed species such as water. Therefore, a three-component model was used for the with OER samples, incorporating oxide, hydroxide, and this higher BE feature.

The parameters for the Voigt profile for the oxide peak, such as the Gaussian width and shape (inherently representing the Lorentzian width of the profile) were constrained globally across all samples to ensure consistency and reduce the number of variables for the fit. Contrastingly, the parameters for the hydroxide and adsorbed water components were allowed to vary freely to optimize the fits, enabling the model to account for their variable characteristics. The O-H bond is flexible and readily reorients itself via proton exchange, which can lead to variations in the local chemical environment[175,176]. These factors can contribute to the O 1s spectra in the form of peak broadening and asymmetry. Literature reports have attributed these observations to vibrational excitations and changing chemical environments[176,177].

Representative fit plots are shown in Figure 48(a) and (b) for the samples x=20, wo OER and x=20, wt OER respectively.

A linear background was allowed to fit along with the Voigt profiles, shown in yellow. The oxide component is shown in green, the hydroxide component is shown in blue and the third component used to account for the higher binding energy components is shown in purple. The fit sum plot is shown in red. The overall fit closely reproduces the experimental data, shown by black circles and the residuals shown in pink confirms the high quality of the fit throughout the energy window for the fit.

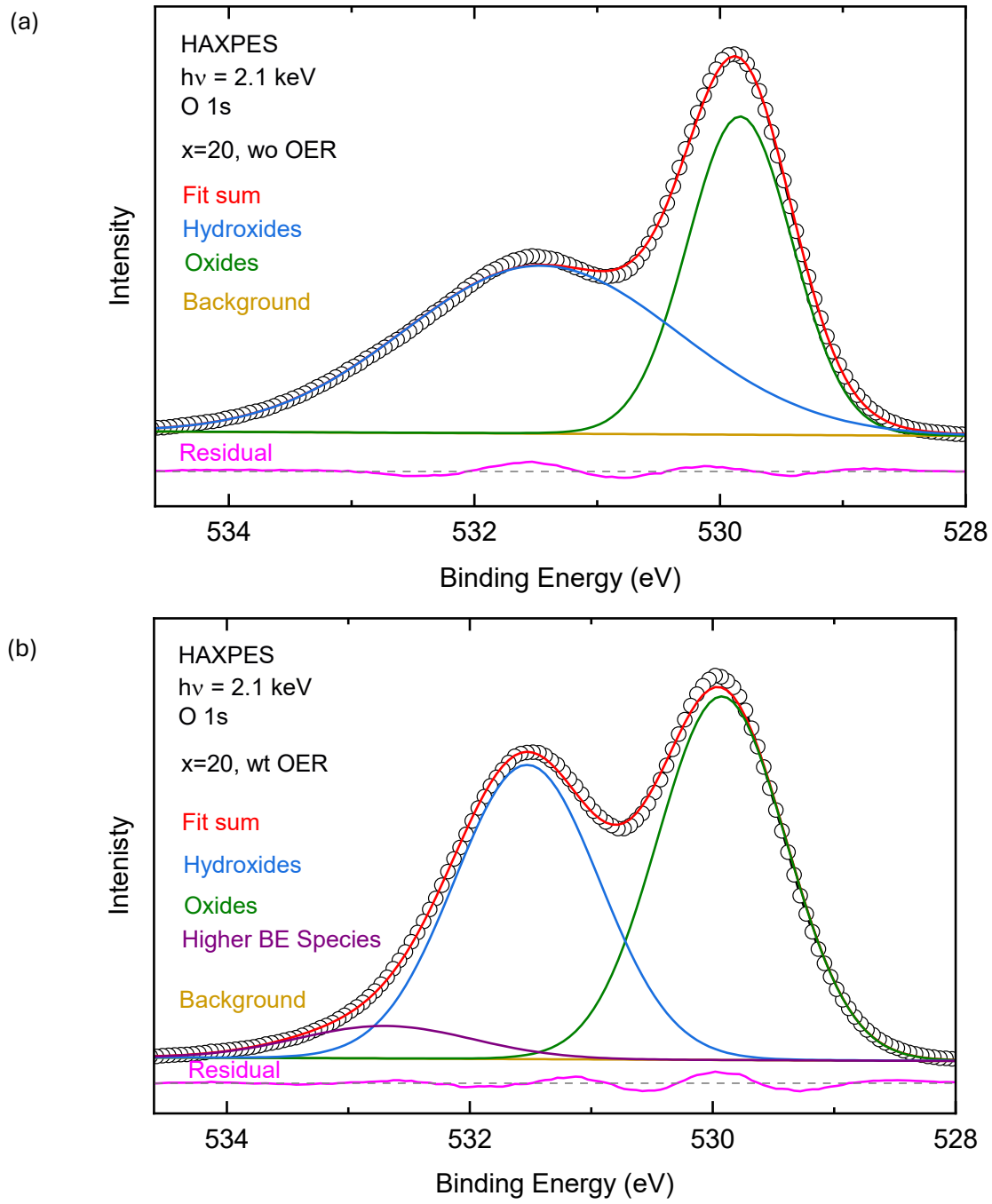

Figure 48: O 1s spectra of (a) x=20, wo OER and (b) x=20, wt OER fit with two and three Voigt profiles respectively, accounting for oxides (green), hydroxides (blue) and a profile dedicated to higher binding energy peaks (purple) in the sample wt OER which has been identified as surface absorbed water, which becomes a significant contributor post OER.

Figure 49 presents the results of the fits performed. For ease of understanding the changing trends in relative oxide and hydroxide contribution in the spectra, the changing oxide component relative to the complete O 1s signal as a function of nominal iron content and OER is shown, in orange for the data before OER and green for post OER.

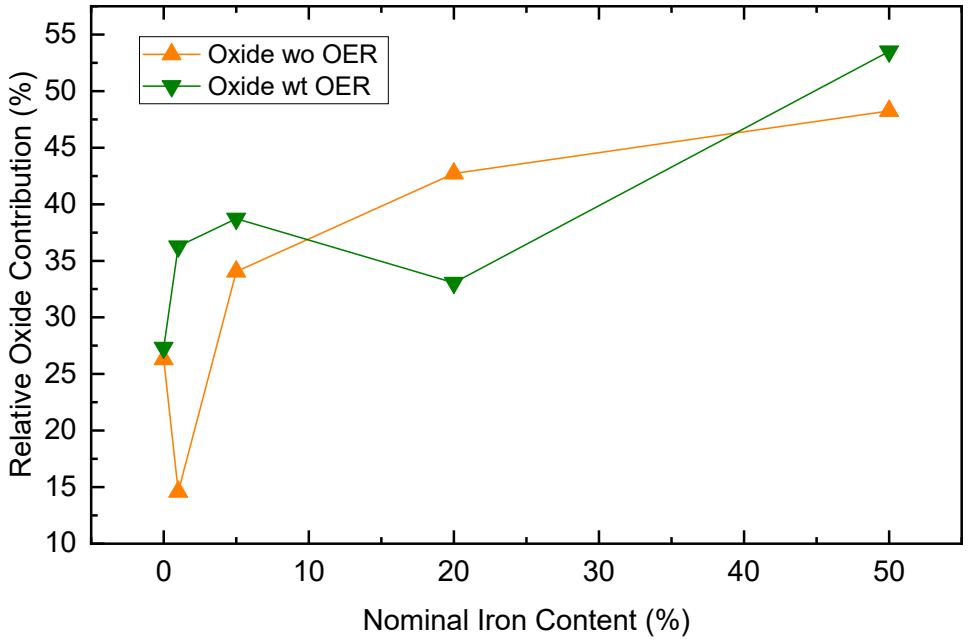

Figure 49: Contribution of the oxide component relative to the entire O 1s spectra. The contribution before OER is shown in orange and after OER is shown in green.

The data shows a nonlinear evolution of the oxide character as a function of Fe content and OER. At x=0, the oxide contribution is comparable before and after OER. For x=1, a sharp increase can be observed in the oxide fraction following OER. This increase can be attributed to the stabilizing nature of Fe, and its promotion of structural synergy between Fe, Ni and O, which has been pointed out in several sections before. Under OER conditions, Fe can stabilize higher oxidation states and promote the formation of oxide-like species, thereby shifting the balance from hydroxide towards oxide contributions. This highlights the unique sensitivity of the system to small amounts of Fe substitution, which plays a significant role in modifying the chemical environment of the surface during OER. At x=5, contributions from both states of the material converge, before the occurrence of an inflection point at x=20 again, where the oxide fraction before OER is significantly higher than the same before OER. This is indicative of consumption of existing oxide-like species on the surface under reaction conditions. As seen earlier, x=10-20 at. % Fe has emerged as the compositional window which is the most electrocatalytically active, as well as showing the most changes in terms of chemical and electronic structure of the transition metals, this phenomenon at x=20 reinforces that observation. At x=50 again, there is enhancement of oxide character post OER.

Therefore, there is no linear trend of changes in contribution from oxide and hydroxide like species, OER does appear to increase the oxide like species for samples in general, except for=20.

The observed patterns in changing hydroxide and oxide contribution to the whole spectra show that apart from the Fe content, OER also plays a significant role in determining the chemical environment of the oxygen species in the samples. Surface bound hydroxide groups are often directly involved in the reaction mechanism. The changes in hydroxide contribution relate directly to the catalytic ability of the electrocatalysts, as surface hydroxide groups act as intermediates during the OER reaction, in alkaline conditions. An increase in the oxide signal, hence corresponding decrease in the hydroxide contribution after OER could imply that some of the reactive species are consumed during the reaction, resulting in a less ordered surface. Contrarily, a decrease in the oxide signal might suggest that the surface becomes more hydroxide rich under operating conditions, possibly due to changes that expose more reactive sites.

5.5 Probing metal-oxygen interactions through O-K absorption

While O 1s HAXPES enables differentiation between surface-bound oxide and hydroxide species based on binding energy shifts, it does not provide information about the electronic structure or the unoccupied states of oxygen. To further investigate how the oxygen environment evolves with Fe incorporation and OER treatment, O K-edge X-ray absorption spectroscopy (XAS) is employed. This technique probes transitions from the O 1s core level to unoccupied 2p orbitals, which are hybridized with metal 3d states, offering element-specific sensitivity to changes in covalency and coordination[178].

Figure 50 shows the O K-edge spectra of the samples before and after OER in black and red respectively obtained in total electron yield mode. Spectra of some known references are shown in blue for comparison. The spectra display a pronounced pre-edge region beginning just below 530 eV and extending to ~535 eV. These features are highly sensitive to local coordination and oxidation environments of oxygen-bound transition metals[179,180]. Evidently, a distinct pre edge feature characteristic of molecular water is absent in the O-K edge XAS spectra, as visible from the comparison with the reference spectra from literature[181]. This is in contrast with the observation from the O 1s HAXPES spectra, where a peak centered around a higher binding energy peak of ~532.5 eV was needed for the deconvolution of the spectra of samples post OER, which is consistent with weakly bound or surface adsorbed water. This disparity may arise due to the fact that the adsorbed water species seen in HAXPES may be disordered, hydrogen-bonded or partially dissociated, which would alter their electronic structure compared to isolated water molecules. As a result, the well defined unoccupied molecular orbitals that give rise to the sharp pre-edge structure seen in the pre-edge of O K XAS spectra of water is absent in the spectra of the samples.

In the Ni rich samples (x=0 and x=1), both before and after OER treatment, the O K-edge pre-edge region displays one broad feature at ~529.4 eV and another, smaller feature at ~532.9 eV. The latter feature closely resembles the corresponding peak in the $Ni(OH)_2$ reference in the samples before OER and is more pronounced in these low-Fe compositions, suggesting dominant O 2p–Ni 3d hybridization in a relatively uniform ligand environment. Ni has persistently shown indications of existing in a mixed valence state, but this similarity with the $Ni(OH)_2$ reference for the O-K edge suggests that some of the Ni species exist in a hydroxide environment. A partition develops in this feature after OER, indicating a change in the chemical environment of Ni brought on about OER. The

x=5 spectra remains unchanged after OER, suggesting that the hybridized states probed in this particular sample remain stable after the reaction. However, this is in contrast to what is observed in Fe, Ni and even O 1s HAXPES spectra, where significant changes occur post OER in the x=5 sample. This implies that Fe-Ni-O systems can show site specific behavior, where oxygen ligand fields stabilize earlier and exist in a state that is already ideal for catalysis and does not need further adjustments.

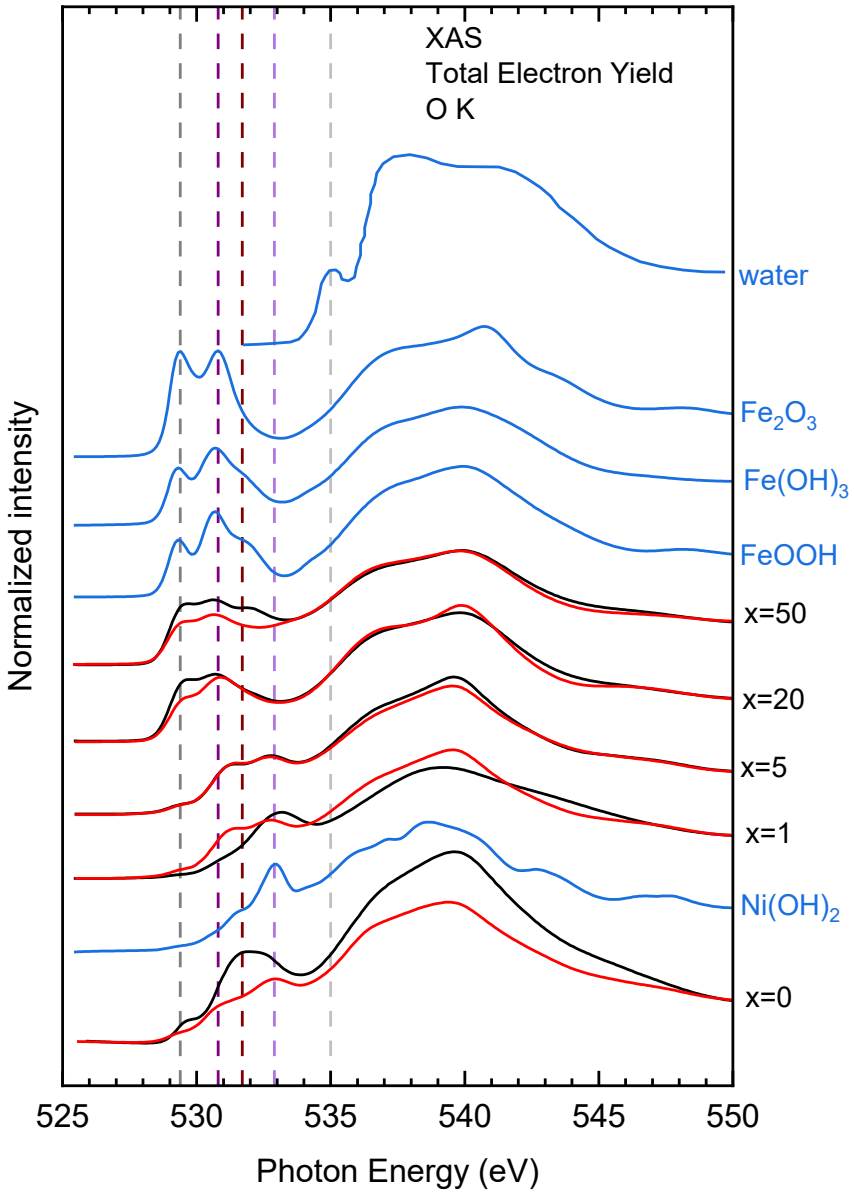

Figure 50: O K-edge XAS spectra of FeNiOOH thin films measured in total electron yield mode, for samples wo OER (black) and wt OER (red). Reference spectra for selected oxide, hydroxide, and water-containing phases are shown in blue. Vertical dashed lines mark the pre-edge region (~530–535 eV), corresponding to O 1s → 2p transitions hybridized with transition metal 3d states.

As Fe is introduced into the sample, the spectral shape of the pre-edge evolves. The ~529.4 eV feature increases in relative intensity with Fe content and aligns with that observed in $Fe(OH)_3$, FeOOH, and Fe_2O_3 references, indicating growing contributions from O 2p–Fe 3d hybridization. In x=20 however, post OER, this feature is suppressed. This redistribution of relative intensities in the pre-edge region suggests the emergence of new hybridized states, specifically with Fe–O-H character[182,183] . A similar behavior is noted in x=50, where after OER the pre-edge feature is suppressed. The reshaping of the pre-edge in higher Fe content samples, especially post OER, reflects a transition from Ni oriented to a mixed Fe-Ni electronic structure, consistent with trends observed in Ni and Fe L-edge spectra and surface-sensitive measurements.

The spectra were also obtained in partial fluorescence yield (PFY) mode and overlaid with the corresponding total electron yield (TEY) spectra in Figure 51 shown in black and red, respectively.

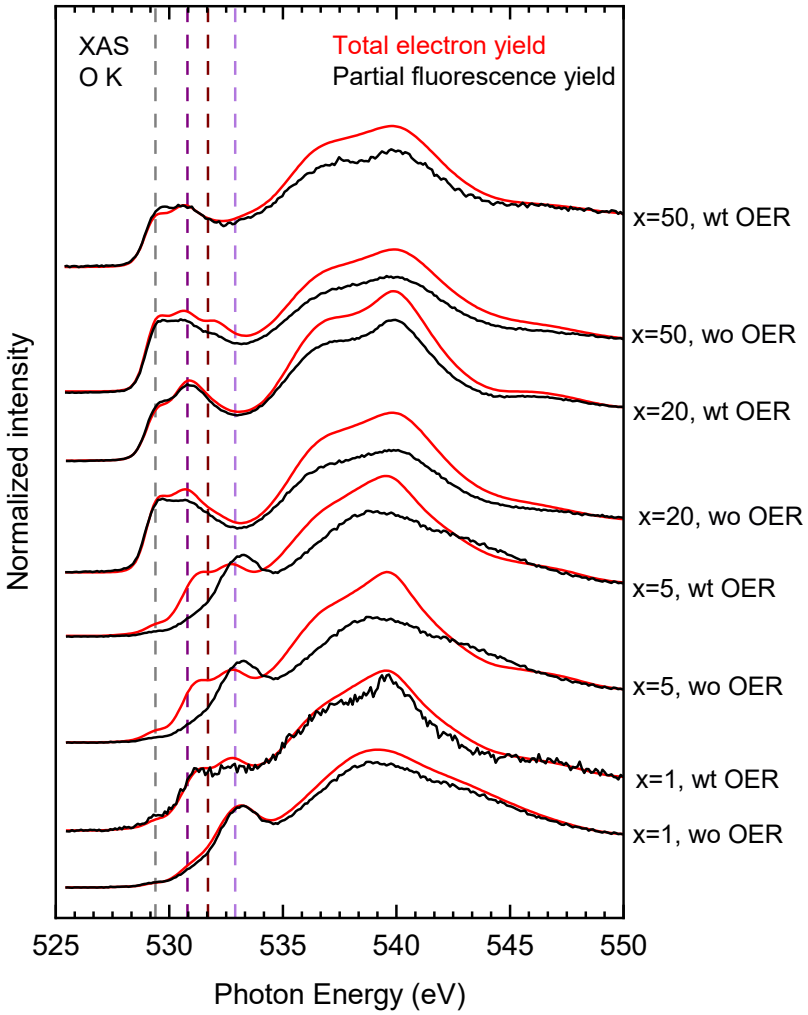

Figure 51: O-K edge XAS spectra of $Fe_xNi_{1-x}(O,OH)_y$ electrocatalysts recorded in total electron yield (TEY) mode, shown in red and partial fluorescence (PFY) mode, shown in black. Clear differences can be spotted in the pre-edge region between the two modes, representative of differences between the surface and bulk.

Across the sample series, distinct differences between TEY and PFY in the pre-edge region can be seen, reflecting depth-dependent variation in the local oxygen environment. In x=1, wo OER, both TEY and PFY spectra remain the same before and after OER, as the peak at ~533 eV maintains its shape and intensity across the different probing depths, implying that the sample is homogeneous with respect to O 2p-Ni 3d hybridization. Post OER, there is a clearer separation between the peaks at ~533 eV and ~531.7 eV, implying the development of a more heterogeneous environment across the bulk and surface when OER is performed with the sample. x=5, wo OER, the TEY spectra shows a distinct doublet with peaks at ~533 eV ad ~530.8 eV, while the PFY spectra resembles both spectra of the x=1, wo OER sample. The same pattern is observed in the sample x=5, wt OER, reinforcing that no changes are brought on to this sample with OER.

In x=20, before OER the TEY and PFY spectra resemble each other closely, except for the intensity at ~529.4 eV which is enhanced in TEY, indicating a subtle difference between the surface and the bulk. After OER, both spectra are rather identical. OER therefore causes a convergence of the chemical environment at the surface and the bulk.

Similarly, in x=50, before OER the spectra resemble each other with slight suppression of the whole pre-edge region in the PFY spectra. After OER, similar to x=20, the TEY and PFY spectra converge as the bulk and surface states become similar.

These trends highlight the depth-dependent evolution of the chemical and electronic structure of the oxygen environment, indicating that both similarity and divergence of the oxygen chemical environment is a function of both Fe content and OER.

5.6 Tracking OER-induced changes in occupied oxygen states

As discussed in Chapter 2, oxygen K-edge x-ray emission spectroscopy (XES) probes the occupied states with O 2p character, including those hybridized with transition metal 3d orbitals. Figure 52 presents the O K-edge XES spectra for the $Fe_xNi_{1-x}(O,OH)_y$ samples before (black) and after (red) OER, normalized to total area of spectra. Reference spectra of relevant Fe and Ni oxides and hydroxides are shown in green for comparison.

All samples exhibit a broad emission feature centered at approximately 525 eV, which has been previously attributed to transitions involving O 2p states hybridized with metal 3d orbitals in Ni and Fe compounds.

In the x=1 and x=5 samples, a shoulder near ~524 eV becomes more pronounced, particularly after OER. This feature closely resembles that in hydroxide reference compounds such as $Fe(OH)_3$ and $Ni(OH)_2$, suggesting that the OER enhances OH^- rich coordination environments in these samples. These findings are consistent with the TEY spectra shown in Figure 51, where similar spectral shifts were observed near the surface. Together, the XES and XAS data indicate that hydroxide-like oxygen configurations dominate in Ni-rich samples, while increasing Fe content leads to more uniform oxide-type coordination in the valence band structure.

In comparison, the Fe rich samples, namely x=20 and x=50 show broader peaks that are more symmetric in nature that lack a distinct shoulder structure, and the changes brought about by OER are more subtle, such as slight broadening of the main peak at ~524 eV. These changes reflect differences in the local oxygen environment.

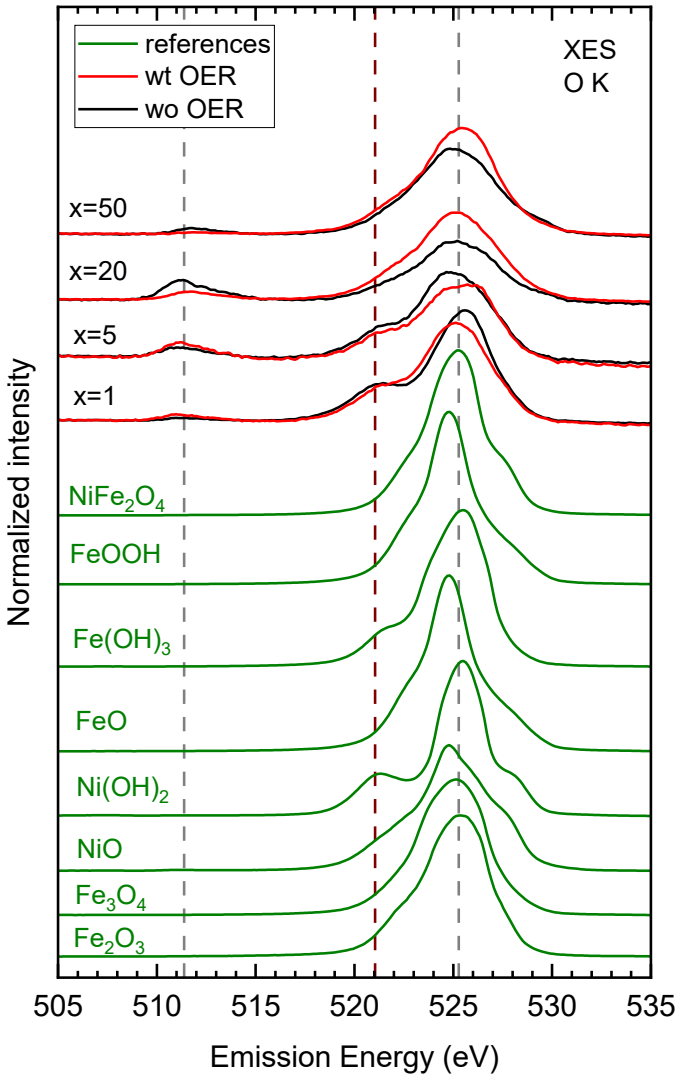

Figure 52: O K-edge x-ray emission spectra (XES) of the FeNiOOH samples before(black) and after (red) OER, shown with the spectra of some known references.

A low-intensity shoulder at approximately 511 eV is visible in all sample spectra but is not present in the reference compounds. Its exact origin is unclear, however, it may arise from oxygen states in environments that are hard to identify based on the depth of knowledge in present circumstances, specific to the catalyst films.

As demonstrated in the soft x-ray study by Holliday in 1975[184], oxide layers on transition metals and alloys often exhibit broadened or asymmetric features due to structural disorder, mixed-valence bonding, and chemically inhomogeneous surface layers. Holliday's work further emphasizes that

such deviations from ideal spectra are characteristic of real-world catalytic surfaces, especially those undergoing redox cycling or electrochemical restructuring. In this context, the spectral features observed here are consistent with a dynamically evolving oxygen environment shaped by Fe incorporation and OER treatment, where local disorder, rather than discrete phase transitions, dominates the electronic structure of oxygen.

6. Summary of Findings

The cumulative insights from the spectroscopic and electrochemical investigations enable a broader understanding of the relationship between the electronic and chemical structure of the FeNiOOH electrocatalysts and their activity in the oxygen evolution reaction. Individual measurement techniques allow for localized snippets of the chemical and electronic states of the transition metal centers, as well as oxygen, but when looked at from a broader perspective, a more coherent picture emerges. Spectroscopy and electrochemistry each provide partial insights into oxidation states, bonding, and activity trends, the following synthesis shows how these pieces connect to explain the relationship between structure and activity of the FeNiOOH electrocatalysts.

A consistent theme that persists throughout the dataset is the central role of iron in controlling the catalytic behavior of the electrocatalytic system. With increasing Fe content, both Fe and Ni become progressively more oxidized, with indications of strong Fe-O-Ni covalency. The synergistic interaction between the elements peaks within the compositional window of 10-20 at. % Fe, which is also where the catalytic activity of the material system is the maximum.

Beyond this window, which is associated with peak catalytic performance, deviations in spectroscopic trends. These include changes in oxidation states, binding energies for the metal centers with less consistent oxygen coordination. Together, these features point to structural and electronic environments that no longer favor optimal catalytic behavior. This implies a breakdown of the synergistic Fe-O-Ni interactions seen in the 10-20 at. % Fe. This supports the interpretation that Fe actively shapes the surface properties of the catalyst.

Furthermore, the chemical heterogeneity between the surface and the bulk of the material system, which becomes most evident in the Fe-L edge XAS spectra, underlines the importance of performing a more depth resolved inspection, when interpreting the changes in the structure of the catalysts with reference to their electrocatalytic activity. The Fe spectra therefore show distinct differences depending on probing depth. In contrast, the Ni spectra remain largely unchanged with both increasing Fe content and after OER in the bulk, with modifications only at the surface.

Crucially, the oxygen environment emerges as a key driving force behind the evolution of the catalyst structure. Within the critical compositional window of 10-20 at. % Fe, both oxide and hydroxide related species at the surface increase simultaneously, reflecting a more complex oxygen-transition metal interaction. Post OER, the oxygen spectra become more oxide-like in character, which when viewed in parallel to the increased oxidation of the metal centers, highlights the strong covalent relation forming between the metals and oxygen. As these changes coincide directly with the peak in catalytic activity, it suggests that oxygen, beyond being merely a ligand, actively participates in the catalysis.

Collectively, these findings suggest an evolving metal-oxygen framework, where Fe, Ni and O interact synergistically to influence the catalytic activity of the material system. Instead of determining one catalytically active metal center, which has been the general approach for these materials in the research community[13,15,81,183] , the data studied propose a model in which oxygen acts as somewhat of a bridge, coordinating the redistribution of electrons between the metal centers and changing chemical environments, as a function of composition and electrochemical treatment.

7 Operando cell: structure and design

7.1 Introduction

To understand the catalytic behavior of an electrocatalyst during electrolysis, it is essential to study the material *operando*, that is, while it functions under reaction conditions, with simultaneous acquisition of spectroscopic and electrochemical data. This is distinctively different from in situ experiments, where the material may be exposed to a reactive environment, but not necessarily under active operating conditions. *Operando* soft x-ray spectroscopy offers unique insights into surface and interface chemistry, which are critical for reactions such as the oxygen evolution reaction (OER). Unlike hard x-rays, which primarily probe bulk structure, soft x-rays can access shallow core levels, such as the O K-edge, enabling direct observation of oxygen related species at the catalyst-electrolyte interface, which is the site of catalytic activity.

Successful *operando* experiments using soft x-rays require several conditions. First, proximity to a high-flux beamline capable of accommodating an in situ or *operando* set-up, such as the X-SPEC beamline at the KIT Light Source (detailed in Chapter 3). Second, a dedicated electrochemical cell is required, one that integrates beam access, vacuum sealing, electrolyte compatibility, and real-time control over reaction conditions. Third, the working electrode must be electrically accessible: in this system, the catalyst-coated membrane is in contact with an external circuit, allowing the application of controlled potentials to drive the electrochemical reactions for OER, which have been explained at length in Chapter 2. Lastly, the entire cell assembly must be compatible with high-vacuum environments, since soft x-rays are strongly attenuated by air[185], limiting their effective transmission over even short distances.

In the preceding chapters, the structural and compositional evolution of FeNiOOH catalysts was analyzed extensively through ex-situ techniques, both in the as-prepared state and following electrochemical cycling. While these results provided critical insight into the structural evolution and phase behavior of the catalyst, they remain inherently limited in their ability to track the behavior of short-lived intermediates and dynamic states that emerge only under applied potential. To address this limitation, the present chapter describes the design and validation of a custom-built *operando* electrochemical cell. The cell is tailored for soft x-ray spectroscopy and optimized for implementation at the X-SPEC beamline[29].

7.2 Challenges in soft x-ray *operando* measurements

Implementing soft x-ray spectroscopic techniques in an *operando* electrochemical environment comes with several technical and practical challenges. These arise from the inherent properties of soft x-rays, such as their short attenuation length, already talked about in the introduction, and from the specifics that arise from requiring to conduct electrochemical reactions within a confined, vacuum-compatible cell geometry. This section outlines the core limitations imposed by these

constraints and highlights how each has influenced the material choices, mechanical layout, and operational parameters of the *operando* cell developed in this work.

7.2.1 Vacuum requirements

Soft x-rays (below ~2.1 keV) are strongly attenuated by air, particularly near the O K-edge (~530 eV), where the attenuation length is less than 0.3 mm. This implies that even the minutest exposure to air can significantly reduce photon flux and degrade signal quality. To minimize absorption thus, soft x-ray spectroscopy is typically carried out under vacuum, particularly along the beam path and in the sample chamber. While ultra-high vacuum is sometimes used to reduce contamination and improve stability, the sample region can often operate at lower pressures, such as below 1 mbar, or in helium-filled environments where absorption is less severe than in air.

In *operando* experiments involving liquid or ambient-pressure environments, a core design challenge is presented: creating isolation between the sample environment and the vacuum in the beamline. The most common solution is to use a thin, x-ray transmissive membrane to form a sealed interface between the vacuum and the sample chamber. This membrane must be thin enough to ensure high x-ray transmission, yet robust enough to withstand the pressure difference across its surface, often exceeding 1 bar. Membrane rupture is a known risk in such setups and must be alleviated through mechanical reinforcement, differential pumping, or fast-closing interlock valves. These requirements impose strict constraints on material selection, membrane support structures, and overall cell geometry.

7.2.2 Bubble formation within the cell and beam damage

Many *operando* environments involve dynamic chemical reactions, temperature changes, and radiation exposure, all of which can result in gas evolution and physical instability. In liquid-phase studies, high photon flux can lead to local heating and radiolysis of the solvent, producing gas bubbles that interfere with measurement stability[186]. However, in electrochemical systems such as water electrolysis, the focus of this work, bubble-formation is not merely a side effect but a direct result of the catalytic reactions themselves. During the oxygen evolution reaction (OER) and hydrogen evolution reaction (HER), molecular oxygen and hydrogen are continuously generated at the working and counter electrodes, respectively, and emerge as gas bubbles near the electrode surface.

These bubbles can scatter or absorb the incident x-ray beam, disrupt local electrolyte composition, and in some cases block the catalyst surface and prevent further reaction from occurring[187,188]. To mitigate these effects, *operando* cells must incorporate continuous electrolyte flow, carefully optimized chamber geometry, and mechanisms for thermal and gas dispersion.

7.2.3 Attenuation of signal by liquids

In classical soft x-ray liquid cell configurations, where the x-ray beam must pass through a bulk liquid layer, film thicknesses are typically restricted to less than 100–200 nm to reduce absorption and preserve spectral features[189]. However, this constraint does not directly apply to the present cell design. While the catalyst is electrochemically active and is in contact with the liquid electrolyte on one side of the membrane, the soft x-rays enter from the opposite side, the surface of the membrane

that faces the vacuum, thereby not travelling through the liquid. This geometric design choice eliminates the possibility of attenuation of x-ray signal by liquid.

Even so, liquid near the membrane surface can introduce scattering, reduce stability of beam alignment, or contribute to secondary absorption if not properly controlled. These risks are mitigated through careful optimization of the flow path, and incidence angle of the beam, ensuring that signal loss from the surrounding electrolyte is minimized without compromising electrochemical operation.

7.2.4 Sample conductivity and electrical accessibility

The *operando* cell developed in this work is designed specifically for electrolysis reactions, while performing soft x-ray spectroscopy experiments simultaneously. While the membrane (which acts as the working electrode and will be discussed in detail later in the chapter) on which the FeNiOOH is electrodeposited in this setup is conductive, owing to a gold layer beneath the electrodeposited FeNiOOH catalyst, a key challenge lies in reliably establishing electrical contact between this surface and the external power source during *operando* measurements. The contact must be mechanically secure, chemically stable in electrolyte, and precisely positioned to avoid obstructing the x-ray beam or stressing the membrane. Without such accessibility, electrolysis cannot proceed, and the *operando* functionality of the cell is compromised. Ensuring this connection is therefore a central design consideration in the development of the electrochemical *operando* cell.

7.3 Survey of existing cell designs

Several *operando* and in situ cell designs have been developed to enable soft x-ray measurements in liquid or electrochemical environments. These designs vary widely in terms of materials, mechanical aspects and compatibility with vacuum systems. While each contributed important solutions to the challenges discussed above, additional input had to be made to tailor the design for the requirements specific to the material system being studied here. The following section reviews key designs, grouped by their core features, and highlights their relevance to the cell developed in this work.

7.3.1 Cell to study gas/solid interface

Heske et al.[190] in 2003 developed a stainless-steel mini cell to study the interfaces of liquids and solids by soft XES. The design consists of a stainless-steel body, glued to the surface of the sample being studied, which in this case is $CuIn(S,Se)_2$, with a UHV compatible epoxy glue. An aluminum spacer defines a narrow channel between the sample and a polyamide window. The latter is filled with high resistivity water and subsequently sealed with the same epoxy glue, together with the polyamide window, thus making it safe to be transferred into the UHV chamber. This configuration enables photon-in/photon-out measurements through the liquid layer and allows the detection and study of reactions taking place at the interface. As the incident x-rays are required to traverse through both the liquid layer and the polyamide window, its intensity is significantly attenuated. As a result, only synchrotron sources with very high photon flux could provide spectra of sufficient quality, and this limits the usefulness of the design for routine or more demanding operando studies.

Benkert et al.[191] in 2014 developed a gas cell designed to study the electronic structure of gases and gas/solid interfaces using soft x-ray emission and absorption spectroscopies. The cell allows in situ measurements under atmospheric pressure, with the sample gas separated from the vacuum of the analysis chamber by a thin window membrane. Temperature regulation up to approximately 600 °C is possible, for which the cell was constructed with metallic components, and a constant mass flow can be maintained with gas flow lines to refresh the gaseous sample continuously. The cell also accommodates solid-state samples, enabling studies of gas/solid interfaces for surface catalytic reactions at elevated temperatures.

The cell is particularly effective for functioning at elevated temperatures, however, the design is not compatible with liquid environments.

7.3.2 Liquid microjet system

Lange et al.[192] in 2010 introduced a high-resolution setup for soft x-ray emission spectroscopy of liquids using the microjet technique. By injecting a fine stream of liquid directly into vacuum, the design eliminates the need for x-ray transparent membranes, enabling very high spectral resolution and minimizing window-related losses. Because no chamber walls or membranes were involved in the beam path, material compatibility issues were largely avoided. The setup required continuous high-speed flow through a glass capillary, with the vacuum chamber built from standard stainless-steel capable of withstanding UHV conditions.

This design successfully avoids membrane failure risks by eliminating physical windows. However, such a design is incompatible with electrochemical studies that require a defined working electrode, stable sample positioning, and the ability to apply and control potential during measurement.

7.3.3 Liquid cells with membrane windows

Fuchs et al.[186] in 2008 developed a membrane-based liquid cell designed for temperature-controlled soft x-ray studies. The cell encloses a liquid layer behind a thin membrane, allowing operation under vacuum while enabling x-ray absorption spectroscopy of liquids. It also includes a temperature control mechanism for the sample volume. The cell body is made of Teflon, which was chosen for its chemical inertness and thermal stability. Temperature control was integrated via a copper heat-exchange plate attached to the chamber body, and the sample volume was confined behind the membrane without active flow.

This design is well suited for soft x-ray absorption and emission studies of liquid samples at controlled temperatures, offering good vacuum compatibility and stability.

The lack of the possibility of integration with electrode feedthroughs limits its suitability for electrochemical applications, particularly those involving gas evolution. Without active bubble removal or electrode control, it cannot be adapted for *operando* electrolysis measurements.

Blum et al.[193] developed one of the first soft x-ray compatible flow through liquid cells, integrated into the SALSA end-station at Beamline 8.0.1 of the Advanced Light Source (ALS). The design features a thin silicon nitride window to isolate the liquid sample from the vacuum chamber, enabling high-

resolution x-ray absorption spectroscopy (XAS) of liquids. The cell was optimized for stability under beam exposure and included provisions for sample exchange and temperature control.

This design provided a working demonstration of stable soft x-ray transmission through the windows and introduced sealing under vacuum with the help of a membrane. The cell however was not equipped for the mitigation of bubble accumulation, hence was limited in its ability to study reactions that involved the evolution of gases.

Schwanke et al.[194] in 2014 presented an electrochemical cell compatible with soft x-rays, which integrates a three-electrode configuration within a vacuum isolated system. The body of the cell was constructed from PEEK (polyether-ether ketone), a chemically resistant polymer compatible with vacuum and possessing excellent mechanical stability, making it well-suited for *operando* electrochemical environments. A thin Si_3N_4 membrane serves both as the x-ray window and as the substrate for the working electrode, allowing soft x-ray transmission while also maintaining electrical connectivity. The cell can support continuous electrolyte flow and was used to investigate electrochemical depositions and catalytic processes under *operando* conditions.

This design provided a strong foundation for integrating electrochemical control with soft x-ray spectroscopy and its use of PEEK as the structural material was a key inspiration for the cell developed in this work.

7.4 Mechanical layout of the *operando* cell designed

The *operando* electrochemical cell developed in this work was designed with the dual aim of supporting electrochemical water-splitting reactions and enabling simultaneous soft x-ray spectroscopic measurements at the X-SPEC beamline. Its mechanical structure reflects a deliberate effort to resolve the specific design challenges outlined in Section 7.2. The layout takes inspiration from several earlier designs, detailed in Section 7.3. Numerous modifications were necessary however, to adapt to the needs of dynamic, gas-evolving electrochemical water splitting or electrolysis experiments using the FeNiOOH catalysts.

Figure 53 (a) and (b) show the design and internal structure of the *operando* electrochemical cell. Figure 53(a) shows an exploded schematic of the main components, namely the central catalysis chamber, where the sample or the working electrode is placed, the left and right copper sheets, the gold coated silicon nitride membrane supported by a silicon wafer, and the Viton O-rings used for sealing. The cooper sheets are positioned such that external contact can be established between the sample and the source of electric potential that drives the electrochemical reaction. Figure 53(b) shows a top-down view through the translucent cell body, highlighting the internal layout of the catalysis chamber, fluid channels and electrode feedthroughs. The channels are configured such that the two liquid inlets and outlets are positioned perpendicular to the electrode connections. The central region, marked with a red circle, is the convergence point of all four channels and is essentially the catalysis chamber that aligns with the x-ray transmission window.

The cell body is made of PEEK, selected for its robustness against chemicals, vacuum compatibility and ability to hold its structural integrity under vacuum. PEEK is also non-conductive and thermally stable. The internal liquid chamber is sealed using Viton O-rings. Of the two, one O-ring provides the

primary seal between the liquid chamber and the membrane, while the other acts as a buffer to prevent over compression of the membrane at the time of assembly.

The membrane is clamped with the help of a stainless-steel compression plate. Mechanical hard stops are built in into the design of the cell to protect the membrane from unwarranted stress.

The x-ray beam is directed through the center of the stainless-steel compression plate as shown in Figure 53(a).

(a)

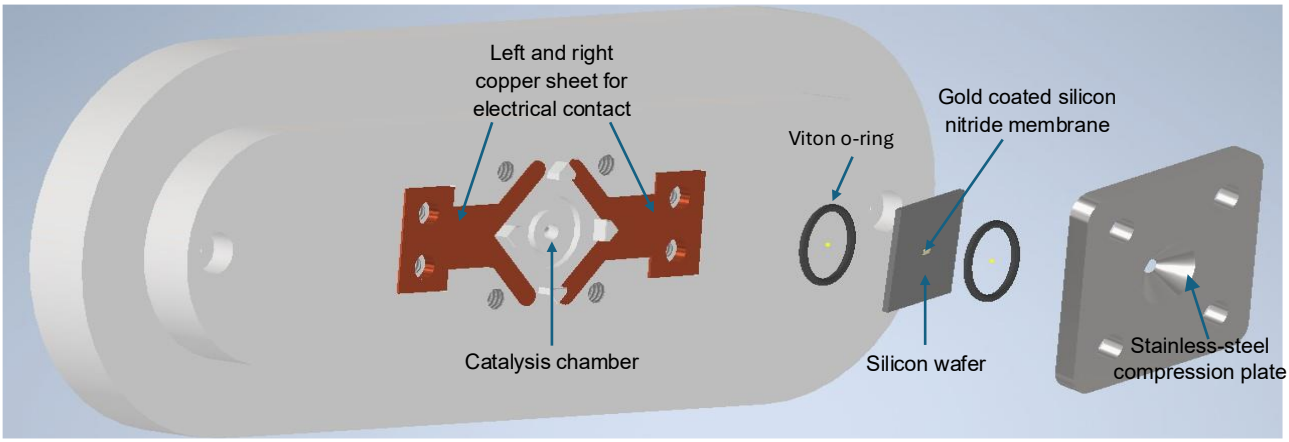

(b)

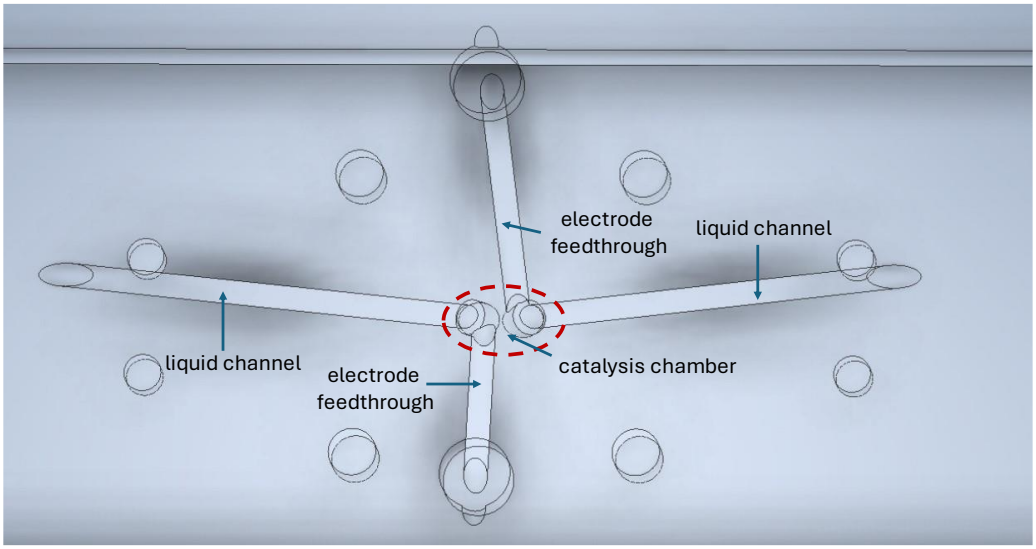

Figure 53: (a) Exploded 3d view of the operando electrochemical cell assembly. The central catalysis chamber, flanked by copper sheets, the gold coated silicon nitride membrane, supported by silicon wafer, sealed by Viton O-rings. (b) internal schematic view of the operando cell, showing the layout of the liquid channels and electrode and liquid feedthroughs.

The electrode feedthroughs house the counter electrode and the reference electrode, a Pt and Ag wire respectively. Together with the working electrode, they replicate a three-electrode configuration

suitable for electrochemical measurements, the details of which have been discussed at length in Chapter 2.

The internal liquid chamber is elliptical in shape, aiming to promote a smoother electrolyte flow across the membrane and eliminate sharp corners that might lead to uneven circulation. While the effects of this geometry on the flow of electrolyte and removal of the gases formed as a result of electrolysis have not been tested previously, this design was motivated with the aim of reducing the angular, stagnant regions within the chamber thereby facilitating the passage of gas bubbles, a phenomenon found difficult in existing rectangular cell layouts. The chamber is connected to four ports, each designated for electrolyte inlet, outlet, reference electrode and counter electrode. The inlet and outlet are offset at obtuse angles to the electrode feedthroughs, allowing for a lateral flow path across the membrane surface, supporting continuous electrolyte exchange. Figure 54 shows the cross-sectional view of the cell.

The circulation of the liquid is achieved by a peristaltic pump, maintaining continuous flow through the chamber during electrochemical measurements. This helps in the stabilization of the reaction conditions within the catalysis chamber. The total volume of the chamber is approximately 3.4 µL.

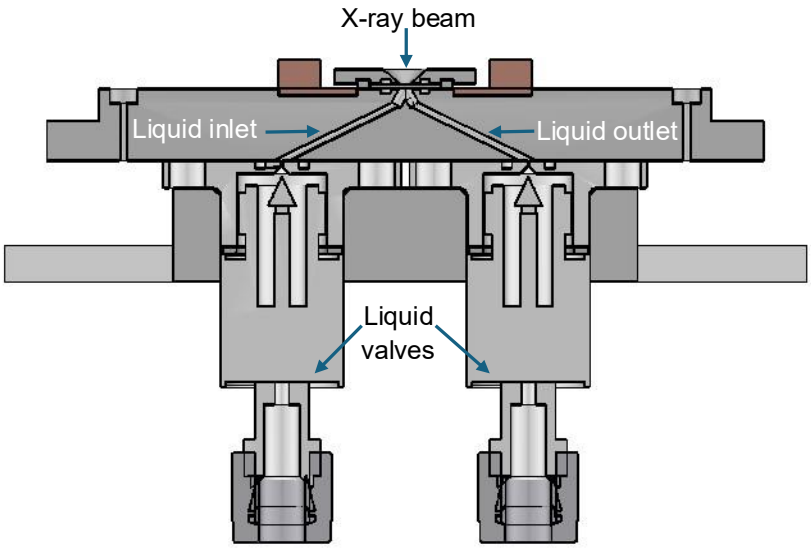

Figure 54: Cross-sectional view of the operando electrochemical cell showing the internal flow geometry, including the liquid inlet and outlet, x-ray beam path through the membrane and position of the fast-acting liquid valves.

A safety interlock system is implemented to protect the beamline in the event of membrane failure. Pressure activated valves are installed at the electrolyte inlet and outlet at the time of assembling the cell. The valves theoretically have a response time of 2 milliseconds. Fast response gauges at the

beamline end station are capable of automatically detecting a pressure increase, in the event of membrane breakage, which trigger the valves to close down and isolate the liquid circuit to prevent backflow into the vacuum chamber.

The valves are mechanically supported by a stainless-steel 'X'- shaped bracket, which anchors the cell and maintains proper alignment with the beamline flange, shown in Figure 55.

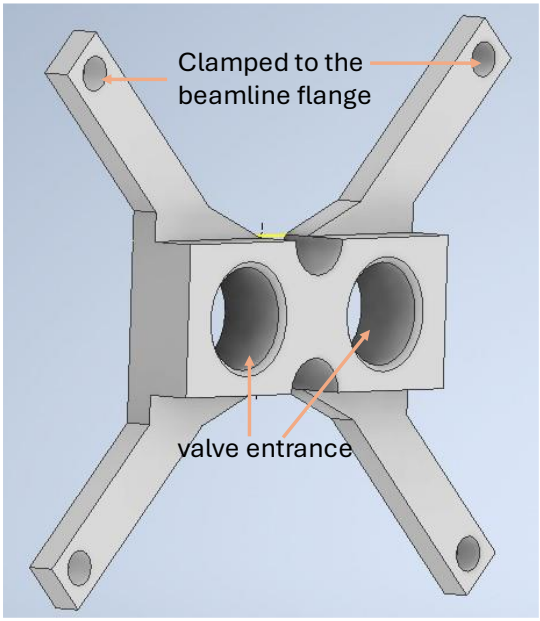

Figure 55: Stainless-steel support bracket for assembling of the operando electrochemical cell. The bracket is clamped to the beamline flange through the holes indicated in the image. The central ports are meant for accommodating the fast-closing valves.

The silicon nitride (Si_3N_4) membrane is 100 nm thick, which serves as the substrate for catalyst depositions, as well as the soft x-ray transparent window for the x-ray spectroscopic experiments and were obtained from Silson limited. To ensure electrical conductivity, the membrane is sputter coated with a 10 nm gold layer, over a 5 nm titanium adhesion layer. This conductive surface allows the membrane to act as the working electrode during electrolysis, while sufficiently transmitting soft x-ray photon at the O K, Fe L and Ni L edges.

The choice of membrane material is made based on an assessment of chemical and thermal stability, minimal x-ray absorption, mechanical strength and compatibility with vacuum and alkaline electrolytes.

The copper sheets, as explained earlier, establish electrical contact between the membrane which acts as the working electrode and the external source of potential. Importantly, this configuration allows for the checking of electrical connections even when the cell remains under vacuum. By measuring continuity across the cables connected to the copper sheets used for establishing external contact, it is possible to assess the membrane's connectivity and whether it has been adequately tightened.

The x-ray transmission characteristics of the different components of the membrane were evaluated using the Center for X-Ray Optics (CXRO) online attenuation length calculator. The calculations were performed at photon energies corresponding to O K-edge, Fe L-edge and Ni L-edge, which represent the spectral regions which can be probed in the FeNiOOH catalysts. Each layer's transmission was evaluated individually, and the total effective transmission was calculated by squaring each value to account for the two-way passage of beam through the electrolyte and membrane. The values were ultimately obtained by multiplying across the cumulative layers. The results are summarized in Table 4. The results indicate that the membrane adequately transmits soft x-rays across all the relevant absorption edges. The same evaluation protocol can be used to assess performance of the membrane materials at other photon energies, as well as to evaluate the usability of other commonly used membranes such as silicon carbide (SiC).

Layer thickness	**O K**	**Fe L**	**Ni L**
100 nm Si_3N_4	0.7	0.8	0.72
10 nm Au	0.75	0.8	0.85
5 nm Ti	0.95	0.97	0.98
Net	24%	38%	49%

Table 4: Simulated x-ray transmission of the multilayered membrane, 100 nm Si_3N_4 / 5 nm Ti / 10 nm Au at photon energies corresponding to the O K (~530 eV), Fe L (~708 eV), and Ni L (~852 eV) absorption edges. Transmission for each layer was calculated using the CXRO attenuation length tool, then squared and multiplied to determine the net membrane transmission.

7.5 Preliminary results and functional validation

To assess the workability of the *operando* electrochemical cell, a series of preliminary laboratory tests were conducted, with the aim of verifying the structural integrity of the cell, liquid circulation and electrical connectivity under conditions replicating those that would be encountered at the beamline.

The three-electrode setup described in Section 7.4 was used to perform cyclic voltammetry in 1 M KOH at a scan rate of 100 mV/s. The resulting voltammogram is shown in Figure 56, which exhibits redox features suggestive of an active electrochemical interface, confirming that the cell is operable. However, the observed peak positions deviate from those expected for clean polycrystalline gold, which could be due to several factors such as a drifting reference electrode (pseudo reference electrodes tend to drift after prolonged use), unintentional exposure of the copper connections or

any other unprecedented factor. Further refinements and tests specific to beamline conditions will be necessary for further operation of the cell.

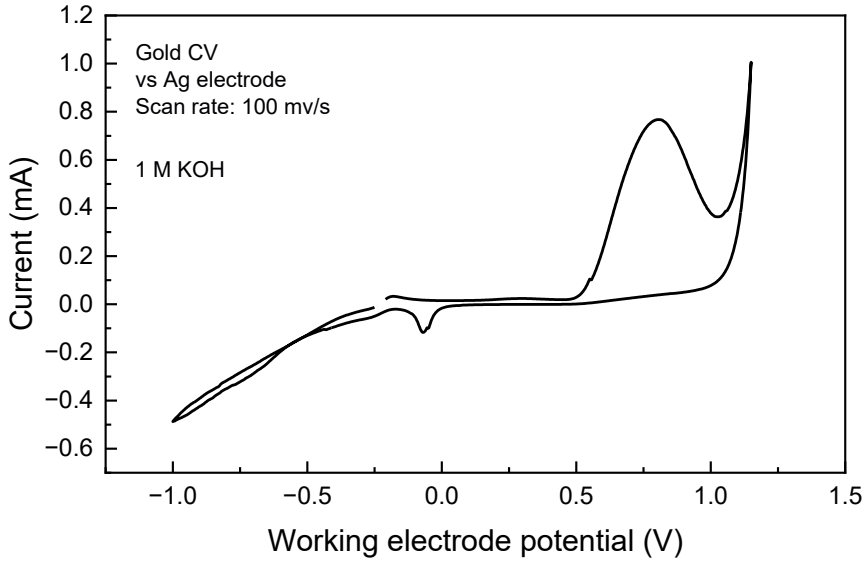

Figure 56: Cyclic voltammogram of a gold coated Si_3N_4 membrane in 1 M KOH, recorded at a scan rate of 100 mV/s using the operando cell. The reference electrode used is a Ag wire.

Figure 57 shows the assembled *operando* cell with the three electrodes mounted and the working electrode externally connected. The layout shown here is a laboratory-based replication of what the beamline configuration would look like.

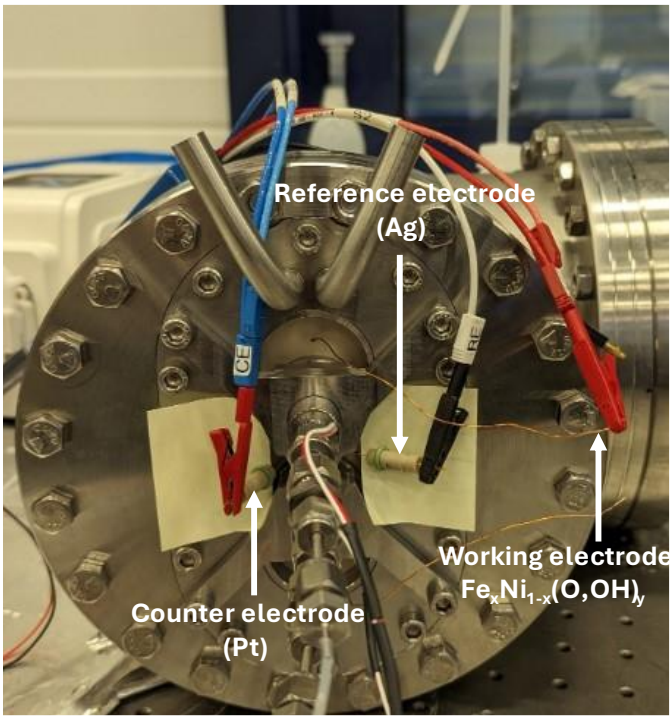

Figure 57: Photograph of the operando electrochemical cell fully assembled in its beamline-compatible flange setup. The three-electrode configuration with the wires for establishing external contact with the working electrode are shown.

8 Conclusion and outlook

In the preceding chapters, detailed spectroscopic investigations were performed on $Fe_xNi_{1-x}(O,OH)_y$ thin films, which in recent years, have emerged as promising electrocatalysts for electrolysis of water. They were studied as a function of iron content and chemical history: before and after participation in the oxygen evolution reaction (OER). A wide range of x-ray and electron spectroscopic techniques have been used to shed light upon the evolving chemical and electronic structure of the samples. One of the key goals of this study is to determine the effect of Fe incorporation in the predominantly Ni-based oxides and hydroxides and track the evolution of the electronic and chemical structure of the catalyst as a function of Fe content. Additionally, the work also analyses the changes brought on to the catalyst by electrochemical cycling, thereby attempting to identify the catalytically active framework within the material system.

To gain a preliminary understanding of the FeNiOOH thin films, they were initially studied as synthesized. Conventional laboratory-based XPS studies were deemed inconclusive, as it was found that the core level peaks of Fe and Ni were interrupted by the Auger lines. Thus, all relevant further measurements were carried out at the X-SPEC beamline at the KIT Light Source. HAXPES measurement at 2.1 keV and soft XAS measurements at the Fe and Ni L-edges revealed strong covalent Fe-O-Ni interactions within the samples in varying degrees across different compositions. With the incorporation of Fe, this covalent interaction became stronger and Ni became increasingly oxidized. The compositional window within 10-20 at. % Fe was identified as a critical point as it showed consistent spectral and quantitative transitions, including shifts in the Fe and Ni oxidation states and the spectral weight of the different components in the O 1s spectra. The attempt made to express the intermediate samples as a linear combination of the two extreme components, namely the x=1 and x=50 samples for the Fe 2p spectra revealed a sharp transition within this window, marking an increase of the x=50 component, indicating increased oxidation. A similar trend was observed within the 13-20 at. % Fe window, for the Ni 2p spectra. The O 1s spectra were deconvoluted to determine the relative contributions of oxide and hydroxide and a pronounced increase in hydroxide contribution peaking near 20 at. % Fe coupled with a decrease in oxide contribution was observed.

These findings become a strong basis for the hypothesis that this is the most electronically relevant compositional window, where both Fe and Ni undergo increased oxidation. The oxygen environment too reflects these results. The observations from the L-edge XAS spectra of Fe and Ni corroborate these findings. Additionally, as XAS was obtained in both TEY and PFY modes, a depth resolved picture can be drawn of the samples, which indicated that at the Fe L-edge, while the surface showed pronounced changes as a function of changing composition, the bulk remained rather unchanged. The surface and the bulk can therefore be considered as chemically heterogeneous in terms of ligand field effects, with respect to Fe. However, the Ni L-edge showed no significant differences between the surface and the bulk. This strengthens the idea that Fe is seat of major activity in the FeNiOOH electrocatalysts, as widely acknowledged by current research.

Once such a baseline was established, the samples were investigated in pairs as the same composition was studied before and after they participated in the OER process. Quantitative analyses were performed to determine the effect of OER on the Fe and Ni environments on the

surface. Tougaard backgrounds were subtracted from the Fe 2p and Ni 2p core level spectra of the samples before and after OER, by modelling the inelastic loss functions of each, by blending REELS spectra of NiO and Fe_2O_3. The background subtracted spectra were then used to estimate the stoichiometric Fe:Ni, using a simplified transition probability estimate based on the Fermi's golden rule, allowing the intensities of the peaks to be related to the relative content of Fe and Ni. Post OER, a consistent increase in the Fe:Ni ratio was observed, especially for samples within the intermediate compositional window with the 10–20 at% Fe. Fe enrichment on the surface as a result of OER thus can be noted, with a corresponding increase in oxidation of Fe, with little change in the Ni spectra post OER, as seen from the Ni L edge XAS data. Post OER, the Fe L edge TEY XAS show significant changes, such as increased oxidation, while the PFY spectra remain mostly unchanged, indicating that OER does not affect the bulk of the samples as much as it does the surface. The Ni L edge spectra on the other hand show only subtle variations at the surface and almost none within the bulk, reinforcing the hypothesis that Fe plays a more active role in the redox reaction taking place during OER, while Ni is less active, providing structural support.

This was reinforced by the preliminary results obtained when scaling factors of the spectra were compared, before background subtraction. At this point, it was imperative that the changing catalytic structure be compared with the activity of the catalysts. The catalytic activity was seen to peak within a narrow compositional window of 10-20 at. % Fe, beyond which, the catalytic activity declines. This is proof that the changes observed within this window in the spectroscopic measurements bear direct relation to the catalytic activity of the samples. Furter increase of Fe concentration within the sample destabilizes the catalytically active Fe-O-Ni configuration, thereby resulting in the decline of the catalyst's efficiency.

The oxygen environment was also seen to evolve depending on the composition and as a result of OER. Again, the x=20 sample was observed as a critical transition point within the sample set. Within the compositional window mentioned above, an increase in both oxide and hydroxide environments was noted. Post OER, however, there was an overall increase in the oxide-like features, hinting at the formation of more covalent interactions between the metal centers and oxygen.

Another major aspect of this dissertation is the design and development of a custom *operando* electrochemical cell, compatible with high vacuum environments. The cell enables in situ and *operando* spectroscopic measurements under the application of external electrochemical potential. The design of the cell integrates electrolyte flow, electrical conductivity, gas bubble passage, while remaining vacuum compatible. First offline tests were conducted with the cell in the laboratory, in a set up replicating the physical conditions of the beamline. Satisfactory results were obtained, indicating that the *operando* electrochemical cell is functional.

The study thus has given information regarding the chemical and electronic state of the samples before and after OER and inferences have been based on how OER ultimately affected the local bonding environments of the transition metal centers as well as oxygen. As a next step, the samples have to be studied under *operando* conditions, for the purpose of which the *operando* electrochemical cell has been developed.

An important consideration is the fact that all analyses and inferences have been based on the assumption that the samples are homogeneous or as homogeneous as possible. However, the

possibility that some of the samples might be inhomogeneous exists. This would then affect the properties of the samples in different spots.

9 Bibliography

(1) You, B.; Sun, Y. Innovative Strategies for Electrocatalytic Water Splitting. *Acc. Chem. Res.* **2018**, *51* (7), 1571–1580. https://doi.org/10.1021/acs.accounts.8b00002.

(2) Li, J.; Zeng, J.; Zhao, F.; Sun, X.; Wang, S.; Lu, X. F. A Review on Highly Efficient Ru-Based Electrocatalysts for Acidic Oxygen Evolution Reaction. *Energy Fuels* **2024**, *38* (13), 11521–11540. https://doi.org/10.1021/acs.energyfuels.4c02080.

(3) Lee, Y.; Suntivich, J.; May, K. J.; Perry, E. E.; Shao-Horn, Y. Synthesis and Activities of Rutile IrO_2 and RuO_2 Nanoparticles for Oxygen Evolution in Acid and Alkaline Solutions. *J. Phys. Chem. Lett.* **2012**, *3* (3), 399–404. https://doi.org/10.1021/jz2016507.

(4) Hong, W. T.; Stoerzinger, K. A.; Lee, Y.-L.; Giordano, L.; Grimaud, A.; Johnson, A. M.; Hwang, J.; Crumlin, E. J.; Yang, W.; Shao-Horn, Y. Charge-Transfer-Energy-Dependent Oxygen Evolution Reaction Mechanisms for Perovskite Oxides. *Energy Environ. Sci.* **2017**, *10* (10), 2190–2200. https://doi.org/10.1039/C7EE02052J.

(5) Mefford, J. T.; Rong, X.; Abakumov, A. M.; Hardin, W. G.; Dai, S.; Kolpak, A. M.; Johnston, K. P.; Stevenson, K. J. Water Electrolysis on $La_{1-x}Sr_xCoO_{3-\delta}$ Perovskite Electrocatalysts. *Nat Commun* **2016**, *7* (1), 11053. https://doi.org/10.1038/ncomms11053.

(6) Menezes, P. W.; Indra, A.; Bergmann, A.; Chernev, P.; Walter, C.; Dau, H.; Strasser, P.; Driess, M. Uncovering the Prominent Role of Metal Ions in Octahedral versus Tetrahedral Sites of Cobalt–Zinc Oxide Catalysts for Efficient Oxidation of Water. *J. Mater. Chem. A* **2016**, *4* (25), 10014–10022. https://doi.org/10.1039/C6TA03644A.

(7) Cui, B.; Lin, H.; Li, J.-B.; Li, X.; Yang, J.; Tao, J. Core–Ring Structured $NiCo_2O_4$ Nanoplatelets: Synthesis, Characterization, and Electrocatalytic Applications. *Advanced Functional Materials* **2008**, *18* (9), 1440–1447. https://doi.org/10.1002/adfm.200700982.

(8) Dong, C.; Yuan, X.; Wang, X.; Liu, X.; Dong, W.; Wang, R.; Duan, Y.; Huang, F. Rational Design of Cobalt–Chromium Layered Double Hydroxide as a Highly Efficient Electrocatalyst for Water Oxidation. *J. Mater. Chem. A* **2016**, *4* (29), 11292–11298. https://doi.org/10.1039/C6TA04052G.

(9) Sadiek, I. M.; Mohammad, A. M.; El-Shakre, M. E.; El-Deab, M. S. Electrocatalytic Activity of Nickel Oxide Nanoparticles-Modified Electrodes: Optimization of the Loading Level and Operating pH towards the Oxygen Evolution Reaction. *International Journal of Hydrogen Energy* **2012**, *37* (1), 68–77. https://doi.org/10.1016/j.ijhydene.2011.09.097.

(10) Li, L.-F.; Li, Y.-F.; Liu, Z.-P. Oxygen Evolution Activity on NiOOH Catalysts: Four-Coordinated Ni Cation as the Active Site and the Hydroperoxide Mechanism. *ACS Catal.* **2020**, *10* (4), 2581–2590. https://doi.org/10.1021/acscatal.9b04975.

(11) Liao, C.; Yang, B.; Zhang, N.; Liu, M.; Chen, G.; Jiang, X.; Chen, G.; Yang, J.; Liu, X.; Chan, T.-S.; Lu, Y.-J.; Ma, R.; Zhou, W. Constructing Conductive Interfaces between Nickel Oxide Nanocrystals and Polymer Carbon Nitride for Efficient Electrocatalytic Oxygen Evolution Reaction. *Advanced Functional Materials* **2019**, *29* (40), 1904020. https://doi.org/10.1002/adfm.201904020.

(12) Gallenberger, J.; Moreno Fernández, H.; Alkemper, A.; Li, M.; Tian, C.; Kaiser, B.; Hofmann, J. P. Stability and Decomposition Pathways of the NiOOH OER Active Phase of NiO_x Electrocatalysts at Open Circuit Potential Traced by Ex Situ and in Situ Spectroscopies. *Catal. Sci. Technol.* **2023**, *13* (16), 4693–4700. https://doi.org/10.1039/D3CY00674C.

(13) Friebel, D.; Louie, M. W.; Bajdich, M.; Sanwald, K. E.; Cai, Y.; Wise, A. M.; Cheng, M.-J.; Sokaras, D.; Weng, T.-C.; Alonso-Mori, R.; Davis, R. C.; Bargar, J. R.; Nørskov, J. K.; Nilsson, A.; Bell, A. T. Identification of Highly Active Fe Sites in (Ni,Fe)OOH for Electrocatalytic Water Splitting. *J. Am. Chem. Soc.* **2015**, *137* (3), 1305–1313. https://doi.org/10.1021/ja511559d.
(14) Louie, M. W.; Bell, A. T. An Investigation of Thin-Film Ni–Fe Oxide Catalysts for the Electrochemical Evolution of Oxygen. *J. Am. Chem. Soc.* **2013**, *135* (33), 12329–12337. https://doi.org/10.1021/ja405351s.
(15) Trotochaud, L.; Young, S. L.; Ranney, J. K.; Boettcher, S. W. Nickel–Iron Oxyhydroxide Oxygen-Evolution Electrocatalysts: The Role of Intentional and Incidental Iron Incorporation. *J. Am. Chem. Soc.* **2014**, *136* (18), 6744–6753. https://doi.org/10.1021/ja502379c.
(16) Bonzel, H. P.; KLEINTt, C. ON THE HISTORY OF PHOTOEMISSION.
(17) Siegbahn, K. M. Kai M. Siegbahn – Facts - NobelPrize.Org.
(18) Siegbahn, K. Electron Spectroscopy - an Outlook. *Journal of Electron Spectroscopy and Related Phenomena* **1974**, *5* (1), 3–97. https://doi.org/10.1016/0368-2048(74)85005-X.
(19) Handbook of X-Ray Photoelectron Spectroscopy: A Reference Book of Standard Spectra for Identification and Interpretation of XPS Data, Update.; Moulder, J. F., Chastain, J., Eds.; *Perkin-Elmer Corporation: Eden Prairie, Minn,* **1992**.
(20) Hüfner, S. Photoelectron Spectroscopy; *Advanced Texts in Physics*; *Springer Berlin Heidelberg: Berlin*, Heidelberg, **2003**. https://doi.org/10.1007/978-3-662-09280-4.
(21) Seah, M. P.; Anthony, M. T. Quantitative XPS: The Calibration of Spectrometer Intensity—Energy Response Functions. 1—The Establishment of Reference Procedures and Instrument Behaviour. *Surface and Interface Analysis* **1984**, 6 (5), 230–241. https://doi.org/10.1002/sia.740060506.
(22) Seah, M. P.; Dench, W. A. Quantitative Electron Spectroscopy of Surfaces: A Standard Data Base for Electron Inelastic Mean Free Paths in Solids. *Surface and Interface Analysis* **1979**, *1* (1), 2–11. https://doi.org/10.1002/sia.740010103.
(23) Fadley, C. S.; Shirley, D. A. MULTIPLEX SPLITTING OF CORE-ELECTRON BINDING ENERGIES IN TRANSITION-METAL IONS. *PHYSICAL REVIEW LETTERS* **1969**, *23* (24).
(24) Kuzmany, H. Solid-State Spectroscopy: An Introduction; *Springer Berlin Heidelberg: Berlin*, Heidelberg, **2009**. https://doi.org/10.1007/978-3-642-01479-6.
(25) Dolbilkin, B. S.; Ratner, B. S. *PHYS-USP* **2007**, *50* (8), 853. https://doi.org/10.1070/PU2007v050n08ABEH006357.
(26) McMillan, E. M. The Synchrotron—A Proposed High Energy Particle Accelerator. *Phys. Rev.* **1945**, *68* (5–6), 143–144. https://doi.org/10.1103/PhysRev.68.143.
(27) KIT - IBPT - Discover - Test Facilities - KARA.Html. Discover – Test Facilities: KARA. Karlsruhe Institute of Technology. https://www.kit.edu/research/KARA
(28) MERIL.Html. Mapping of the European Research Infrastructure Landscape (MERIL). https://portal.meril.eu/
(29) Weinhardt, L.; Steininger, R.; Kreikemeyer-Lorenzo, D.; Mangold, S.; Hauschild, D.; Batchelor, D.; Spangenberg, T.; Heske, C. X-SPEC: A 70 eV to 15 keV Undulator Beamline for X-Ray and Electron Spectroscopies. *J Synchrotron Rad* **2021**, *28* (2), 609–617. https://doi.org/10.1107/S1600577520016318.
(30) Repoux, M. Comparison of Background Removal Methods for XPS. *Surface and Interface Analysis* **1992**, *18* (7), 567–570. https://doi.org/10.1002/sia.740180719.
(31) Van De Hulst, H. C.; Reesinck, J. J. M. Line Breadths and Voigt Profiles. *ApJ* **1947**, *106*, 121. https://doi.org/10.1086/144944.
(32) Kossel, W. Zum Bau der Rontgenspektren.

(33) Rehr, J. J.; Albers, R. C. Theoretical Approaches to X-Ray Absorption Fine Structure. *Rev. Mod. Phys.* **2000**, *72* (3), 621–654. https://doi.org/10.1103/RevModPhys.72.621.
(34) (Springer Series in Surface Sciences) Joachim Stöhr - NEXAFS Spectroscopy-Springer (**2010**).Pdf.
(35) Norman, D. X-Ray Absorption Spectroscopy (EXAFS and XANES) at Surfaces. *J. Phys. C: Solid State Phys.* **1986**, *19* (18), 3273–3311. https://doi.org/10.1088/0022-3719/19/18/006.
(36) Abbate, M.; Goedkoop, J. B.; de Groot, F. M. F.; Grioni, M.; Fuggle, J. C.; Hofmann, S.; Petersen, H.; Sacchi, M. Probing Depth of Soft X-Ray Absorption Spectroscopy Measured in Total-Electron-Yield Mode. *Surface and Interface Analysis* **1992**, *18* (1), 65–69. https://doi.org/10.1002/sia.740180111.
(37) Erbil, A.; Cargill Iii, G. S.; Frahm, R.; Boehme, R. F. Total-Electron-Yield Current Measurements for near-Surface Extended x-Ray-Absorption Fine Structure. *Phys. Rev. B* **1988**, *37* (5), 2450–2464. https://doi.org/10.1103/PhysRevB.37.2450.
(38) Petersen, H.; Jung, C.; Hellwig, C.; Peatman, W. B.; Gudat, W. Review of Plane Grating Focusing for Soft X-Ray Monochromators. *Review of Scientific Instruments* **1995**, *66* (1), 1–14. https://doi.org/10.1063/1.1145258.
(39) Jhi, S.-H.; Louie, S. G.; Cohen, M. L. Electronic Properties of Oxidized Carbon Nanotubes. *Phys. Rev. Lett.* **2000**, *85* (8), 1710–1713. https://doi.org/10.1103/PhysRevLett.85.1710.
(40) Eisebitt, S.; Böske, T.; Rubensson, J.-E.; Eberhardt, W. Determination of Absorption Coefficients for Concentrated Samples by Fluorescence Detection. *Phys. Rev. B* **1993**, *47* (21), 14103–14109. https://doi.org/10.1103/PhysRevB.47.14103.
(41) Trevorah, R. M.; Chantler, C. T.; Schalken, M. J. Solving Self-Absorption in Fluorescence. *IUCrJ* **2019**, *6* (4), 586–602. https://doi.org/10.1107/S2052252519005128.
(42) Bianconi, A. Multiplet Splitting of Final-State Configurations in x-Ray-Absorption Spectrum of Metal VO_2 : Effect of Core-Hole-Screening, Electron Correlation, and Metal-Insulator Transition. *Phys. Rev. B* **1982**, *26* (6), 2741–2747. https://doi.org/10.1103/PhysRevB.26.2741.
(43) Miedema, P. S.; De Groot, F. M. F. The Iron L Edges: Fe 2p X-Ray Absorption and Electron Energy Loss Spectroscopy. *Journal of Electron Spectroscopy and Related Phenomena* **2013**, *187*, 32–48. https://doi.org/10.1016/j.elspec.2013.03.005.
(44) Trzhaskovskaya, M. B.; Nefedov, V. I.; Yarzhemsky, V. G. PHOTOELECTRON ANGULAR DISTRIBUTION PARAMETERS FOR ELEMENTS Z=1 TO Z=54 IN THE PHOTOELECTRON ENERGY RANGE 100–5000 eV. *Atomic Data and Nuclear Data Tables* **2001**, *77* (1), 97–159. https://doi.org/10.1006/adnd.2000.0849.
(45) Millet, P. Fundamentals of Water Electrolysis. In *Hydrogen Production*; Godula-Jopek, A., Ed.; Wiley, **2015**; pp 33–62. https://doi.org/10.1002/9783527676507.ch2.
(46) Wang, H.; Zhang, K. H. L.; Hofmann, J. P.; De La Peña O'Shea, V. A.; Oropeza, F. E. The Electronic Structure of Transition Metal Oxides for Oxygen Evolution Reaction. *J. Mater. Chem. A* **2021**, *9* (35), 19465–19488. https://doi.org/10.1039/D1TA03732C.
(47) Chatenet, M.; Pollet, B. G.; Dekel, D. R.; Dionigi, F.; Deseure, J.; Millet, P.; Braatz, R. D.; Bazant, M. Z.; Eikerling, M.; Staffell, I.; Balcombe, P.; Shao-Horn, Y.; Schäfer, H. Water Electrolysis: From Textbook Knowledge to the Latest Scientific Strategies and Industrial Developments. *Chem. Soc. Rev.* **2022**, *51* (11), 4583–4762. https://doi.org/10.1039/D0CS01079K.
(48) Arun, A.; Gupta, C.; Howe, R. Polyether Ether Ketone (PEEK) Fluidic Cell to Study Electrochemistry of Microelectrodes on Silicon Substrate. *ECS Solid State Letters* **2015**, *4* (10), P67–P71. https://doi.org/10.1149/2.0021510ssl.

(49) Handbook of Reference Electrodes; Inzelt, G., Lewenstam, A., Scholz, F., Eds.; *Springer Berlin Heidelberg*: Berlin, Heidelberg, **2013**. https://doi.org/10.1007/978-3-642-36188-3.
(50) Ilic, B.; Czaplewski, D.; Neuzil, P.; Stanczyk, T.; Blough, J.; Maclay, G. J. Preparation and Characterization of Platinum Black Electrodes.
(51) Naumann, R.; Alexander-Weber, Ch.; Baucke, F. G. K. High-Precision pH Measurement by Means of Electrochemical Cells with Transference. *Fresenius J Anal Chem* **1994**, *349* (8–9), 639–642. https://doi.org/10.1007/BF00323470.
(52) Bard, A. J.; Faulkner, L. R. *Electrochemical Methods: Fundamentals and Applications*, 2nd ed.; Wiley: New York, **2001**.
(53) Jerkiewicz, G. Applicability of Platinum as a Counter-Electrode Material in Electrocatalysis Research. *ACS Catal.* **2022**, *12* (4), 2661–2670. https://doi.org/10.1021/acscatal.1c06040.
(54) Elgrishi, N.; Rountree, K. J.; McCarthy, B. D.; Rountree, E. S.; Eisenhart, T. T.; Dempsey, J. L. A Practical Beginner's Guide to Cyclic Voltammetry. *J. Chem. Educ.* **2018**, *95* (2), 197–206. https://doi.org/10.1021/acs.jchemed.7b00361.
(55) Ali-Löytty, H.; Louie, M. W.; Singh, M. R.; Li, L.; Sanchez Casalongue, H. G.; Ogasawara, H.; Crumlin, E. J.; Liu, Z.; Bell, A. T.; Nilsson, A.; Friebel, D. Ambient-Pressure XPS Study of a Ni–Fe Electrocatalyst for the Oxygen Evolution Reaction. *J. Phys. Chem. C* **2016**, *120* (4), 2247–2253. https://doi.org/10.1021/acs.jpcc.5b10931.
(56) Anwar, S.; Muthu, K. S.; Ganesh, V.; Lakshminarasimhan, N. A Comparative Study of Electrochemical Capacitive Behavior of $NiFe_2O_4$ Synthesized by Different Routes. *J. Electrochem. Soc.* **2011**, *158* (8), A976. https://doi.org/10.1149/1.3601863.
(57) Trasatti, S. Water Electrolysis: Who First? *Journal of Electroanalytical Chemistry* **1999**, *476* (1), 90–91. https://doi.org/10.1016/S0022-0728(99)00364-2.
(58) Shirvanian, P.; Van Berkel, F. Novel Components in Proton Exchange Membrane (PEM) Water Electrolyzers (PEMWE): Status, Challenges and Future Needs. A Mini Review. *Electrochemistry Communications* **2020**, *114*, 106704. https://doi.org/10.1016/j.elecom.2020.106704.
(59) Anantharaj, S.; Ede, S. R.; Sakthikumar, K.; Karthick, K.; Mishra, S.; Kundu, S. Recent Trends and Perspectives in Electrochemical Water Splitting with an Emphasis on Sulfide, Selenide, and Phosphide Catalysts of Fe, Co, and Ni: A Review. *ACS Catal.* **2016**, *6* (12), 8069–8097. https://doi.org/10.1021/acscatal.6b02479.
(60) Bi, J.; Ying, H.; Hao, J.; Li, Z. Application of Metal Chalcogenide-Based Anodic Electrocatalyst toward Substituting Oxygen Evolution Reaction in Water Splitting. *Current Opinion in Electrochemistry* **2022**, *33*, 100963. https://doi.org/10.1016/j.coelec.2022.100963.
(61) Kim, J.-H.; Lee, J.-G.; Choi, M.-J. Progress of Metal Chalcogenides as Catalysts for Efficient Electrosynthesis of Hydrogen Peroxide. *Materials* **2024**, *17* (17), 4277. https://doi.org/10.3390/ma17174277.
(62) Song, F.; Bai, L.; Moysiadou, A.; Lee, S.; Hu, C.; Liardet, L.; Hu, X. Transition Metal Oxides as Electrocatalysts for the Oxygen Evolution Reaction in Alkaline Solutions: An Application-Inspired Renaissance. *J. Am. Chem. Soc.* **2018**, *140* (25), 7748–7759. https://doi.org/10.1021/jacs.8b04546.
(63) Hong, W. T.; Risch, M.; Stoerzinger, K. A.; Grimaud, A.; Suntivich, J.; Shao-Horn, Y. Toward the Rational Design of Non-Precious Transition Metal Oxides for Oxygen Electrocatalysis. *Energy Environ. Sci.* **2015**, *8* (5), 1404–1427. https://doi.org/10.1039/C4EE03869J.
(64) Jiang, M.; Li, Y.; Lu, Z.; Sun, X.; Duan, X. Binary Nickel–Iron Nitride Nanoarrays as Bifunctional Electrocatalysts for Overall Water Splitting. *Inorg. Chem. Front.* **2016**, *3* (5), 630–634. https://doi.org/10.1039/C5QI00232J.

(65) Tamaki, Y.; Seino, S.; Shinyoshi, N.; Uetake, Y.; Nagai, T.; Monden, R.; Ishihara, A.; Nakagawa, T. Synthesis and Characterization of Titanium Oxynitride Catalyst via Direct Ammonia Nitridation of Titanium Polyacrylate for Oxygen Reduction Reaction. *J Mater. Sci: Mater Eng.* **2024**, *19* (1), 40. https://doi.org/10.1186/s40712-024-00189-1.

(66) Zhang, C.; Zhang, C.; Xie, Y.; Su, J.-W.; He, X.; Demaree, J. D.; Griep, M. H.; Atwood, J. L.; Lin, J. A Supramolecular Coordination-Polymer-Derived Electrocatalyst for the Oxygen Evolution Reaction. *Chemistry – A European Journal* **2019**, *25* (16), 4036–4039. https://doi.org/10.1002/chem.201805152.

(67) Pham Truong, T. N.; Randriamahazaka, H.; Ghilane, J. Polymer Brushes Ionic Liquid as a Catalyst for Oxygen Reduction and Oxygen Evolution Reactions. *ACS Catal.* **2018**, *8* (2), 869–875. https://doi.org/10.1021/acscatal.7b03158.

(68) Goryachev, A.; Etzi Coller Pascuzzi, M.; Carlà, F.; Weber, T.; Over, H.; Hensen, E. J. M.; Hofmann, J. P. Electrochemical Stability of RuO2(110)/Ru(0001) Model Electrodes in the Oxygen and Chlorine Evolution Reactions. *Electrochemical Acta* **2020**, *336*, 135713. https://doi.org/10.1016/j.electacta.2020.135713.

(69) Spöri, C.; Briois, P.; Nong, H. N.; Reier, T.; Billard, A.; Kühl, S.; Teschner, D.; Strasser, P. Experimental Activity Descriptors for Iridium-Based Catalysts for the Electrochemical Oxygen Evolution Reaction (OER). *ACS Catal.* **2019**, *9* (8), 6653–6663. https://doi.org/10.1021/acscatal.9b00648.

(70) Tüysüz, H. Alkaline Water Electrolysis for Green Hydrogen Production. *Acc. Chem. Res.* **2024**, *57* (4), 558–567. https://doi.org/10.1021/acs.accounts.3c00709.

(71) Schalenbach, M.; Tjarks, G.; Carmo, M.; Lueke, W.; Mueller, M.; Stolten, D. Acidic or Alkaline? Towards a New Perspective on the Efficiency of Water Electrolysis. *J. Electrochem. Soc.* **2016**, *163* (11), F3197–F3208. https://doi.org/10.1149/2.0271611jes.

(72) *Perovskites in catalysis and electrocatalysis*. https://doi.org/10.1126/science.aam7092.

(73) Cheng, X.; Fabbri, E.; Nachtegaal, M.; Castelli, I. E.; El Kazzi, M.; Haumont, R.; Marzari, N.; Schmidt, T. J. Oxygen Evolution Reaction on $La_{1-x}Sr_xCoO_3$ Perovskites: A Combined Experimental and Theoretical Study of Their Structural, Electronic, and Electrochemical Properties. *Chem. Mater.* **2015**, *27* (22), 7662–7672. https://doi.org/10.1021/acs.chemmater.5b03138.

(74) Shen, Z.; Zhuang, Y.; Li, W.; Huang, X.; Oropeza, F. E.; Hensen, E. J. M.; Hofmann, J. P.; Cui, M.; Tadich, A.; Qi, D.; Cheng, J.; Li, J.; Zhang, K. H. L. Increased Activity in the Oxygen Evolution Reaction by Fe^{4+} -Induced Hole States in Perovskite $La_{1-x}Sr_xFeO_3$. *J. Mater. Chem. A* **2020**, *8* (8), 4407–4415. https://doi.org/10.1039/C9TA13313E.

(75) Zhao, Q.; Yan, Z.; Chen, C.; Chen, J. Spinels: Controlled Preparation, Oxygen Reduction/Evolution Reaction Application, and Beyond. *Chem. Rev.* **2017**, *117* (15), 10121–10211. https://doi.org/10.1021/acs.chemrev.7b00051.

(76) Wei, C.; Feng, Z.; Scherer, G. G.; Barber, J.; Shao-Horn, Y.; Xu, Z. J. Cations in Octahedral Sites: A Descriptor for Oxygen Electrocatalysis on Transition-Metal Spinels. *Advanced Materials* **2017**, *29* (23), 1606800. https://doi.org/10.1002/adma.201606800.

(77) Cui, M.; Ding, X.; Huang, X.; Shen, Z.; Lee, T.-L.; Oropeza, F. E.; Hofmann, J. P.; Hensen, E. J. M.; Zhang, K. H. L. Ni^{3+}-Induced Hole States Enhance the Oxygen Evolution Reaction Activity of $Ni_xCo_{3-x}O_4$ Electrocatalysts. *Chem. Mater.* **2019**, *31* (18), 7618–7625. https://doi.org/10.1021/acs.chemmater.9b02453.

(78) Miles, M. H. EVALUATION OF ELECTROCATALYSTS FOR WATER ELECTROLYSIS IN ALKALINE SOLUTIONS.

(79) Corrigan, D. A. The Catalysis of the Oxygen Evolution Reaction by Iron Impurities in Thin Film Nickel Oxide Electrodes. *J. Electrochem. Soc.* **1987**, *134* (2), 377–384. https://doi.org/10.1149/1.2100463.
(80) Seh, Z. W.; Kibsgaard, J.; Dickens, C. F.; Chorkendorff, I.; Nørskov, J. K.; Jaramillo, T. F. Combining Theory and Experiment in Electrocatalysis: Insights into Materials Design. *Science* **2017**, *355* (6321), eaad4998. https://doi.org/10.1126/science.aad4998.
(81) Corrigan - 1987 - The Catalysis of the Oxygen Evolution Reaction by .Pdf.
(82) Ahn, H. S.; Bard, A. J. Surface Interrogation Scanning Electrochemical Microscopy of $Ni_{1-x}Fe_xOOH$ ($0 < x < 0.27$) Oxygen Evolving Catalyst: Kinetics of the "Fast" Iron Sites. *J. Am. Chem. Soc.* **2016**, *138* (1), 313–318. https://doi.org/10.1021/jacs.5b10977.
(83) Chen, J. Y. C.; Dang, L.; Liang, H.; Bi, W.; Gerken, J. B.; Jin, S.; Alp, E. E.; Stahl, S. S. Operando Analysis of NiFe and Fe Oxyhydroxide Electrocatalysts for Water Oxidation: Detection of Fe4+ by Mössbauer Spectroscopy. *J. Am. Chem. Soc.* **2015**, *137* (48), 15090–15093. https://doi.org/10.1021/jacs.5b10699.
(84) Görlin, M.; Chernev, P.; Ferreira De Araújo, J.; Reier, T.; Dresp, S.; Paul, B.; Krähnert, R.; Dau, H.; Strasser, P. Oxygen Evolution Reaction Dynamics, Faradaic Charge Efficiency, and the Active Metal Redox States of Ni–Fe Oxide Water Splitting Electrocatalysts. *J. Am. Chem. Soc.* **2016**, *138* (17), 5603–5614. https://doi.org/10.1021/jacs.6b00332.
(85) Li, N.; Bediako, D. K.; Hadt, R. G.; Hayes, D.; Kempa, T. J.; Von Cube, F.; Bell, D. C.; Chen, L. X.; Nocera, D. G. Influence of Iron Doping on Tetravalent Nickel Content in Catalytic Oxygen Evolving Films. *Proc. Natl. Acad. Sci. U.S.A.* **2017**, *114* (7), 1486–1491. https://doi.org/10.1073/pnas.1620787114.
(86) Zhang, J.; Winkler, J. R.; Gray, H. B.; Hunter, B. M. Mechanism of Nickel–Iron Water Oxidation Electrocatalysts. *Energy Fuels* **2021**, *35* (23), 19164–19169. https://doi.org/10.1021/acs.energyfuels.1c02674.
(87) Xiao, H.; Shin, H.; Goddard, W. A. Synergy between Fe and Ni in the Optimal Performance of (Ni,Fe)OOH Catalysts for the Oxygen Evolution Reaction. *Proc. Natl. Acad. Sci. U.S.A.* **2018**, *115* (23), 5872–5877. https://doi.org/10.1073/pnas.1722034115.
(88) Oliver-Tolentino, M. A.; Vázquez-Samperio, J.; Manzo-Robledo, A.; González-Huerta, R. de G.; Flores-Moreno, J. L.; Ramírez-Rosales, D.; Guzmán-Vargas, A. An Approach to Understanding the Electrocatalytic Activity Enhancement by Superexchange Interaction toward OER in Alkaline Media of Ni–Fe LDH. *J. Phys. Chem. C* **2014**, *118* (39), 22432–22438. https://doi.org/10.1021/jp506946b.
(89) Wartner, G.; Hein, D.; Bergmann, A.; Wendt, R.; Roldan Cuenya, B.; Seidel, R. Insights into the Electronic Structure of Fe–Ni Thin-Film Catalysts during the Oxygen Evolution Reaction Using *Operando* Resonant Photoelectron Spectroscopy. *J. Mater. Chem. A* **2023**, *11* (15), 8066–8080. https://doi.org/10.1039/D2TA08961K.
(90) Drevon, D.; Görlin, M.; Chernev, P.; Xi, L.; Dau, H.; Lange, K. M. Uncovering The Role of Oxygen in Ni-Fe(O_xH_y) Electrocatalysts Using In Situ Soft X-Ray Absorption Spectroscopy during the Oxygen Evolution Reaction. *Sci Rep* **2019**, *9* (1), 1532. https://doi.org/10.1038/s41598-018-37307-x.
(91) Daneshpour, R, Synthesis and Electrocatalytic Performance of Nickel-Iron Electrocatalysts for Oxygen Evolution Reaction, **2025** .Pdf.
(92) Yeh, J. J.; Lindau, I. Atomic Subshell Photoionization Cross Sections and Asymmetry Parameters: $1 \leqslant Z \leqslant 103$. *Atomic Data and Nuclear Data Tables* **1985**, *32* (1), 1–155. https://doi.org/10.1016/0092-640X(85)90016-6.

(93) Weinhardt, L.; Wansorra, C.; Steininger, R.; Spangenberg, T.; Hauschild, D.; Heske, C. High-Transmission Spectrometer for Rapid Resonant Inelastic Soft X-Ray Scattering (rRIXS) Maps. *J Synchrotron Rad* **2024**, *31* (6), 1481–1488. https://doi.org/10.1107/S160057752400804X.
(94) Kuai, L.; Geng, J.; Chen, C.; Kan, E.; Liu, Y.; Wang, Q.; Geng, B. A Reliable Aerosol-Spray-Assisted Approach to Produce and Optimize Amorphous Metal Oxide Catalysts for Electrochemical Water Splitting. *Angewandte Chemie International Edition* **2014**, *53* (29), 7547–7551. https://doi.org/10.1002/anie.201404208.
(95) Ma, J.; Lu, X.; Wang, C.; Wang, S.; He, W.; Zhang, B.; Shao, L.; Zhai, X.; Han, J.; Feng, S.; Fu, Y.; Qi, W. Synthesis of Amorphous FeNiCo Trimetallic Hybrid Electrode from ZIF Precursors for Efficient Oxygen Evolution Reaction. *Nanotechnology* **2022**, *33* (3), 035403. https://doi.org/10.1088/1361-6528/ac2dc9.
(96) Fayad, R.; Dhainy, J.; Ghandour, H.; Halaoui, L. Electrochemical Study of the Promoting Effect of Fe on Oxygen Evolution at Thin 'NiFe–Bi' Films and the Inhibiting Effect of Al in Borate Electrolyte. *Catal. Sci. Technol.* **2017**, *7* (17), 3876–3891. https://doi.org/10.1039/C7CY00873B.
(97) Smith, A. M.; Trotochaud, L.; Burke, M. S.; Boettcher, S. W. Contributions to Activity Enhancement via Fe Incorporation in Ni-(Oxy)Hydroxide/Borate Catalysts for near-Neutral pH Oxygen Evolution. *Chem. Commun.* **2015**, *51* (25), 5261–5263. https://doi.org/10.1039/C4CC08670H.
(98) Klaus, S.; Louie, M. W.; Trotochaud, L.; Bell, A. T. Role of Catalyst Preparation on the Electrocatalytic Activity of $Ni_{1-x}Fe_xOOH$ for the Oxygen Evolution Reaction. *J. Phys. Chem. C* **2015**, *119* (32), 18303–18316. https://doi.org/10.1021/acs.jpcc.5b04776.
(99) Gong, M.; Li, Y.; Wang, H.; Liang, Y.; Wu, J. Z.; Zhou, J.; Wang, J.; Regier, T.; Wei, F.; Dai, H. An Advanced Ni–Fe Layered Double Hydroxide Electrocatalyst for Water Oxidation. *J. Am. Chem. Soc.* **2013**, *135* (23), 8452–8455. https://doi.org/10.1021/ja4027715.
(100) Wilschefski, S. C.; Baxter, M. R. Inductively Coupled Plasma Mass Spectrometry: Introduction to Analytical Aspects. *Clin Biochem Rev* **2019**, *40* (3), 115–133. https://doi.org/10.33176/AACB-19-00024.
(101) Reed, S; Introduction to Energy Dispersive X-Ray Spectrometry (EDS) **1995** .Pdf.
(102) Nasirpouri, F. Electrodeposition of Nanostructured Materials; *Springer Series in Surface Sciences*; Springer International Publishing: Cham, **2017**; Vol. 62. https://doi.org/10.1007/978-3-319-44920-3.
(103) Horkans, J. On the Role of Buffers and Anions in NiFe Electrodeposition. *J. Electrochem. Soc.* **1979**, *126* (11), 1861–1867. https://doi.org/10.1149/1.2128816.
(104) Qi, Y.; He, C.; Zhang, R.; Wang, W. Analysis of Fe(II)-Ni(II) Electrochemical Reduction Process and Electrodeposition of FeNi Films. *Processes* **2022**, *10* (2), 198. https://doi.org/10.3390/pr10020198.
(105) Yang, R.; Xie, H.; Sun, Y.; Huang, W.; Fang, Y.; Liu, J. Codeposition Behavior of Fe-Ni Alloys: A Review in Mechanisms, Preparation and Effects on Composition. *Materials Science and Engineering: B* **2024**, *310*, 117723. https://doi.org/10.1016/j.mseb.2024.117723.
(106) Pedeferri - **2018** - Pourbaix Diagrams.Pdf.
(107) Nakano, H.; Matsuno, M.; Oue, S.; Yano, M.; Kobayashi, S.; Fukushima, H. Mechanism of Anomalous Type Electrodeposition of Fe-Ni Alloys from Sulfate Solutions.
(108) Pedeferri, P. Pourbaix Diagrams. In *Corrosion Science and Engineering*; Engineering Materials; Springer International Publishing: Cham, **2018**; pp 57–72. https://doi.org/10.1007/978-3-319-97625-9_4.

(109) Tambe, C. E.; Green, T. A.; Roy, S. The Multifaceted Role of Boric Acid in Nickel Electrodeposition and Electroforming. *J. Electrochem. Soc.* **2024**, *171* (10), 102503. https://doi.org/10.1149/1945-7111/ad80d3.
(110) Yin, K.-M.; Lin, B.-T. Effects of Boric Acid on the Electrodeposition of Iron, Nickel and Iron-Nickel. *Surface and Coatings Technology* **1996**, *78* (1–3), 205–210. https://doi.org/10.1016/0257-8972(94)02410-3.
(111) QUASES-Tougaard=20Ver5=20Manual.Pdf. http://www.quases.com/data/documents/QUASES-Tougaard=20Ver5=20Manual.pdf (accessed **2023-08-07**).
(112) Wojdyr, M. *Fityk* : A General-Purpose Peak Fitting Program. *J Appl Crystallogr* **2010**, *43* (5), 1126–1128. https://doi.org/10.1107/S0021889810030499.
(113) Louie, M. W.; Bell, A. T. An Investigation of Thin-Film Ni–Fe Oxide Catalysts for the Electrochemical Evolution of Oxygen. *J. Am. Chem. Soc.* **2013**, *135* (33), 12329–12337. https://doi.org/10.1021/ja405351s.
(114) Torabinejad, V.; Aliofkhazraei, M.; Assareh, S.; Allahyarzadeh, M. H.; Rouhaghdam, A. S. Electrodeposition of Ni-Fe Alloys, Composites, and Nano Coatings–A Review. *Journal of Alloys and Compounds* **2017**, *691*, 841–859. https://doi.org/10.1016/j.jallcom.2016.08.329.
(115) Grey, L. H.; Nie, H.-Y.; Biesinger, M. C. Defining the Nature of Adventitious Carbon and Improving Its Merit as a Charge Correction Reference for XPS. *Applied Surface Science* **2024**, *653*, 159319. https://doi.org/10.1016/j.apsusc.2024.159319.
(116) Greczynski, G.; Hultman, L. Impact of Sample Storage Type on Adventitious Carbon and Native Oxide Growth: X-Ray Photoelectron Spectroscopy Study. *Vacuum* **2022**, *205*, 111463. https://doi.org/10.1016/j.vacuum.2022.111463.
(117) Frischat, G. H.; Szurman, M.; Pfeiffer, T. Role of Sulfur and Its Diffusion in Silicate Glass Melts. *Int J of Appl Glass Sci* **2011**, *2* (1), 47–51. https://doi.org/10.1111/j.2041-1294.2011.00041.x.
(118) Grosvenor, A. P.; Kobe, B. A.; Biesinger, M. C.; McIntyre, N. S. Investigation of Multiplet Splitting of Fe 2p XPS Spectra and Bonding in Iron Compounds. *Surface and Interface Analysis* **2004**, *36* (12), 1564–1574. https://doi.org/10.1002/sia.1984.
(119) Wan, W.; Zhao, Y.; Wei, S.; Triana, C. A.; Li, J.; Arcifa, A.; Allen, C. S.; Cao, R.; Patzke, G. R. Mechanistic Insight into the Active Centers of Single/Dual-Atom Ni/Fe-Based Oxygen Electrocatalysts. *Nat Commun* **2021**, *12* (1), 5589. https://doi.org/10.1038/s41467-021-25811-0.
(120) Nesbitt, H. W.; Legrand, D.; Bancroft, G. M. Interpretation of Ni 2p XPS Spectra of Ni Conductors and Ni Insulators. *Physics and Chemistry of Minerals* **2000**, *27* (5), 357–366. https://doi.org/10.1007/s002690050265.
(121) Bagus, P. S.; Nelin, C. J.; Brundle, C. Richard.; Crist, B. V.; Ilton, E. S.; Lahiri, N.; Rosso, K. M. Main and Satellite Features in the Ni 2p XPS of NiO. *Inorg. Chem.* **2022**, *61* (45), 18077–18094. https://doi.org/10.1021/acs.inorgchem.2c02549.
(122) Mansour, A. N.; Melendres, C. A. Characterization of α -$Ni(OH)_2$ by XPS. *Surface Science Spectra* **1994**, *3* (3), 255–262. https://doi.org/10.1116/1.1247754.
(123) Hariki, A.; Uozumi, T.; Kuneš, J. LDA+DMFT Approach to Core-Level Spectroscopy: Application to 3 d Transition Metal Compounds. *Phys. Rev. B* **2017**, *96* (4), 045111. https://doi.org/10.1103/PhysRevB.96.045111.
(124) Wu, J.; Ma, Z.; Yu, L.; Wang, S.; Yang, F.; Feng, L. Phase and Chemical State Tuning of FeNi Oxides for Oxygen Evolution Reaction. *Sci. China Chem.* **2024**, *67* (8), 2755–2766. https://doi.org/10.1007/s11426-024-2077-2.

(125) Stevens, M. B.; Trang, C. D. M.; Enman, L. J.; Deng, J.; Boettcher, S. W. Reactive Fe-Sites in Ni/Fe (Oxy)Hydroxide Are Responsible for Exceptional Oxygen Electrocatalysis Activity. *J. Am. Chem. Soc.* **2017**, *139* (33), 11361–11364. https://doi.org/10.1021/jacs.7b07117.
(126) Merino, N. A.; Barbero, B. P.; Eloy, P.; Cadús, L. E. $La_{1-x}Ca_xCoO_3$ Perovskite-Type Oxides: Identification of the Surface Oxygen Species by XPS. *Applied Surface Science* **2006**, *253* (3), 1489–1493. https://doi.org/10.1016/j.apsusc.2006.02.035.
(127) Longo, F.; Billeter, E.; Kazaz, S.; Cesarini, A.; Nikolic, M.; Chacko, A.; Schmutz, P.; Novotny, Z.; Borgschulte, A. Hard X-Ray Photoelectron Spectroscopy Reveals Self-Organized Structures of Electrocatalytic Nickel Oxy-Hydroxides. *Surface Science* **2024**, *739*, 122397. https://doi.org/10.1016/j.susc.2023.122397.
(128) Radinger, H.; Connor, P.; Tengeler, S.; Stark, R. W.; Jaegermann, W.; Kaiser, B. Importance of Nickel Oxide Lattice Defects for Efficient Oxygen Evolution Reaction. *Chem. Mater.* **2021**, *33* (21), 8259–8266. https://doi.org/10.1021/acs.chemmater.1c02406.
(129) Carley, A. F.; Rassias, S.; Roberts, M. W. THE SPECIFICITY OF SURFACE OXYGEN IN THE ACTIVATION OF ADSORBED WATER AT METAL SURFACES.
(130) Biesinger, M. C.; Payne, B. P.; Grosvenor, A. P.; Lau, L. W. M.; Gerson, A. R.; Smart, R. St. C. Resolving Surface Chemical States in XPS Analysis of First Row Transition Metals, Oxides and Hydroxides: Cr, Mn, Fe, Co and Ni. *Applied Surface Science* **2011**, *257* (7), 2717–2730. https://doi.org/10.1016/j.apsusc.2010.10.051.
(131) Francàs, L.; Corby, S.; Selim, S.; Lee, D.; Mesa, C. A.; Godin, R.; Pastor, E.; Stephens, I. E. L.; Choi, K.-S.; Durrant, J. R. Spectroelectrochemical Study of Water Oxidation on Nickel and Iron Oxyhydroxide Electrocatalysts. *Nat Commun* **2019**, *10* (1), 5208. https://doi.org/10.1038/s41467-019-13061-0.
(132) Govind Rajan, A.; Martirez, J. M. P.; Carter, E. A. Strongly Facet-Dependent Activity of Iron-Doped β-Nickel Oxyhydroxide for the Oxygen Evolution Reaction. *Phys. Chem. Chem. Phys.* **2024**, *26* (20), 14721–14733. https://doi.org/10.1039/D4CP00315B.
(133) He, B.; Bai, F.; Jain, P.; Li, T. A Review of Surface Reconstruction and Transformation of 3d Transition-Metal (Oxy)Hydroxides and Spinel-Type Oxides during the Oxygen Evolution Reaction. *Small* **2025**, *21* (10), 2411479. https://doi.org/10.1002/smll.202411479.
(134) De Groot, F. M. F. X-Ray Absorption and Dichroism of Transition Metals and Their Compounds. *Journal of Electron Spectroscopy and Related Phenomena* **1994**, *67* (4), 529–622. https://doi.org/10.1016/0368-2048(93)02041-J.
(135) Abbate, M.; De Groot, F. M. F.; Fuggle, J. C.; Fujimori, A.; Strebel, O.; Lopez, F.; Domke, M.; Kaindl, G.; Sawatzky, G. A.; Takano, M.; Takeda, Y.; Eisaki, H.; Uchida, S. Controlled-Valence Properties of $La_{1-x}Sr_xFeO_3$ and $La_{1-x}Sr_xMnO_3$ Studied by Soft-x-Ray Absorption Spectroscopy. *Phys. Rev. B* **1992**, *46* (8), 4511–4519. https://doi.org/10.1103/PhysRevB.46.4511.
(136) Miedema, P. S.; De Groot, F. M. F. The Iron L Edges: Fe 2p X-Ray Absorption and Electron Energy Loss Spectroscopy. *Journal of Electron Spectroscopy and Related Phenomena* **2013**, *187*, 32–48. https://doi.org/10.1016/j.elspec.2013.03.005.
(137) Ikeno, H.; De Groot, F. M. F.; Stavitski, E.; Tanaka, I. Multiplet Calculations of $L_{2,3}$ x-Ray Absorption near-Edge Structures for 3d Transition-Metal Compounds. *J. Phys.: Condens. Matter* **2009**, *21* (10), 104208. https://doi.org/10.1088/0953-8984/21/10/104208.
(138) Hocking, R. K.; DeBeer George, S.; Raymond, K. N.; Hodgson, K. O.; Hedman, B.; Solomon, E. I. Fe L-Edge XAS Determination of Differential Orbital Covalency of Siderophore Model Compounds: Electronic Structure Contributions to High Stability Constants. *J Am Chem Soc* **2010**, *132* (11), 4006–4015. https://doi.org/10.1021/ja9090098.

(139) Wasinger, E. C.; de Groot, F. M. F.; Hedman, B.; Hodgson, K. O.; Solomon, E. I. L-Edge X-Ray Absorption Spectroscopy of Non-Heme Iron Sites: Experimental Determination of Differential Orbital Covalency. *J. Am. Chem. Soc.* **2003**, *125* (42), 12894–12906. https://doi.org/10.1021/ja034634s.
(140) de Groot, F. The 2p X-Ray Absorption Spectra of Transition Metal Systems: New Developments and Ab-Initio Routes.
(141) Sorgenfrei, F.; Alouani, M.; Schött, J.; Jönsson, H. J. M.; Eriksson, O.; Thunström, P. Theory of X-Ray Absorption Spectroscopy for Ferrites. *Phys. Rev. B* **2024**, *109* (11), 115126. https://doi.org/10.1103/PhysRevB.109.115126.
(142) Chen, S.; Kang, Z.; Zhang, X.; Xie, J.; Wang, H.; Shao, W.; Zheng, X.; Yan, W.; Pan, B.; Xie, Y. Highly Active Fe Sites in Ultrathin Pyrrhotite Fe7S8 Nanosheets Realizing Efficient Electrocatalytic Oxygen Evolution. *ACS Cent Sci* **2017**, *3* (11), 1221–1227. https://doi.org/10.1021/acscentsci.7b00424.
(143) Moschkowitsch, W.; Zion, N.; Honig, H. C.; Levy, N.; Cullen, D. A.; Elbaz, L. Mixed-Metal Nickel–Iron Oxide Aerogels for Oxygen Evolution Reaction. *ACS Catal.* **2022**, *12* (19), 12162–12169. https://doi.org/10.1021/acscatal.2c03351.
(144) Zou, S.; Burke, M. S.; Kast, M. G.; Fan, J.; Danilovic, N.; Boettcher, S. W. Fe (Oxy)Hydroxide Oxygen Evolution Reaction Electrocatalysis: Intrinsic Activity and the Roles of Electrical Conductivity, Substrate, and Dissolution. *Chem. Mater.* **2015**, *27* (23), 8011–8020. https://doi.org/10.1021/acs.chemmater.5b03404.
(145) Ou, Y.; Twight, L. P.; Samanta, B.; Liu, L.; Biswas, S.; Fehrs, J. L.; Sagui, N. A.; Villalobos, J.; Morales-Santelices, J.; Antipin, D.; Risch, M.; Toroker, M. C.; Boettcher, S. W. Cooperative Fe Sites on Transition Metal (Oxy)Hydroxides Drive High Oxygen Evolution Activity in Base. *Nat Commun* **2023**, *14* (1), 7688. https://doi.org/10.1038/s41467-023-43305-z.
(146) Lee, K. B.; Jo, S.; Choi, H.; Lee, Y.-W.; Sohn, J. I. Boosting Catalyst Activity with High Valency Metal Species through Fe Doping on Normal Spinel $NiCr_2O_4$ for Superior Water Oxidation. *Applied Surface Science* **2023**, *609*, 155326. https://doi.org/10.1016/j.apsusc.2022.155326.
(147) Guo, M.; Temperton, R.; D'Acunto, G.; Johansson, N.; Jones, R.; Handrup, K.; Ringelband, S.; Prakash, O.; Fan, H.; de Groot, L. H. M.; Hlynsson, V. F.; Kaufhold, S.; Gordivska, O.; Velásquez González, N.; Wärnmark, K.; Schnadt, J.; Persson, P.; Uhlig, J. Using Iron L-Edge and Nitrogen K-Edge X-Ray Absorption Spectroscopy to Improve the Understanding of the Electronic Structure of Iron Carbene Complexes. *Inorg. Chem.* **2024**, *63* (27), 12457–12468. https://doi.org/10.1021/acs.inorgchem.4c01026.
(148) Henderson, G. S.; De Groot, F. M. F.; Moulton, B. J. A. X-Ray Absorption Near-Edge Structure (XANES) Spectroscopy. *Reviews in Mineralogy and Geochemistry* **2014**, *78* (1), 75–138. https://doi.org/10.2138/rmg.2014.78.3.
(149) Achkar, A. J.; Regier, T. Z.; Wadati, H.; Kim, Y.-J.; Zhang, H.; Hawthorn, D. G. Bulk Sensitive X-Ray Absorption Spectroscopy Free of Self-Absorption Effects. *Phys. Rev. B* **2011**, *83* (8), 081106. https://doi.org/10.1103/PhysRevB.83.081106.
(150) Kaya, S.; Ogasawara, H.; Nilsson, A. Determination of the Surface Electronic Structure of Fe_3O_4(1 1 1) by Soft X-Ray Spectroscopy. *Catalysis Today* **2015**, *240*, 184–189. https://doi.org/10.1016/j.cattod.2014.07.025.
(151) McLeod, J. A.; Boukhvalov, D. W.; Zatsepin, D. A.; Green, R. J.; Leedahl, B.; Cui, L.; Kurmaev, E. Z.; Zhidkov, I. S.; Finkelstein, L. D.; Gavrilov, N. V.; Cholakh, S. O.; Moewes, A. Local Structure of Fe Impurity Atoms in ZnO: Bulk versus Surface. *arXiv* February 16, **2014**. https://doi.org/10.48550/arXiv.1402.3799.

(152) Esaka, F.; Yamamoto, H.; Udono, H.; Matsubayashi, N.; Yamaguchi, K.; Shamoto, S.; Magara, M.; Kimura, T. Surface Characterization of Homoepitaxial β - $FeSi_2$ Film on β - $FeSi_2$ (111) Substrate by X-Ray Photoelectron and Absorption Spectroscopy. *Physics Procedia* **2011**, *11*, 150–153. https://doi.org/10.1016/j.phpro.2011.01.043.
(153) De Groot, F. M. F. Differences between L_3 and L_2 X-Ray Absorption Spectra. *Physica B: Condensed Matter* **1995**, *208–209*, 15–18. https://doi.org/10.1016/0921-4526(94)00817-F.
(154) Chang, Y. K.; Lin, K. P.; Pong, W. F.; Tsai, M.-H.; Hseih, H. H.; Pieh, J. Y.; Tseng, P. K.; Lee, J. F.; Hsu, L. S. Charge Transfer and Hybridization Effects in Ni_3Al and Ni_3Ga Studies by X-Ray-Absorption Spectroscopy and Theoretical Calculations. *Journal of Applied Physics* **2000**, *87* (3), 1312–1317. https://doi.org/10.1063/1.372015.
(155) Chen, X.; Choi, J.; Jiang, Z.; Mei, J.; Jiang, K.; Li, J.; Agrestini, S.; Garcia-Fernandez, M.; Sun, H.; Huang, X.; Shen, D.; Wang, M.; Hu, J.; Lu, Y.; Zhou, K.-J.; Feng, D. Electronic and Magnetic Excitations in La3Ni2O7. *Nat Commun* **2024**, *15* (1), 9597. https://doi.org/10.1038/s41467-024-53863-5.
(156) Al Samarai, M.; Hahn, A. W.; Beheshti Askari, A.; Cui, Y.-T.; Yamazoe, K.; Miyawaki, J.; Harada, Y.; Rüdiger, O.; DeBeer, S. Elucidation of Structure–Activity Correlations in a Nickel Manganese Oxide Oxygen Evolution Reaction Catalyst by Operando Ni L-Edge X-Ray Absorption Spectroscopy and 2p3d Resonant Inelastic X-Ray Scattering. *ACS Appl. Mater. Interfaces* **2019**, *11* (42), 38595–38605. https://doi.org/10.1021/acsami.9b06752.
(157) Bagyinka, C.; Whitehead, J. P.; Maroney, M. J. An X-Ray Absorption Spectroscopic Study of Nickel Redox Chemistry in Hydrogenase. *J. Am. Chem. Soc.* **1993**, *115* (9), 3576–3585. https://doi.org/10.1021/ja00062a022.
(158) Kuai, C.; Zhang, Y.; Wu, D.; Sokaras, D.; Mu, L.; Spence, S.; Nordlund, D.; Lin, F.; Du, X.-W. Fully Oxidized Ni–Fe Layered Double Hydroxide with 100% Exposed Active Sites for Catalyzing Oxygen Evolution Reaction. *ACS Catal.* **2019**, *9* (7), 6027–6032. https://doi.org/10.1021/acscatal.9b01935.
(159) Togonon, J. J. H.; Chotard, J.-N.; Longo, A.; Stievano, L.; Croguennec, L.; Iadecola, A. Insights on the Role of the Covalent Ni-O Bonds in $LiNiO_2$ Positive Electrodes: A Correlative Hard X-Ray Spectroscopy Study.
(160) Azfar Shaida, M.; Verma, S.; Talukdar, S.; Kumar, N.; Salim Mahtab, M.; Naushad, Mu.; Haq Farooqi, I. Critical Analysis of the Role of Various Iron-Based Heterogeneous Catalysts for Advanced Oxidation Processes: A State-of-the-Art Review. *Journal of Molecular Liquids* **2023**, *374*, 121259. https://doi.org/10.1016/j.molliq.2023.121259.
(161) Grosvenor, A. P.; Kobe, B. A.; Biesinger, M. C.; McIntyre, N. S. Investigation of Multiplet Splitting of Fe 2p XPS Spectra and Bonding in Iron Compounds. *Surface and Interface Analysis* **2004**, *36* (12), 1564–1574. https://doi.org/10.1002/sia.1984.
(162) Habibimarkani, H.; Abram, S.-L.; Guilherme Buzanich, A.; Prinz, C.; Sahre, M.; Hodoroaba, V.-D.; Radnik, J. In-Depth Analysis of FeNi-Based Nanoparticles for the Oxygen Evolution Reaction. *Sci Rep* **2025**, *15* (1), 8339. https://doi.org/10.1038/s41598-025-92720-3.
(163) Li, F.; Li, Y.; Li, L.; Luo, W.; Lu, Z.; Zhang, X.; Zheng, Z. Heterostructured FeNi Hydroxide for Effective Electrocatalytic Oxygen Evolution. *Chem. Sci.* **2022**, *13* (32), 9256–9264. https://doi.org/10.1039/D2SC02767D.
(164) Avval, T. G.; Gallagher, N.; Morgan, D.; Bargiela, P.; Fairley, N.; Fernandez, V.; Linford, M. R. Practical Guide on Chemometrics/Informatics in x-Ray Photoelectron Spectroscopy (XPS). I. Introduction to Methods Useful for Large or Complex Datasets. *Journal of Vacuum Science & Technology A* **2022**, *40* (6). https://doi.org/10.1116/6.0002082.

(165) Pielsticker, L.; Nicholls, R. L.; DeBeer, S.; Greiner, M. Convolutional Neural Network Framework for the Automated Analysis of Transition Metal X-Ray Photoelectron Spectra. *Analytica Chimica Acta* **2023**, *1271*, 341433. https://doi.org/10.1016/j.aca.2023.341433.
(166) Yubero, F.; González-Elipe, A. R.; Tougaard, S. Determination of Growth Mechanisms by X-Ray Photoemission and Ion Scattering Spectroscopies: Application to Thin Iron Oxide Films Deposited on SiO_2. *Surface Science* **2000**, *457* (1–2), 24–36. https://doi.org/10.1016/S0039-6028(00)00370-8.
(167) Pauly, N.; Yubero, F.; García-García, F. J.; Tougaard, S. Quantitative Analysis of Ni 2p Photoemission in NiO and Ni Diluted in a SiO_2 Matrix. *Surface Science* **2016**, *644*, 46–52. https://doi.org/10.1016/j.susc.2015.09.012.
(168) Hüfner, S. *Photoelectron Spectroscopy: Principles and Applications*; Springer Science & Business Media, **2013**.
(169) Linke, J.; Rohrbach, T.; Clark, A. H.; Borca, C.; Huthwelker, T.; Buchauer, F. L.; Kraglund, M. R.; Chatzichristodoulou, C.; Meade, E.; Guehl, J.; Wojtas, M.; Ranocchiari, M.; Schmidt, T. J.; Fabbri, E. The Role of Fe Incorporation into Ni-MOF-74 Derived Oxygen Evolution Electrocatalysts for Anion Exchange Membrane Water Electrolysis. *EES Catal.* **2025**, *3* (3), 505–514. https://doi.org/10.1039/D4EY00250D.
(170) Dionigi, F.; Strasser, P. NiFe-Based (Oxy)Hydroxide Catalysts for Oxygen Evolution Reaction in Non-Acidic Electrolytes. *Advanced Energy Materials* **2016**, *6* (23), 1600621. https://doi.org/10.1002/aenm.201600621.
(171) Hocking, R. K.; DeBeer George, S.; Raymond, K. N.; Hodgson, K. O.; Hedman, B.; Solomon, E. I. Fe L-Edge XAS Determination of Differential Orbital Covalency of Siderophore Model Compounds: Electronic Structure Contributions to High Stability Constants. *J Am Chem Soc* **2010**, *132* (11), 4006–4015. https://doi.org/10.1021/ja9090098.
(172) Zheng, X.; Zhang, B.; De Luna, P.; Liang, Y.; Comin, R.; Voznyy, O.; Han, L.; García De Arquer, F. P.; Liu, M.; Dinh, C. T.; Regier, T.; Dynes, J. J.; He, S.; Xin, H. L.; Peng, H.; Prendergast, D.; Du, X.; Sargent, E. H. Theory-Driven Design of High-Valence Metal Sites for Water Oxidation Confirmed Using in Situ Soft X-Ray Absorption. *Nature Chem* **2018**, *10* (2), 149–154. https://doi.org/10.1038/nchem.2886.
(173) Fan, Y.; Zhang, C.; Zhang, L.; Zhou, J.; Li, Y.; Huang, Y.-C.; Ma, J.; Chan, T.-S.; Chen, C.-T.; Jing, C.; Mijit, E.; Hu, Z.; Wang, J.-Q.; Zhang, L. Novel Mechanism of Fe^{4+}/Ni^{3+} Synergistic Effect via Exchange Energy Gain for Boosting Water Oxidation. *Chem Catalysis* **2024**, *4* (5), 100981. https://doi.org/10.1016/j.checat.2024.100981.
(174) Radinger, H.; Connor, P.; Tengeler, S.; Stark, R. W.; Jaegermann, W.; Kaiser, B. Importance of Nickel Oxide Lattice Defects for Efficient Oxygen Evolution Reaction. *Chem. Mater.* **2021**, *33* (21), 8259–8266. https://doi.org/10.1021/acs.chemmater.1c02406.
(175) Yang, C.; Ling, W.; Zhu, Y.; Yang, Y.; Dong, S.; Wu, C.; Wang, Z.; Yang, S.; Li, J.; Wang, G.; Huang, Y.; Yang, B.; Cheng, Q.; Liu, Z.; Yang, H. Surface Hydroxylation Engineering to Boost Oxygen Evolution Reaction on IrO2/TiO2 for PEM Water Electrolyzer. *Applied Catalysis B: Environment and Energy* **2024**, *358*, 124462. https://doi.org/10.1016/j.apcatb.2024.124462.
(176) Chen, B.; Ivanov, I.; Park, J. M.; Parrinello, M.; Klein, M. L. Solvation Structure and Mobility Mechanism of OH^-: A Car−Parrinello Molecular Dynamics Investigation of Alkaline Solutions. *J. Phys. Chem. B* **2002**, *106* (46), 12006–12016. https://doi.org/10.1021/jp026504w.
(177) Bagus, P. S.; Nelin, C. J.; Brundle, C. R. Chemical Significance of X-Ray Photoelectron Spectroscopy Binding Energy Shifts: A Perspective. *Journal of Vacuum Science & Technology A* **2023**, *41* (6), 068501. https://doi.org/10.1116/6.0003081.

(178) de Groot, F. High-Resolution X-Ray Emission and X-Ray Absorption Spectroscopy. *Chem. Rev.* **2001**, *101* (6), 1779–1808. https://doi.org/10.1021/cr9900681.
(179) Huang, H.; Russell, A. E. Approaches to Achieve Surface Sensitivity in the in Situ XAS of Electrocatalysts. *Current Opinion in Electrochemistry* **2021**, *27*, 100681. https://doi.org/10.1016/j.coelec.2020.100681.
(180) Figueiredo, M. O.; Mirão, J. Electronic State of Oxygen in Oxide Minerals: An XAS Study on the Influence of Cationic Environment. *ejm* **2002**, *14* (6), 1061–1067. https://doi.org/10.1127/0935-1221/2002/0014-1061.
(181) Näslund, L.-Å.; Lüning, J.; Ufuktepe, Y.; Ogasawara, H.; Wernet, Ph.; Bergmann, U.; Pettersson, L. G. M.; Nilsson, A. X-Ray Absorption Spectroscopy Measurements of Liquid Water. *J. Phys. Chem. B* **2005**, *109* (28), 13835–13839. https://doi.org/10.1021/jp052046q.
(182) He, Z.; Zhang, J.; Gong, Z.; Lei, H.; Zhou, D.; Zhang, N.; Mai, W.; Zhao, S.; Chen, Y. Activating Lattice Oxygen in NiFe-Based (Oxy)Hydroxide for Water Electrolysis. *Nat Commun* **2022**, *13* (1), 2191. https://doi.org/10.1038/s41467-022-29875-4.
(183) Dionigi, F.; Zeng, Z.; Sinev, I.; Merzdorf, T.; Deshpande, S.; Lopez, M. B.; Kunze, S.; Zegkinoglou, I.; Sarodnik, H.; Fan, D.; Bergmann, A.; Drnec, J.; Araujo, J. F. D.; Gliech, M.; Teschner, D.; Zhu, J.; Li, W.-X.; Greeley, J.; Cuenya, B. R.; Strasser, P. In-Situ Structure and Catalytic Mechanism of NiFe and CoFe Layered Double Hydroxides during Oxygen Evolution. *Nat Commun* **2020**, *11* (1), 2522. https://doi.org/10.1038/s41467-020-16237-1.
(184) Holliday, J. E. OF SURFACES BY SOFT X-RAY.
(185) CXRO X-Ray Interactions with Matter. https://henke.lbl.gov/optical_constants/ (accessed **2025-05-09**).
(186) Fuchs, O.; Maier, F.; Weinhardt, L.; Weigand, M.; Blum, M.; Zharnikov, M.; Denlinger, J.; Grunze, M.; Heske, C.; Umbach, E. A Liquid Flow Cell to Study the Electronic Structure of Liquids with Soft X-Rays. *Nuclear Instruments and Methods in Physics Research Section A: Accelerators, Spectrometers, Detectors and Associated Equipment* **2008**, *585* (3), 172–177. https://doi.org/10.1016/j.nima.2007.10.029.
(187) Dastafkan, K.; Wang, S.; Song, S.; Meyer, Q.; Zhang, Q.; Shen, Y.; Zhao, C. *Operando* Monitoring of Gas Bubble Evolution in Water Electrolysis by Single High-Frequency Impedance. *EES Catal.* **2023**, *1* (6), 998–1008. https://doi.org/10.1039/D3EY00182B.
(188) Prajapati, A.; Hahn, C.; Weidinger, I. M.; Shi, Y.; Lee, Y.; Alexandrova, A. N.; Thompson, D.; Bare, S. R.; Chen, S.; Yan, S.; Kornienko, N. Best Practices for In-Situ and Operando Techniques within Electrocatalytic Systems. *Nat Commun* **2025**, *16* (1), 2593. https://doi.org/10.1038/s41467-025-57563-6.
(189) Bluhm, H. Photoelectron Spectroscopy of Surfaces under Humid Conditions. *Journal of Electron Spectroscopy and Related Phenomena* **2010**, *177* (2–3), 71–84. https://doi.org/10.1016/j.elspec.2009.08.006.
(190) Heske, C.; Groh, U.; Fuchs, O.; Weinhardt, L.; Umbach, E.; Schedel-Niedrig, Th.; Fischer, Ch.-H.; Lux-Steiner, M. Ch.; Zweigart, S.; Niesen, T. P.; Karg, F.; Denlinger, J. D.; Rude, B.; Andrus, C.; Powell, F. Monitoring Chemical Reactions at a Liquid–Solid Interface: Water on $CuIn(S,Se)_2$ Thin Film Solar Cell Absorbers. *The Journal of Chemical Physics* **2003**, *119* (20), 10467–10470. https://doi.org/10.1063/1.1627328.
(191) Benkert, A.; Blum, M.; Meyer, F.; Wilks, R. G.; Yang, W.; Bär, M.; Reinert, F.; Heske, C.; Weinhardt, L. Setup for *in Situ* Investigation of Gases and Gas/Solid Interfaces by Soft x-Ray Emission and Absorption Spectroscopy. *Review of Scientific Instruments* **2014**, *85* (1), 015119. https://doi.org/10.1063/1.4862059.

(192) Lange, K. M.; Könnecke, R.; Ghadimi, S.; Golnak, R.; Soldatov, M. A.; Hodeck, K. F.; Soldatov, A.; Aziz, E. F. High Resolution X-Ray Emission Spectroscopy of Water and Aqueous Ions Using the Micro-Jet Technique. *Chemical Physics* **2010**, *377* (1–3), 1–5. https://doi.org/10.1016/j.chemphys.2010.08.023.
(193) Blum, M.; Weinhardt, L.; Fuchs, O.; Bär, M.; Zhang, Y.; Weigand, M.; Krause, S.; Pookpanratana, S.; Hofmann, T.; Yang, W.; Denlinger, J. D.; Umbach, E.; Heske, C. Solid and Liquid Spectroscopic Analysis (SALSA)–a Soft x-Ray Spectroscopy Endstation with a Novel Flow-through Liquid Cell. *Review of Scientific Instruments* **2009**, *80* (12), 123102. https://doi.org/10.1063/1.3257926.
(194) Schwanke, C.; Golnak, R.; Xiao, J.; Lange, K. M. Electrochemical Flowcell for *in-Situ* Investigations by Soft x-Ray Absorption and Emission Spectroscopy. *Review of Scientific Instruments* **2014**, *85* (10), 103120. https://doi.org/10.1063/1.4899063.

Acknowledgements

This dissertation would be impossible to complete without the guidance, support and mentorship of several people.

I would like to thank the National Science Foundation (NSF) and Deutsche Forschungsgemeinschaft (DFG) for funding this project.

I would like to extend my heartfelt gratitude to Prof. Dr. Clemens Heske for giving me the opportunity to work on this exciting project in the Spectroscopy group at IPS in KIT. Thank you for your mentorship and all our scientific discussions throughout the years. Moreover, I would like to thank you for the advice you gave me which might not have been related directly to the science discussed in this thesis, but more importantly that helped me keep myself calm and collected through stressful situations and that have helped me take several career-shaping decisions.

I would also like to thank Prof. Dr. Tonya Vitiova for agreeing to be my second supervisor from the faculty of Chemistry and Biosciences.

I would like to thank Dr. Lothar Weinhardt for being a very approachable and involved PI for this NSF-DFG funded project that we were part of.

Thank you to Prof. Dr. Clemens Heske, Dr. Lothar Weinhardt and Dr. Dirk Hauschild and Dr. Constantin Wansorra for teaching me everything I know about spectroscopy. Thank you for always being open to answering my queries, helping me with answering my own questions myself, learning everything I could about the different aspects of conducting the different experiments both in the laboratory and at the beamline. Thank you, Lothar, for encouraging me to take decisions regarding my research work and data analysis myself, which in turn have helped shape me into an independent researcher and thank you for always pushing me to clarify my basic concepts. Thank you, Dirk, for helping me understand and navigate several scientific aspects of data analysis and learning the use of different software and methods to extract meaningful trends from the measured data. Additionally, also thank you for teaching me to plot and present data in ways that are scientifically accurate. Thank you, Constantin, for helping me conduct experiments at the beamline by optimizing the beamline optics and helping me learn the correct methods for energy calibration of the data without which no further analysis would have been possible. Thank you for also listening to several of my ideas that were not always necessarily viable. Thank you everyone for always providing me with constructive feedback, which helped me learn and become a better scientist, as well as a better person. I will forever be grateful to all of you.

I would also like to thank Dr. Raheleh Daneshpour at the Pennsylvania State University, who was my collaboration partner for this project and for synthesizing the samples that I have studied. Thank you for being my companion on this journey and for being a friend who I could share both research and life-related problems with. Thank you also for being a gracious host and showing me around when I visited Penn State and teaching me everything about sample synthesis.

Thank you, Dr. Ezra Clark and Prof. Dr. Mike Janik of Penn State University, for being a part of the team and always providing valuable insights about the data I presented in our monthly project meetings.

I would like to thank the other members of the Spectroscopy group for their help and support. Thank you, Dr. Ralph Steininger, for helping me out at the beamline with optimizing the beamline optics and setting up along with Dr. Constantin Wansorra. Thank you, Dr. Raju Edla, for helping me understand some of the electrochemical aspects of conducting experiments with the electrochemical and the operando electrochemical cells and for our conversations regarding both work and life. Thank you, Dr. Elizaveta Pyatenko, for being a very kind and supportive office mate and for always being ready to grab a cup of coffee with me. Thank you, Mary Blankenship, for also being a kind officemate.

I would also like to thank the Heske team at UNLV, for letting me be a part of the several scientific discussions that took place during the group meetings.

Lastly, I would like to thank my friends and family. I would like to thank my mother and father, Nipa and Partha Sengupta, for being wonderfully encouraging and helping me realize my potential throughout my life and while I was working on my thesis. I would also like to thank my grandparents, aunt, uncle and cousin for always believing in me. I would like to thank Siddhartha Banerjee, for his constant presence in my life, especially during my most vulnerable moments while completing my dissertation, his incomparable patience, support and encouragement which helped me stay motivated and grounded during this journey. Last but not the least, I would like to thank my oldest friend, who has always helped me hold on to a part of my childhood over the years.